2014

Nucleation and growth of metals on carbon surfaces

David Victor Appy
Iowa State University

Nucleation and growth of metals on carbon surfaces

by

David V. Appy

A dissertation submitted to the graduate faculty

in partial fulfillment of the requirements for the degree of

DOCTOR OF PHILOSOPHY

Major: Analytical Chemistry

Program of Study Committee:
Patricia A. Thiel, Major Professor
James W. Evans
Robert S. Houk
Emily Smith
Joseph W. Burnett

Iowa State University

Ames, Iowa

2014

Dedicated to my parents, who guided me through difficult times, and to Werner Willoughby, who inspired me to become a chemist and teacher.

TABLE OF CONTENTS

NOMENCLATURE

a-C	Amorphous Carbon
AFM	Atomic Force Microscopy
DC	Direct Current
FCC	Face-centered Cubic
HOPG	Highly Ordered Pyrolitic Graphite
HV	High Voltage
i	Tunneling current (in STM imaging)
I	Current (general)
MBE	Molecular Beam Epitaxy
ML	Monolayer
MPI	Max-Planck Institute (Stuttgart)
NW	Nanowire
P	Power (general)
PBN	Pyrolitic Boron Nitride
PVD	Physical Vapor Deposition
R	Resistance (general)
RF	Radio Frequency
RMS	Root-mean-squared
RT	Room Temperature (300 K)
SEM	Scanning Electron Microscopy
STM	Scanning Tunneling Microscopy

TC	Thermocouple
TEM	Transmission Electron Microscopy
TPD	Temperature-programmed Desorption
UHV	Ultra High Vacuum
VT-SPM	Variable-temperature Scanning Probe Microscopy
V_{tip}	Tip-sample bias (in STM imaging)
XPS	X-ray Photoelectron Spectrometry

ABSTRACT

This thesis work presents an investigation of the basic interaction between metals and the carbon surfaces HOPG and amorphous carbon. This work was motivated by the discovery of a family of metal nanowires which grow as single crystals protruding substantially perpendicular to a substrate, where the substrate is held at elevated temperature (800-1100 K). The most prolific growth is seen for Cu on amorphous carbon substrates. The fabrication and properties of these wires have been pioneered by our collaborator, Dr. Gunther Richter, at the Max Planck Institute for Intelligent Systems in Stuttgart, Germany. They have potential uses in nanoscale mechanical/electrical devices, as chemical/optical sensors and, in the case of magnetic wires, non-rare-earth permanent magnets and high density magnetic storage media. We aim to develop an understanding of the nucleation and growth of these structures, with the ultimate goal of being able to fine-tune their growth with respect to aspect ratio, density, and orientation.

HOPG provides a good starting point for our investigation of NW growth because it is a flat, homogeneous surface with a simple atomic arrangement that can be easily analyzed with STM. Determining the basic energetic parameters for the Cu/HOPG system could ultimately prove useful for modeling nanowire growth. Diffusion barrier (E_d) and critical nucleus size (i) can be extracted from systems exhibiting homogeneous nucleation based on the dependence of island density on temperature and flux, respectively. We present experiments which determine the extent to which homogeneous nucleation occurs in this system. In fact, we find that Cu island nucleation, under the conditions of our experiments, is mediated by defects that are created during the Cu deposition process itself.

Since nanowire growth occurs at elevated temperature, we also explore the Cu/HOPG system at elevated temperatures (300-1300 K) and address the issues of coarsening, desorption, and possible intercalation in this system. We find that coarsening begins at temperatures of 600 K - 700 K, and desorption at 800 K - 900 K.

To determine the differences or similarities between the model carbon substrate (HOPG), and the actual form used in nanowire growth (amorphous carbon), we investigate the interaction between Cu, Ag, and amorphous carbon. We explore changes in the Cu/amorphous carbon surface as a function of coverage and temperature. Ag nanowire samples are annealed to remove the Ag, and then scanned to determine the affect of nanowire growth on the underlying substrate morphology. We identify holes in the amorphous carbon which have the same number density as the metal nanostructures, and were probably caused by growth of the nanostructures.

This work concludes with the growth of metal nanowires on various substrates by MBE and magnetron sputtering, including nanowires of magnetic materials Fe and Ni. Nanowire growth was done both at MPI Stuttgart and at the Ames Laboratory. Long nanowires are grouped as bundles on the surface. We interpret this to mean that growth occurs—at least in part—by incorporation of metal atoms at the base of the nanowire.

CHAPTER 1 - INTRODUCTION

A REVIEW OF TRANSITION METALS ON THE (0001) SURFACE OF GRAPHITE: FUNDAMENTAL ASPECTS OF ADSORPTION, DIFFUSION, AND MORPHOLOGY

Abstract

Presented here is a review of basic information about the interaction of transition metal atoms with the (0001) surface of graphite, especially fundamental phenomena related to growth. Those phenomena involve adatom-surface bonding, diffusion, morphology of metal clusters, interactions with steps and sputter-induced defects, condensation, and desorption. General traits emerge which have not been summarized previously. Some of these features are rather surprising when compared with metal-on-metal adsorption and growth. Opportunities for future work are pointed out.

1.1 Introduction

Graphite is an intriguing support for metals because of its inertness in aggressive environments, as well as its low cost and high abundance. A major application for graphite-supported metals is lithium ion batteries [1, 2]. In fact, the market for these batteries is expanding so quickly that it currently drives the international market in graphite [1]. An important application on the horizon is biofuel conversion, where graphite (or other carbon-based materials) may provide robust supports for catalysts in aqueous media [3].

Adsorption of transition metals and noble metals on graphite has been studied for many years—starting well before the discovery of graphene, carbon nanotubes, or even C_{60}. Actually, adsorption of metals on graphite provides a benchmark and point of entry for understanding

metal interaction with these more-recently discovered forms of carbon. Even more broadly, graphite has been regarded as a good substrate for model investigations of surface phenomena, e.g. catalysis by supported metal particles [4].

Among the metals, alkali metals have received special attention because of their role in batteries, and they have been reviewed thoroughly by Caragiu and Finberg [5]. In this article, we focus on the transition metals including the coinage metals, i.e. metals in groups 3-11, and we exclude the rare earths. ("Metal" henceforth designates this defined set.) We review the literature in addition to providing some new data. We do not attempt to provide a comprehensive overview of the literature (much of which is rather phenomenological), but rather we focus on the *fundamental aspects* of the interaction of metal atoms with a graphite surface. These fundamental aspects include: (1) strength of the metal-carbon adsorption bond; (2) diffusion coefficient; (3) adsorption and desorption kinetics; (4) long-range electronic response of the substrate; (5) shapes of atomic aggregates; and (6) the influence of defects.

It will also be informative to compare some of these aspects of metals on *graphite* with those of metals on *metals*. For the latter, a broad understanding of mechanisms, kinetics, and thermodynamics of deposition, nucleation, and growth has been established [6-9]. To some extent, this conceptual framework is very useful and it can be applied to metals on graphite, but we will show that there are also significant differences. One example is the condensation coefficient as defined in Section 9. For a metal atom on a *metal* surface, at room temperature (nominally 300 K), this quantity can be safely assumed to be unity. For a metal atom on a *graphite* surface, there is considerable evidence that this quantity is less than unity. Another example is the diffusion barrier of a single atom. For metals on metals, diffusion barriers are typically a few tenths of eV, whereas for the same metals on graphite, diffusion barriers can be

lower by an order of magnitude. Differences, such as these in condensation coefficient and diffusion barrier, can require widely different interpretive frameworks for experimental data in the two types of systems.

In this article, we focus on metals deposited via physical vapor deposition, because this technique is most favorable for understanding metal deposition in terms of a sequence of simple atomic processes, beginning with *impingement of single atoms* at the surface. The subsequent sequence can then include diffusion of atoms, nucleation and growth of clusters, desorption, and/or interaction with step edges. There exists a considerable body of complementary work in which *pre-formed metal clusters* are deposited onto the graphite surface. Because that approach can provide a high level of control and surface homogeneity, it holds considerable promise for nanotechnology, but it is not emphasized here. Aspects of that body of work have been summarized elsewhere [10-12].

1.2 Overview of the Experimental Context

Metals can be deposited on graphite using a wide variety of techniques, ranging from wet (chemical) methods to gas-phase methods [11, 13-16]. As mentioned in the Introduction, this article focuses on the method of physical vapor deposition, because in that process, single atoms impinge on the graphite surface, leading most directly to atomic-scale insights.

Before the early to mid-1990s, it was common for the metal to be evaporated in a vacuum chamber normally dedicated to coating samples in preparation for electron microscopy. In these coaters, the base pressure was as high as 10^{-5} mbarr. The sample was then transferred in air to an electron or optical microscope, or (starting in 1986) it could be analyzed via scanning probe microscopies [17-21]. The environments of air, and of low to high vacuum—rather than

continuous ultrahigh vacuum (UHV)—were assumed to be acceptable because of the inertness of graphite. It is true that, even in air, graphite surfaces can often be imaged as smooth terraces that are on the order of a micron wide. On these terraces, atomic-scale images that reflect the honeycomb carbon structure (shown in Fig. 1) are commonly reported, especially using STM [17-21]. Examples of micron-wide terraces, and atomic-scale resolution are shown in Fig. 2(a-b). In fact, because of HOPG's atomic-scale perfection in air, undergraduate laboratory experiments have been designed to image graphite or modified graphite surfaces with scanning probe microscopies, e.g. [22-24].

However, graphite is not completely inert. In a study of Au deposition in the 1960s, it was already reported that exposure to water or cleaning solvents had a strong effect on the density of Au clusters on graphite, based on electron microscopy [25]. More recently, it was found that Au nucleation and growth is significantly different on graphite that has been cleaved in UHV, than on graphite cleaved and allowed to rest in air for several hours [26]. This is probably explained by the adsorption of hydrocarbons, which causes the surface properties of graphene and graphite to change during exposure to air (over a few tens of minutes) [27]. Presumably, the hydrocarbons are too mobile to be imaged effectively with scanning probe techniques, at least at the typical observation temperature of 300 K, so the surface may appear deceptively clean when analyzed with such techniques.

Independent of the environment's effect on the graphite substrate, environment may affect the chemical state of the metal or the distribution of metal on the surface during or after deposition, especially via oxidation or via enhancement of restructuring rates [28]. Recently, for instance, it has been reported that exposure to CO(g) accelerates coarsening of Pd nanoclusters on a graphene surface [29]. In short, there are many reasons to be skeptical about the total

inertness of metal-on-graphite systems, and to value UHV as a component of these experimental studies.

There are various grades and sources of graphite. Highly-oriented pyrolytic graphite (HOPG) is a synthetic form available in large samples with high purity and high structural perfection. (A synthetic form of graphite known as Kish graphite, with lower purity and smaller sample size, can be considered the historical precursor of HOPG [30].) The highest-quality material is employed in X-ray and neutron optics, where the structural quality of HOPG is judged by its mosaic spread.. Grades are usually designated ZYH, ZYB, and ZYA, with ZYA having the smallest mosaic spread ($0.4^{o} \pm 0.1^{o}$) and largest grain size (up to 3 mm) [30].

HOPG cleaves easily along the basal plane. A fresh surface is prepared by pressing on, then peeling off, a piece of tape. A thin sheet of HOPG (as thin as one atomic layer—graphene [31, 32]) clings to the tape and leaves a fresh graphite surface behind. Often, these graphite surfaces exhibit flat, micron-size terraces, but defects are occasionally found. These defects fall into two classes: (1) dislocations and associated stacking faults [25, 33-41], including folds of the top carbon sheet [38]; and (2) small localized defects which may be single-atom vacancies in the top carbon sheet, inclusions, or adsorbates [42-47]. For illustration, an extensively-folded region (type 1 defect) is illustrated in Fig. 2(c). An inclusion (type 2 defect)—with the HOPG lattice visible over the inclusion—is illustrated in Fig. 2(d). Defects of type 1 can be modified or even created under the influence of a scanning probe tip. Defects of type 2 occur at densities ranging from 1×10^{-8} nm^{-2} to 1×10^{-4} nm^{-2} [42-47], with no obvious correlation to HOPG grade. The latter values correspond to 8×10^{-10} to 8×10^{-6} defects per C atom in the surface plane.

Even in the most careful studies, graphite is usually cleaved in air and then transferred to UHV, rather than being cleaved in situ. Following transfer, the surface is often heated before

metal is deposited. The highest reported cleaning temperature, in UHV, is 2500 K [48, 49]. In our own work, we have experimented with thermal treatments in the range 300 K to 1300 K, and have found that heating ZYA or ZYH to 800 K for several tens of minutes in UHV is effective.

Because fundamental energetic and mechanistic information is the objective of this study, this review relies most heavily on experimental studies from the recent literature where deposition and analysis were conducted entirely in UHV, although some papers from other types of experiments are also noted.

As a final comment, in our experience, metals on graphite surfaces are surprisingly difficult to work with, using scanning probe techniques. This is because the tip interacts strongly with the metal particles. The reason for this is discussed further in the following section. Consequently, tip stability and experimental reproducibility can be more challenging than in metal-on-metal experiments. Tip effects are illustrated in Fig. 3.

1.3 Bonding of a Metal Adatom to the Basal Plane

Theory is the source of all information currently available about the adsorption energy (E_a) and adsorption site of metal atoms on graphite. However, two comments about the theoretical landscape are relevant. First, a number of papers nominally model metal adsorption on graphite, but they use a single sheet of sp^2-hybridized carbon to model the carbon surface. Hence, they are more appropriately regarded as models of free-standing *graphene* than *graphite*. This is especially true of work that was conducted before the experimental characterization of graphene in 2004 [31, 32]. Table 1 summarizes values of adsorption energy for several metals. Only a small number of results are shown, because we apply a filter to the literature: models must incorporate two or more carbon sheets in order to be included in this Table.

Second, it is known that London dispersion forces are important in the bonding between graphite sheets. However, before the late 2000's, it was not common to include dispersion forces in DFT. Perhaps for this reason, some theoretical papers reported that a metal atom's adsorption energy was the same, regardless of whether one carbon sheet or multiple carbon sheets were used as the model of graphite [50, 51]. But the values for Cr and Au in Table 1, from the work of Hardcastle et al. [52], clearly show that the metal atom's adsorption energy increases significantly as the number of carbon sheets increases from 1 to 3 when dispersion forces are included. Hence, results for metals on (1-layer) graphene cannot be simply transposed to graphite. Instead, the adsorption energy for a metal on graphene sets the *lower limit* on the value for graphite.

Table 2 compares good values (selected in accord with the discussion above) for adsorption energies of metal adatoms at optimal sites on three substrates: single-layer graphene ($E_{a/graphene}$), graphite ($E_{a/graphite}$), and the densest low-index surface of the respective metal ($E_{a/metal}$). Note that, for the fcc or hcp metals, $E_{a/metal}$ is the binding energy of a single metal atom on the close-packed surface of the same metal, in the natural three-fold hollow growth site. For the bcc metal Cr, $E_{a/metal}$ is the binding energy at the long-bridge site of the (110) surface, which is expected to be the preferred site.

Table 2 shows that a simple qualitative relationship holds true for the 5 metals:

$$E_{a/graphene} < E_{a/graphite} < E_{a/metal} \quad (1)$$

This relationship can probably be applied as a check on the reasonableness of measured or calculated values of $E_{a/graphite}$ for metals not included in the Table. To do this, of course, one

needs access to reliable values for $E_{a/graphene}$ and $E_{a/metal}$. Values of $E_{a/graphene}$ are available elsewhere [53, 54]. With regard to $E_{a/metal}$, this is relatively simple to calculate but it has not been tabulated elsewhere and values are in fact difficult to find in the literature. Therefore, some values are given in Table 3 [55].

Because $E_{a/graphene}$ sets the lower limit in Eq. (1), we briefly review its trends among 3d metals [53, 54]. First consider the variation along a single row. For the first-row 3d-transition metals V through Ni, $E_{a/graphene}$ falls in the range 0.87-1.54 eV except for Cr and Mn. The values for the latter two metals define a deep minimum (corresponding to weak binding) at only 0.18 and 0.16 eV, respectively. Next consider the metals in a single column, group 10: Ni, Pd, Pt. For these metals, $E_{a/graphene}$ ranges from 1.08 to 1.55 eV, i.e. within the same range as most of the first-row transition metals. Finally, consider the coinage metals, group 11: Cu, Ag, and Au. Here, the interaction with graphene is very weak, only 0.02 to 0.23 eV. Based upon this information, the variation in absolute value across a row (up to but not including the coinage metals) is greater than the variation within a column. Specifically, the variation across the first row is 1.38 eV, much greater than the variation in groups 10 and 11, which is only 0.47 and 0.21 eV respectively. Metals near half-filled d-shells (Cr, Mn) and formally filled d-shells (Cu, Ag, Au) have adsorption energies below 0.25 eV, and interact more weakly with graphene than do other metals. In fact, the metals with adsorption energies below about 0.5 eV can be described as *physisorbed*, while the others are *chemisorbed* [56]. Of course, calculations (and measurements!) for more transition metals on graphene will surely emerge to test and refine these generalizations.

For the chemisorbed metals, bonding with the graphene surface is covalent. The bonding-induced change in electron density is mainly localized on the carbon atoms closest to the metal

adatom [53, 54]. Among the physisorbed metals, Au exhibits net electron transfer *from* the substrate *to* the metal adatom, in keeping with the fact that Au is a very electronegative metal [57, 58]. Ag is also exceptional, in that $E_{a/graphene}$ is nearly zero (0.02 eV) and there is little charge transfer, i.e. Ag barely interacts with graphene at all. The other coinage metals, Au and Cu, interact weakly but their bond strengths are not negligible, at 0.10 and 0.23 eV respectively.

As stated in Eq. (1), bonding of metal adatoms with graph*ite* is stronger than bonding to graph*ene*, but to first order, one expects the trends in E_a noted above to be similar for graph*ite*. The reason for the higher adsorption energies on graphite is undoubtedly related to the dispersion forces which bind the carbon sheets, as noted by Hardcastle et al.[52]. However, no detailed analysis is available (to our knowledge) and this topic is ripe for rigorous investigation.

To our knowledge, there are *no direct experimental* measurements or indications of $E_{a/graphite}$. The classic means of measuring adsorption energies is temperature programmed desorption (TPD). However, this is not useful for metals on graphite, because the metal particles grow as three-dimensional clusters (vide infra). Thus, the barrier for a single metal atom to desorb into the gas phase is controlled by its bonding to the metal cluster, not its bonding to graphite. Results from an elegant TPD study of Cu on graphite by Arthur and Cho [48] are consistent with this feature. There, it was found that the desorption barrier of Cu on graphite converged to the enthalpy of vaporization of bulk Cu at a Cu coverage of about 3 layer-equivalents. Deviation to smaller desorption energies at lower Cu coverage can be ascribed to the increasing difference between smaller Cu clusters and bulk metal.

The basal plane of graphite is shown schematically in Fig. 1, with high-symmetry sites labeled. The possible high-symmetry adsorption sites on the basal plane of graphite are the same as on graphene—hollow (H), bridge (B), and top (T)—with one exception. On graphite there are

two types of T sites, due to the ABAB stacking of the carbon sheets. In the T_α site, a carbon atom in the second layer sits directly beneath a carbon atom in the top layer, whereas in the T_β site, the second layer is empty. The best calculations available at present (Table 1) show that the favored site of a Cr adatom is H, of a Pt adatom is B (bridge, also called bond center), and the site of Ag, Au, and Cu adatoms is T_β. The prediction of the T_β site for Au is confirmed by experimental results [52, 59].

The relatively weak interaction between metals and graphite may be related to the common observation of time-dependent changes during STM imaging of these surfaces [60-63]. For example, Clark et al.[61] reported that a small 2D Pt cluster on graphite moved by tens of nm, relative to a defect site, from one image to the next. It is difficult to determine the extent to which such changes are tip-induced, or represent intrinsic dynamic phenomena at the surface. In either case, however, one expects motion and instability to be facilitated by the relatively low value of $E_{a/graphite}$.

The issue of intercalation of metals in graphite also relates to surface adsorption. It is known that adsorbed metals—not only transition metals, but also other types of metals—can be buried beneath sheets of supported *graphene,* e.g. [64-69]. It is also known that some *non-transition metals* can intercalate in graphite surfaces, e.g. [70, 71]. However, we know of no evidence for intercalation of *transition* metal atoms in *graphite* surfaces, at least under the conditions typical of surface science experiments. There is no obvious reason why intercalation of transition metals should not occur, at least at sufficiently high temperature and high metal supersaturation. However, this possibility has rarely (if ever) been entertained when interpreting surface data for adsorption of transition metals on graphite.

1.4 Surface Diffusion

To a good approximation, the diffusion barrier on graphite (and graphene) can be equated to the minimum *difference* in adsorption energies between the favored sites, and high-symmetry locations between favored sites along physically-accessible pathways. This value, ΔE, has been calculated for a few metals on graphite (Table 1). Comparing only values from Ref. [72], for the sake of self-consistency, the trends in $\Delta E_{graphite}$ parallel those in $E_{a,graphite}$. For instance, $\Delta E_{graphite}$ is highest for the strongly-bonded metal Pt, and lowest for the weakly-bonded metal Ag.

Furthermore, the diffusion barrier for a metal on graphite consistently falls below the corresponding metal-on-metal diffusion barrier, but it can be either higher or lower than its diffusion barrier on graphene. For example, for the strongly-bound metal Pt, $\Delta E_{graphite} = 0.16$ eV (Table 1), which is lower than the value $\Delta E_{graphene} = 0.19$ eV [53]. By contrast, for Cu, $\Delta E_{graphite} = 0.02$ eV (Table 1), which is much higher than the value $\Delta E_{graphene} = 0.004$ eV [53]. These trends can be summarized as: $\Delta E_{graphene} \lesssim \Delta E_{graphite} < \Delta E_{metal}$.

There are some experimentally-derived values for the diffusion barrier of metals on HOPG, but these are rather inconsistent. Ganz et al. reported $\Delta E > 0.65$ eV for Ag on HOPG, based on transient observation of a few species thought to be isolated Ag atoms, using STM [59]. However, this is unreasonable, since then for this system $\Delta E >> E_{a/graphite}$ where $E_{a/graphite} = 0.01$ eV according to Table 1. Anton et al. estimated the *difference* $E_{a/graphite}-\Delta E = 0.40$ eV for Au on HOPG [73-75]. To achieve this, they derived the mean diffusion length of an Au atom (before desorption), from densities of metal islands imaged with TEM. Invoking the data of Arthur and Cho [48] to estimate an upper limit of $E_{a/graphite}$, Anton et al. could then set a limit of $\Delta E < 0.24$

eV for Au [73]. This limit is consistent with all of the calculated values shown in Table 1. Comparing the work of Ganz et al. [59] with that of Anton et al. [73-75], implies that the diffusion barrier of Au on graphite is < 0.24 eV while that of Ag is > 0.65 eV. This would be very surprising, and fosters further doubt about the value for Ag.

Diffusion of metal clusters, rather than single metal atoms, is also possible. On some metal surfaces, diffusion of small metal clusters containing several metal atoms is known [9, 76], and is sure to be facilitated even further by the relatively weak binding between metals and graphite. In two interesting studies, large, spherical, size-selected clusters of Au and Pt—containing hundreds or even thousands of atoms—were deposited on graphite. These large clusters were observed to diffuse and (at least for Au) coalesce at 300 K [77, 78]. Diffusion of smaller clusters that form by aggregation of individual atoms on the surface may be similarly feasible, provided that the cluster shape is reasonably compact.

1.5 Morphology of Metal Clusters on Graphite

Kern et al. have derived an approximate energetic criterion by which 2D vs. 3D growth can be predicted under conditions of thermodynamic equilibrium [8]. In terms of the variables we have defined, the condition for 3D growth is

$$E_{a/graphite} < E_{a/metal} \tag{2}$$

(and the inverse is true for 2D growth). It is clear from the discussion in Section 3 [cf. Eq. (1)], and the data in Table 2, that the condition for 3D growth is met easily for Cr, Pt, Cu, Au, and Ag, and one can reasonably expect this condition to be met for most, if not all, other metals. The

expectation of 3D growth is thus based on the relatively weak metal-graphite bond introduced in Section 3.

In general, metals on graphite do exhibit compact 3D growth. Examples of compact 3D clusters are shown in Fig. 4(a-d) [60, 73, 79-81]. (Note that these islands all exist on the terraces of the basal plane.) Sometimes the clusters have discernible facets, although often the facets are only visible after annealing above 300 K. Heating also induces island coarsening, and the consequent increase in the average size makes facets easier to resolve.

There are at least two notable exceptions to the phenomenon of compact 3D growth.

First, a few metals form dendritic multilayer islands around 300 K, as shown in Fig. 4(e-f). Metals which form dendritic islands after growth on graphite at 300 K (or slightly higher) are Au [26, 73, 82-87]. and Pt [81]. (Similar dendritic growth has been observed for the rare earth metal Eu on graphene at 300 K [54, 88, 89].) Dendritic-type shapes are also well known in metal-on-metal growth systems [90-92]. This growth shape is a signature of diffusion-limited aggregation, in which particles attach at edges of islands but have limited mobility along the edges after attachment. Fractal or fractal-like islands of Au and Pt on graphite are more than a single atom thick (hence 3D-like) but are rather flat (hence 2D-like). For instance, Au dendrites are 1 to 2 nm tall (roughly 4-8 atomic layers high), in the low coverage regime where they are separated laterally [73, 83]. This indicates that upward diffusion of Au and Pt atoms becomes improbable beyond a certain thickness. The fact that the dendritic shape is kinetically limited is consistent with the existence of compact 3D crystallites after growth at elevated temperature [74, 82, 84]. Note that most studies of dendritic growth have involved some exposure to non-UHV environments, but dendritic growth is not due to contamination [26].

The second exception is this. Several authors have reported that 3D growth of large clusters, like those shown in Fig. 4, is preceded by the establishment of much smaller 2D islands. This has been reported for Mo [62], Pt [61, 93], Ag [59, 94, 95], Cu [59], and Au [59, 95]. Examples are shown in Fig. 5. Some authors report that these small 2D islands are less susceptible to change during STM scanning, than their larger 3D counterparts [62, 94]. Atomic-scale images indicate a variety of arrangements of metal atoms in these small islands, even within a single investigation [59, 61, 95]. The existence of these small 2D islands on HOPG is difficult to rationalize, in light of the discussion of Section 3, and warrants further clarification.

1.6 Charge Density Modulations

Metal atoms and clusters on graphite induce charge density modulations (CDMs) in the carbon support [96]. CDMs have been reported in STM studies of Ag [94], Mo [62], and Pt [93] on graphite. A signature of the CDM is an apparent $(\sqrt{3} \times \sqrt{3})R30^{o}$ periodicity in the carbon lattice, extending a few nm out from the metal [62, 93, 94, 96]. CDMs are not observed universally, however. For instance, CDMs were observed in one STM study of Ag on graphite [94] but not in another [59].

In metal-on-metal epitaxy, it is known that CDMs in the metal surface can lead to long- and intermediate-range electronic interactions between metal adsorbates [97, 98]. This in turn can influence nucleation and growth of metal islands [97]. Hence, it is not unreasonable to expect that CDMs may influence metal nucleation and growth on graphite, although that topic has not been explored to our knowledge.

1.7 Step Edge Decoration

In addition to forming clusters and islands on the terraces, metals decorate step edges on graphite surfaces [46, 60, 94, 99-102]. This has been shown for many metals under many different conditions. Examples are shown in Fig. 6. Step decoration is also clearly visible in Fig. 4(a) and (e). The steps thus serve as potential templates for one-dimensional nanowires, though individual clusters at steps do not usually merge into uniform, single crystalline nanowires.

Step decoration reflects low binding energy and fast diffusion for metal atoms or small metal clusters on terraces of the basal plane, as discussed above. Consistent with this, calculations show that the binding energy of a metal adatom is higher at the edge of a graphene sheet—which can be taken as a model of a graphite step—than on the 2D part of (1 to 3-layer) graphene [52]. This can be ascribed to the dangling bonds present at the edge of the sheet.

But other adsorbates should also bond more strongly at step edges. Our own work, exemplified in Fig. 7, shows that there is significant variation among step edge shapes on nominally-clean graphite. Fig. 7(a) shows the most common case: The step edge has a square-step-profile, as expected for a clean step, in some regions. In other places the same step shows an upward bump in its profile, which is likely a contaminant. (Note that metals also produce this upward bump.) We thus believe that there is heterogeneity in the cleanliness of step edges on "clean" graphite. Perhaps the binding energies of metals at graphite steps are sufficiently high that they displace typical contaminants, leading to the consistent observations of metal step decoration noted above.

Typically, metal-decorated step edges co-exist with metal clusters on the terraces. However, it has been shown that some conditions of growth yield step decoration exclusively, at least at low metal coverage (a few monolayers or less). One such technique is deposition at—or

annealing to—elevated temperature, as demonstrated with Au [84, 94], and with Fe [79]. This can be viewed as a manifestation of coarsening, and is not unexpected. Another technique leading to pure step decoration is growth from an organometallic precursor, demonstrated with Pt [16].

There have been two reports that HOPG steps of different heights are decorated differently, though both involved sample transfers in air [25, 94]. In the first, Hennig reported SEM data showing that "the capacity for a [HOPG] step to capture an adatom [of Ag or Au], i.e. to act as a perfect adatom 'sink' and then nucleate a cluster, seems to increase with step height." He concluded that heights below 3 atomic layers were inactive [25]. Later, Francis et al. reached the same conclusion based upon STM work with the same systems [94]. In spite of many experimental observations of step decoration, these are the only two reports of a dependence on step height in the literature.

Our own work indicates that the reported height-dependence of metal attachment may be spurious. Fig. 8 shows steps on graphite that are 1-, 2-, 3-, and 5-layers high, following physical vapor deposition of Cu. Steps are preferentially decorated in all cases, with the Cu clusters significantly higher than the adjoining graphite terraces. Each image was taken in a separate experiment. There is no evidence that smaller steps are more inert. Any difference in the probability for metal capture at different steps is more likely to be due to the degree of pre-decoration (contamination), illustrated in Fig. 7.

An interesting variant of step decoration involves circular step edges, which can be formed by oxidizing graphite at elevated temperature [25, 46, 99-101, 103]. Oxidation etches away the graphite, starting at pre-existing defects and moving outward in a circle. This forms circular, flat-bottom pits, sometimes called "vacancy loops"[25] or "molecule corrals." [46]

These circular step edges can then be decorated with metals, as first demonstrated by Hennig [25]. An example of Hennig's early work is shown in Fig. 9(a) [25], and an example of more recent work from McBride et al. [46] in Fig. 9(b). The morphology that can be created in this way is quite striking.

1.8 Role of Terrace Defects

In order to clarify the role of localized terrace defects in metal growth—especially carbon atom vacancies—several groups have created artificial defects via ion sputtering, and have studied metal deposition on these surfaces [60, 79, 81, 104]. Examples of STM images of grown metals are shown in Fig. 11. Comparison with the more perfect surfaces shows that, on the sputtered surfaces, metal clusters are more rounded, have a narrower size distribution, and are much more numerous. This is consistently attributed to preferential nucleation and pinning at the sputter-induced defect sites. The metal coverage is also higher on the sputtered surfaces, which is attributed to an increased condensation coefficient (vide infra). Interestingly, the metal clusters on sputtered graphite are easier to image with STM than on pristine graphite, suggesting that defect sites can help to stabilize the metal clusters against tip interactions.

Considerable work has been done to investigate deposition of *pre-formed metal clusters* on graphite substrates that had been deliberately damaged or patterned with an ion beam, e.g. [105-107]. This approach is quite promising for developing ordered arrays of pinned metal nanoparticles, including nanoparticles of magnetic alloys [105]. It has even been shown that the metal clusters themselves can be deposited with sufficient kinetic energy to create defects in the carbon surface upon impact [11, 108].

1.9 Condensation and Desorption

In this section we will focus on the condensation coefficient, σ. We define this, after Venables [109], as the total amount of metal on the graphite surface divided by the total (time-integrated) metal flux. This is the quantity which is most easily measured and most important in a practical sense, although its derivative, σ', has greater basic physical significance. This quantity, σ', is the instantaneous condensation coefficient, i.e. the instantaneous change in adsorbate population per unit flux. Both quantities reflect the efficiency with which atoms accrue on a surface, as opposed to being reflected, or trapped and then desorbed, into the gas phase. (Our definitions of these terms are noteworthy because condensation coefficient and its derivative belong to a group of closely-related terms, including sticking coefficient and accommodation coefficient, whose usage varies slightly among different communities, e.g. [56, 109-111].)

A number of authors have observed that at 300 K, σ is less than unity for metal atoms on graphite [48, 60, 73, 81]. Usually, this conclusion is based on evaluating the amount of metal on the surface in relation to the total flux that impinged on the surface. For instance, Lopez-Salido et al. [60], using both STM and XPS, found that the amount of Ag deposited on a pristine HOPG surface was only 0.1 times that on a heavily sputtered surface. Howells et al. [81] concluded that $\sigma < 0.1$ for Pt on graphite, by measuring the Pt coverage on graphite vs. its coverage on a Ta plate close to the sample, with XPS.

In a different approach, Arthur and Cho [48] employed the method of King and Wells [112] to obtain σ'. With this method, the intensity of a scattered beam is measured with a mass spectrometer as a function of time, after a shutter is opened to allow impingement of an incident

gas beam on the sample. For Cu and Au on graphite, Arthur and Cho observed that the scattered beam intensity is initially high and decreases steadily with time, as illustrated in Fig. 10. This corresponds to an initially low value of σ' that increases with time (with metal coverage). They interpreted this to mean that a metal atom has only a short lifetime on graphite before it desorbs again into the gas phase. As metal clusters nucleate, incoming metal atoms become increasingly likely to find their way into existing metal clusters, from which desorption is essentially impossible at 300 K. Arthur and Cho found that for both Cu and Au, $\sigma' = 0.05$ initially, and σ' approaches 1 at high metal coverage. The adsorption data were fit well with a kinetic model in which the growing clusters are 2D rather than 3D. This is consistent with the (puzzling) observations of small 2D islands noted above.

The observation of σ (or σ') < 1 may be surprising to scientists who work with metals on other types of solid surfaces (metals, oxides, semiconductors), where condensation coefficients are (reasonably) assumed to be unity at ambient temperature. For some metals, the different behavior on graphite may be attributable to low adsorption energy. For instance, at 300 K, the desorption rate for a coinage metal adatom on graphite is appreciable. For Au, $E_{a,graphite} = 0.56$ eV (cf. Table 1). If the pre-exponential factor for desorption is 10^{13} s^{-1}, then the residence time of an Au adatom on graphite is only 0.5 ms at 300 K. This value is consistent with the upper limit of 10 ms placed by Arthur and Cho [48]. For comparison, $E_{a,metal}$ of an Au adatom on unreconstructed Au(111) is 2.32 eV (Table 3), which corresponds to a residence time of at least 10^{27} s at 300 K.

Desorption cannot be the sole reason, however, for σ (or σ') < 1 for all metals on HOPG. For Pt, $E_{a,graphite} = 2.16$ eV (Table 1), so its residence time at 300 K should be very long—10^{24} s—yet Howells et al. [81] found σ < 0.1. To reconcile these two points, one must conclude that

the adsorption rate is very low, *independent* of the desorption rate, at least for Pt; in other words, many metal atoms are reflected without adsorbing.

Analysis of the residence time for Au, from a different perspective, leads to the same conclusion. A residence time of 0.5 ms at 300 K would allow a diffusing adatom to move ca. 20 μm, using a diffusion barrier of 0.011 eV (from Table 1). Thus, a diffusing Au atom would be captured at a step before it would desorb. So even for Au, which is one of the more weakly-bound metals, desorption is not sufficient to account for $\sigma < 1$.

In adsorption, the incident atom has a certain kinetic energy (at least equal to the thermal energy of the evaporator—of order a few tenths of eV). In order for adsorption to occur, this incident energy must be dissipated efficiently by the surface. Inefficient energy transfer (accommodation) may by the reason $\sigma < 1$ for metals on graphite. In contrast, there have been many studies of metal adsorption on graphene, but no indication that $\sigma < 1$ at 300 K, suggesting that the number of coupled carbon layers is crucial in energy dissipation.

In summary, reflection (without adsorption) must be considered as a possible pathway for metal atoms impinging on the basal plane of graphite. To our knowledge, there have been no studies of the dynamics of metal-graphite scattering, other than the molecular beam work by Arthur and Cho [48]. Further investigations—including theoretical ones—would be enlightening, as well as comparisons of metal condensation on graph*ite* vs. graph*ene*.

1.10 Conclusions

Metal adsorption and growth on the basal plane of graphite has been studied for many years. Experimentally, metals on graphite are surprisingly difficult to work with, due to (possible) effects of non-UHV environments, and difficulties in imaging with scanning probe

techniques due to the relatively-low adsorption energy of the metals. In this review we have summarized some of the consistent observations, and pointed out some of the inconsistent ones as well. There are opportunities for clarification and expansion on many points—systematic trends in energetics of adsorption and diffusion for different metals, trends in energetics with the number of carbon layers (i.e. progressing from graphene to graphite), adsorption dynamics, and stability of 2D vs. 3D clusters. We think that there is a special opportunity for simulations and modeling to contribute to our understanding of these issues at this point in time.

More specifically, with regard to the adsorption energies, we propose that the adsorption energy of a metal on graph*ite* is bracketed by its adsorption energy on graph*ene*, and on itself. This relationship is consistent with values that are currently available, but bears further testing. This relationship leads directly to the expectation that metal clusters on graphite adopt 3D rather than 2D shapes. Hence, it is puzzling that there are several reports of (small) 2D clusters in the literature. These reports exist even for the coinage metals, where the driving force for 3D growth should be strongest.

A limited amount of DFT results suggests that the single-atom diffusion barrier on graphite terraces is greater than or comparable to the diffusion barrier on graphene. On graphite, step edges bind metal atoms more strongly than terraces. This energetic difference, plus the low terrace diffusion barrier, leads to facile decoration of steps. Preferential step decoration has been observed in many experimental studies, despite the possibility that step edges may also be preferential sites for impurities.

Finally, there are several indications that the condensation coefficient of a metal is not unity at 300 K. This may be due the tendency for the metal to reflect rather than adsorb. The

dynamics of metal atom scattering, and how it is influenced by the number of carbon layers, warrants further investigation.

Acknowledgments

Contributions by DA, HL, CZW, MCT, and PAT were supported by the U.S. Department of Energy (USDOE), Office of Basic Energy Sciences, Materials Sciences and Engineering Division through the Ames Laboratory Materials Science program. Work by DJL was supported by the U.S. Department of Energy (USDOE), Office of Basic Energy Sciences, Division of Chemical Sciences, Geosciences, and Biosciences through the Ames Laboratory Chemical Physics program. The work was performed at Ames Laboratory which is operated for the USDOE by Iowa State University under Contract No. DE-AC02-07CH11358. JWE's contribution was supported by NSF Grant CHE-1111500.

References

[1] S. Moores, A. Miller, Industrial Minerals, http://www.indmin.com/Article/3315690/Tesla-battery-plant-will-need-6-new-flake-graphite-mines.html

[2] R. Yazami, P. Touzain, J. Power Sources **9**, 365 (1983).

[3] E.L. Kunkes, D.A. Simonetti, R.M. West, J.C. Serrano-Ruiz, C.A. Gärtner, J.A. Dumesic, **322**, 417 (2008).

[4] A. Piednoir, E. Perrot, S. Granjeaud, A. Humbert, C. Chapon, C.R. Henry, Surf. Sci. **391**, 19 (1997).

[5] M. Caragiu, S. Finberg, J. Phys: Condens. Matter. **17**, R995 (2005).

[6] T. Michely, J. Krug, Islands, Mounds, and Atoms: Patterns and Processes in Crystal Growth Far from Equilibrium, Springer Verlag, Berlin, 2004.

[7] J.W. Evans, P.A. Thiel, M.C. Bartelt, Surf. Sci. Reports **61**, 1 (2006).

[8] R. Kern, G.L. Lay, J.J. Metois, in: E. Kaldis (Ed.), Current Topics in Materials Science, Vol. 3, North-Holland, Amsterdam, 1979, p 135.

[9] G. Antczak, G. Ehrlich, Surface Diffusion. Metals, Metal Atoms, and Clusters, Cambridge University Press, Cambridge, UK (2010).

[10] H. Hövel, I. Barke, Prog. Surf. Sci. **81**, 53 (2006).

[11] C. Xirouchaki, R.E. Palmer, Phil. Trans. Royal Soc. Lond. A **362**, 117 (2004).

[12] A. Perez, P. Melinon, V. Dupuis, L. Bardotti, B. Masenelli, F. Tournus, B. Prevel, J. Tuaillon-Combes, E. Bernstein, A. Tamion, N. Blanc, D. Tainoff, O. Boisron, G.

Guiraud, M. Broyer, M. Pellarin, N. Del Fatti, F. Vallee, E. Cottancin, J. Lerme, J.L. Vialle, C. Bonnet, P. Maioli, A. Crut, C. Clavier, J.L. Rousset, F. Morfin, Int. J. Nanotechnology **7**, 523 (2010).

[13] C.R.I. Rao, D.C. Trivedi, Coordination Chemistry Reviews **249**, 613 (2005).

[14] R. Dolbec, E. Cirissou, M. Chaker, D. Guay, F. Rosei, M.A. El Khakani, Phys. Rev. B **70**, 201406 (2004).

[15] C.-W. Hu, A. Kasuya, A. Wawro, N. Horiguchi, R. Czajka, Y. Nishina, Y. Saito, H. Fujita, Mat. Sci. & Eng. **A217/218**, 103 (1996).

[16] H.-B.-R. Lee, S.H. Baeck, T.F. Jaramillo, S.F. Bent, Nano Lett. (2013).

[17] S.I. Park, C.F. Quate, Appl. Phys. Lett. **48**, 112 (1986).

[18] R.J. Colton, S.M. Baker, R.J. Driscoll, M.G. Youngquist, J.D. Baldeschwieler, W.J. Kaiser, J. Vac. Sci. Technol. A 349 (1988).

[19] G. Binnig, H. Fuchs, C. Gerber, H. Rohrer, E. Stoll, E. Tosatti, Europhys. Lett. **1**, 31 (1986).

[20] P.K. Hansma, V.B. Elings, O. Marti, C.E. Bracker, Science **242**, 209 (1988).

[21] T.R. Albrecht, C.F. Quate, J. Appl. Phys. **62**, 2599 (1987).

[22] C.-J. Zhong, L. Han, M.M. Maye, J. Luo, N.N. Kariuki, W.E. Jones Jr., J. Chem. Ed **80**, 194 (2003).

[23] K. Aumann, K.C. Muyskens, K. Sinniah, J. Chem. Ed **80**, 187 (2003).

[24] B.W. Ewers, l.E. Schuckman, J.D. Batteas, J. Chem. Ed **91**, 283 (2014).

[25] G.R. Hennig, in: P.L. Walker Jr. (Ed.), Chemistry and Physics of Carbon, Vol. 2, Marcel Dekker, Inc., New York (1966) p. 1.

[26] T.P. Darby, C.M. Wayman, J. Cryst. Growth **28**, 41 (1975).

[27] Z. Li, Y. Wang, A. Kozbial, G. Shenoy, F. Zhou, R. McGinley, P. Ireland, B. Marganstein, A. Kunkel, S.P. Surwade, L. Li, H. Liu, Nature Materials **12**, 925 (2013).

[28] P.A. Thiel, M. Shen, D.-J. Liu, J.W. Evans, J. Vac. Sci. Technol. A **28**, 1285 (2010).

[29] T. Gerber, J. Knudsen, P.J. Feibelman, E. Granas, P. Stratmann, K. Schulte, J.N. Andersen, T. Michely, ACS Nano **7**, 2020 (2014).

[30] Structure Probe Inc., http://www.2spi.com/catalog/new/hopgsub.php

[31] K.S. Novoselov, Science **306**, 666 (2004).

[32] A.K. Geim, K.S. Novoselov, Nat Mater **6**, 183 (2007).

[33] S. Amelinckx, P. Delavignette, J. Appl. Phys. **31**, 2126 (1960).

[34] G.K. Williamson, Proc. Royal Soc. Lond. A. **257**, 457 (1960).

[35] S.R. Snyder, T. Foecke, H.S. White, W.W. Gerberich, J. Mat. Res. **7**, 341 (1992).

[36] J.E. Snyder, M.H. Kryder, J. Appl. Phys. **73**, 5551 (1993).

[37] P.J. Ouseph, Phys. Rev. B **53**, 9610 (1996).

[38] H.-V. Roy, C. Kallinger, K. Sattler, Surf. Sci. **407**, 1 (1998).

[39] Y. Kobayashi, K. Takai, K.-i. Fukui, T. Enoki, K. Harigaya, Y. Kaburagi, Y. Hishiyama, Phys. Rev. B **69**, 035418 (2004).

[40] S. Hattendorf, A. Georgi, M. Liebmann, M. Morgenstern, Surf. Sci. **610**, 53 (2013).

[41] S. Amelinckx, P. Delavignette, M. Heerschap, in: P.L. Walker Jr. (Ed.), Chemistry and Physics of Carbon, Vol. 1, Marcel Dekker, Inc., New York (1965) p. 1.

[42] X. Chu, L.D. Schmidt, Carbon **29**, 1251 (1991).

[43] H.-C. Chang, A.J. Bard, J. Am. Chem. Soc. **113**, 5588 (1991).

[44] F. Stevens, L.A. Kolodny, T.P. Beebe Jr., J. Phys. Chem. B **102**, 10799 (1998).

[45] J.G. Kushmerick, K.F. Kelly, H.P. Rust, N.J. Halas, P.S. Weiss, J. Phys. Chem. B **103**, 1619 (1999).

[46] J.D. McBride, B. Van Tassell, R.C. Jachmann, T.P. Beebe, J. Phys. Chem. B **105**, 3972 (2001).

[47] J.R. Hahn, Carbon **43**, 1506 (2005).

[48] J.R. Arthur, A.Y. Cho, Surf. Sci. **36**, 641 (1973).

[49] J.J. Lander, J. Morrison, J. Appl. Phys. **35**, (1964).

[50] D.M. Duffy, J.A. Blackman, P.A. Mulheran, S.A. Williams, J. Magnetism and Magnetic Materials **177–181**, 953 (1998).

[51] J. Akola, H. Häkkinen, Phys. Rev. B **74**, 165404 (2006).

[52] T.P. Hardcastle, C.R. Seabourne, R. Zan, R.M.D. Brydson, U. Bangert, Q.M. Ramasse, K.S. Novoselov, A.J. Scott, Phys. Rev. B **87**, 195430 (2013).

[53] X. Liu, C.Z. Wang, M. Hupalo, W.C. Lu, M.C. Tringides, Y.X. Yao, K.M. Ho, Phys. Chem. Chem. Phys. **14**, 9157 (2012).

[54] X. Liu, C.-Z. Wang, M. Hupalo, H.-Q. Lin, K.-M. Ho, M.C. Tringides, Crystals **3**, 79 (2013).

[55] D.-J. Liu, Unpublished results (2014).

[56] K. Oura, V.G. Lifshits, A.A. Saranin, A.V. Zotov, M. Katayama, Surface Science. An Introduction., Springer, Berlin, 2003.

[57] R.G. Pearson, Inorg. Chem. **27**, 734 (1988).

[58] S.L. Samal, A. Pandey, D.C. Johnston, J.D. Corbett, G.J. Miller, Chem. Mater. **26**, 3209 (2014).

[59] E. Ganz, K. Sattler, J. Clarke, Surf. Sci. **219**, 33 (1989).

[60] I. Lopez-Salido, D.C. Lim, Y.D. Kim, Surf. Sci **588**, 6 (2005).

[61] G.W. Clark, L.L. Kesmodel, J. Vac. Sci. Technol. B **11**, 131 (1993).

[62] H. Xu, H. Permana, Y. Lu, K.Y.S. Ng, Surf. Sci. **325**, 283 (1995).

[63] J. Shen, C. Zhu, Z. Ma, S. Pang, Z. Xue, Appl. Surf. Sci. **60/61**, 648 (1992).

[64] A.G. Starodubov, M.A. Medvetski, A.M. Shikin, V.K. Adamchuk, Phys. Solid State **46**, 1340 (2004).

[65] A.M. Shikin, G.V. Prudnikova, V.K. Adamchuk, F. Moresco, K.H. Rieder, Phys. Rev. B **62**, 13202 (2000).

[66] L. Huang, Y. Pan, M. Gao, W. Xu, Y. Que, H. Zhou, Y. Wang, S. Du, H.-J. Gao, Appl. Phys. Lett. **99**, (2011).

[67] Y.S. Dedkov, A.M. Shikin, V.K. Adamchuk, S.L. Molodtsov, C. Laubschat, A. Bauer, G. Kaindl, Phys. Rev. B **64**, 035405 (2001).

[68] R. Addou, A. Dahal, M. Batzill, Surf. Sci. **606**, 1108 (2012).

[69] C. Virojanadara, S. Watcharinyanon, A.A. Zakharov, L.I. Johansson, Phys. Rev. B **82**, 205402 (2010).

[70] G.V. Prudnikova, A.G. Vjatkin, A.V. Ermakov, A.M. Shikin, V.K. Adamchuk, J. Electron Spectroscopy and Related Phenomena **68**, 427 (1994).

[71] M. Büttner, P. Choudhury, J. Karl Johnson, J.T. Yates Jr, Carbon **49**, 3937 (2011).

[72] H. Lei, D. Appy, P.A. Thiel, K.-M. Ho, M.C. Tringides, M. Hupalo, C.-Z. Wang, in preparation (2014).

[73] R. Anton, I. Schneidereit, Phys. Rev. B **58**, 13874 (1998).

[74] R. Anton, P. Kreutzer, Phys. Rev. B **61**, 16077 (2000).

[75] R. Anton, Phys. Rev. B **70**, 245405 (2004).

[76] G.L. Kellogg, Surf. Sci. Reports **21**, 1 (1994).

[77] P. Jensen, L. Bardotti, J.-L. Barrat, N. Combe, V. Dupuis, M. Jamet, P. Melinon, B. Prevel, J. Tuaillon-Combes, A. Perez, in: H.S. Nalwa (Ed.), Nanoclusters and Nanocrystals, American Scientific Publishers (2003).

[78] L. Bardotti, F. Tournus, P. Mélinon, M. Pellarin, M. Broyer, Phys. Rev. B **83**, 035425 (2011).

[79] I.N. Kholmanov, L. Gavioli, M. Fanetti, M. Casella, C. Cepek, C. Mattevi, M. Sancrotti, Surf. Sci. **601**, 188 (2007).

[80] S.W. Poon, A.T.S. Wee, E.S. Tok, Surf. Sci. **606**, 1586 (2012).

[81] A.R. Howells, L. Hung, G.S. Chottiner, D.A. Scherson, Solid State Ionics **150**, 53 (2002).

[82] C.M. Wayman, T.P. Darby, J. Cryst. Growth **28**, 53 (1975).

[83] R. Nishitani, A. Kasuya, S. Kubota, Y. Nishina, J. Vac. Sci. Technol. B **9**, 806 (1991).

[84] C.E. Cross, J.C. Hemminger, R.M. Penner, Langmuir **23**, 10372 (2007).

[85] T.P. Darby, C.M. Wayman, J. Crystal Growth **29**, 98 (1975).

[86] R. Nishitani, A. Kasuya, S. Kubota, Y. Nishina, Z. Phys. D - Atoms, Molecules and Clusters **19**, 333 (1991).

[87] L. Strong, D.F. Evans, W.L. Gladfelter, Langmuir **7**, 442 (1991).

[88] X. Liu, M. Hupalo, C.-Z. Wang, W.-C. Lu, P.A. Thiel, K.-M. Ho, M. Tringides, Phys. Rev. B **86**, 081414(R) (2012).

[89] M. Hupalo, X. Liu, C.-Z. Wang, W.-C. Lu, Y.-X. Yao, K.-M. Ho, M. Tringides, Advanced Materials **23**, 2082 (2012).

[90] R.Q. Hwang, Phys. Rev. Lett. **76**, 4757 (1996).

[91] R.Q. Hwang, J. Schröeder, C. Günther, R.J. Behm, Phys. Rev. Lett. **67**, 3279 (1991).

[92] E.J. Cox, M. Li, P.-W. Chung, C. Ghosh, T.S. Rahman, C.J. Jenks, J.W. Evans, P.A. Thiel, Phys. Rev. B **71**, 115414 (2005).

[93] J. Xhie, K. Sattler, U. Müller, N. Venkateswaran, G. Raina, Phys. Rev. B **43**, 8917 (1991).

[94] G.M. Francis, I.M. Goldby, L. Kuipers, B. von Issendorff, R.E. Palmer, J. Chem. Soc., Dalton Trans. 665 (1996).

[95] E. Ganz, K. Sattler, J. Clarke, Phys Rev. Lett. **60**, 1856 (1988).

[96] H.A. Mizes, J.S. Foster, Science **244**, 559 (1989).

[97] M.L. Merrick, W. Luo, K.A. Fichthorn, Prog. Surf. Sci. **72**, 117 (2003).

[98] M. Ternes, M. Pivetta, F. Patthey, W.-D. Schneider, Prog. Surf. Sci. **85**, 1 (2010).

[99] Y.-J. Zhu, T.A. Hansen, S. Ammermann, J.D. McBride, T.P. Beebe, J. Phys. Chem. B **105**, 7632 (2001).

[100] H. Hövel, T. Becker, A. Bettac, B. Reihl, M. Tschudy, E.J. Williams, J. Appl. Phys. **81**, 154 (1997).

[101] H. Hövel, T. Becker, A. Bettac, B. Reihl, M. Tschudy, E.J. Williams, Appl. Surf. Sci. **115**, 124 (1997).

[102] C.M. Whelan, C.J. Barnes, Appl. Surf. Sci. **119**, 288 (1997).

[103] J.M. Thomas, in: P.L. Walker Jr. (Ed.), Chemistry and Physics of Carbon, Vol. 1, Marcel Dekker, Inc., New York (1965) p. 121.

[104] R.M. Nielsen, S. Murphy, C. Strebel, M. Johansson, J.H. Nielsen, I. Chorkendorff, Surf. Sci. **603**, 3420 (2009).

[105] A. Hannour, L. Bardotti, B. Prevel, E. Bernstein, P. Melinon, A. Perez, J. Gierak, E. Bourhis, D. Mailly, Surf. Sci. **594**, 1 (2005).

[106] P. Melinon, A. Hannour, L. Bardotti, B. Prevel, J. Gierak, E. Bourhis, G. Faini, B. Canut, Nanotechnology **19**, 235305 (2008).

[107] B. Prevel, L. Bardotti, S. Fanget, A. Hannour, P. Melinon, A. Perez, J. Gierak, G. Faini, E. Bourhis, D. Mailly, Appl. Surf. Sci. **226**, 173 (2004).

[108] S. Gibilisco, M. Di Vece, S. Palomba, G. Faraci, R.E. Palmer, J. Chem. Phys. **125**, 084704 (2006).

[109] J.A. Venables, Introduction to Surface and Thin Film Processes, Cambridge University Press, Cambridge (2000).

[110] M.W. Roberts, C.S. McKee, Chemistry of the Metal-Gas Interface, Clarendon Press, Oxford (1978).

[111] G.A. Somorjai, Y. Li, Introduction to Surface Chemistry and Catalysis, John Wiley & Sons, Inc., Hoboken, New Jersey, USA (2010).

[112] D.A. King, M.G. Wells, Proc. Royal Soc. Lond. A. **339**, 245 (1974).

[113] F. Atamny, T. Bürgi, R. Schlögl, A. Baiker, Surf. Sci. **475**, 140 (2001).

[114] D.M. Duffy, J.A. Blackman, Surf. Sci. **415**, L1016 (1998).

[115] G.M. Wang, J.J. BelBruno, S.D. Kenny, R. Smith, Surf. Sci. **541**, 91 (2003).

[116] G.M. Wang, J.J. BelBruno, S.D. Kenny, R. Smith, Phys. Rev. B **69**, 195412 (2004).

[117] P. Jensen, X. Blase, P. Ordejón, Surf. Sci. **564**, 173 (2004).

[118] Y. Shu, J.-M. Zhang, K.-W. Xu, V. Ji, J. Phys. Chem. C **113**, 16031 (2009).

[119] D.-J. Liu, Phys. Rev. B **81**, 035415 (2010).

[120] M. Marz, K. Sagisaka, D. Fujita, Beilstein J. Nanotechnol. **4**, 406 (2013).

Tables

Table 1
Values of $E_{a/graphite}$ calculated from DFT for various metals. Other parameters are diffusion barrier (ΔE), charge transfer (Δq) relative to the the charge on the neutral adatom, and internuclear distance between adatom and nearest carbon atom (d). Only calculated values using 2 or more carbon sheets are shown, with the exception of cases where 1-layer values are part of a group that includes multi-layer values, since such groups illustrate trends. High-symmetry adsorption sites are on-top over α carbon (T_α), on-top over β carbon (T_β), top unspecified (T), bridge (B), and hollow (H). See Fig. 1. Note that the B site is sometimes named bond center site.

Metal	Ref	Method	No. of Carbon Layers	Corrected for Dispersion Forces?	Preferred Binding Site (see Fig. 1)	$E_{a/graphite}$ (in eV)	$\Delta E_{graphite}$ (in eV)	Δq (in eV)	d (in Å)
Cr	[61]	DFT - GGA	1 2 3	yes	H H H	0.542 0.738 0.832	0.022 0.021 0.022		2.056 2.049 2.025
Pt	[104]	DFT – LSDA	2	no	T_β/B	1.11 (both sites)		0.49(T_β) 0.46(B)	
	[73]	DFT-optB88	4	yes	B	1.87	0.161		1.983
Cu	[73]	DFT-optB88	4	yes	T_β	0.512	0.015		2.10
Ag	[105]	DFT - LDA	2	no	T_β	0.54		0.26	2.46
	[73]	DFT-optB88	4	yes	T_β	0.282	0.006		2.87
Au	[61]	DFT - GGA	1 2 3	yes	T T_β T_β	0.380 0.543 0.612	0.007 0.024 0.025		3.08 2.66
	[60]	DFT - GGA	2	no	T	0.51	0.04-0.05	-0.14	
	[106]	DFT - LDA	4	no	T_β	0.674	0.04-0.06	-0.165	2.70
	[107]	DFT - LDA	1 2	no	T T	0.66-0.89 0.68-0.80			
	[73]	DFT-optB88	4	yes	T_β	0.495	0.010		2.66

Table 2
Comparison between the best available values of $E_{a/graphite}$ (selected from Table 1), $E_{a/graphene}$, and $E_{a/metals}$ (latter values given more fully in Table 3). All values come from DFT calculations. All calculations for $E_{a/graphite}$ include dispersion force correction.

Adatom	$E_{a/graphene}$ (in eV)	$E_{a/graphite}$ (in eV)	$E_{a/metal}$ (in eV)
Cr	0.187 [62]	0.832 [61]	3.41 [64]
Pt	1.552 [62]	1.869 [73]	4.60 [108] 4.50 [64]
Cu	0.227 [62]	0.512 [73]	2.27 [64]
Ag	0.021 [62]	0.282 [73]	1.91 [64]
Au	0.096 [62]	0.495 [73]	2.32 [64]

Table 3
Self-adsorption energies of some transition metals [64]. The adsorption site for adatoms on fcc, hcp, and bcc metals is assumed to be fcc, hcp, and long bridge, respectively. Values are calculated using DFT-PBE, averaging results from 3 to 5 layer slabs, with 4 surface atoms on each side of the clean slab [109].

fcc metal	$E_{a,metal}$ (eV)	hcp metal	$E_{a,metal}$ (eV)	bcc metal	$E_{a,metal}$ (eV)
Rh(111)	4.54	Ti(0001)	4.55	Ta(110)	7.00
Ir(111)	5.52	Zr(0001)	4.76	Cr(110)	3.41
Ni(111)	3.62			Mo(110)	5.54
Pd(111)	2.87			W(110)	7.41
Pt(111)	4.50			Fe(110)	4.42
Cu(111)	2.27				
Ag(111)	1.91				
Au(111)	2.32				

Figures

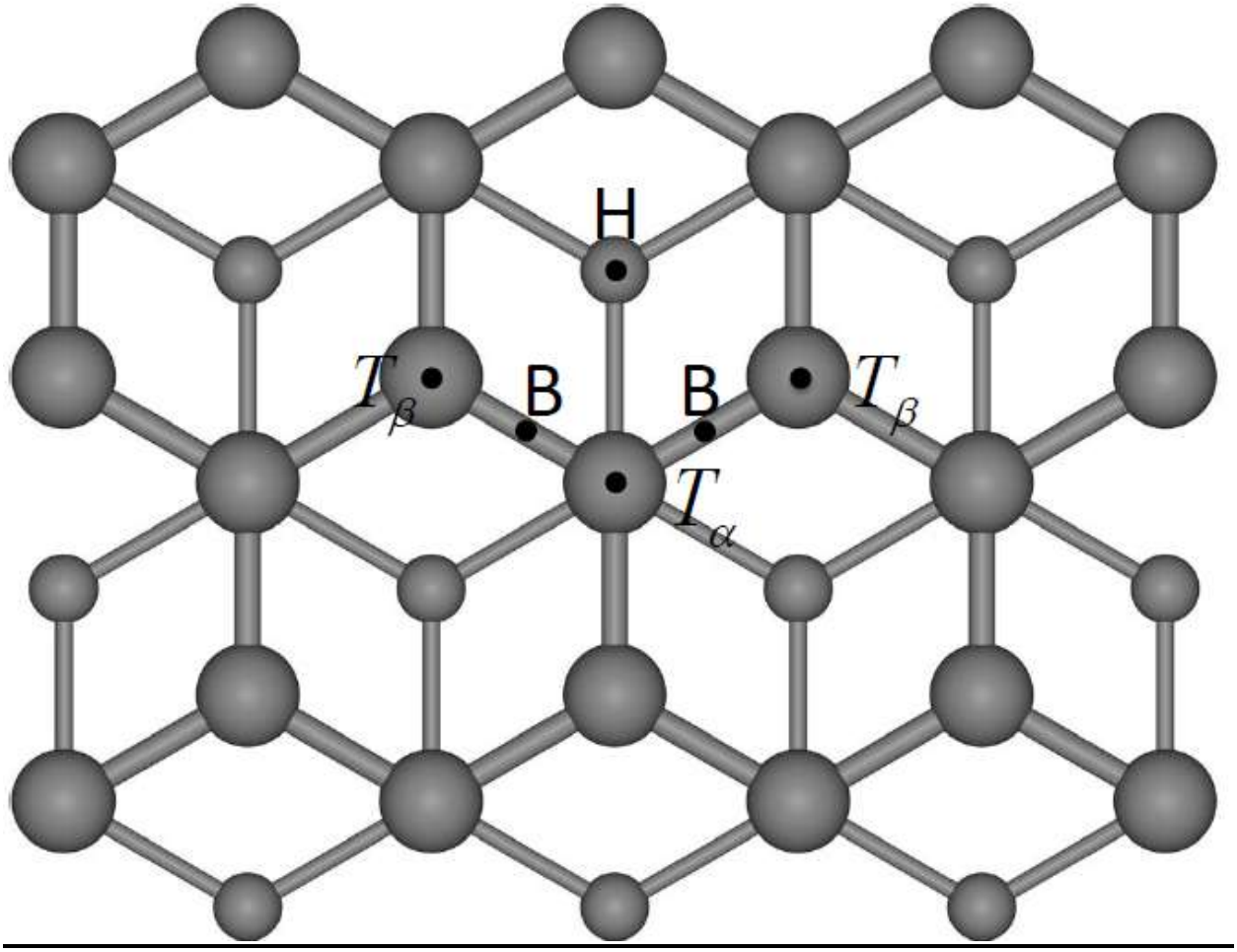

Fig. 1
Schematic diagram of the (0001) plane, i.e. basal plane, of graphite. The ABA stacking pattern of graphite results in two types of surface carbon atoms, one sitting directly above a carbon atom in the layer beneath (labeled alpha (α)), and the other sitting above a void in the layer beneath (labeled beta (β)). Larger gray circles are C atoms in the top plane, while smaller gray circles are C atoms in the second plane.

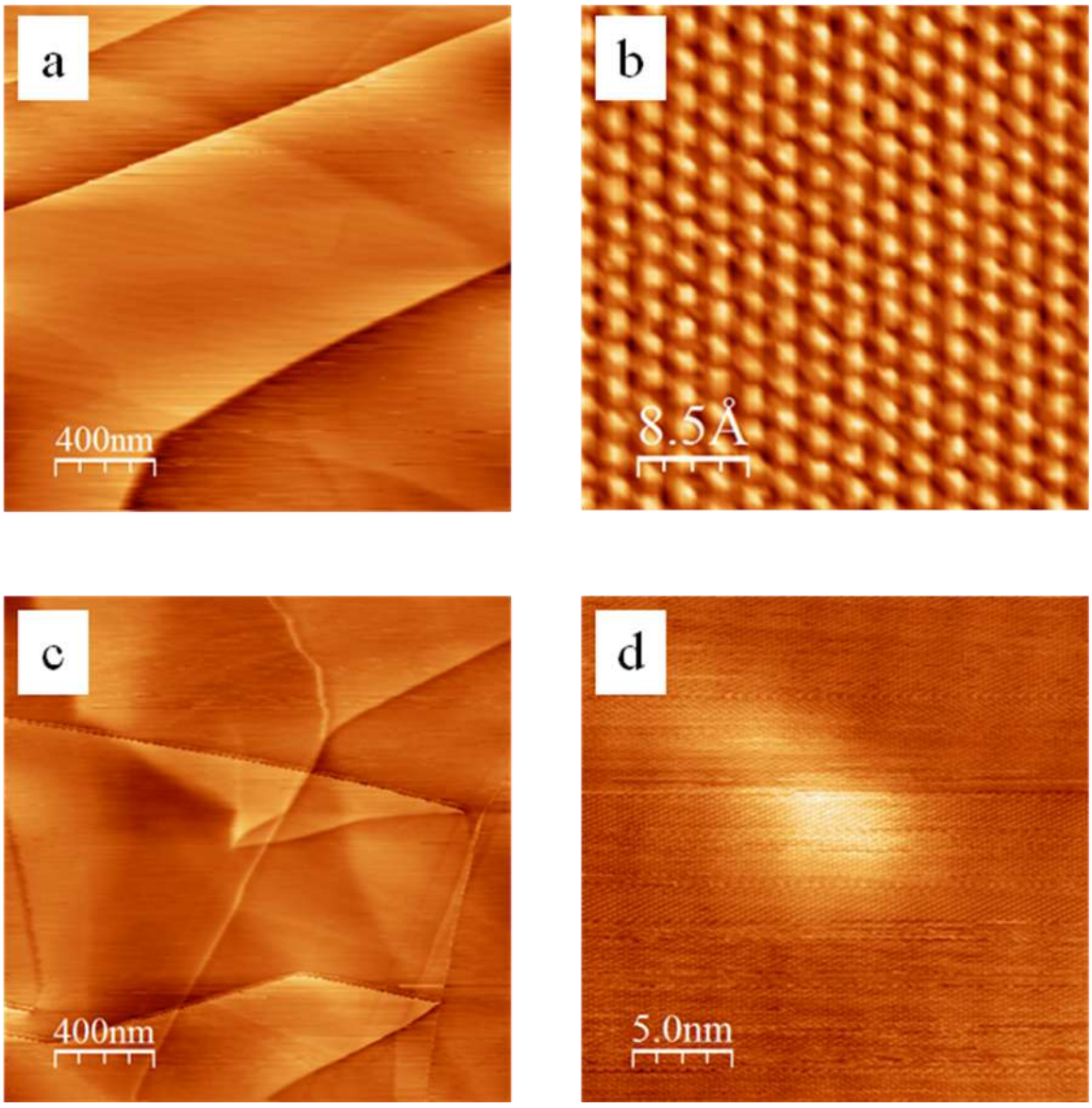

Fig. 2
STM images of clean graphite. (a) Smooth terraces. Image size is 2 μm x 2 μm, 0.1 V tip bias, 0.5 nA tunneling current. (b) Atomic-scale resolution. 3.4 nm x 3.4 nm, 0.08 V, 0.3 nA. (c) Extensive folds. 2 μm x 2 μm, 0.1 V, 0.5 nA. (d) Inclusion. 25 nm x 25 nm, 0.1 V, 0.3 nA.

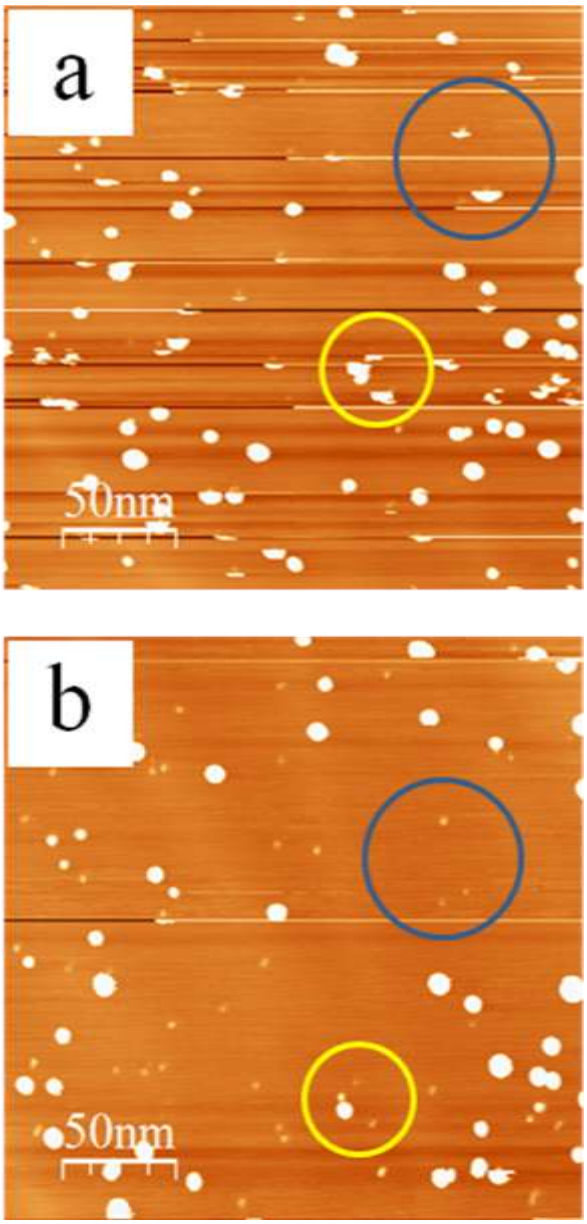

Fig. 3
A sequence of two STM images over the same region of a graphite surface with Cu clusters (0.1 ML Cu), illustrating the changes that scanning can cause in metal clusters. Each image is 250 x 250 nm^2, acquired with -0.8 V tip bias and 0.1 nA tunneling current.

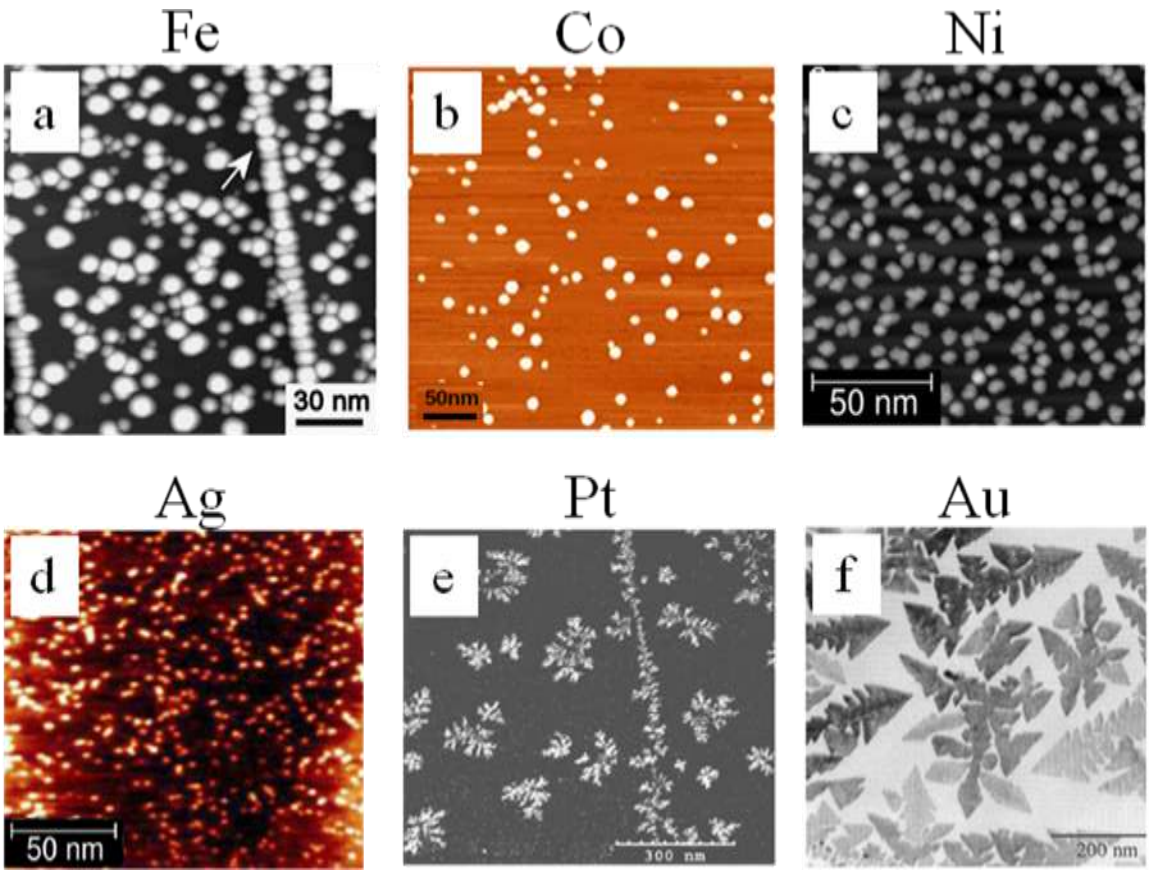

Fig. 4
Morphology of various metals vapor-deposited on HOPG at 300 K unless otherwise specified. (a) Fe, reproduced from Ref. [79]; (b) Co, reproduced from Ref. [80]; (c) Ni (deposited at < 200 K), reproduced from Ref. [110]; (d) Ag, reproduced from Ref. [69]; (e) Pt, reproduced from Ref. [81]; and (f) Au, reproduced from Ref. [51].

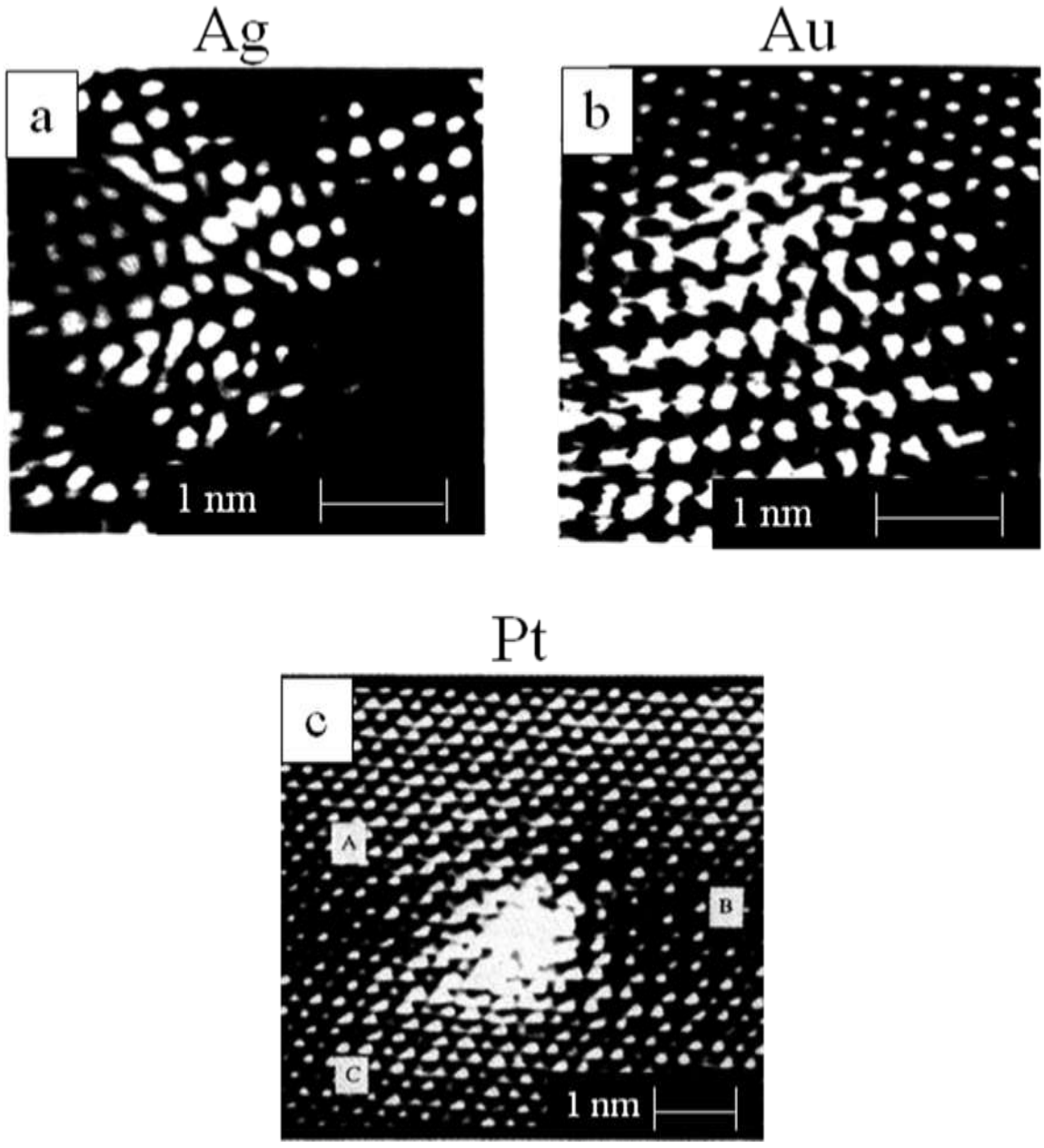

Fig. 5
STM images of small 2D clusters on HOPG which may be precursors to 3D island growth: a) Ag, reproduced from Ref. [87]; b) Au, reproduced from Ref. [87]; and Pt, reproduced from Ref. [85].

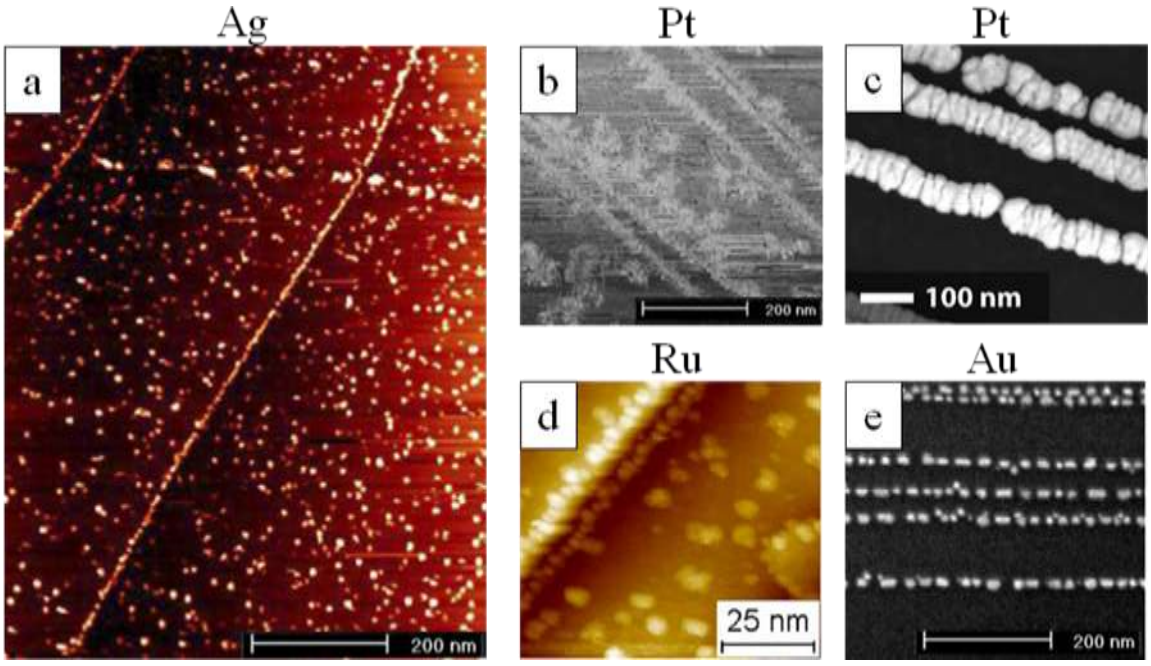

Fig. 6
Preferential decoration of HOPG step edges by various metals, vapor deposited at 300 K unless otherwise specified. (a) Ag, reproduced from Ref. [69]; (b) Pt, reproduced from Ref. [81]; (c) Pt, deposited by atomic layer deposition, reproduced from Ref. [16]; (d) Ru, reproduced from Ref. [95]; and (e) Au deposited at 673 K, reproduced from Ref. [82].

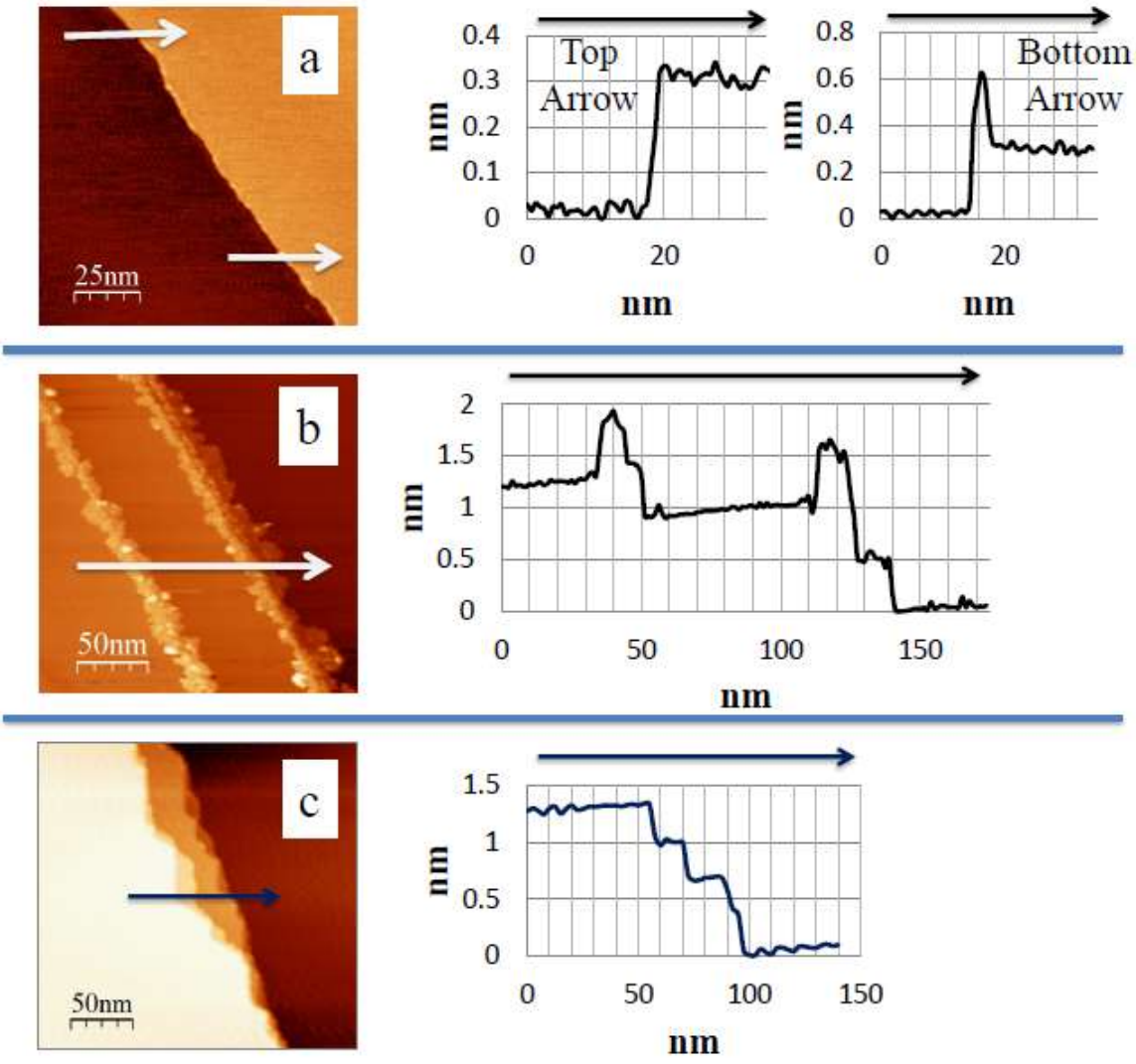

Fig. 7
HOPG steps on a nominally-clean surface, and associated line profiles. (a) Partially-contaminated step—most common type observed. 125 nm x 125 nm, -0.5 V (at tip), 0.2 nA. (b) Highly-contaminated steps—rarely observed. 250 nm x 250 nm, -0.6 V, 0.3 nA. (c) Uncontaminated steps. 250 nm x 250 nm, -0.5 V, 0.5 nA.

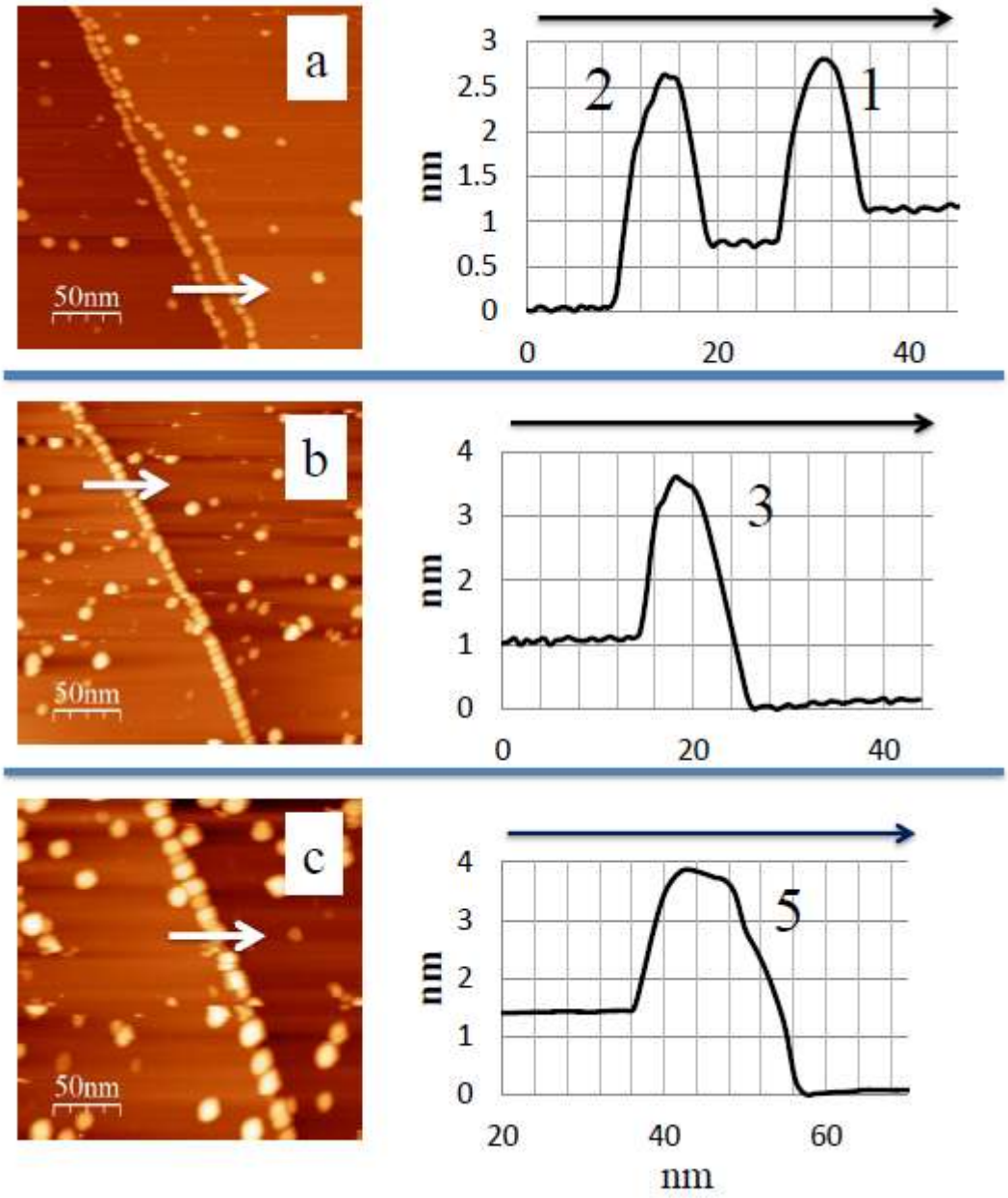

Fig. 8
Cu decoration at HOPG steps of various heights, and corresponding line profiles. All images are 250 nm x 250 nm. Numbers in profiles give carbon layer heights. (a) Left to right: 2-layer and 1-layer graphite steps. -1.5 V at tip, 0.3 nA. (b) 3-layer graphite step. -1.5 V, 0.3 nA. (c) 5-layer graphite step. -1.5 V, 0.1 nA.

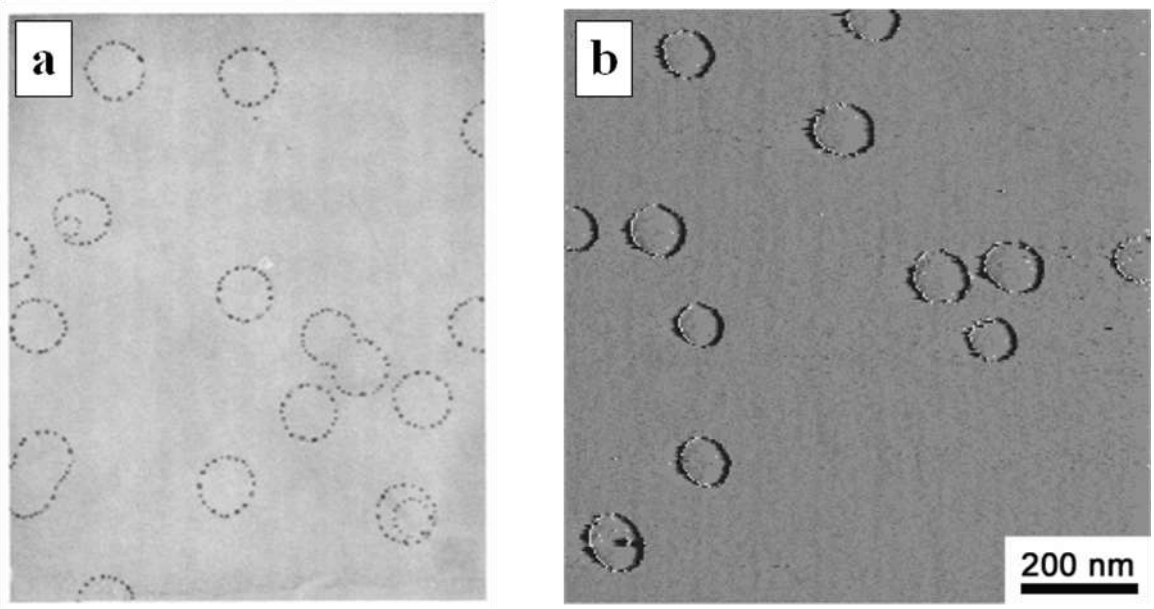

Fig. 9
(a) SEM of Au-decorated vacancy loops at 56,000x. Reproduced from Ref. [25]. (b) STM of Au-decorated vacancy loops. Au was deposited at 623-673 K. Reproduced from Ref. [46].

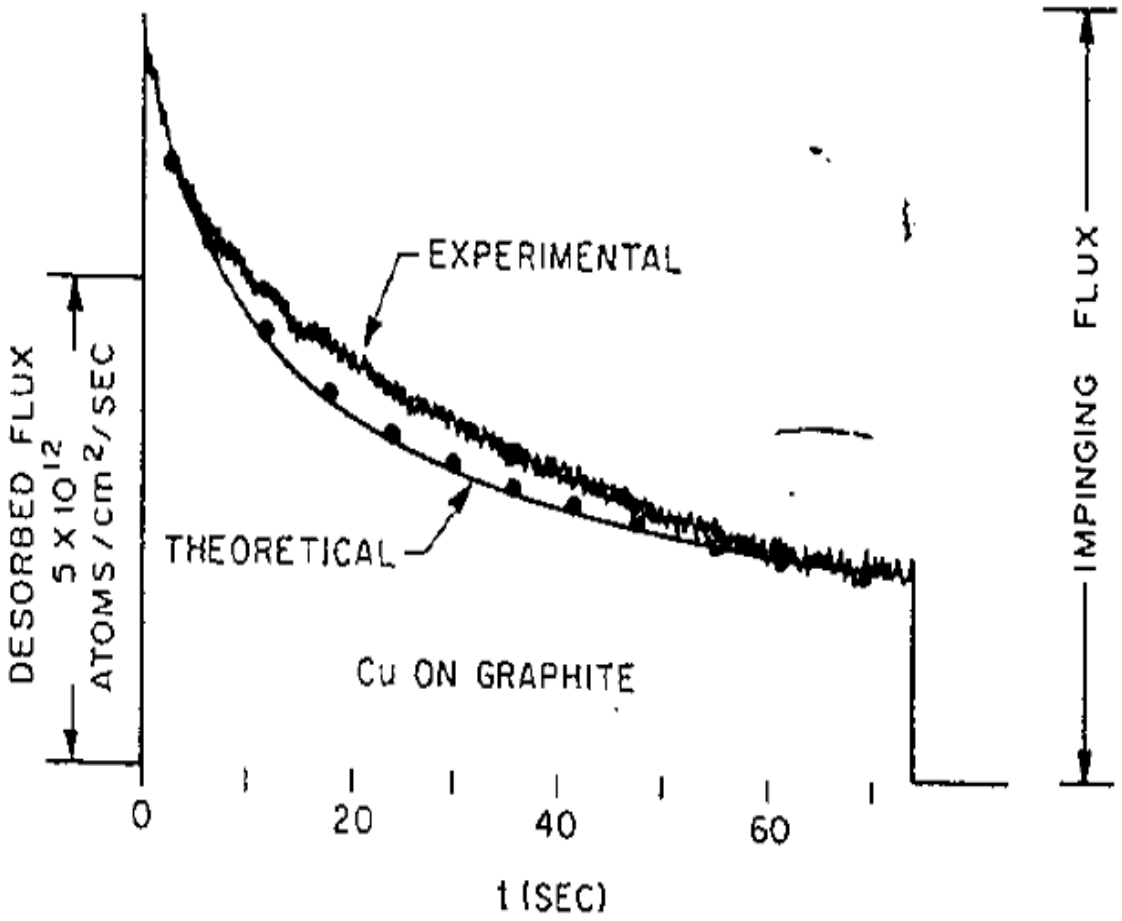

Fig. 10
Time dependence of desorbing Cu flux, with a continuous Cu beam impinging on graphite at 300 K. The solid curve is the best fit to a model in which Cu atoms on graphite have high mobility and a limited lifetime, and can only adsorb irreversibly if they become incorporated at the periphery of 2D Cu islands. Reproduced from Ref. [48].

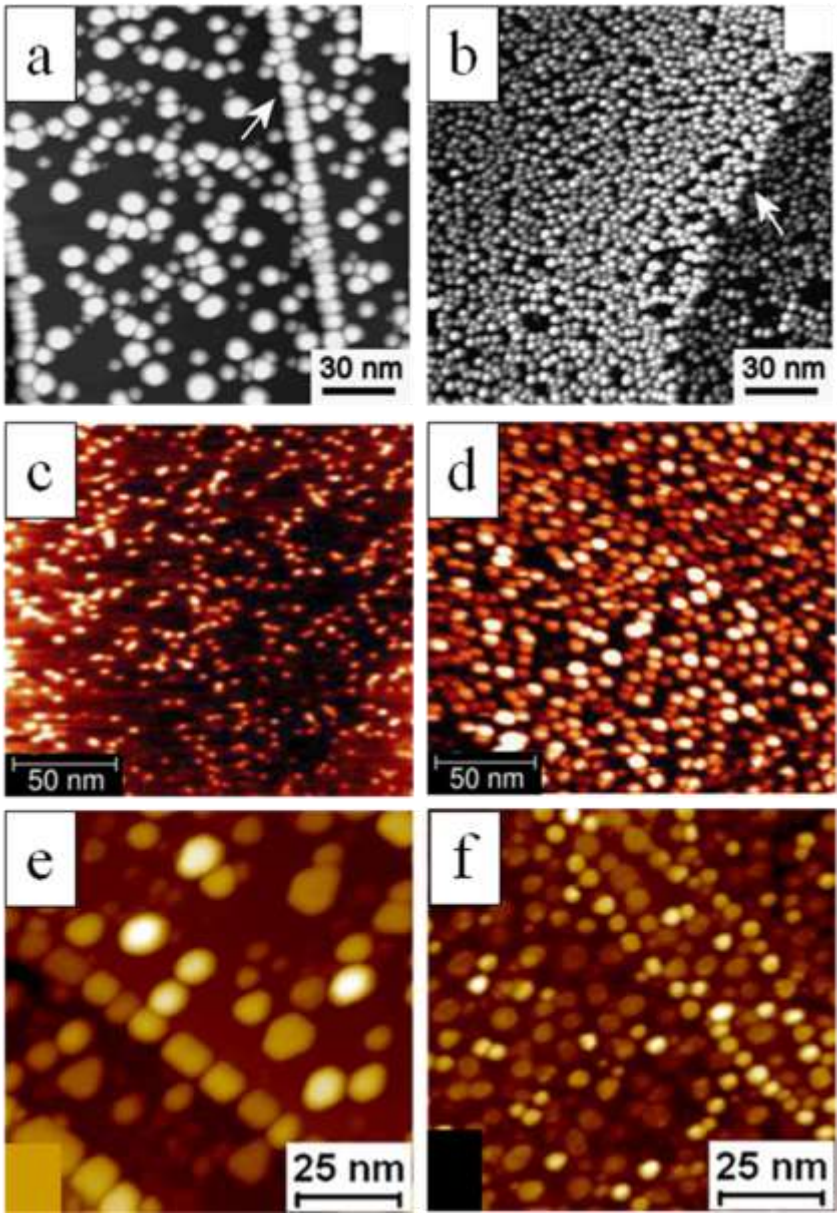

Fig. 11
Comparisons of metals deposited on a normal graphite surface (left) and on a graphite surface that was pre-sputtered (right). (a-b) Fe, from Ref. [79]; (c-d) Ag, from Ref. [69]; (e-f) Ru, from Ref. [95].

CHAPTER 2

EXPERIMENTAL APPROACH AND BACKGROUND

2.1 Experimental Setup

All STM experiments were performed in Ames, under UHV ($P < 2 \times 10^{-10}$ mbar) in an Omicron VT-SPM commercial system equipped with variable temperature STM, and XPS. A simplified schematic of our system is shown in Fig. 1. The sample was mounted either on a manipulator ("manipulator stage") or in the STM ("STM stage,") and was transferred between the two using a wobble stick (not shown). When the sample was in the manipulator, it could be heated up to 1300 K. The manipulator also served as our platform for performing XPS and for annealing STM tips in-situ using a tip-flashing device (described in Appendix A). When the sample was in the STM stage, it could be heated up to 750 K or cooled to 120 K. STM imaging and metal depositions also occurred in the STM stage. STM imaging was done using both chemically etched and mechanically cut W wire tips, which performed comparably, although the mechanically cut tips were more likely to survive a tip crash, which occurred frequently when studying this system. Surface oxide was removed from the W tips before imaging by flashing with direct current in-situ.[1]

2.1.1 STM imaging of HOPG - general

In our work, HOPG samples were cleaved in air with tape and transferred into UHV, typically within a few minutes. A Cu-covered surface was always cleaned by cleaving, never by heating. Two grades of HOPG were used: ZYA and ZYH, and they were heated to temperatures ranging from 300 K (unheated) to 1300 K. Neither the HOPG grade, the heat treatment, nor the

number of days in vacuum since cleaving made a measurable difference in point defect density, nor in Cu island density on terraces. This is notable, because there is wide variety of heating regimens recommended for preparing grahite substrates in the literature.[2-13] Defect characterization is discussed in greater detail in section 3.2. In the end, our normal protocol was to use ZYA grade HOPG, and heat it to 800 K in vacuum (before Cu deposition) until the chamber pressure approached the low 10^{-10} torr range. The outgassing time was typically on the order of tens of minutes, and varied depending on how long the sample and sample plate had been exposed to atmosphere. The primary purpose of heat treatment was to outgas the sample plate.

2.1.1.1 STM imaging of the clean HOPG surface

Tunneling parameters for imaging the clean HOPG surface used in our system were in the range V_{tip} = 0.02 to 2.0 V (either + or – bias) and i = 0.1 to 1.0 nA, in agreement with literature[14-18]. On the clean HOPG surface, positive and negative tip bias produced equally good images. For large images, where scanning speed was fast, or images where a step edge was in-frame, high values of V_{tip} and low values of i were most effective, primarily for the purpose of keeping the tip far enough from the HOPG surface that it would not crash into surface features (primarily step edges). Keeping the loop gain (feedback loop speed) as high as possible without creating noise in the image also helped reduce the risk of tip crash. For atomic-scale images, low values of V_{tip} and high values of i were most effective. Some papers in the literature report tunneling currents in the range of 1.7-3.0 nA for atomic-resolution imaging[16; 19]. However in our system sample currents above 1.0 nA rarely produced quality images. STM images at low magnification (over large areas) or containing 3D features were taken in a constant current mode.

For high-magnification images of the HOPG surface, including some images of defects, constant height mode was more effective. In constant height mode, the loop gain was kept as low as possible without causing distortion in the image.

Both ZYH and ZYA grade HOPG produced micron-size terraces bounded by step edges that were 0.30 to 0.36 nm (one carbon layer) high to several nm high. The accepted literature value for the carbon sheet separation is 0.335 nm[20; 21]. On a real HOPG surface we found that the heights varied from 0.30 to 0.36 nm. Figs. 2(a) and (a′) show a line profile across a typical terrace-step region of HOPG ZYA with steps of various heights. When step edges were in view the terrace regions often appeared smooth. However, if contrast was adjusted, or if a step edge was not in view, the terraced region often exhibited very mild undulations less than an Ångstrom in height. Figs. 2(b) and (b′) show undulations on a terrace in the same vicinity as the region in Fig. 2a. Undulations are seldom as regular as in this image.

Although HOPG surfaces can be broadly described as large terraces bounded by steps, the details of the surface morphology are actually quite diverse. Figs. 3 and 4 show a variety of surface morphologies encountered on ZYH and ZYA grade HOPG, respectively. It should be noted that ZYH and ZYA samples are not easily distinguished based on surface morphology. On very rare occasions, a repeating pattern of triangles was seen, as shown in Fig. 5(a) and (b), or a moiré pattern as shown in Fig. 5(c) and (d). Figs. 5(a) and (b) are of the same area but with the scan angle rotated 90° to show that the features are real. (Real features rotate with scan angle, noise does not.) Fig. 5(d) is an expanded view of the moire in Fig. 5(c), revealing additional structure of the moiré spots. Superstructures such as these are well documented in the literature[15-18; 20; 22-25], and are thought to be caused by dislocations between graphite sheets, such as when a stacking pattern switches from ABAB to ABCABC.

With most STM tips, atomic resolution was easily obtained on the clean HOPG surface, as long as the tip was stable and noise was low. Fig. 6(a) shows an atomic resolution image of the graphite lattice. As mentioned in Chapter 1, graphite stacks in an ABAB fashion, which creates two types of carbon atoms on the surface: C_α, which sits directly above another carbon; and C_β, which sits directly above a hole. The C_β carbons are the ones imaged in STM, as shown in Fig. 6(b). When imaging the graphite lattice it was common to encounter corrugation reversal [19; 26] as in Fig. 6(c) and (d), which is a manifestation of electronic tip states which results in inverted imaging (dark appears as light and light appears as dark). The C_β carbons are still the only atoms being imaged, but they appear as dark spots instead of light spots.

2.1.1.2 – STM imaging of HOPG after Cu deposition

Cu was always deposited onto the sample at room temperature unless stated otherwise. Cu was deposited from a Mantis QUAD-EV-C e-beam evaporator with a ceramic-lined Mo crucible. Cu coverage was calculated from STM images only for the HOPG terraces, i.e. the amount of Cu accumulated at step edges was not included. Coverage on the terraces was calculated using the volume of Cu islands > 1 nm tall, which accounted for > 99% of the total volume of Cu on the terraces. Because lateral dimensions of Cu clusters were unreliable due to convolution between the cluster and the STM tip, cluster volumes were calculated using cluster heights and assuming the shapes to be hemispherical. Other authors[27; 28] have estimated that metal clusters on HOPG have actual widths that are only 50-60% of what they appear in STM images, for cluster diameters around 10 nm. Our Cu clusters had a typical apparent width-to-height ratio of 3.5, so reduction of the width to 50-60% of the apparent value would yield a ratio of 1.8-2.1, consistent with a hemispherical shape (ideal ratio = 2.0). To obtain Cu coverage in

units of monolayers, the Cu volume of a group of clusters was divided by the total (HOPG + Cu) surface area, which yielded an effective film height in nm. This was divided by the effective diameter of a single Cu atom in bulk fcc Cu at 293 K, 0.255 nm, to give an effective film height in monolayers.

Imaging 3D Cu clusters on graphite required a very specific set of tunneling parameters due to the high degree of sample-tip interaction. Cu clusters were easily disturbed by the tip, but this effect was mitigated by using V_{tip} = -1.0 to -2.5 V, i = 0.05 to 0.3 nA, and a scan speed of 800 to 1200 nm/s (for 250 nm x 250 nm images). Faster scanning caused many clusters to be removed and dragged around the surface, and often caused loss of tunneling altogether. Slower scanning was not markedly advantageous. The appropriate loop gain varied between 3-12%, but in general was set as high as possible without causing noise in the image.

Cu cluster statistics were gathered primarily using 250 nm x 250 nm images. This was the largest image size in which the smallest features (ca. 2 nm wide and ca. 0.2 nm tall) could be effectively resolved. Because of tip interactions with the Cu clusters, the first scan over a given area resulted in some Cu clusters being picked up or moved by the STM tip during scanning, which caused them to appear severed in the STM image. Some images also contained sharp streaky features which were likely Cu debris being picked up and dropped by the tip (see Fig. 7). Images of such low quality were typically not used for statistical analysis, but when an image with streaky features was used, the streaks were subjectively discounted in cluster counting. Furthermore, when a cluster was severed by the STM tip, it typically left behind a small residue (see Fig. 8), so there was often ambiguity as to whether a small feature near a severed cluster was a true small cluster or just a residue of the severed cluster. This ambiguity was reduced by imaging every area in duplicate, where the second image was typically much easier

to interpret, at least for the purpose of cluster counting (see Fig. 9). Often a contrast adjustment was necessary in order to see the residues left behind by severed clusters, as can be seen by comparing Fig. 10(a) and (a′) (no contrast adjustment) with Fig. 10(b) and (b′) (after contrast adjustment, residues more visible). Re-scanning each area was implemented as common practice about half-way through this thesis project (on Nov. 13, 2013).

The first scanned images were still useful in that they contained information about the heights of clusters which were partially imaged before being severed. Using the combination of first and second scans provided a more complete picture of the surface than either scan alone. For volume calculations, severed clusters were counted as full clusters. Under good tunneling conditions the percentage of severed clusters in any first scan image was approximately 10-30% of the total cluster count. Images where the percentage of severed clusters exceeded this range were excluded for purposes of determining coverage since so much of the information regarding cluster heights was lost, but the second images from these scans could sometimes still provide accurate counts for cluster densities.

2.1.2 STM imaging of a-C

This work also includes experiments on a-C films. The a-C films were made by magnetron sputtering onto a Si wafer (either (100) or (111) orientation). A schematic diagram for fabrication of amorphous carbon substrates is shown in Fig. 11. The experimental history and properties of the various a-C films studied in this work are detailed in Chapter 5.

STM imaging of a-C films was done in UHV after outgassing the sample between 650 and 1000 K for at least several tens of minutes. This was necessary because XPS showed that

the unheated a-C surface had substantial oxygen peaks compared to a heated sample (see Fig. 12). This indicated that unheated a-C surfaces retained adsorbates from the atmosphere.

In general, a-C is challenging to image with STM due to the roughness of the surface and also the lack of conductivity of some films[29]. As a result, AFM is a more common technique for studying large areas (micron-scale) of amorphous carbon films.[30; 31] There are a few works which study the fine surface structure of a-C films with STM[29; 32; 33], at least one of which shows STM images at the 100 nm-scale[34], but to the best of our knowledge there are no micron-sized surveys of a-C surfaces using STM.

Figs. 13(a-c) show large scale (low-magnification) STM images of an a-C surface. The tunneling parameters used for these images was quite extreme (-5.1 to -6.0 V and 2.4 to 3.0 nA). Typically, a high tunneling current (1-3 nA) was necessary to produce quality images. The appropriate tip bias varied depending on the purpose of the scan. For low-magnification images (large scale and high scan speed), or images of general surface contours, a high tip bias (±1-6 V) was necessary to keep the tip from crashing into the surface. For high-magnification images, where the purpose was to image fine structure, a low tip bias (±0.02-0.05 V) was more effective. In general though, tunneling parameters varied widely as a function of sample and tip condition. Loop gain (speed of the feedback loop) was set as high as possible without causing noise in the instrument. A scan speed (in nm/s) of 4 to 8 times the lateral dimensions of the image (in nm) typically worked well.

2.2 Sample Heating and Temperature Calibrations – General

The experiments in this thesis project were carried out on materials varying in composition and thickness, using three different heaters and two different styles of sample

holder. Therefore, careful and extensive temperature calibrations were necessary. This section details the types of heaters and sample holders used, and shows the temperature calibration curves associated with each.

For experiments involving sample heating, heating rates were approximately 60 K/min. Heat treatments included 15 minutes for equilibration at the target temperature, followed by immediate cooling back to room temperature at approximately 120 K/min. Sample temperature was controlled by adjusting the current supplied by a power supply to the heater.

For resistive-type heaters (PBN heaters), a voltage was displayed along with the current output. The ratio of voltage to current gave the resistance across the PBN heater element (R = V/I), which vary from heater to heater, but are typically in the range of 8-20 Ω. Resistance across the heater was used as a convenient metric to double check that the heater was functioning properly. The product of voltage and current equalled power output from the heater (P = IV). Calibration curves for resistive-type heaters were typically displayed as temperature vs. power.

For e-beam heaters, the power supply displays a filament current as well as an emission current for the electron flow between the filament and sample. Calibration curves for e-beam style heaters are either displayed as temperature vs. filament current (for filament settings below the thermionic emission point) or as temperature vs. emission current (for filament settings above the thermionic emission point).

2.2.1 In the STM stage

The STM stage contains heating and cooling functions, both of which require the use of a double-decker style sample holder, shown schematically in Fig. 14(a) and available in greater detail in the Omicron VT-SPM User's Guide. The sample holder comprises a base plate made of

Ta or Mo, a ceramic top plate with a window cut into the center, a pyrolitic boron nitride (PBN) heater, contact bars for supplying current through the heater to ground through the base plate, and a multitude of screws, washers, nuts and ceramic pieces (not shown). In this assembly the sample is heated radiatively from the back by the PBN heater. This type of heating is referred to as "resistive" (in contrast to "e-beam" heating, described in section 2.2.2.2) since it relies on heat generated via the electrical resistance of the PBN element.

Double decker sample holders were difficult to construct and had a limited lifetime due to failure of various components with usage. For this reason, we avoided using them as much as possible, with the exception of cooling experiments, which required a double-decker sample holder, or during times when the manipulator was non-functional and the STM stage was our only means of heating.

The Omicron VT-SPM User's Guide provides a calibration curve for heating of a generic metal strip 2 mm in thickness in the STM, but the materials used in this work (HOPG and a-C mounted on Si substrates) were sufficiently different from a typical metal sample that we performed our own calibrations. For HOPG especially, extra care was taken to generate calibration curves for samples of varying thickness, since HOPG is thermally conductive along the direction of the basal plane (ca. 1800 W/mK), but insulating perpendicular to the basal plane (ca. 8 W/mK)[35; 36], with thermal conductivity being largely independent of HOPG grade[36]. Due to this anisotropy, we expected surface temperature to be uniform laterally across a sample, but to vary as a function of sample thickness. Contrary to the latter expectation, Fig. 15 shows that there was little difference in temperature between HOPG samples of thickness 0.45 mm and 0.86 mm heated in a double-decker style sample holder. This suggests that we would have to use samples with a larger difference in thicknesses to see the divergence.

Fig. 15 shows heating curves for various samples in a double decker sample holder (with resistive heating, as discussed above) in the STM stage. There are several features to note in this curve. First, the heating curves are limited to T < 750 K due to limited heat tolerance of certain components in the STM stage. The heater itself, however, is capable of much higher temperatures (as described in section 2.2.2.1, below). Second, the three HOPG samples used lag behind the Omicron estimated temperature for a metal strip by approximately 50 K regardless of the HOPG thickness. This result was not surprising given that HOPG is a poor conductor of heat perpendicular to the basal plane. Third, our attempt to reproduce the Omicron curve by using a strip of NiAl of similar dimension failed in that our curve lagged the Omicron estimated curve by approximately 200 K. This is probably due to the relatively low thermal conductivity of NiAl (75 W/mK)[37] compared to other metals (e.g. Cu 400 W/mK),.

For sample cooling below room temperature, a liquid-nitrogen-cooled block was lowered into contact with the base plate of the sample holder. Fig. 16 shows cooling curves for various samples in a double decker sample holder in the STM stage. In this trial, the HOPG samples of various thicknesses all cooled equally well to a minimum temperature of approximately 125 K, in agreement with the Omicron estimated curve, with the exception of the thinnest HOPG sample (0.45 mm), which only reached 160 K.

2.2.2 In the manipulator

The manipulator can heat samples either in a double decker sample holder (Fig. 14(a)) or strapped to a single plate (Fig. 14(b)). Heating in the manipulator was preferred to the STM stage due to the limited maximum temperature in the STM stage (750 K), and also because it was much easier to work with single plate sample holders than double-decker sample holders. Most

samples were easily mounted on a Ta or Mo base plate, held down with Ta foil straps spot-welded onto the base plate. Ta base plates were preferred over Mo because Ta is much easier to spot-weld.

Although we rarely used double decker sample holders for our HOPG heating experiments, there is a calibration plot available in the manipulator in the Omicron VT-SPM User's Guide. The curve is similar in shape to the one shown in Fig. 15 (Omicron estimated for a double decker in the STM stage), except taken to higher temperature.

For calibrations in the manipulator, temperatures were monitored by three methods: 1) a remote thermocouple which was lowered directly onto the sample surface ("remote thermocouple"); 2) a thermocouple fixed directly to the manipulator head ("manipulator thermocouple"); and 3) a hand-held optical pyrometer ("pyrometer") which measured sample temperature by line of sight through a window in the chamber.

The remote thermocouple was a Type K thermocouple. This thermocouple was generally effective in the temperature range of 300-700 K. Above this range, it underestimated sample temperature, as seen in Fig. 18. The remote thermocouple became unreliable in May, 2013, when it began underestimating all temperatures (e.g. see Fig. 19). After this time, we stopped using it for temperature calibration.

The manipulator thermocouple is located at the end of the manipulator head. The manipulator thermocouple always displays a temperature lower than the actual sample temperature and must be calibrated against actual sample temperature (either provided by the remote thermocouple or optical pyrometer). The benefit of the manipulator thermocouple is that it provides a consistent reading at all temperatures and does not require special positioning of the manipulator arm.

To complement the other thermocouples, and for all calibrations above 800 K, we used a hand-held optical pyrometer. 800 K is the approximate temperature at which all substances begin to glow.[38] The optical pyrometer requires a user to set the emissivity (ε) of the material being measured, where ε is the ratio of the radiation from the target substance compared with the radiation from a perfect black body (ε = 1). There are a number of emissivity tables online. [39; 40] For our experiments, we used $\varepsilon_{HOPG} = 0.98$, $\varepsilon_{Si} = 0.5\text{-}0.7$ depending on temperature[41], and ε_{Cu} (polished) = 0.03. For a-C samples, ε_{Si} was used since the a-C was grown on a Si substrate and the a-C layer was thin enough to be optically transparent.

2.2.2.1 Resistive (PBN) heater

Prior to October 2, 2013, the manipulator head was fitted with a PBN heater for heating samples mounted on a single-plate sample holder, as shown in Fig. 17a. The PBN heater radiatively heated the back of the sample plate. Fig. 17a is a schematic diagram for heating a sample in the manipulator with a PBN heater.

Fig. 18 shows a calibration plot for HOPG mounted on a single plate heated in the manipulator by a PBN heater. Note that the remote thermocouple curve began to underestimate actual surface temperature above 700 K, but was complemented by the optical pyrometer. Also shown in Fig. 18 is the Omicron estimated curve for a bare sample plate, which was always higher than sample temperature.

Fig. 19 shows a calibration plot for a-C on Si (0.30 mm) mounted on a single plate heated in the manipulator with a PBN heater. Of note here is that the remote thermocouple was grossly underestimating sample temperature, even at low temperatures. From this time forward (in this thesis work), the remote thermocouple was not used.

2.2.2.2 E-beam heater

An Omicron Dual Filament E-beam Heater was installed on the manipulator head on October 2, 2013. The e-beam heater allows heating of samples on a single plate up to 1300 K. The e-beam heater acts by bombarding the back of a sample plate with electrons generated from a hot filament at a negative bias with respect to ground (the sample is at ground), as illustrated in Fig. 17(b). The e-beam heater has five bias settings: 0 V, -150 V, -300 V, -450 V, and -600 V. Each bias is effective over a different temperature range, with overlap between the ranges. Each bias setting required a different calibration. Calibrations were performed using a combination of the manipulator thermocouple and the optical pyrometer (for T > 800 K).

The e-beam heater was excellent for heating at high temperatures (> 800 K), but difficult to use at lower temperatures. This difficulty arose because the power output of the heater increased rapidly near the point of thermionic emission of the filament, which occurred around 1.5 A, but changed slightly from day to day, and increased slowly during the lifetime of the filament. This, in conjunction with the fact that our remote thermocouple was unreliable and the optical pyrometer was only functional for temperatures above 800 K, made calibrating temperatures in the range of 500-700 K especially difficult.

To address this issue we calibrated the *manipulator* thermocouple reading against the optical pyrometer reading (only available > 800 K), and then extrapolated this curve based on the ratio of absolute temperature between the pyrometer and manipulator thermocouple readings. For any given bias this ratio was fairly constant over the optical pyrometer's output range, and we assumed that the relationship held at lower temperatures.

Fig. 20 shows the calibration curve for the e-beam heater using the 0 bias setting, which was used only for low-end sample heating (< 600 K). The filament was taken to near maximum current (≈ 2 A) to get a pyrometer reading. In this case, the ratio between pyrometer and manipulator thermocouple reading was 1.19. This was used to create the "Extrapolation" curve by multiplying the manipulator thermocouple reading by 1.19 at each point.

Fig. 21 shows the calibration curve for the e-beam heater using the -150 V setting. The -150 V setting was effective in the range of 500-1000 K. As with the 0 bias setting, temperatures below the range of the optical pyrometer were extrapolated by multiplying the manipulator thermocouple reading by the ratio of the readings of the two devices at higher temperature, in this case 1.17.

Fig. 22 shows sample temperature as a function of emission current measured with the pyrometer. This was the set of curves used for temperatures above 800 K.

Fig. 23 shows temperature equilibration times for heating at no bias vs. at -300 V bias using the manipulator thermocouple. Equilibration time was approximately 15 minutes for the biased setting and slightly longer for the unbiased setting. These equilibration times are treated as an upper limit for true equilibration time because the manipulator thermocouple measures the temperature at the end of the manipulator head, which is both larger than the sample and father away from the heating unit.

Fig. 24 shows miscellaneous temperature calibrations for a Cu foil (used for flux calibrations, below), as well as for a-C on Si (0.60 mm thick) at 800 K, the target temperature for a coarsening study in Chapter 6.

2.3 Flux Calibrations on Cu Foil

A Cu foil created by magnetron-sputtering, provided by Mr. Jim Anderegg, was used to test the total flux coming from our Cu evaporator. An atomically flat Cu surface was useful for determining total flux because the sticking coefficient of Cu on Cu is 1 and the deposited material forms easily-imaged 1-atom-high islands on the surface, in the submonolayer regime. Cu terraces were produced on the Cu foil by lightly sputtering the surface with argon ions (1 kV for 5 minutes @ $P_{Ar} = 2 \times 10^{-6}$ mbar) followed by heating to 900 K and cooling slowly at 3 K/min down to 700 K (cooling quickly below 700 K was fine). Terraces formed after only a few cleaning cycles, and once formed, further sputtering was not necessary. A typical Cu terrace is shown in Fig. 25(a).

Coverage in monolayers was calculated based on the percentage of the surface covered by islands. The shape of the Cu islands depends on the nature of the surface. For fcc metals like Cu, the (100) surface produces square islands, as shown in Fig. 25(b), while the (111) surface produces hexagonal islands (fewer and larger) as in Fig. 25(c). The elongated appearance of these particular islands is due to instrument drift. Our Cu surface was dominated by (100) type terraces.

2.3.1 Early calibrations (June 19-29, 2013, performed by Emma Kwolek)

A set of experiments was conducted on Cu foil to determine the Cu flux at 23.5 W evaporator power, which was a power commonly used for Cu depositions on HOPG up to that point in the study. Calibrations like this are useful if the Cu evaporator produces a consistent flux at a given power. Unfortunately, the flux from our evaporator changed (quite drastically) over time. Fig. 26 shows a Cu/Cu(100) flux calibration curve in comparison with several

Cu/HOPG experiments from various dates. The straight line shows a fit to the data which is forced to go through the origin, and the agreement is satisfactory. STM images from this Cu/Cu(100) calibration are shown in Fig. 27, and STM images from Cu/HOPG depositions in this era are shown in Fig. 28. Cu/HOPG coverage was determined by measuring cluster heights and assuming the clusters to be hemispherical. A 10-minute, 23.5 W deposition of Cu on HOPG on 2/21/14 (7 months after the depositions represented in Figs. 28) produced no copper at all. Therefore, any comparison of Cu coverage on Cu foil vs. HOPG should be done with data acquired as close in time as possible to minimize the effect of evaporator drift, as in the following section.

2.3.2 Later calibrations (April 4, 2014, performed by David Appy)

A later set of calibrations was done to compare Cu/Cu(100) coverage vs. Cu/HOPG coverage within a single day. Fig. 29 shows coverage vs. time for Cu/Cu(100) and Cu/HOPG using a hemispherical model (red squares) and a spherical model (green triangles). The slope for the spherical model is exactly ¼ that for the hemispherical model because a sphere of a given diameter, d, has a volume ¼ that of a hemisphere with radius r = d. In principle, the Cu/Cu(100) curve sets an upper limit for the amount of copper on the surface since the sticking coefficient for Cu/Cu at 300 K is 1. However for both Cu/HOPG depositions, the calculated coverage is higher than that for Cu/Cu(100). For the hemispherical model, $\text{slope}_{\text{Cu/HOPG/hemi}}/\text{slope}_{\text{Cu/Cu}}$ = 0.20/.038 = 5.3; and for the spherical model, $\text{slope}_{\text{Cu/HOPG/Sphere}}/\text{slope}_{\text{Cu/Cu}}$ = 0.050/0.038 = 1.3. This tells us that the actual shape of the Cu particles is probably closer to spherical than to hemispherical, although the true shape is likely polyhedral.

2.4 Imaging Metal Nanowires

Chapter 6 describes the fabrication processes for a variety of metal nanowires. Optical microscopy was often the first step in imaging these wires. Most metal nanowires were easily seen under an optical microscope with a 40+ objective lens. If the wires were perpendicular to the surface they appeared as fuzzy dots which moved laterally as the focus moved in/out. If the wires were parallel to the surface, then they were seen outright, appearing either brightly colored or black depending on whether light was reflected effectively off of a facet or not. Once the presence of NW's was confirmed, those samples were taken to an SEM. The substrates used (even a-C on Si) were conductive enough that sample charging was not an issue. SEM was a good instrument for determining general NW morphology and surface density. For determining crystallinity or resolving atoms, TEM was more effective. TEM sample prep involved gently brushing a TEM grid over the face of the NW sample. A few of the NW's would adhere to the TEM grid. Their presence on the grid was confirmed with an optical microscope. TEM imaging itself (and the proper interpretation of images) requires years of training and is beyond the scope of this thesis work.

Acknowledgements

This work was supported by the Office of Science, Basic Energy Sciences, Materials Sciences and Engineering Division of the U.S. Department of Energy (USDOE), under Contract No. DE–AC02–07CH11358 with the U.S. Department of Energy. We thank Gunther Richter for his contribution of a-C substrates, Jim Anderegg for donation of the magnetron-sputtered Cu foil, and Emma Kwolek for her early work with the Cu/Cu flux calibrations. We also thank Ryan Ott

and Matt Besser of Ames Laboratory for preparation of amorphous carbon substrates by magnetron sputtering.

References

[1] B. Ünal, A. Belianinov, P.A. Thiel, in: J.T. Yates Jr. (Ed.), Experimental Innovations in Surface Science: A Guide to Practical Laboratory Methods and Instruments, Springer Verlag, in progress.

[2] E. Ganz, K. Sattler, J. Clarke, Surface Science 219 (1989) 33-67.

[3] J. Xhie, K. Sattler, M. Ge, N. Vankateswaran, Phys. Rev B 47 (1993).

[4] G.W. Clark, L.L. Kesmodel, Journal of Vacuum Science & Technology B: Microelectronics and Nanometer Structures 11 (1993) 131-136.

[5] A. Humbert, M. Dayez, S. Sangay, C. Chapon, C.R. Henry, Journal of Vacuum Science & Technology A: Vacuum, Surfaces, and Films 8 (1990) 311-313.

[6] R. Nishitani, A. Kasuya, S. Kubota, Y. Nishina, Dendritic aggregation of gold particles on graphite surface, AVS, 1991, 806-809.

[7] R. Anton, I. Schneidereit, Physical Review B 58 (1998) 13874-13881.

[8] R. Anton, Physical Review B 70 (2004) 245405.

[9] J.G. Kushmerick, K.F. Kelly, H.P. Rust, N.J. Halas, P.S. Weiss, Physical Chemistry B 103 (1999).

[10] M. Büttner, P. Oelhafen, Surface Science 600 (2006) 1170-1177.

[11] I.N. Kholmanov, L. Gavioli, M. Fanetti, M. Casella, C. Cepek, C. Mattevi, M. Sancrotti, Surface Science 601 (2007) 188-192.

[12] S.S. Kushvaha, Z. Yan, W. Xiao, M.-J. Xu, Q.-K. Xue, X.-S. Wang, Nanotechnology 18 (2007) 145501.

[13] J.J. Metois, J.C. Heyraud, Y. Takeda, This Solid Films 51 (1978) 105-117.

[14] J. Cervenka, C.F.J. Flipse, Journal of Physics: Conference Series 61 (2007).

[15] S. Hattendorf, A. Georgi, M. Liebmann, M. Morgenstern, Surface Science 610 (2013) 53-58.

[16] Y. Kobayashi, K. Takai, K.-i. Fukui, T. Enoki, K. Harigaya, Y. Kaburagi, Y. Hishiyama, Physical Review B 69 (2004) 035418.

[17] P.J. Ouseph, Physical Review B 53 (1996) 9610-9613.

[18] S.R. Snyder, T. Foecke, H.S. White, W.W. Gerberich, J. Mater. Res. 7 (1991).

[19] K.F. Kelly, Thesis, Rice University (1996).

[20] H. Lipson, A.R. Stokes, Proceedings of the Royal Society of London 181 (1942) 101-105.

[21] http://en.wikipedia.org/wiki/Graphite.

[22] S. Amelinckx, P. Delavignette, Journal of Applied Physics 31 (1960) 2126-2135.

[23] P. Delavignette, S. Amelinckx, Journal of Applied Physics 31 (1960) 1691-1692.

[24] G.K. Williamson, Proceedings of the Royal Society of London 257 (1960) 457-463.

[25] S.R. Snyder, W.W. Gerberich, H.S. White, Phys. Rev B 47 (1993).

[26] C.J. Chen, Journal of Vacuum Science & Technology B 12 (1994) 2193-2199.

[27] H. Hövel, T. Becker, A. Bettac, B. Reihl, M. Tschudy, E.J. Williams, J. App. Phys. 81 (1997) 154.

[28] I. Lopez-Salido, D.C. Lim, Y.D. Kim, Surf. Sci 588 (2005) 6-18.

[29] B. Marchon, M. Salmeron, W. Siekhaus, Physical Review B 39 (1989) 12907-12910.

[30] S.B. W. Mróz, A. Prokopiuk, M. Jedynski, B. Budner, a.M.L. Korwin-Pawlowskib, Proceedings of the III National Conference on Nanotechnology NANO 2009 116 (2009).

[31] N. Paik, Applied Surface Science 226 (2004) 412-421.

[32] V. Ivanov-Omskii, A. Lodygin, S. Yastrebov, Semiconductors 34 (2000) 1355-1362.

[33] N.H. Cho, D.K. Veirs, J.W. Ager, M.D. Rubin, C.B. Hopper, Journal of Applied Physics 71 (1992).

[34] I. Rusman, L. Klibanov, L. Burstein, Y. Rosenberg, V. Weinstein, E. Ben-Jacob, N. Croitoru, A. Seidman, Thin Solid Films 287 (1996) 36-44.

[35] http://nanoprobes.aist-nt.com/apps/HOPG%20info.htm.

[36] http://www.2spi.com/catalog/new/hopgsub.php.

[37] Y. Terada, K. Ohkubo, T. Mohri, T. Suzuki, Materials Transactions 43 (2002) 3167-3176.

[38] http://en.wikipedia.org/wiki/Incandescence.

[39] http://www.engineeringtoolbox.com/emissivity-coefficients-d_447.html.

[40] http://www.omega.com/literature/transactions/volume1/emissivityb.html.

[41] T. Satō, Japanese Journal of Applied Physics 6 (1967) 339.

Figures

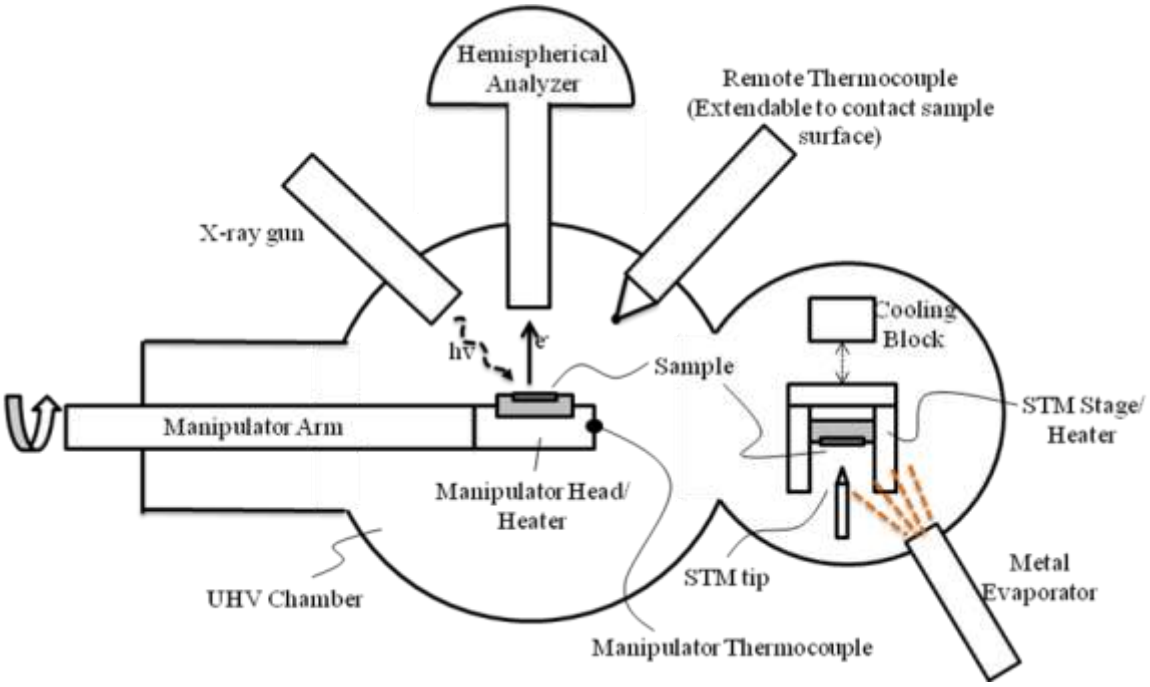

Fig. 1
Simplified schematic diagram of the Omicron VT-SPM commercial system.

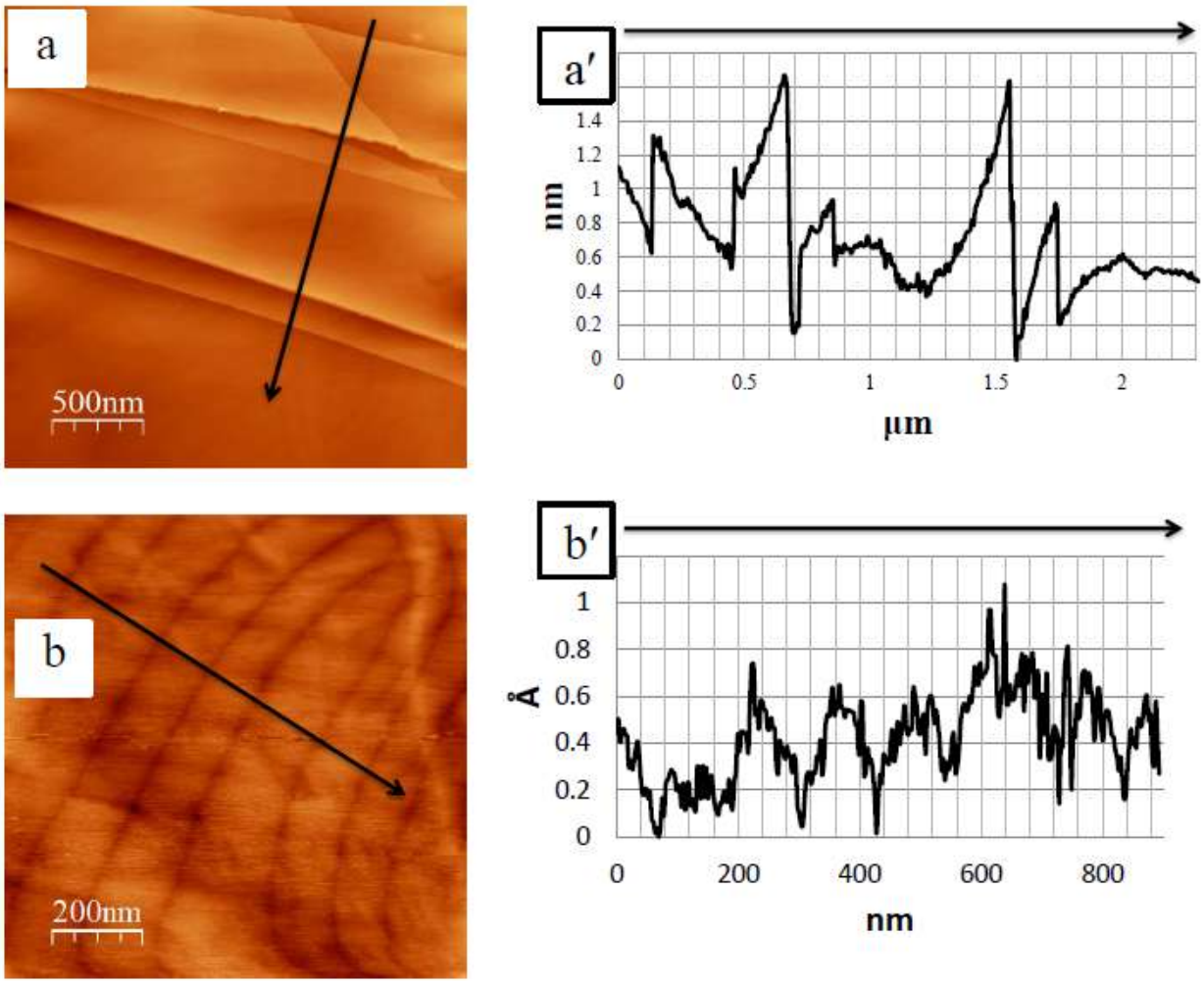

Fig. 2
STM images and line profiles of the clean HOPG surface showing; (a) steps and terraces, 2.5 µm x 2.5 µm, V_{tip} = 0.3 V, i = 0.3 nA; (b′) line profile from (a); (b) subtle undulations on a terrace without step edges in view, 1 µm x 1 µm, V_{tip} = 0.3 V, i = 0.3 nA; and (b′) line profile from (b).

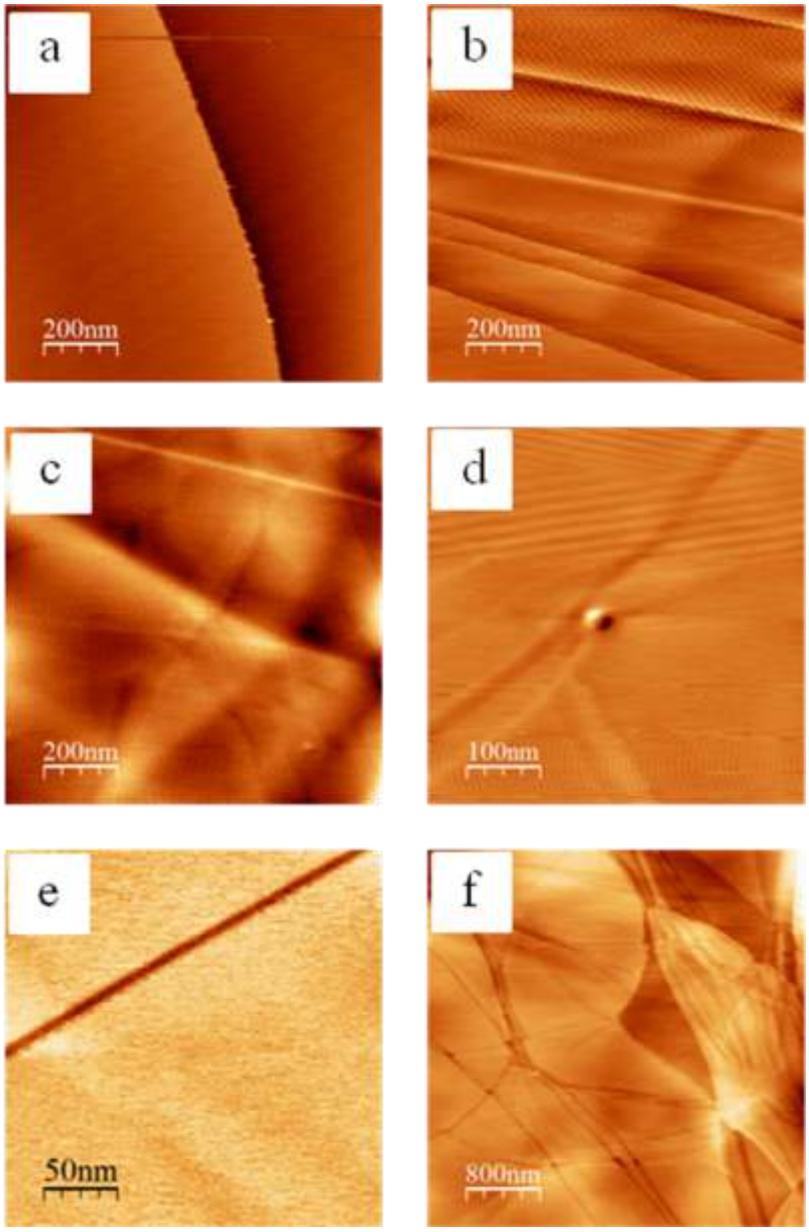

Fig. 3
STM images of the clean HOPG ZYH surface showing various features, including (a) a step edge with large flat terraces, 1 μm x 1 μm, V_{tip} = 2.0 V, *i* = 0.3 nA; (b) bunched terraces, 1 μm x 1 μm, V_{tip} = 0.1 V, *i* = 0.5 nA; (c) a terrace with undulations, 1 μm x 1 μm, V_{tip} = 0.1 V, *i* = 0.5 nA; (d) an inclusion, 500 nm x 500 nm, V_{tip} = 0.1 V, *i* = 0.5 nA (e) a straight trench one atomic layer deep, 250 nm x 250 nm, V_{tip} = -0.1 V, *i* = 0.5 nA; and (f) a mixture of complex features, 4 μm x 4 μm, V_{tip} = 0.1 V, *i* = 0.5 nA.

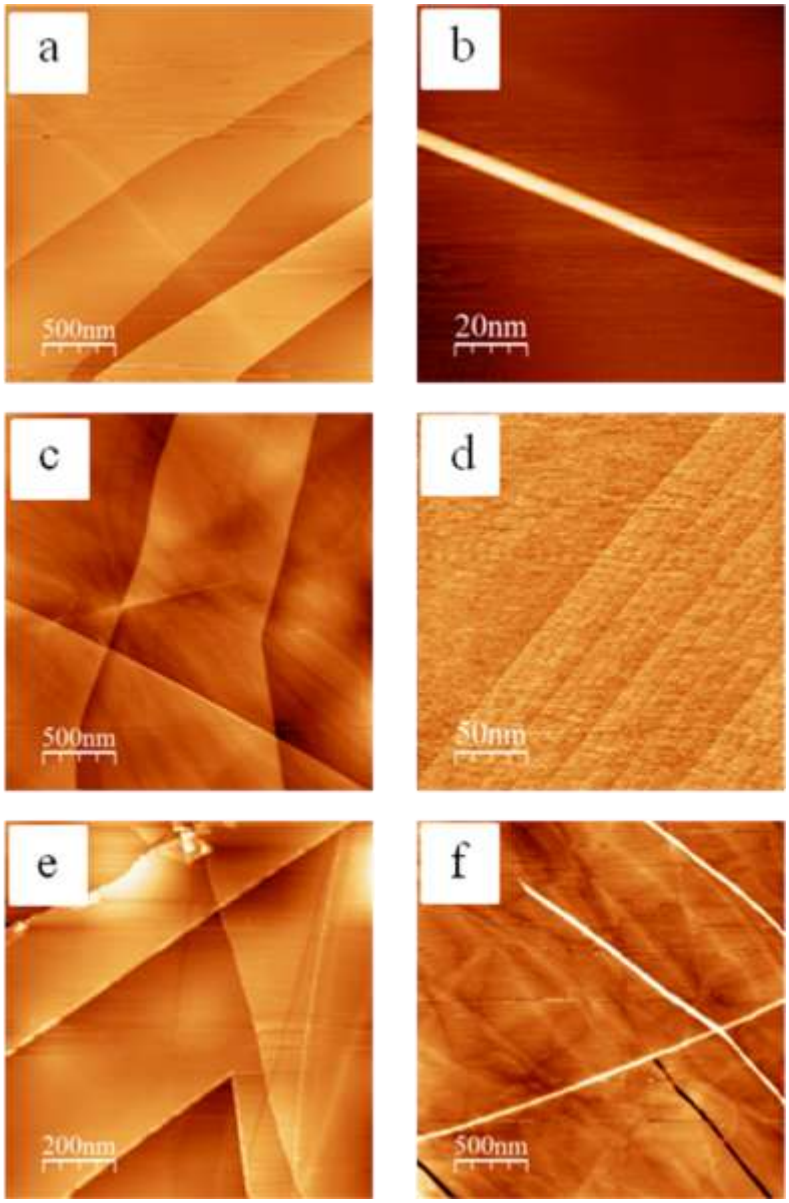

Fig. 4
STM images of the clean HOPG ZYA surface showing various features, including (a) a flat terrace-step area, 2.5 μm x 2.5 μm, V_{tip} = 0.3 V, *i* = 0.3 nA; (b) a long straight strip 1 atomic layer high, 100 nm x 100 nm, V_{tip} = 0.3 V, *i* = 0.1 nA; (c) a region of intersecting steps and folds, 2.5 μm x 2.5 μm, V_{tip} = 0.75 V, *i* = 0.3 nA; (d) a pattern of subtle but regularly-spaced striations, 250 nm x 250 nm, V_{tip} = 0.3 V, *i* = 0.1 nA; (e) triangular features and step edges, 1 μm x 1 μm, V_{tip} = 0.3 V, *i* = 0.1 nA; and (f) a large terrace with undulations and intersecting strips and trenches, 2.5 μm x 2.5 μm, V_{tip} = 0.5 V, *i* = 0.2 nA.

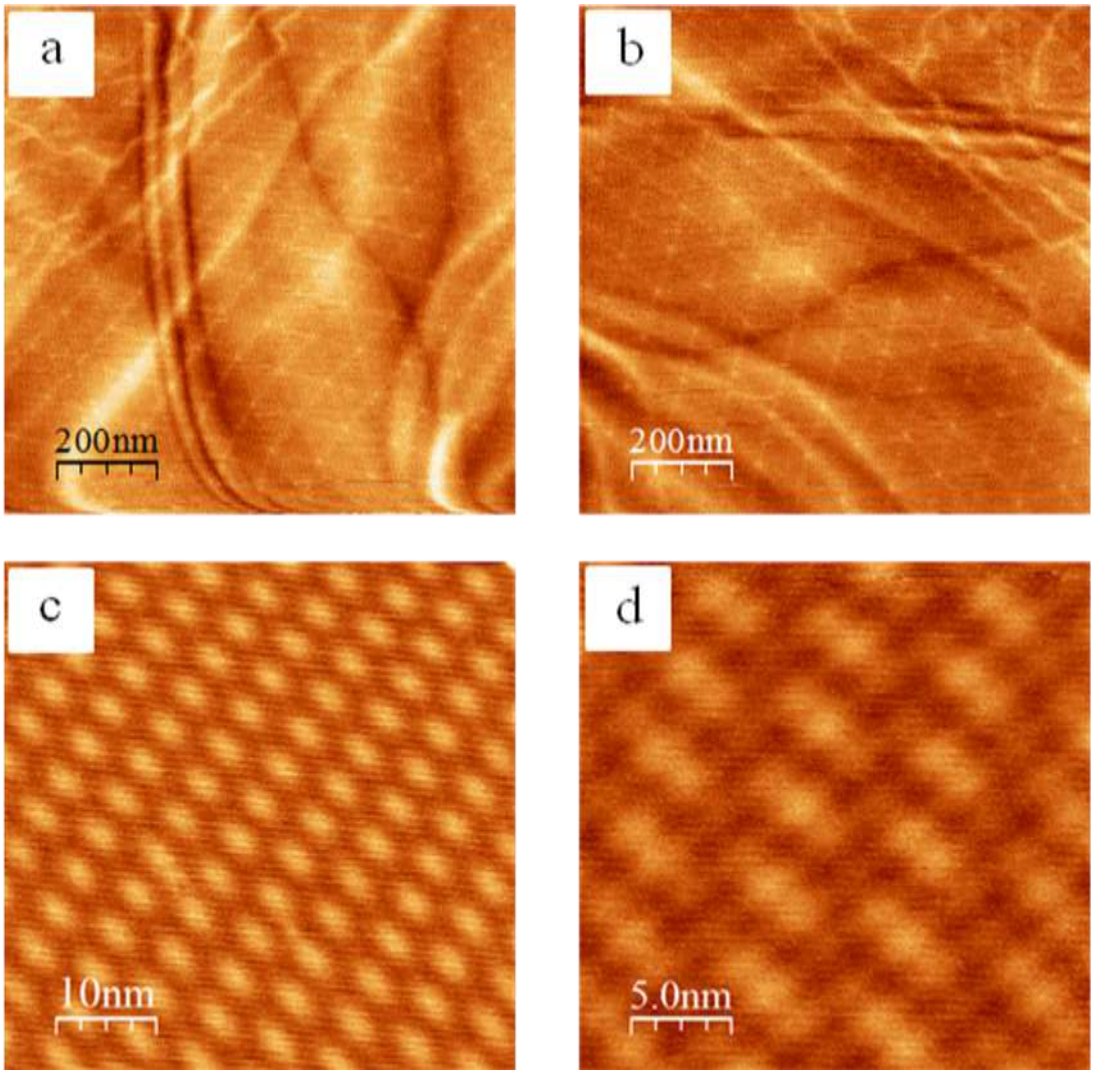

Fig. 5
STM images of rare superstructures found on the HOPG surface; (a) triangular patter on an undulating terrace, 1 μm x 1 μm, V_{tip} = 0.3 V, *i* = 0.2 nA; (b) the same area, but with scan angle rotated 90° to show that the triangular features are real; (c) a moiré pattern, 50 nm x 50 nm, V_{tip} = -2.0 V, *i* = 0.5 nA; and (d) the same moiré under higher magnification (25 nm x 25 nm), showing additional detail in the moiré structure.

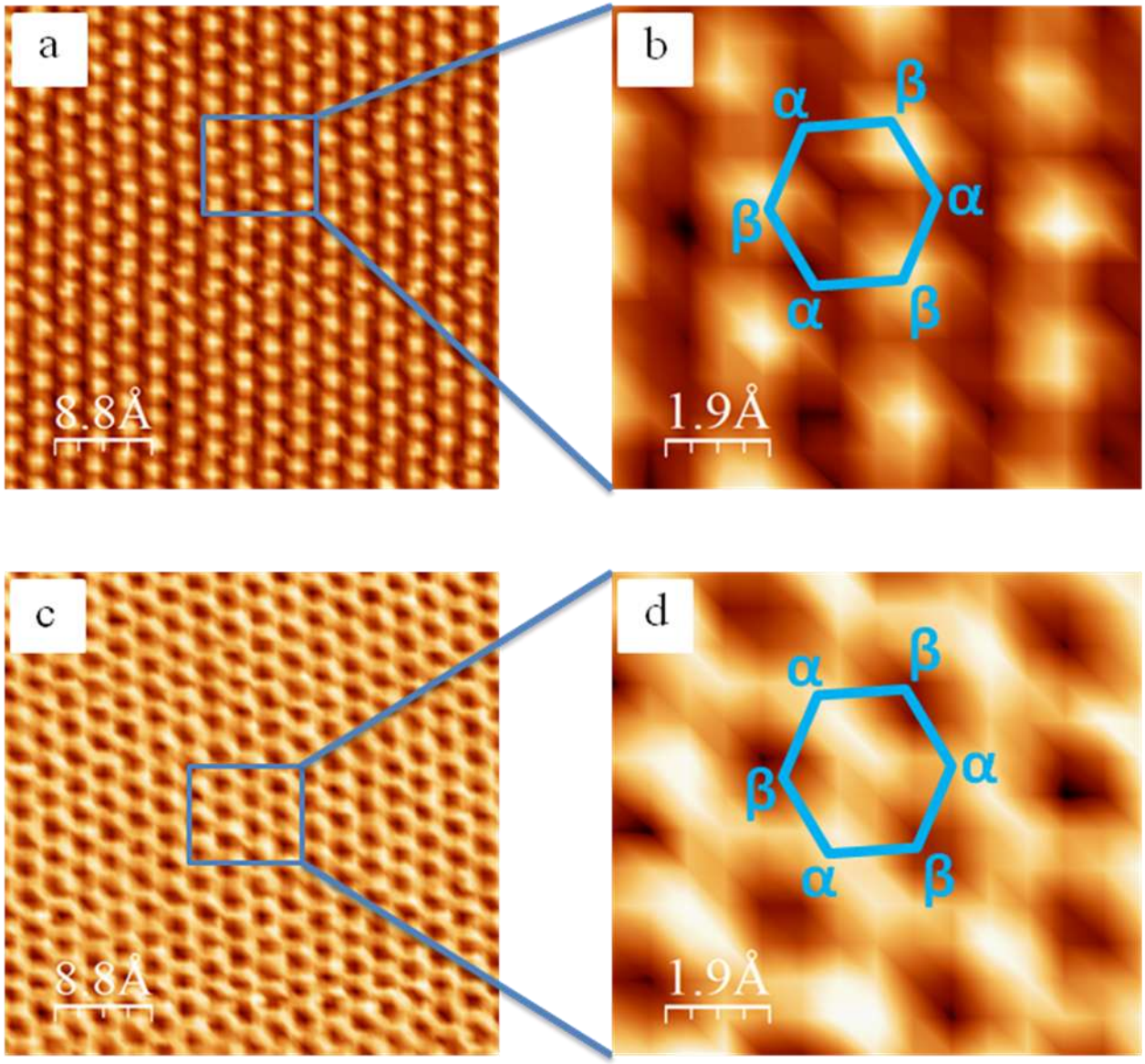

Fig. 6
Atomic resolution ATM images of the HOPG surface; (a) a normal atomic resolution image, 44 nm x 44 nm, V_{tip} = 0.05 V, *i* = 0.3 nA; (b) zoom-in of (a) with overlay of the hexagonal lattice showing the position of α and β carbons, 9.5 nm x 9.5 nm; (c) atomic resolution image with corrugation reversal, 44 nm x 44 nm, V_{tip} = 0.05 V, *i* = 0.3 nA; and (d) zoom-in of (c) with overlay of the hexagonal lattice showing the position of α and β carbons, 9.5 nm x 9.5 nm.

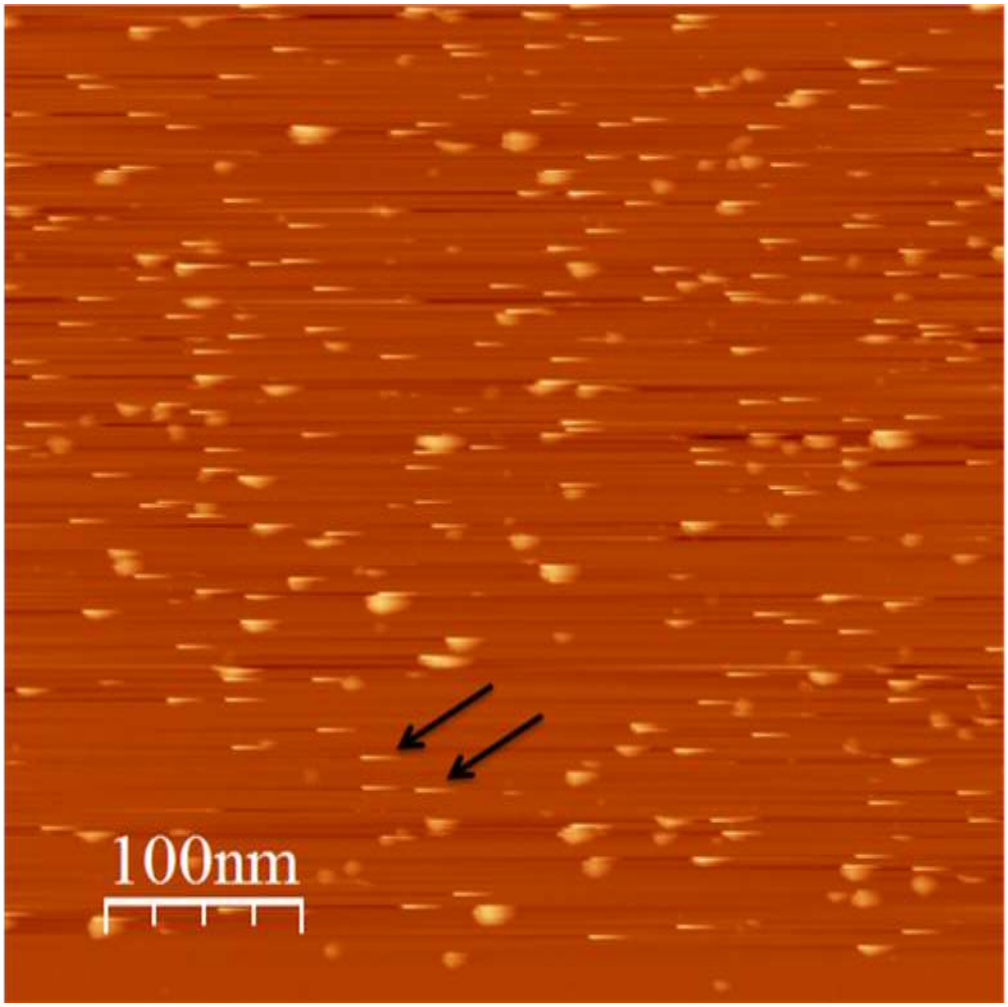

Fig. 7
A poor-quality STM scan of Cu on HOPG, showing many sharp streaky features (indicated with arrows), 500 nm x 500 nm, V_{tip} = -2.2 V, i = 0.15 nA

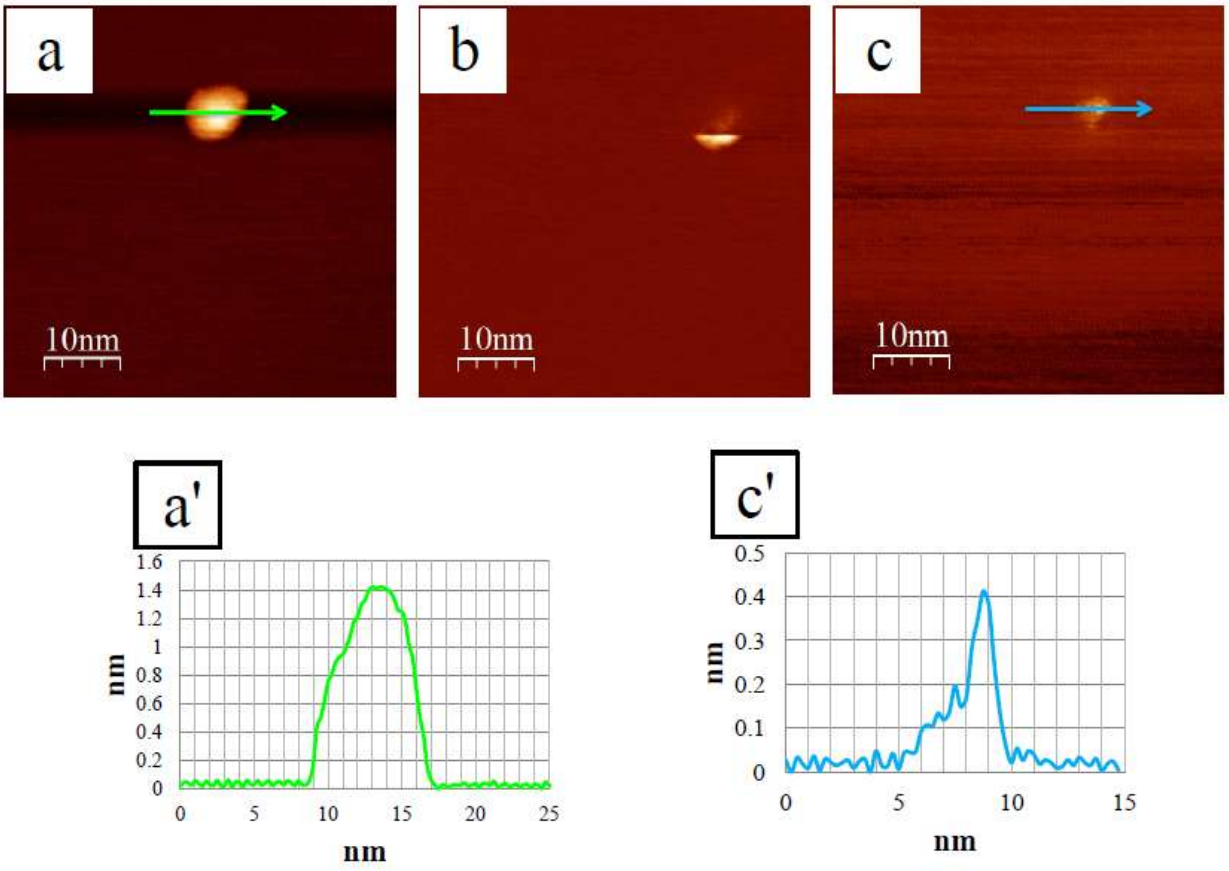

Fig. 8
(a), (b), and (c), are consecutive STM images showing a Cu island being severed by the STM tip, all images 50 nm x 50 nm, V_{tip} = 0.1 V, i = 0.1 nA. (a') and (c') show line profiles of the unsheared island (a) and the residue left after shearing (c), respectively.

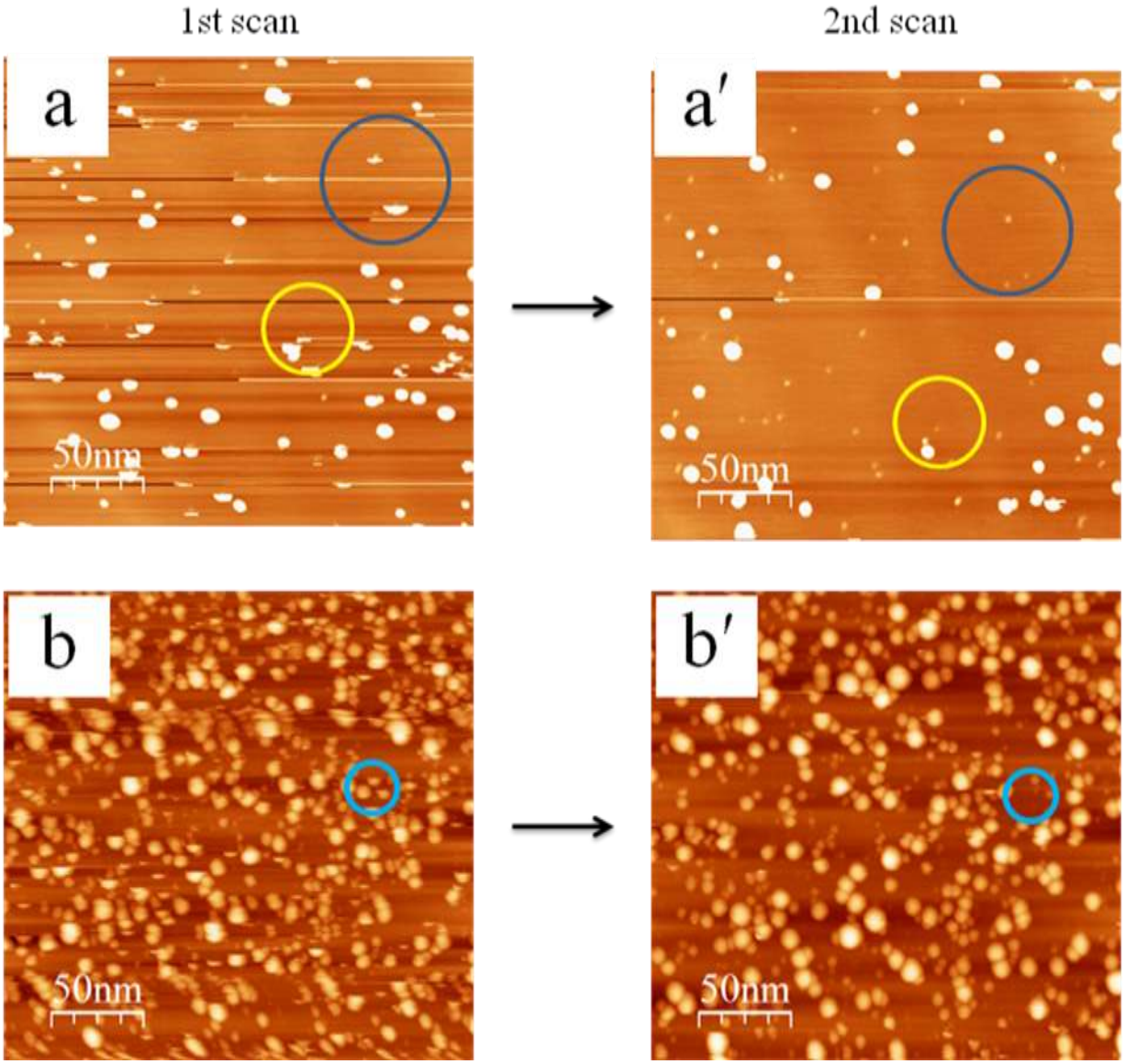

Fig. 9
STM images illustrating tip-sample interaction in the Cu-HOPG system at various Cu coverages. (a) and (a′) Consecutive scans of the same area, 0.10 ML Cu, V_{tip} = -0.9 V, i = 0.1 nA. (b) and (b′) Consecutive scans of the same area, 0.78 ML Cu, V_{tip} = -1.9 V, i = 0.1 nA. The circles show areas where islands are sheared in the first image and gone in the second image. All images are 250 nm x 250 nm.

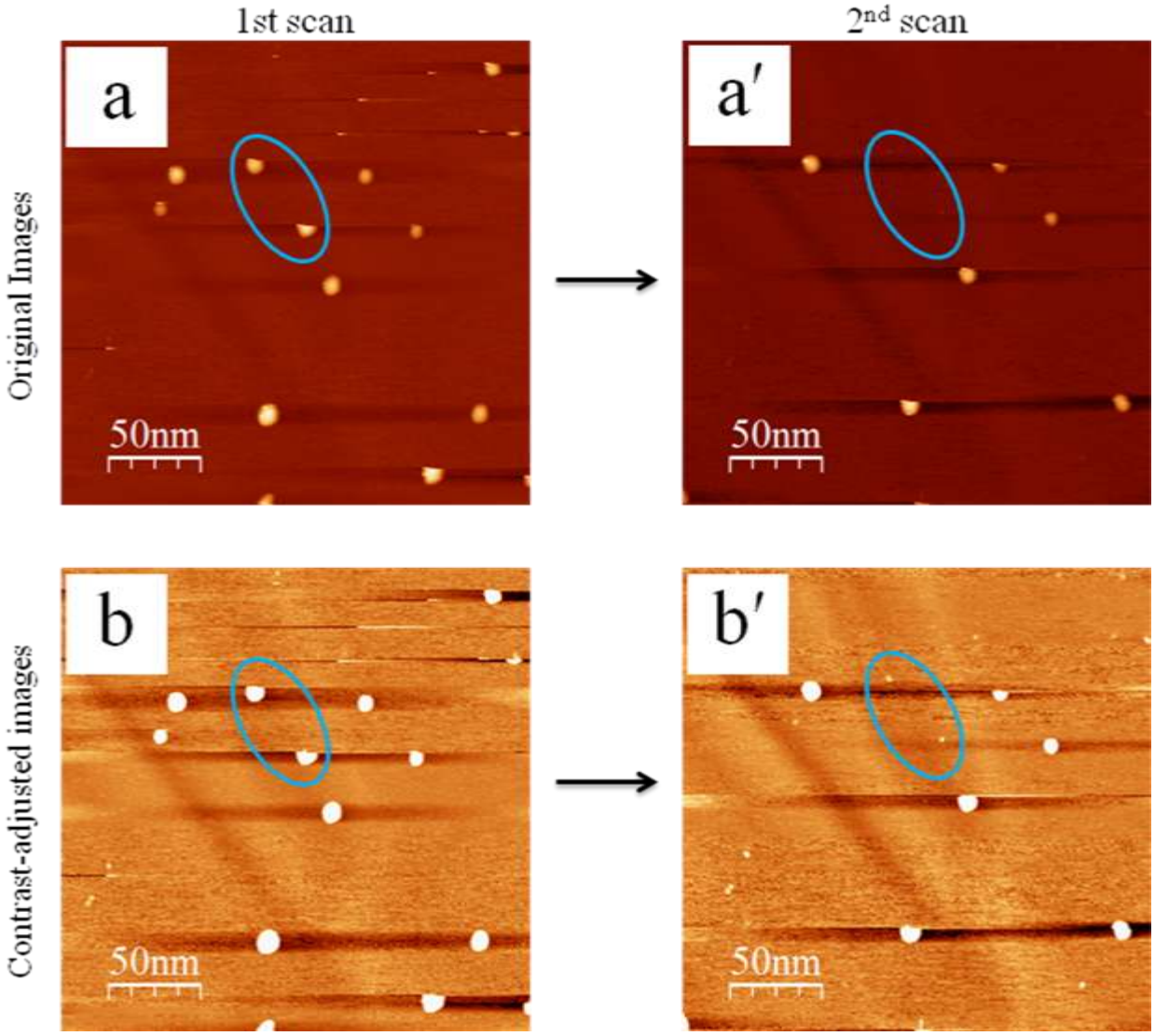

Fig. 10
STM images illustrating tip-sample interaction in the Cu-HOPG system at using different post-processing contrast adjustments. (a) and (a′) Consecutive scans of the same area. (b) and (b′) Consecutive scans of the same area as in (a) and (a′), but with image contrast adjusted to highlight subtle surface features. The circles show areas where islands are sheared in the first image and gone in the second image. All images are for 0.01 ML Cu and 250 nm x 250 nm, V_{tip} = -0.9 V, i = 0.8 nA.

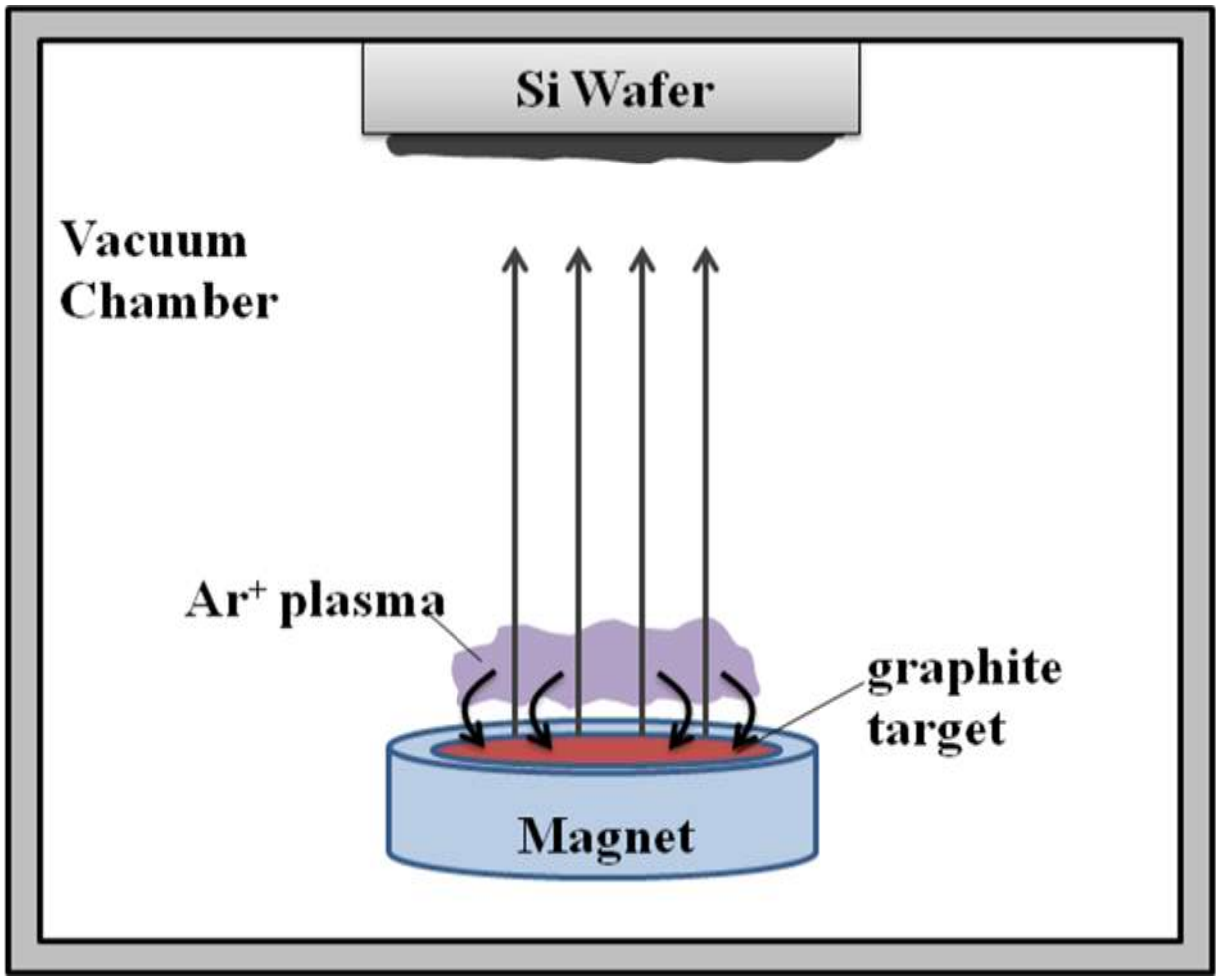

Fig. 11
Schematic diagram of a magnetron sputter system for fabricating a-C films.

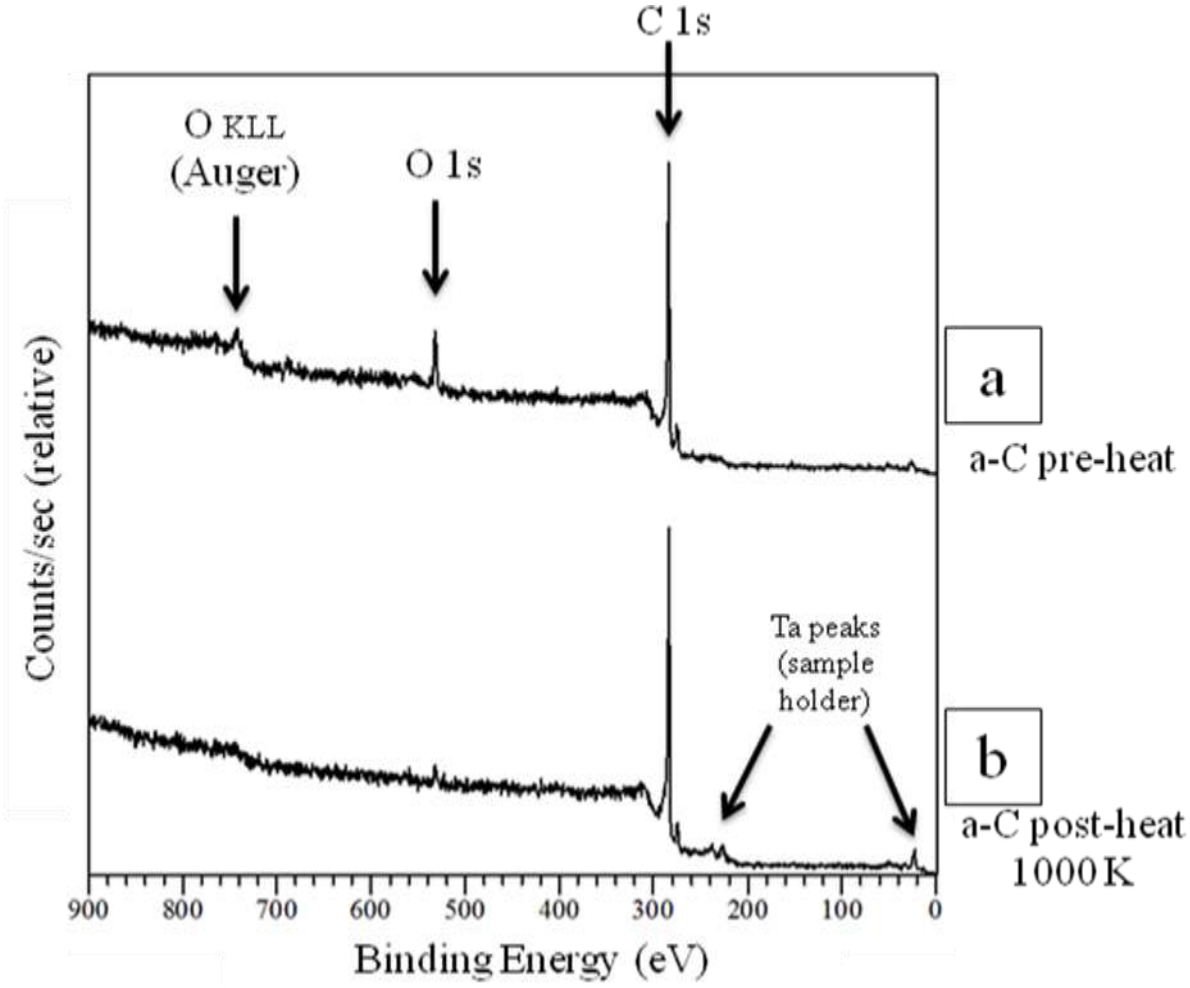

Fig. 12
XPS spectra of an amorphous carbon surface (a) pre-heat; and (b) after heating to 1000 K for 6 hrs. The small residual oxygen peaks in the post-heated spectrum are attributed to the Ta sample plate, which was slightly in view.

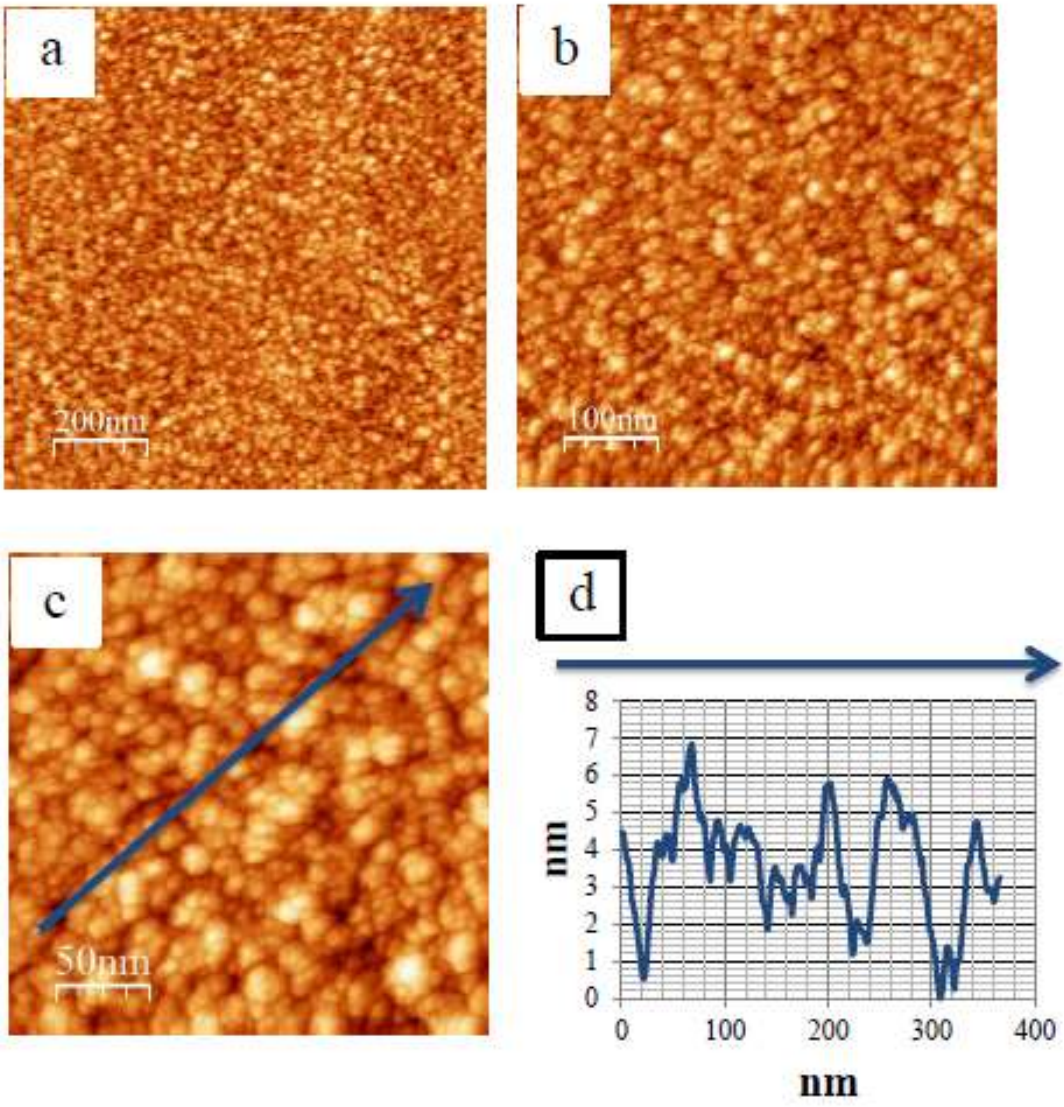

Fig. 13
STM images of an a-C surface at different magnification, (a) 1 μm x 1 μm, V_{tip} = -6.0 V, *i* = 3.0 nA; (b) 500 nm x 500 nm, V_{tip} = -5.1 V, *i* = 2.4 nA; (c) 250 nm x 250 nm, V_{tip} = -5.1 V, *i* = 2.4 nA; and (d) a line profile from (c).

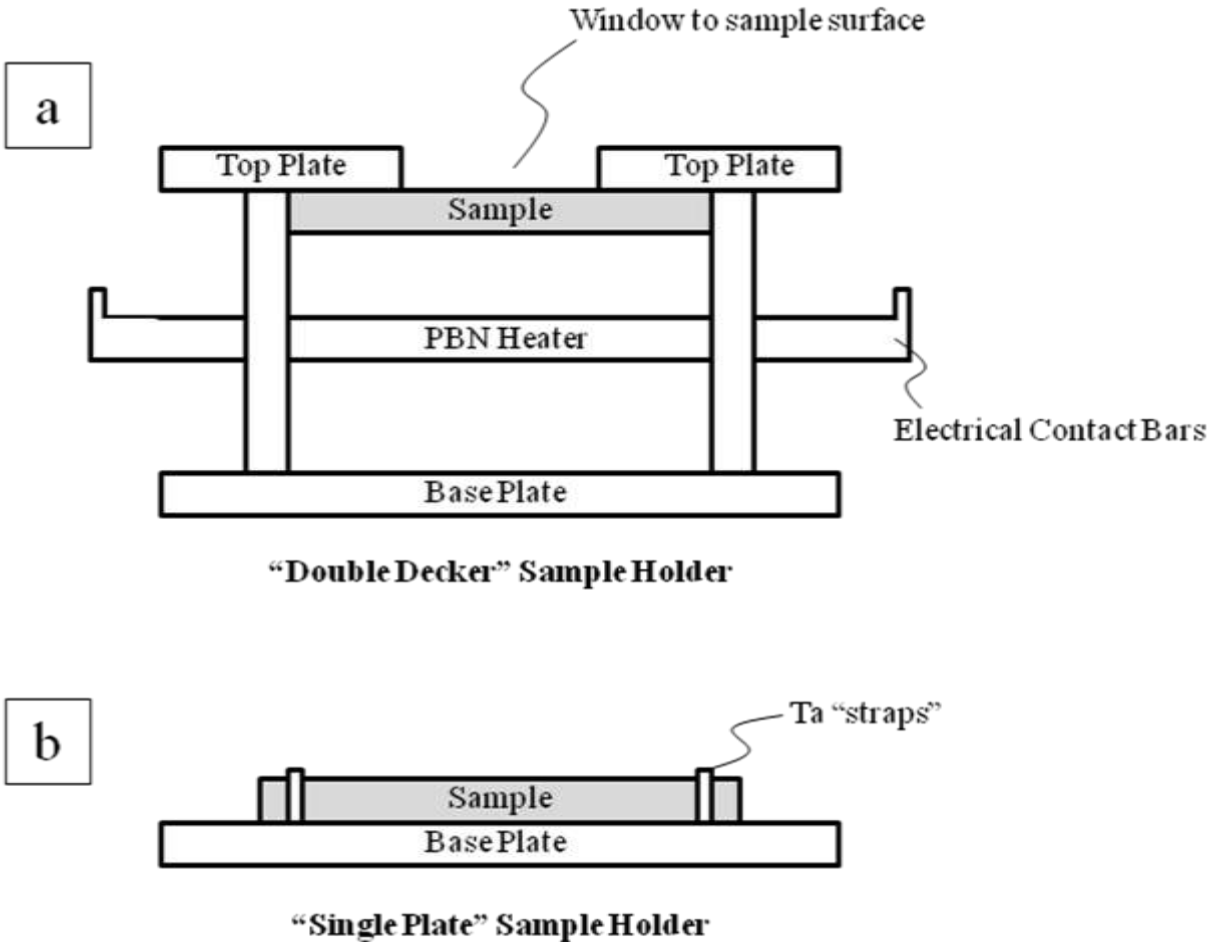

Fig. 14
Cross-sectional schematic of sample holder types used in this work; (a) double decker; and (b) single-plate.

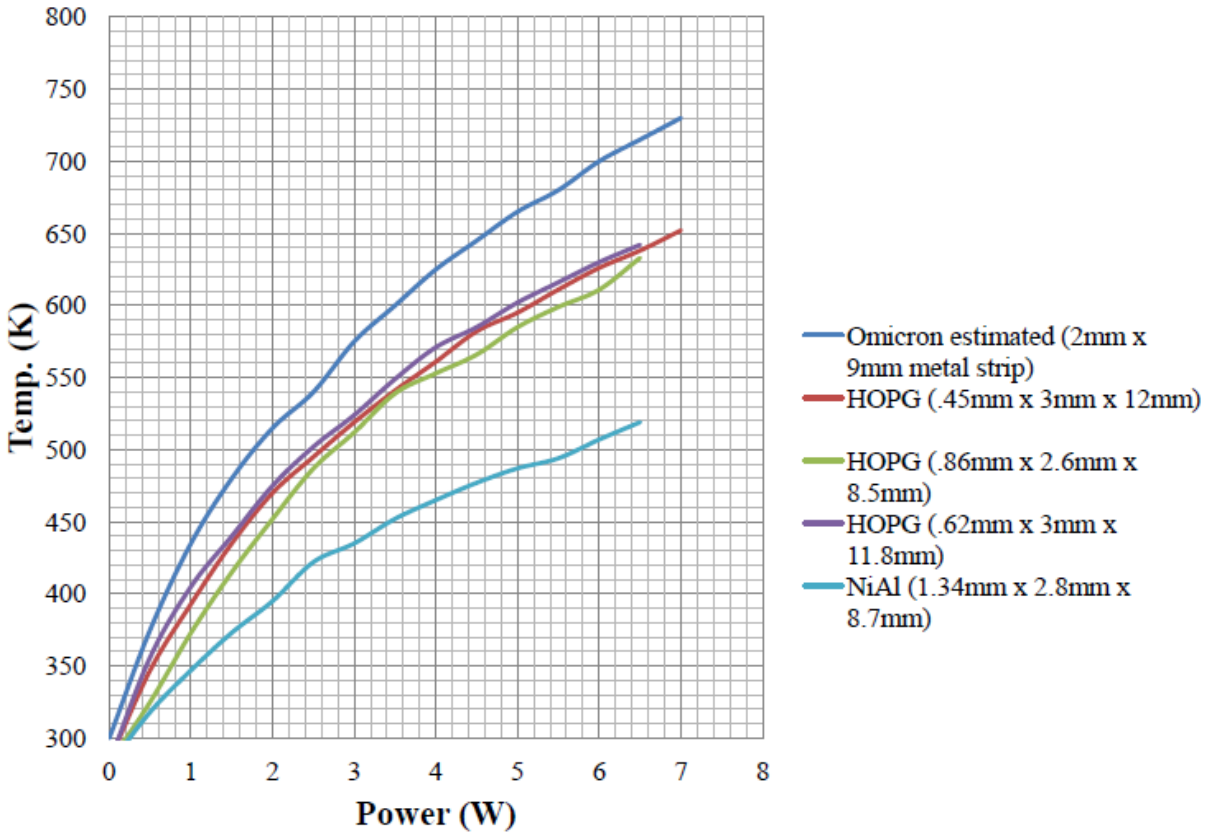

Fig. 15
Calibration curves for resistive heating various samples in a double decker sample holder in the STM stage. Thermocouple sandwiched between sample and top plate.

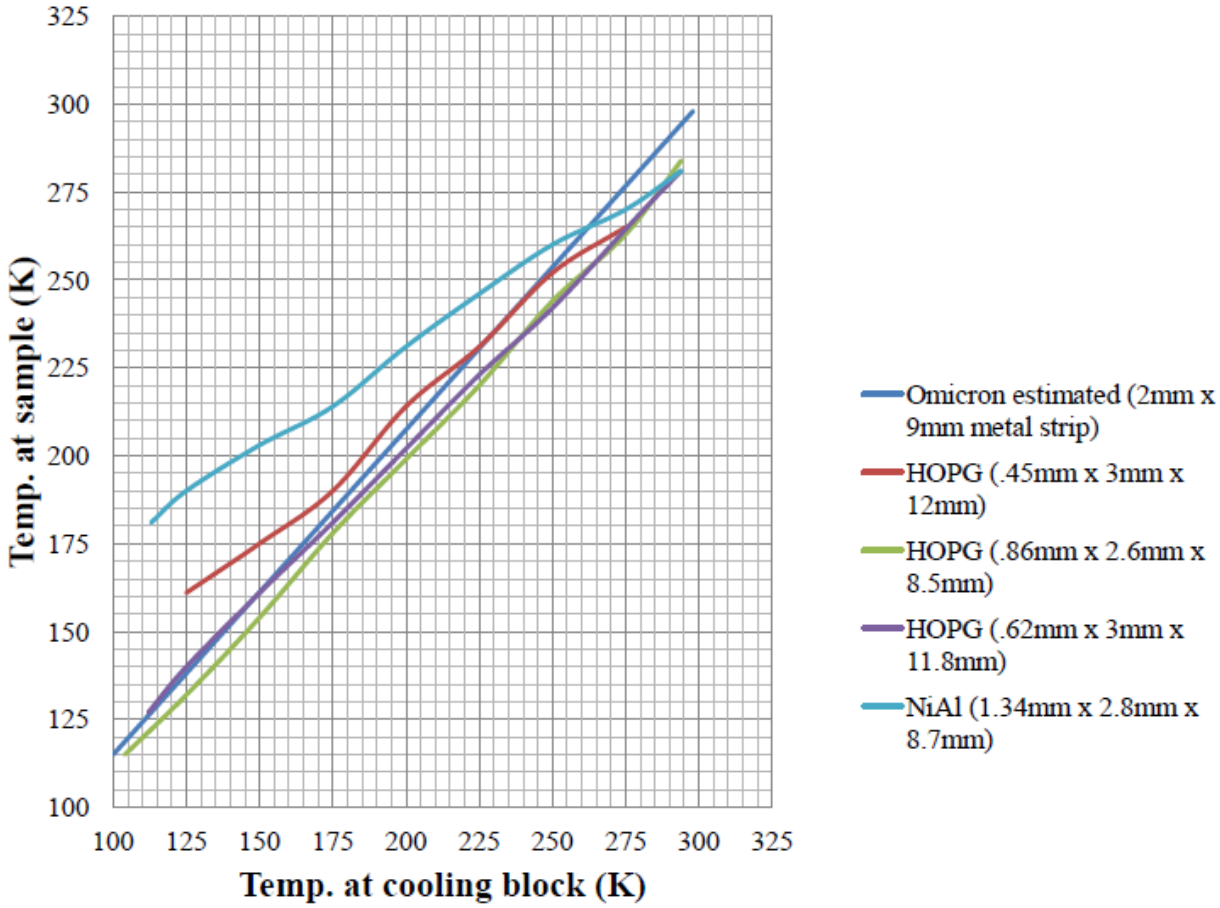

Fig. 16
Calibration curves for LN_2 cooling of various samples in a double decker sample holder in the STM stage. Thermocouple sandwiched between sample and top plate.

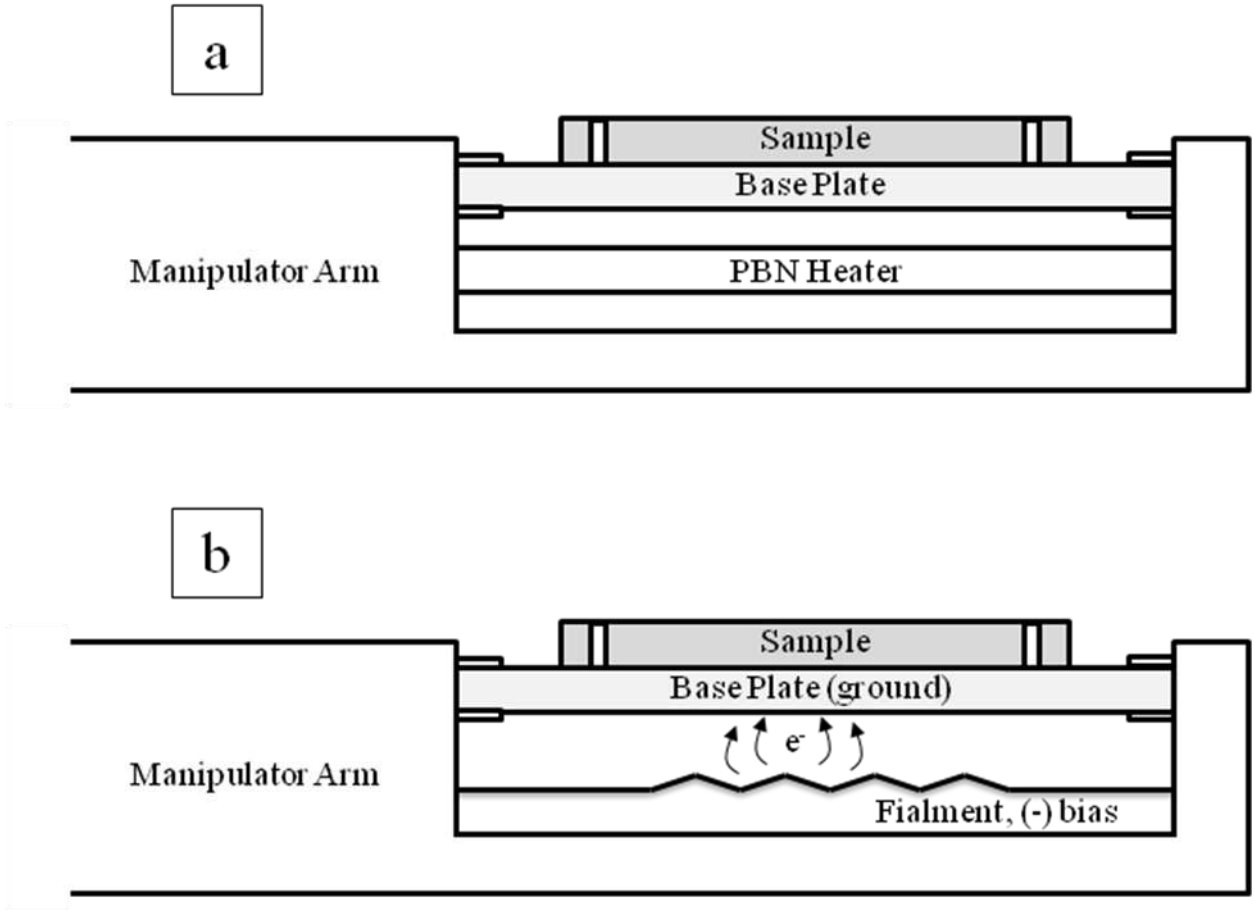

Fig. 17
Schematic diagram of two different heater heads for heating single plate samples in the manipulator (a) with a PBN heater (resistive heating); and (b) with an e-beam heater.

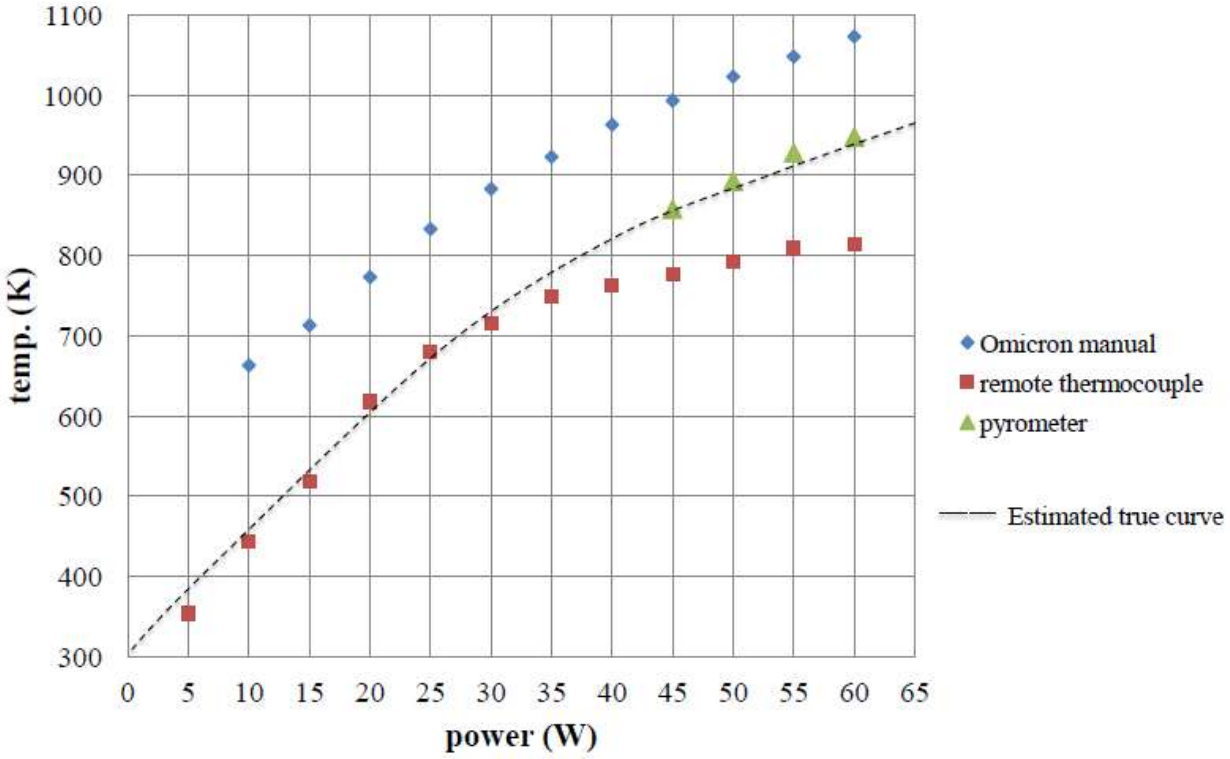

Fig. 18
Heating calibration curve for a 0.4 mm thick HOPG sample mounted on a Ta plate in the manipulator (PBN heater). Estimated curve is forced through origin.

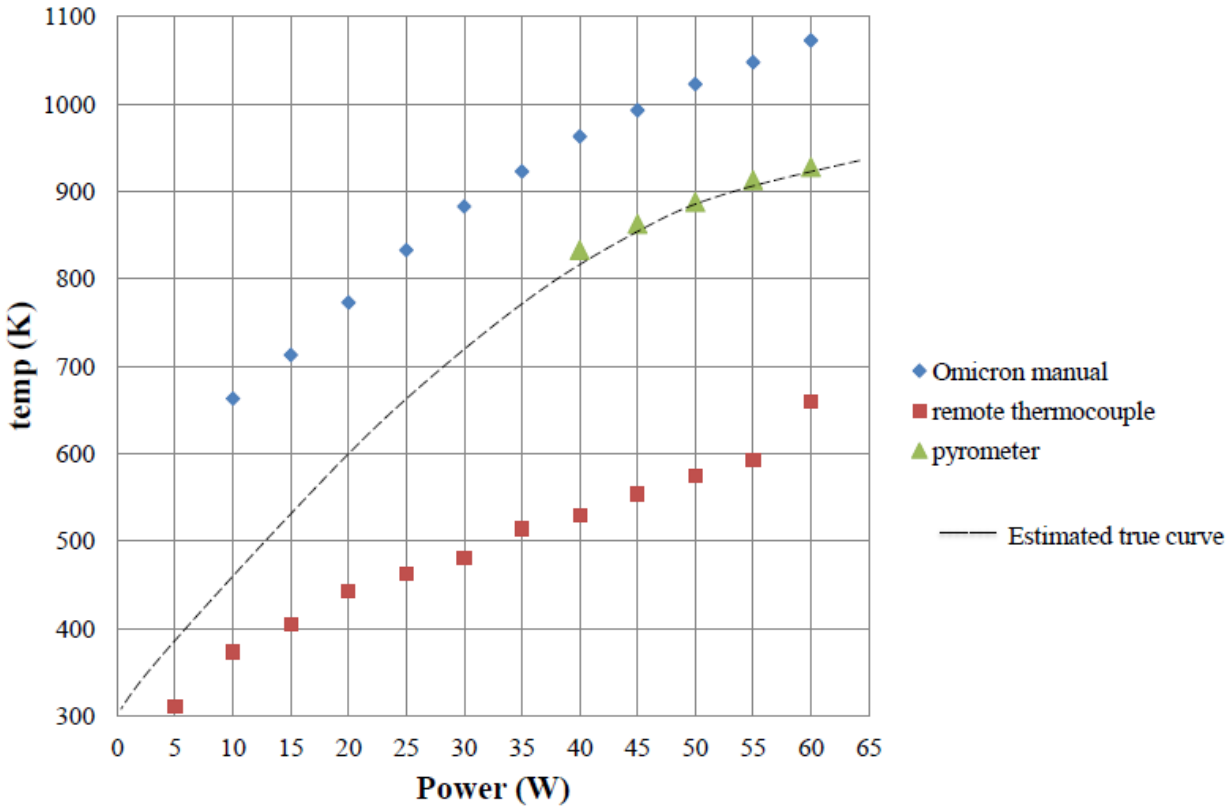

Fig. 19
Heating calibration curve for an a-C on 0.30 mm-thick Si wafer mounted on a Ta plate in the manipulator (PBN heater). Estimated curve is forced through origin.

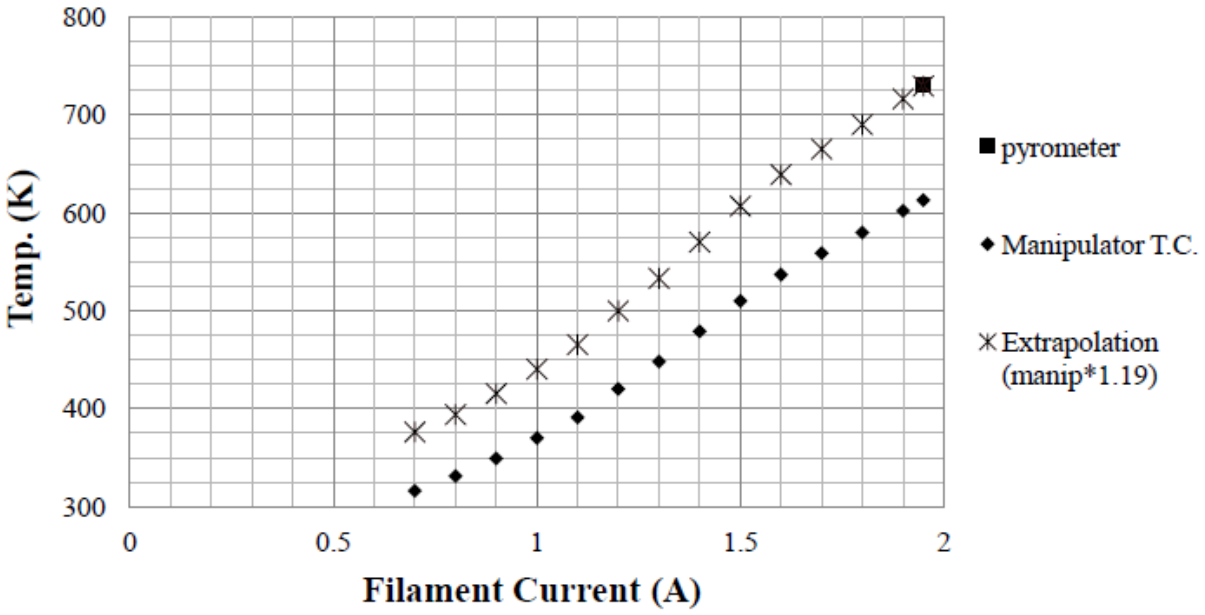

Fig. 20
Heating curves (Temp v. Filament Current) for 0.40 mm HOPG mounted on a Ta plate in the manipulator (e-beam heater) using the 0 V bais setting.

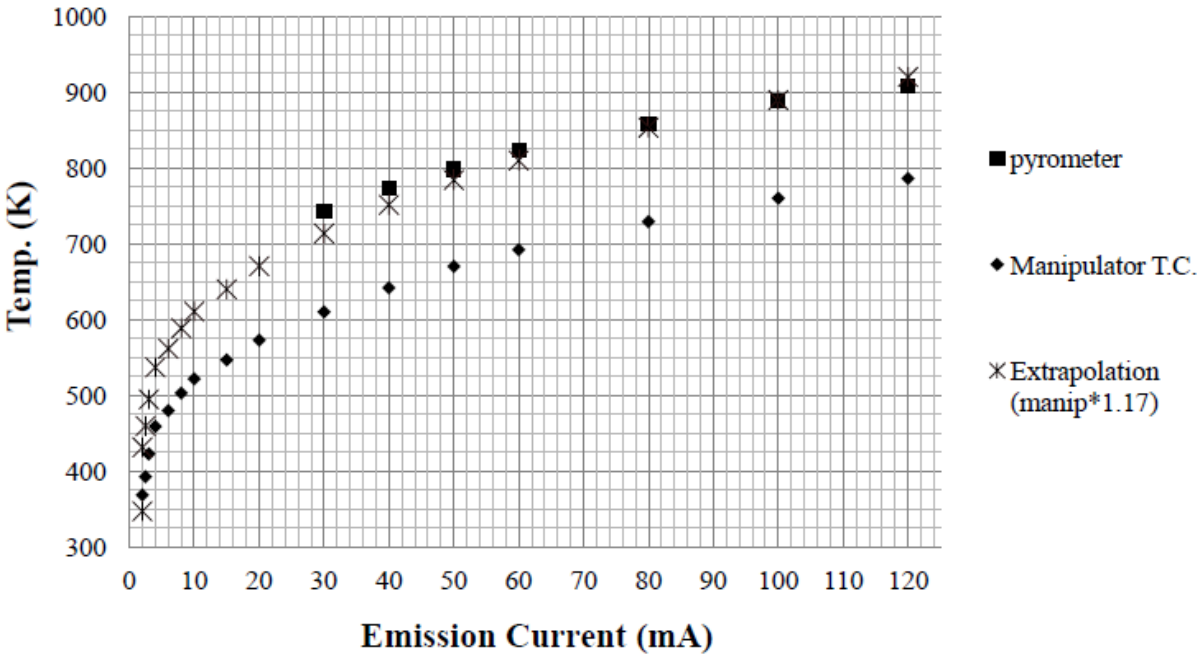

Fig. 21
Heating curves (Temp v. Emission Current) for 0.40 mm HOPG mounted on a Ta plate in the manipulator (e-beam heater) using the -150 V bais setting.

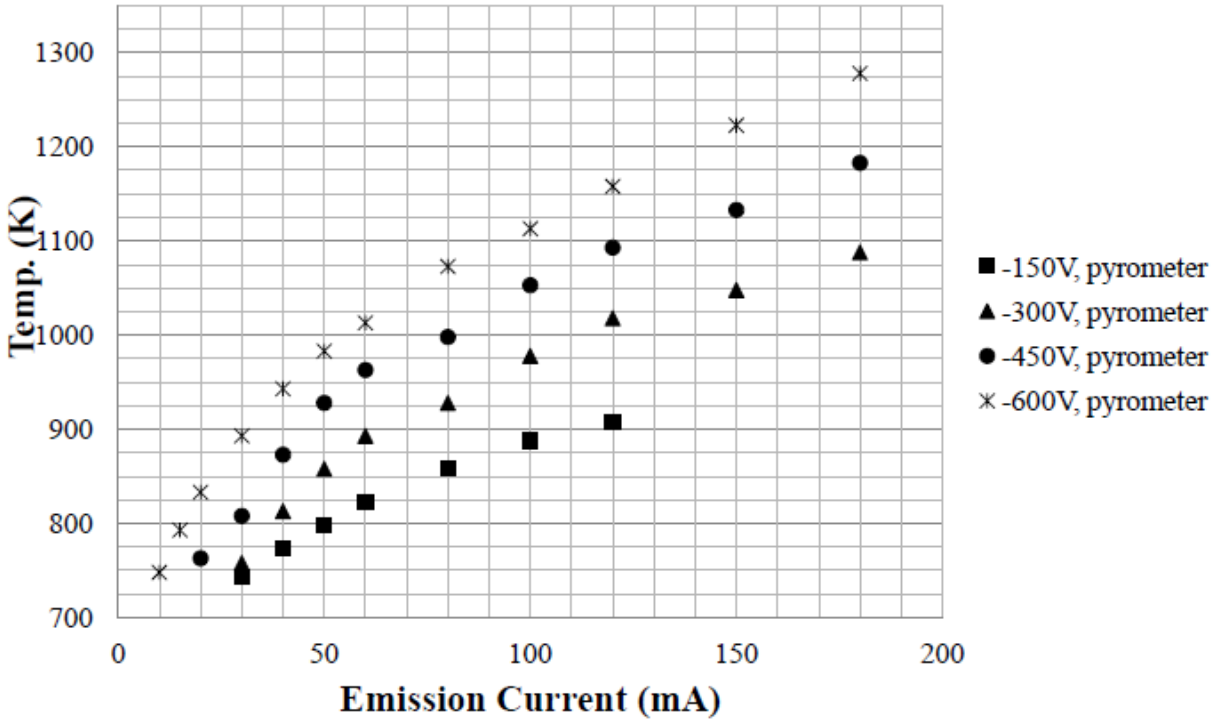

Fig. 22
Heating curves (Temp. v. Emission Current) for 0.40 mm HOPG mounted on a Ta plate in the manipulator (e-beam heater) at various bias settings. High temperature regime only.

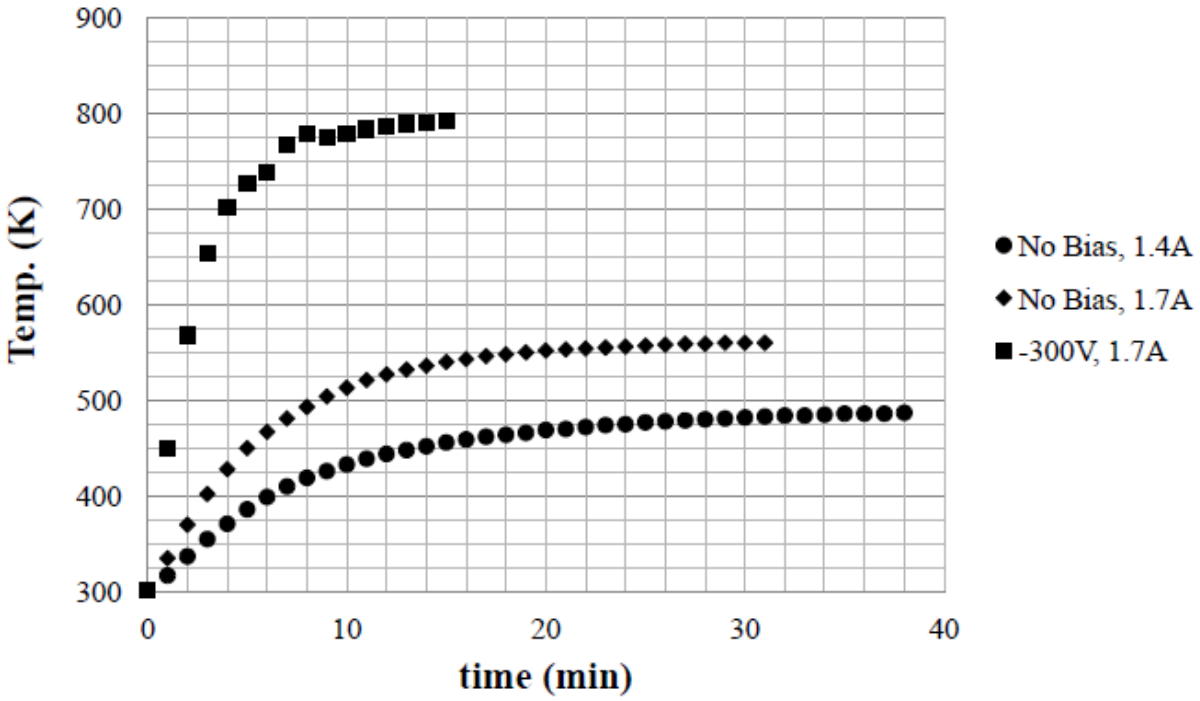

Fig. 23
Heating equilibration time curves for 0.40 mm HOPG mounted on a Ta plate in the manipulator (e-beam heater) using the manipulator thermocouple.

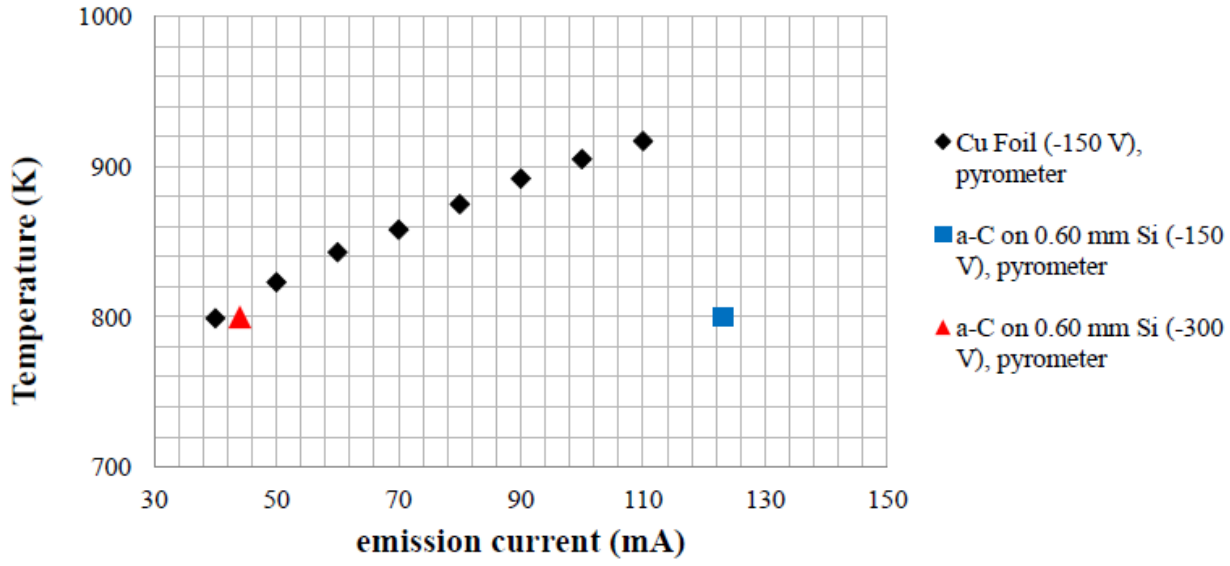

Fig. 24
Heating curves (Temp. v. Emission Current) for miscellaneous samples in the manipulator (e-beam heater).

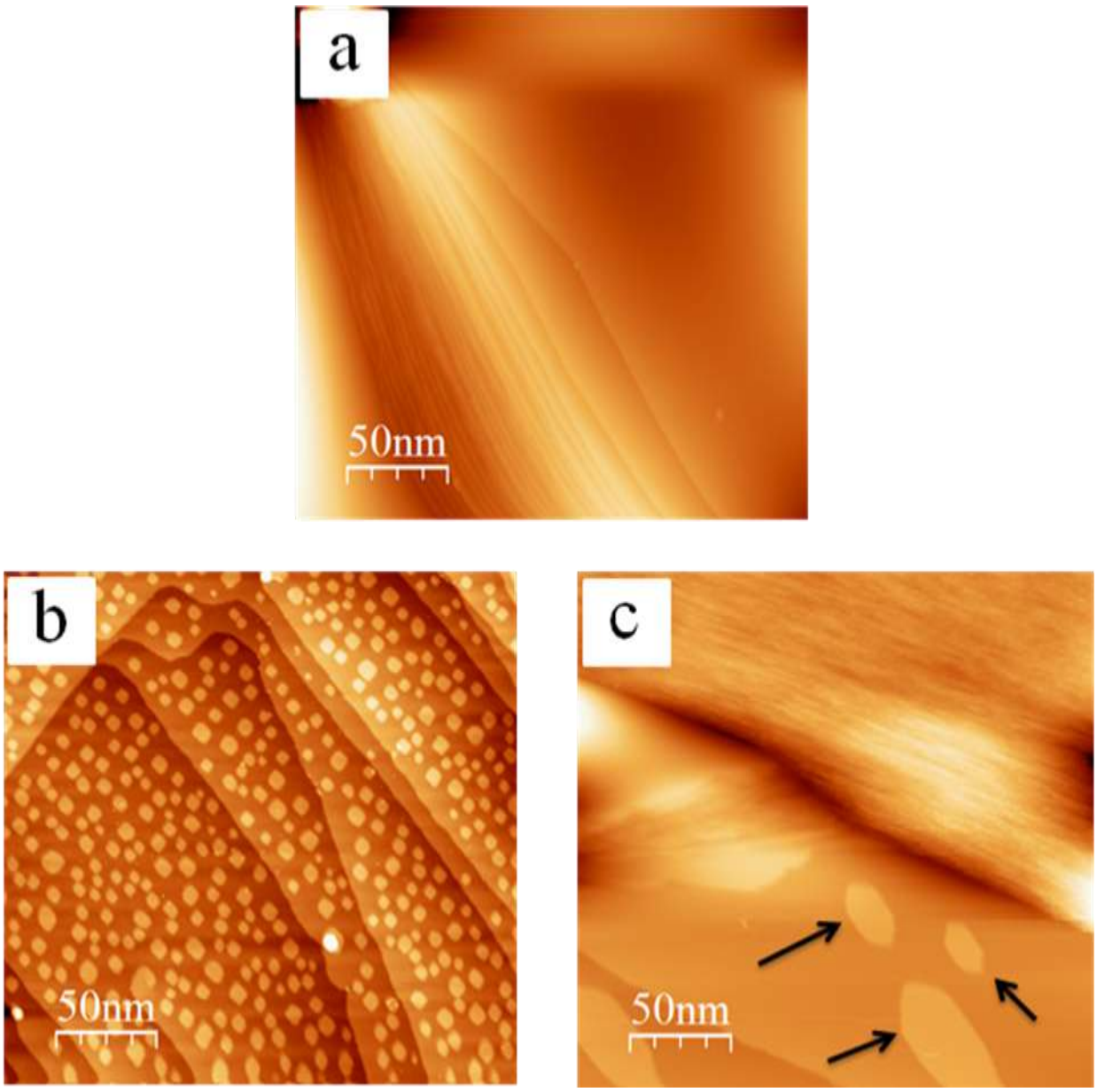

Fig. 25
STM images of (a) The clean Cu surface showing a terrace (upper right area), V_{tip} = -2.0 V, *i* = 0.1 nA; (b) square Cu island on Cu(100) terraces, V_{tip} = -3.1 V, *i* = 0.1 nA; and (c) hexagonal Cu islands on a Cu(111) terrace, V_{tip} = -3.5 V, *i* = 0.1 nA. All images 250 nm x 250 nm.

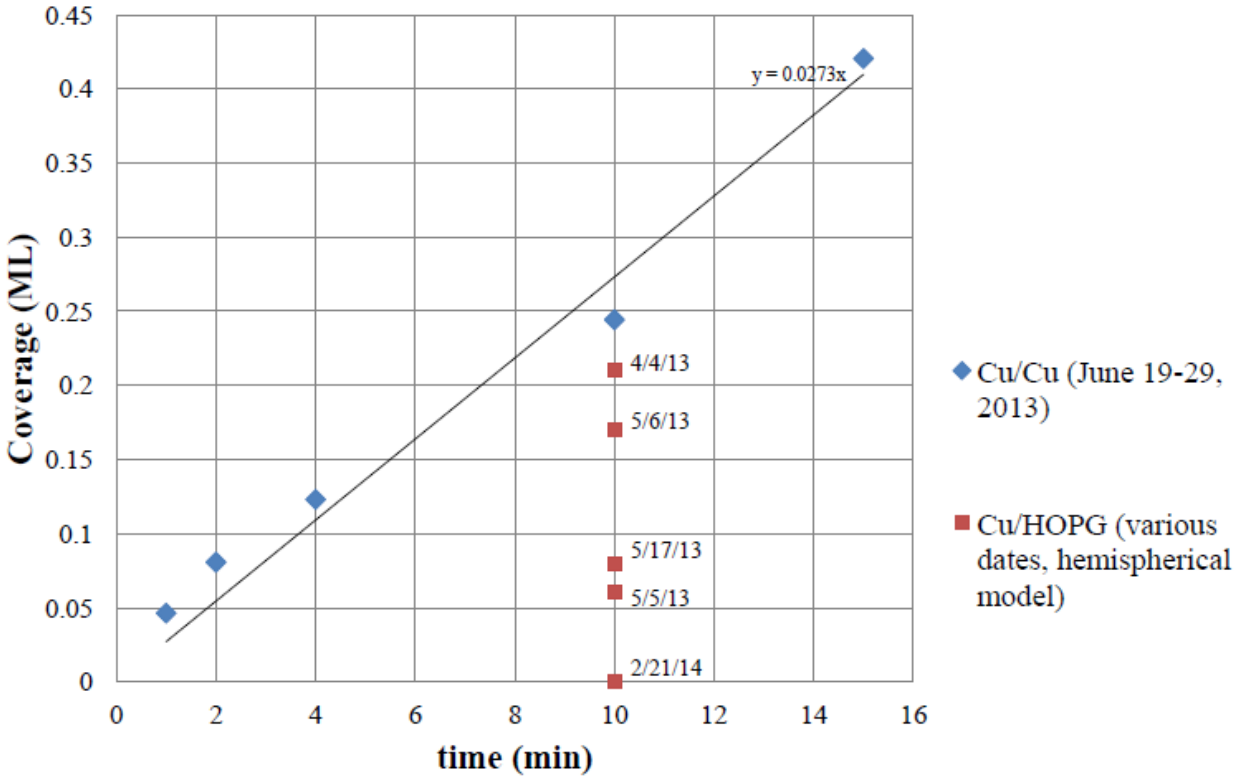

Fig. 26
Cu calibration plot comparing Cu/Cu(100) coverages at 23.5 W versus Cu coverages on HOPG at the same power but different dates.

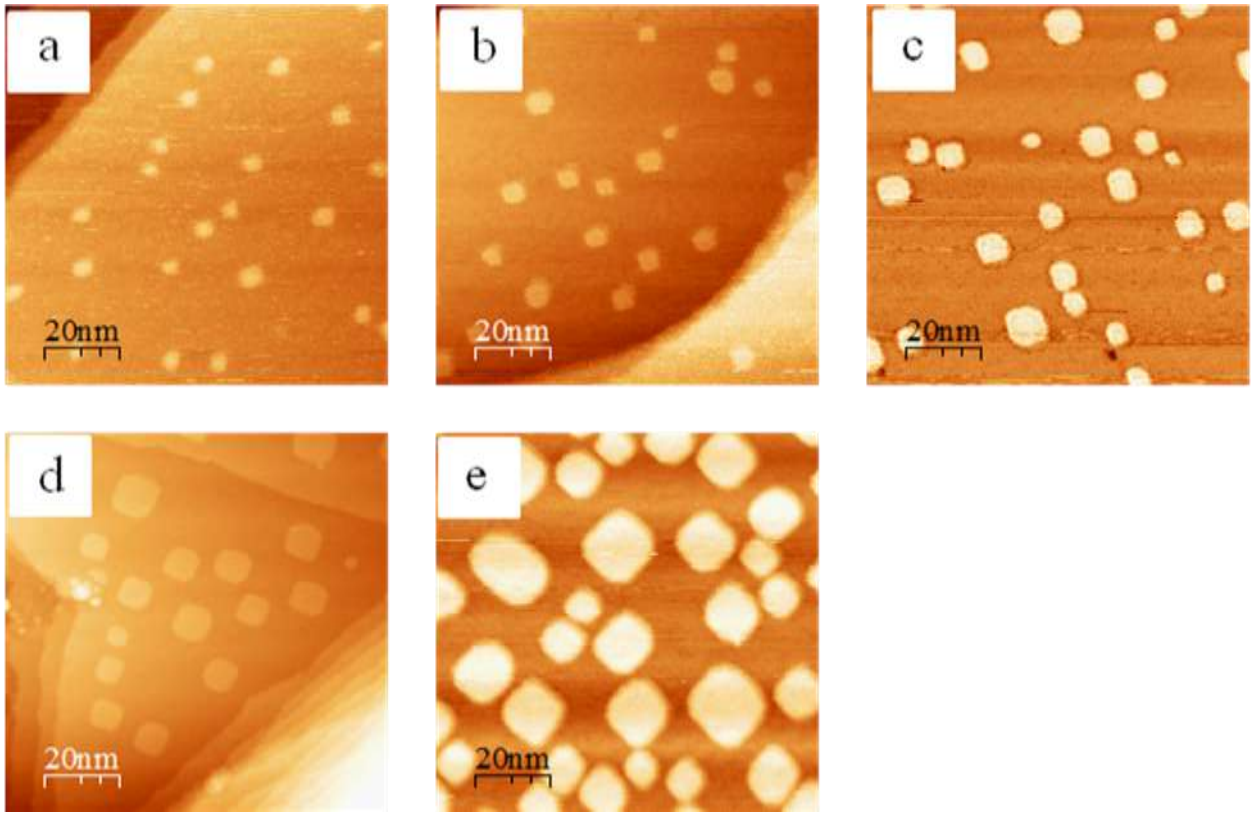

Fig. 27
STM images of the Cu/Cu(100) calibration (23.5 W) from Fig. CUEARLY1. (a) 1 min, 0.05 ML; (b) 2 min, 0.08 ML; (c) 4 min, 0.12 ML; (d) 10 min, 0.24 ML; and (e) 15 min, 0.42 ML. All images 100 nm x 100 nm, V_{tip} = 1.7 V, *i* = 0.1 nA. All images 100 nm x 100 nm.

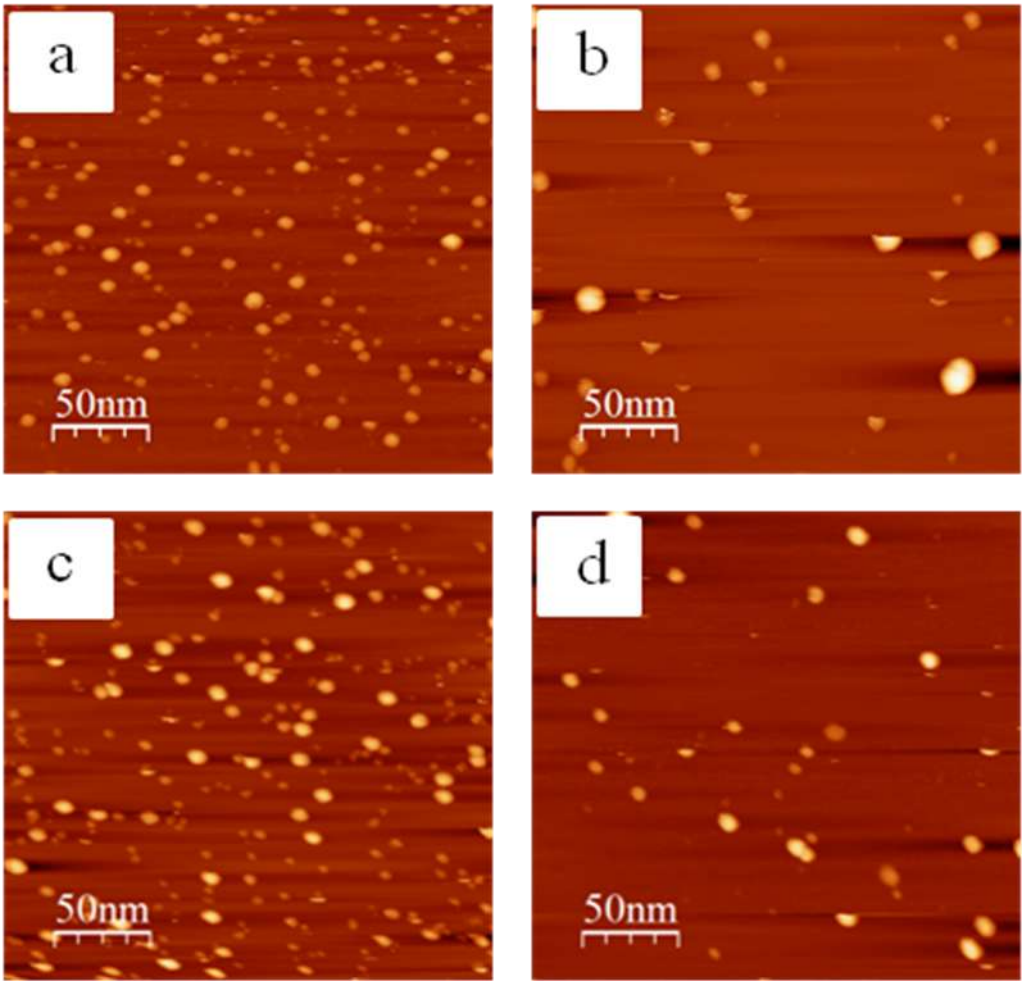

Fig. 28
STM images of the Cu/HOPG data points (23.5 W at various dates) from Fig. CUEARLY1. (a) 4/4/13, 0.21 ML, V_{tip} = -1.5 V, *i* = 0.3 nA; (b) 5/5/13, 0.06 ML, V_{tip} = -1.0 V, *i* = 0.3 nA; (c) 5/6/13, 0.17 ML, V_{tip} = -1.5 V, *i* = 0.3 nA; and (d) 5/17/13, 0.08 ML, V_{tip} = -1.5 V, *i* = 0.3 nA. All images 250 nm x 250 nm.

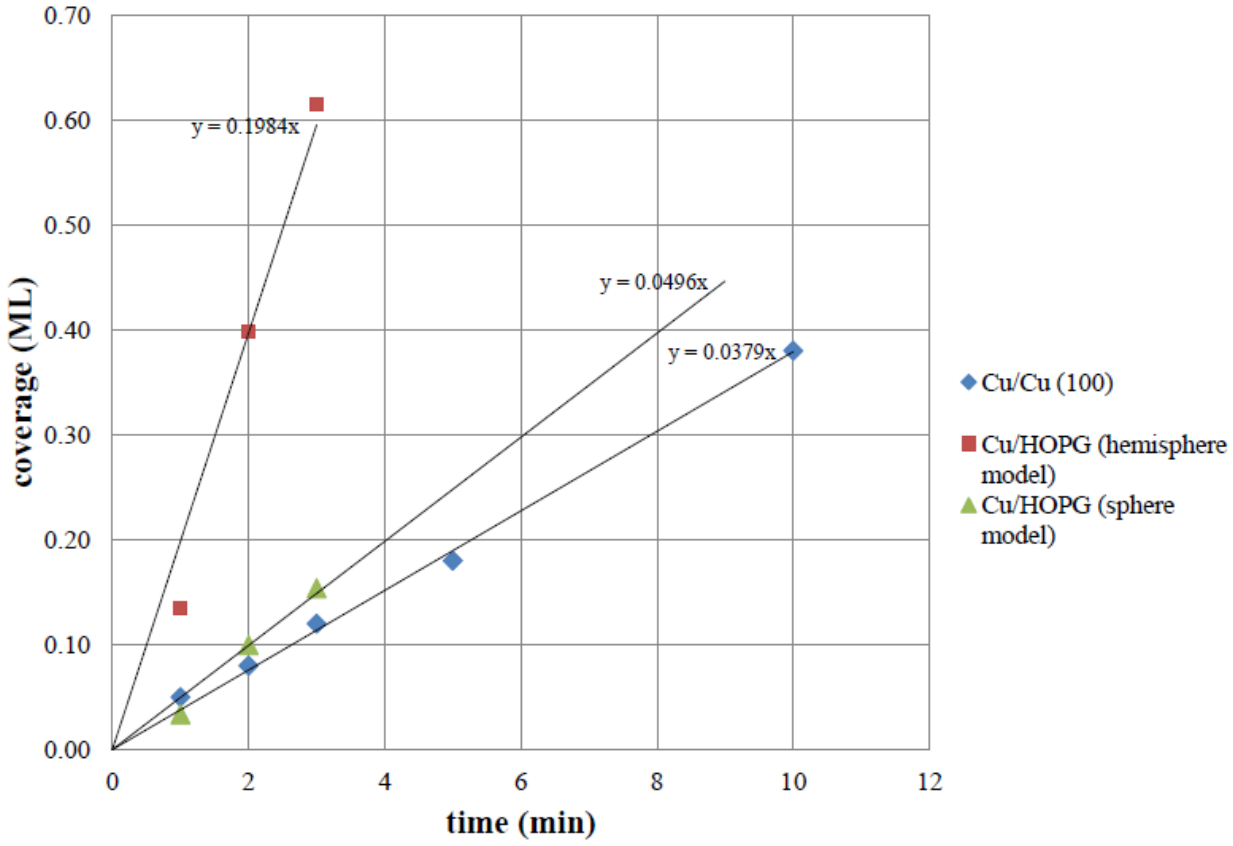

Fig. 29
Cu calibration plot comparing Cu/Cu(100) coverage vs. Cu/HOPG coverage on the same day at 32 W power, but using different models for the shape of Cu/HOPG clusters.

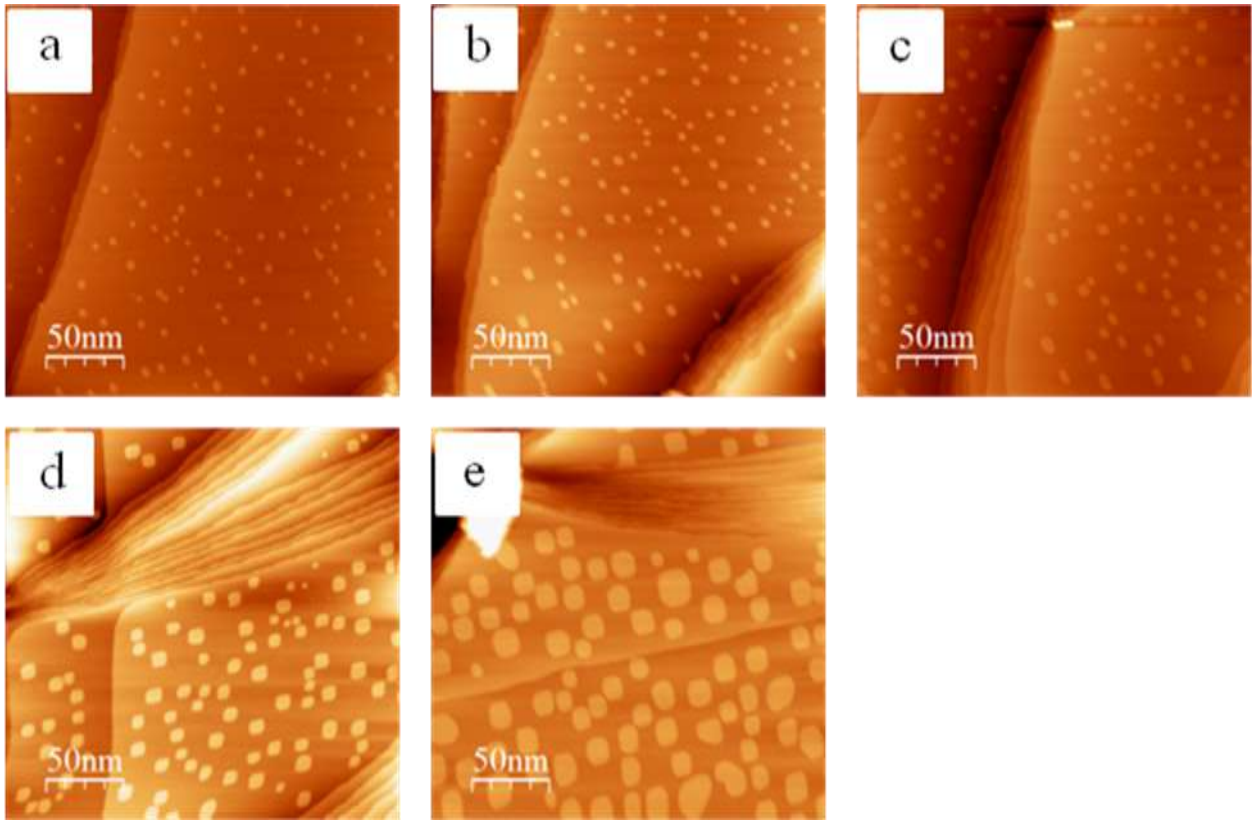

Fig. 30
STM images of the Cu/Cu(100) calibration (32 W) from Fig. CULATER1. (a) 1 min, 0.05 ML; (b) 2 min, 0.08 ML; (c) 3 min, 0.12 ML; (d) 5 min, 0.18 ML; and (e) 10 min, 0.38 ML. All images 100 nm x 100 nm, V_{tip} = -2.0 V, *i* = 0.1 nA. All images 250 nm x 250 nm.

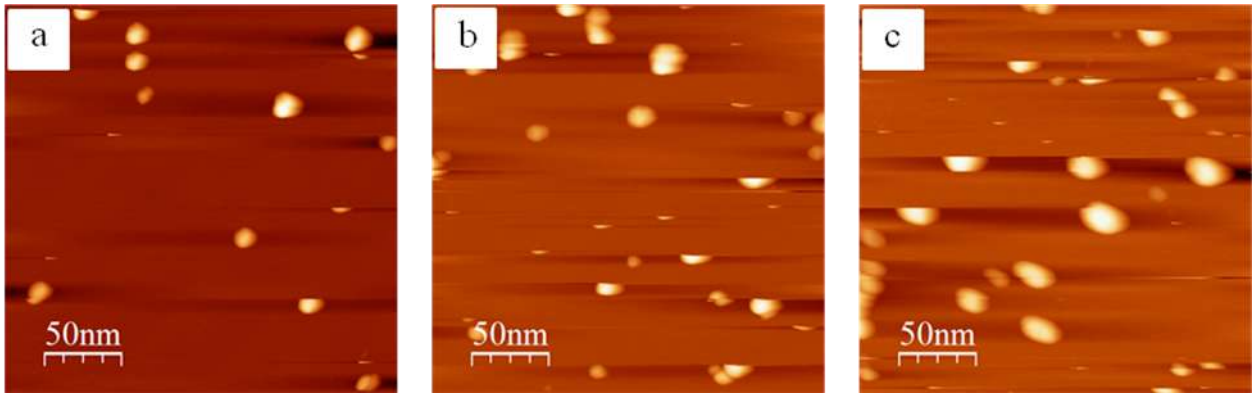

Fig. 31
STM images of the Cu/HOPG calibration (32 W) from Fig. CULATER1. (a) 1 min; (b) 2 min; and (c) 3 min. All images 250 nm x 250 nm and V_{tip} = -1.0 V, *i* = 0.05 nA.

CHAPTER 3

CU ON HOPG AT T ≤ 300 K

3.1 Introduction

This work was motivated by the discovery of a family of metal nanowires (NW's) which grow as single crystals protruding substantially perpendicular to a substrate.[1-3] Single crystalline metal nanowires were grown for a variety of metal/substrate systems, but the most prolific growth was seen for Cu on carbon surfaces, especially amorphous carbon (a-C), but also highly ordered pyrolytic graphite (HOPG) (see Fig. 1). HOPG provides a good starting point for our investigation of NW growth because it is a flat, homogeneous surface easily analyzed with scanning tunneling microscopy (STM).

To the best of our knowledge there have only been two STM studies done on the Cu/HOPG system, only one of which was a UHV study. Ganz et al. [4] studied Ag, Au, Al, and Cu on HOPG in UHV. They found that Cu decorated step edges but they had limited data regarding features on the terraces besides a single rectangular crystallite. Ganz's study focused more on Ag and Au, which they found to form 2D clusters incommensurate with the graphite lattice. Whelan and Barnes [5] studied Cu on HOPG by depositing Cu at 10^{-6} torr and imaging with STM in air. They worked exclusively in high coverage regimes (3-75 ML) and found large aggregations of clusters both on the terraces and steps, with highly mobile Cu clusters diffusing along step edges. Imaging in air raises questions as to the role of atmospheric contaminants in the processes they were observing. There are no reports (to our knowledge) of experimentally derived values for basic energetics parameters like diffusion barrier (E_d) and critical nucleus size (i) for the Cu/HOPG system. However, there has been some theoretical work for the

Cu/*graphene* system which predicts a very low diffusion barrier in the range of 0.008-0.09 eV[6]. Experimental studies of a related system, Au on HOPG, are in sharp disagreement regarding a value for E_d, with estimates of < 0.24 eV[7] and ≥ 0.8 eV[4].

Determining the basic energetic parameters for the Cu/HOPG system could ultimately prove useful for modeling nanowire growth. Diffusion barrier (E_d) and critical nucleus size (i) can be extracted from systems exhibiting homogeneous nucleation based on the dependence of cluster density on temperature and flux, respectively.[8-10] Therefore a primary goal of this study was to determine the extent to which homogeneous nucleation occurs in the Cu/HOPG system.

3.2 Clean Surfaces - Defect Characterization

We began our study of the nucleation and growth of Cu on HOPG terraces with a survey of the defect density on the clean terraces since defects could, in principle, affect nucleation of Cu clusters. Previous reports in the literature, based on direct STM imaging of defects on terraces, or on densities of etch pits created by oxidation, have ranged from 1.0×10^{-8} to 8.0×10^{-5} nm^{-2}.[11-16] Based on extensive examination of clean HOPG surfaces, we estimate that the upper limit of the density of small defects on terraces is about 1×10^{-5} nm^{-2} (5×10^{-7} per C atom in the surface plane), independent of HOPG grade or heat treatment (see Table 1). The defect density of 1×10^{-5} nm^{-2} corresponds to just under 1 point defect in a 250 nm x 250 nm image.

Defect densities were measured in two ways. First, an area of approximately 1×10^{6} nm^2 for each grade (ZYH and ZYA) was sampled using high-quality images of 500 nm x 500 nm or smaller (see Figs. 2-3). This image size was sufficient to locate point defects on the surface, in agreement with Kelly[17]. In the second approach, approximately two hundred 25 nm x 25 nm

non-overlapping atomic-resolution images (see Fig. 4) of the ZYA graphite lattice (the equivalent of two 250 nm x 250 nm images) were taken to search for small defects or adsorbates perhaps not visible at the larger scale, but none were found. Table 1 shows a summary of the defect survey. A high-magnification image of a typical clean-surface defect in our work is shown in Fig. 5. This could be a single-C-atom vacancy, an absorbed impurity, or an intercalated impurity. Fig. 6 shows a rare cluster of defects. The green and yellow insets show smaller defects which changed in size and placement from scan to scan. These smaller defects were probably part of the larger defect originally, but were moved by the STM tip. The defect in Fig. 6 is probably an adsorbate, but it also may be sitting atop another defect such as a vacancy.

3.3 Overview of Cu Deposition Results

Figs. 7-10 show the development of Cu clusters on HOPG terraces at 300 K, over about two orders of magnitude of Cu coverage, i.e. 0.003 ML to 3.9 ML. As coverage increased, the average cluster size remained approximately constant but the main effect was an increase in the cluster density. Cu preferentially decorated the step edges even at the lowest coverage (marked with arrows in Figs 7-10), as expected for metals on HOPG.[18-23] Our focus in this study was Cu interaction with the terraces, however. Although maximum image size was typically limited to 250 nm x 250 nm due to sample-tip interaction and ability to see small features, at very high coverages (Fig. 10(h-h″)), it was surprisingly easy to maintain good tunneling, which allowed imaging of a the large area in (h″).

Cu clusters were often disturbed by the tip. Typical observations are shown in a series of consecutive images in Figs. 11. Some Cu clusters (encircled) appeared cut horizontally in the first image, and were completely absent in the second. This demonstrates that some clusters

were removed by the STM tip during scanning. Changing image contrast also helped to resolve flatter features on the surface (see Fig. 12). Similar instability in STM has been reported previously for other metals on HOPG.[18; 24; 25] Small clusters seemed more stable against tip effects than large clusters. When a cluster was removed by the tip, it usually left a small 2D residue, as shown in Fig. 13(a-c). The residues were in the range of 0.1 nm to 0.8 nm high, with most being 0.2 to 0.6 nm high, and from 2 to 6 nm wide. The nature of these residues is discussed more fully in section 3.9.

3.4 Cu Cluster Morphology and Size Distribution

Most Cu clusters were 3D, i.e. their height far exceeded 0.2 nm and hence they consisted of multiple Cu layers. Even at the lowest terrace coverage of 0.003 ML represented in Fig. 7(a-a″), cluster heights ranged from 0.6 to 2.3 nm. It is important to note that in this low coverage experiment there were very few clusters shorter than 0.6 nm, which is good evidence that cluster growth is 3D even from the very beginning.

The true lateral shape of Cu clusters was difficult to discern due to tip convolution. However, in some images a hexagonal shape was visible, as in Fig. 14. If this apparent shape was real, it indicates that the clusters adopt an FCC-like structure. Another curious feature of Fig. 14 is that all of the hexagons face in the same direction, which suggests that the cluster bases were commensurate with the graphite lattice, but this is not the only conclusion that can be drawn. In Fig. 14 it is also apparent that all imaged features, even small clusters which were likely residues of sheared clusters, are hexagonal. The residue in Fig. 13(c) is clearly irregularly shaped, so the apparent hexagons in Fig. 14 could be the products of a hexagonally-shaped STM tip apex rather than hexagonal cluster shape. The literature provides some insight as to the

possibility of cluster alignment with the graphite lattice. A TEM study showed that Au dendrites show some preferential alignment with the graphite lattice[26], as do faceted Au crystallites at higher temperatures[27]. The crystallites, however, were very diverse in their shapes. Al forms flat-topped triangular crystallites which align preferentially with the graphite lattice at 300 K[28]. Based on these findings it is plausible that the Cu clusters we see in our experiments are faceted and aligned with the substrate lattice.

The distribution of cluster heights (*H*) and widths (*W*) at three coverages is shown in Fig. 15. These plots include an accounting of all real imaged features. For each population, there is a clustering of features with widths 3-6 nm and heights < 0.6 nm, which suggests small, 2D clusters. However, DFT indicates that 2D Cu clusters should not exist on HOPG based on the relatively small Cu/HOPG adsorption energy (0.51 eV[29]) compared with bulk cohesive energy of Cu (2.27 eV[30]). This data, in conjunction with the presence of residues left behind by cluster removal, lends to the conclusion that the apparent 2D clusters we saw were not true small clusters, but residues left behind by larger clusters removed by the STM tip.

Fig. 16 shows cluster height histograms for two series of depositions, using two different fluxes: (a) 3×10^{-5} ML/s and (b) 1×10^{-2} ML/s. Fig. 17 shows relative cluster size histograms for the same two data sets, where cluster size (S/S_{av}) can be defined as either relative cluster volume or number of atoms. The monomodal decay in cluster size is atypical for homogeneous nucleation systems (where one expects a maximum at small S), and lends support to a heterogeneous nucleation model.

Most histograms (and coverage calculations) do not include clusters < 1 nm high. Excluding small features in coverage calculations was done primarily for time-saving purposes, since clusters < 1 nm high account for < 1 % of the total Cu volume yet may account for 10-50%

of the total cluster population (10-30% under good tunneling conditions), as shown in Table 2. The data set used to construct this table had a particularly large number of clusters with height < 1 nm, which sets a soft upper limit for all data sets. We chose not to adjust our coverages upward based on projections of the volumes of missing clusters, but acknowledge that 10-30% of clusters are removed by the STM tip. For purposes of cluster densities, however, small clusters were counted because they were likely to be residues left behind by larger clusters that were removed by the STM tip.

Fig. 18 is an expanded histogram for the 0.1 ML coverage of the 11/13/13 data set, which was one of the best data sets. In this histogram, particular care was taken in selecting the small clusters to consider. We used clusters > 0.6 nm that were not obvious residues of a sheared cluster.

There is a hypothetical exercise which might justify excluding the small clusters in our images. In a normal analysis of nucleation and growth, the flux of adatoms at an island is controlled by the capture area. However, if one assumes that all clusters present on the surface receive approximately the same Cu flux, then it follows that cluster size (either expressed as a volume or a number of atoms) correlates roughly with cluster age. Because cluster volume is a function of h^3, the relative volume of a 3 nm high cluster compared to a 1 nm high cluster is 27:1, or approximately 4%. So in a system where the average cluster height is 3 nm (as is common in our system), if cluster density changes linearly with coverage (and with time), at the instant that deposition ends we expect a maximum of 1/27 (4%) of the cluster population to be < 1 nm high. In contrast, we found that 10-50% of the clusters imaged (as in Table 2) are < 1 nm high, which far exceeds the hypothetical upper limit of 4%. Therefore most of the small clusters imaged were probably not true clusters, but remnants of larger clusters.

3.5 Cu Cluster Density and Coverage-dependence of Cluster Density

The density of Cu clusters on terraces varied from about 2 x 10^{-4} nm^{-2} to 1.8 x 10^{-2} nm^{-2}. The variation was linear with terrace coverage up to the point of saturation at ca. 1 ML, independent of graphite grade and independent of flux over three orders of magnitude, as shown in Fig. 19. The grade-independence of cluster density was not surprising since the ZYH and ZYA surfaces had similar point defect densities which were at least an order of magnitude lower than the lowest coverages. The flux independence was a bit more surprising, as discussed below.

3.6 Comparison with Theory – Homogeneous Nucleation

One of the primary objectives of this study was to determine the extent to which homogeneous nucleation occurs, meaning nucleation caused by two or more copper atoms forming a cluster at random on the pristine graphite lattice. In contrast, heterogeneous nucleation means nucleation caused by a copper atom coming into contact with a defect or some heterogeneity on the graphite surface. The fact that our cluster density was one to three orders of magnitude higher than the defect density on the clean graphite surface supports a hypothesis of homogeneous nucleation. However, when we applied nucleation theory to our system based on reasonable estimates of the energetic parameters, we found that our experimental cluster densities far exceeded the predicted homogeneous nucleation densities as well.

According to surface nucleation theory as developed by Venables[8] and others[9; 10], in a homogeneous growth system with i = 1, the average cluster density is given by the proportionality:

$$N_{av} \sim (F/\nu)^{1/3}\, e\text{^}[E_d/k_B T] \quad (1)$$

where F is the flux, ν is the vibrational attempt frequency ≈ $10^{13} s^{-1}$, k_b is the Boltzmann constant, E_d is the diffusion barrier, and T is absolute temperature. The vibrational frequency and exponential terms can be consolidated to simplify the relationship:

$$N_{av} \sim (F/r)^{1/3} \quad (2)$$

where r is the hopping rate. Using a DFT calculated value of E_d = 20 meV[29], a typical flux from our experiments of F = 1 x 10^{-4} ML/s and a reasonable estimate for hop rate of $10^{12.5}$ s^{-1}, we expect $N_{av} \approx 10^{-5}$ nm^{-2}. Referring again to Fig. 19, a value of 10^{-5} nm^{-2} is one to three orders of magnitude less than the experimentally observed values.

Equations (1) and (2) also indicate that in a homogeneous nucleation system N_{av} changes as a function of $F^{1/3}$. This means that changing flux by a factor of 10^3 changes the cluster density by a factor of 10. Referring again to Fig. 19, we have varied the flux by three orders of magnitude in experiments, with no apparent correlation to changes in cluster density. Even the outlier data points in Fig. 19 (for instance, the green triangle at (0.5, 34), were only approximately a factor of 2 different than their main-trend counterparts (red square at 0.5, 72). Therefore a series of data points differing from this trend by a factor of 10 would be well within the sensitivity of our cluster accounting methods. This supports the hypothesis that nucleation is not homogeneous.

3.7 Comparison of Coverages on HOPG vs. Cu Foil

This section overlaps with section 2.3 (Flux calibrations on Cu Foil).

Cu coverages on HOPG were difficult to estimate for two reasons: 1) the initial sticking coefficient of Cu on graphite is less than unity[31]; and 2) lateral dimensions of Cu clusters were unreliable due to convolution between the cluster and the STM tip. Therefore we turned to a different system for calibration. Deposited Cu forms one-atom-high islands on atomically-flat Cu terraces, as discussed in section 2.3. Using a magnetron-sputtered copper foil, we prepared atomically-flat (100) and (111) Cu terraces after only a couple of cleaning cycles. A problem was that the copper output of our evaporator changed over the course of days, especially if vacuum was broken. Due to the large number of Cu on HOPG depositions performed at various fluxes, it was impractical to re-calibrate the evaporator for every experiment since the calibration itself could take an entire day. So, for our standard data analysis procedure we estimated our Cu on HOPG coverage from the STM images based on cluster volumes extracted from cluster heights and assuming clusters to be hemispheres in shape.

Only late in the project (after ~ 2 years) did our procedures become streamlined enough to do a meaningful coverage comparison of Cu/Cu versus Cu/HOPG. Fig. 21 shows coverage vs. time for Cu/Cu(100) and Cu/HOPG using a hemispherical model (red squares) and a spherical model (green triangles). The slope of the spherical model is exactly ¼ that of the hemispherical model because a sphere of diameter H has a volume ¼ that of a hemisphere of radius h. In principle the Cu/Cu curve sets an upper limit for the amount of copper on the surface since the sticking coefficient for Cu/Cu is 1. However for both Cu/HOPG depositions, the calculated coverage was higher than that for Cu/Cu. For the hemispherical model, $\text{slope}_{\text{Cu/HOPG/hemi}}/\text{slope}_{\text{Cu/Cu}} = 0.20/.038 = 5.3$; and for the spherical model,

$slope_{Cu/HOPG/Sphere}/slope_{Cu/Cu}$ = 0.050/0.038 = 1.3. This data suggests that the actual shape of the Cu particles is probably closer to spherical than to hemispherical, although the true shape is likely polyhedral.

3.8 Temperature Dependence of Cluster Density, 100 K vs. 300 K

Given that experimental cluster density was one to three orders of magnitude higher than predicted for a case of homogeneous nucleation with E_d = 20 meV, it was useful to conduct an experiment to verify whether 20 meV is actually a reasonable value for E_d. According to equation (1), the hop rate r varies not only as a function of E_d, but also as a function of T. However, for a system where the diffusion barrier is 20 meV, one can show that there should be little temperature dependence. Fig. 22 is a plot of calculated values of N_{av} vs. 1/T for various E_d. For a system with a typical diffusion barrier of 0.3 eV, N_{av} is expected to increase by over 3 orders of magnitude as temperature falls from 300 K to 100 K. For a system with E_d = 0.02 eV, there is less than an order of magnitude change in N_{av} over that temperature range.

We conducted an experiment by depositing equivalent amounts of Cu on HOPG at 300 K and 125 K (deposition temperature) over three coverages to test for the temperature dependence of N_{av}. The resultant images are shown in Fig. 23. It should be noted that tunneling conditions were poor for both imaging sessions, and the 125 K images also displayed an unusual tip effect which caused the clusters to look somewhat like seashells. Despite this, the cluster densities were still determined well enough to conclude that N_{av} at 300 K and 125 K are very similar. N_{av} on the 300 K surface ranged from 7 x 10^{-4} nm^{-2} at the lowest coverage to 3 x 10^{-3} nm^{-2} at the highest coverage, while at 125 K, N_{av} ranged similarly from 7 x 10^{-4} nm^{-2} to 2 x 10^{-3} nm^{-2}, respectively. This result provides support for one of two conclusions: (1) in the event that

nucleation is homogeneous, the value of E_d is in fact very low; or (2) nucleation is not homogeneous.

3.9 Ion Damage Experiments

After heating the Cu/HOPG surface to temperatures > 700 K (discussed in detail in Chapter 4), the terraces became sufficiently depleted in Cu clusters that we could safely adjust the tunneling parameters to image residues without crashing the STM tip. The residues shown in Fig. 24 were obtained after annealing the HOPG surface to 700 K. Fig. 25 shows a cluster of residues from Fig. 24 imaged in a constant height mode, which were similar in appearance to images of ion damage from argon sputtering in the literature[32] (shown in comparison to our data in Fig. 26). The insets of Figs. 24b and 26 show characteristic $(\sqrt{3} \times \sqrt{3})R30°$ scattering associated with point defects on graphite[33-35].

E-beam evaporators, such as the one used in these experiments, generate a small fraction of high-energy ions[36; 37], and these ions can, in at least one metal-on-metal system (Pb/Cu(111)), alter nucleation behavior[38]. The metal-on-carbon literature, however, is largely silent as to this effect, with the exception of Lopez-Salido (Ag on HOPG) [39] and Nielsen (Ru on HOPG) [40] who mentioned the possibility of nucleation due to ion-induced defects, but did not draw a conclusion as to whether that was responsible for their nucleation.

We designed an experiment to investigate whether high-energy ions from our evaporator were causing Cu nucleation on the HOPG surface. A schematic diagram of our e-beam evaporator is shown in Fig. 27. A hot filament emitted electrons by thermionic emission. The electrons were accelerated toward the crucible which is at a bias of +2 kV. The filament current and HV on the crucible were independently controlled. The experiment involved turning off

power to the evaporator immediately before deposition. This way the evaporator operated like a resistively-heated evaporator. Of course, with the power off, the crucible temperature dropped quickly, thereby limiting the amount of time during which a substantial Cu flux is expected. We arbitrarily chose a short deposition time of 10 seconds and relatively high evaporator power of 38 W and measured the difference in total flux between components "ON" and "OFF" using our atomically flat copper foil (see Figs. 28-31). The calibration was repeated twice and averaged over both trials. With evaporator components OFF the total flux dropped by 26±5 % compared to components ON. It did not matter whether only the HV was turned off or whether the filament and HV were both turned off; the flux drop was approximately the same in both cases. If ion damage from the evaporator was indeed the cause of nucleation, we expected to see a drastic difference in N_{av} between the components "ON" and "OFF". If not, then we expected to see a drop in N_{av} of only 26% based on the linear relationship between N_{av} and coverage as discussed in section 3.5.

The ion damage experiment was conducted in triplicate at three different powers (38 W, 43 W, and 48 W), all 10 second depositions. For the 38 W and 48 W experiments, all combinations of Filament ON/OFF and HV ON/OFF were tried (four possible combinations). For the 43 W experiment, which was an abbreviated experiment, only the fully ON and fully OFF combinations were used. The control experiment (all components ON) was done in duplicate for each experiment as the first and last run. The results are shown in Figs. 32-34. For all images, a step edge is in view to show that Cu was indeed deposited on the surface. The clear result was that terrace nucleation only occurred when both the filament and HV were ON. Otherwise there was no appreciable nucleation on the HOPG terraces. This was conclusive evidence that nucleation in the Cu/HOPG system was mediated by ion-induced defects from the

e-beam evaporator. These experiments also disclosed the method of ion formation within the evaporator. Ion damage only occurred when both the filament and HV were on, which means that ions were generated in the e-beam and accelerated by the HV on the crucible. Ions generated as a natural, thermal product of Cu evaporation were either insufficient in number to produce a measurable effect on the surface, or were insufficiently ionized to achieve the energy needed to cause defects on the HOPG surface.

We also estimated the approximate ionized fraction of the flux in our evaporator based on these results. If we assume that one energized ion causes one defect on the surface, and that all defects act as nucleation sites, then the effective ionized fraction = # clusters / total atoms deposited. We can extract this fraction from the slope of our N_{av} vs. coverage curve (Fig. 19), which crosses the coordinate (1 ML, 1.36×10^{-2} clusters/nm^2). Using the surface density of Cu atoms in the fcc(111) unit cell (18 atoms/nm^2), we obtain:

$(1.36 \times 10^{-2}$ clusters/nm$^2)(1$ nm$^2/18$ atoms$) = 7.6 \times 10^{-4}$ clusters/atom

So the ionized fraction of our flux is approximately 1/1300. A consequence of this is that an average cluster in the main trend of Fig. 19 contains approximately 1300 Cu atoms. Since ionizing the flux requires interaction of the flux with the e-beam, we expect that the effective ionized fraction is sensitive to the relative placement of the filament with respect to the top of the crucible, and will be unique to each evaporator.

Changes in the ion yield of the evaporator over time also explain the high degree of scatter in our N_{av} vs. coverage plots. Fig. 35 shows the effect of changing ion yield on our data as a function of time. After 1/29/14, there was a noticeable shift toward producing fewer, but

larger clusters. The relationship between N_{av} and coverage was somewhat linear within each time frame, but there was a definite change in the approximate slope of the data between the early and later experiments.

As an interesting side note, other than the 26±5 % drop in Cu coverage, there was no marked change in the nucleation behavior of Cu/Cu with the evaporator components ON vs. OFF (as seen by comparing Figs. 28-31 with Fig. 32). Apparently the Cu surface was self-healing, whereas the HOPG surface was not.

We also conducted a set of experiments to determine how the flux reading (in nA) on the evaporator display changed as a function of time when various components were turned off. The flux monitor readings as a function of time were captured by video recording the flux monitor next to a digital stopwatch during the experiments. Fig. 36 shows the decay in displayed flux as a function of time for various combinations of components being shut off at the same initial starting power. For all combinations of components off, there was an instantaneous drop in the flux reading of approximately 20% and then a gradual decline afterward. Fig. 37 shows the decay in displayed flux as a function of time after turning HV off from different initial starting powers. Again, an approximately 20% instantaneous decrease in displayed flux was observed. Fig. 38 shows the effect of opening the shutter on the displayed flux for HV on vs. HV off. There was an additional gradual decrease in displayed flux with the shutter opened. These flux display experiments are shown here for completeness although we did not use them in this study. Further work would be necessary to assign physical interpretations for these observations. For now, they must be regarded as phenomenological and possibly useful.

3.10 Conclusions

Cu deposited on the HOPG basal plane at 300 K forms 3D clusters. The cluster densities observed were one to three orders of magnitude higher than the expected values based on nucleation theory for homogeneous nucleation with i = 1 and with the diffusion barrier derived from DFT[29]. The monomodal decay in the cluster size histograms is atypical for homogeneous nucleation. The linear dependence of N_{av} vs. coverage and the lack of flux dependence are consistent with a system where defects are produced by the deposition source itself. Depositions conducted with the e-beam off showed no appreciable terrace decoration, which is conclusive evidence that the degree of homogeneous nucleation in this system is negligible. Thus we conclude that the nucleation mechanism for Cu on the basal plane of HOPG is a heterogeneous nucleation mediated by ion-induced defects caused by high-energy Cu ions from the e-beam evaporator.

Acknowledgements

This work was supported by the Office of Science, Basic Energy Sciences, Materials Sciences and Engineering Division of the U.S. Department of Energy (USDOE), under Contract No. DE–AC02–07CH11358 with the U.S. Department of Energy. We thank Jim Anderegg for his contribution of HOPG substrates, Jim Evans and Huaping Lei for the theoretical modeling accompanying this work, and Emma Kwolek for assistance with STM experiments.

References

[1] G. Richter, K. Hillerich, D.S. Gianola, R. Mönig, O. Kraft, C.A. Volkert, Nano Letters 9 (2009) 3048-3052.

[2] M. Kolb, G. Richter, AIP Conference Proceedings 1300 (2010) 98-105.

[3] M. Schamel, C. Schopf, D. Linsler, S.T. Haag, L. Hofacker, C. Kappel, H.P. Strunk, G. Richter, Int. J. Mat. Res. 102 (2011).

[4] E. Ganz, K. Sattler, J. Clarke, Surface Science 219 (1989) 33-67.

[5] C.M. Whelan, C.J. Barnes, Applied Surface Science 119 (1997) 288-300.

[6] M. Amft, S. Lebègue, O. Eriksson, N.V. Skorodumova, Journal of Physics: Condensed Matter 23 (2011) 395001.

[7] R. Anton, I. Schneidereit, Physical Review B 58 (1998) 13874-13881.

[8] J.A. Venables, G.D.T. Spiller, M. Hanbucken, Rep. Prog. Phys. 47 (1984) 399-459.

[9] P. Thiel, J.W. Evans, The Journal of Physical Chemistry B 104 (2000).

[10] J.W. Evans, P.A. Thiel, M.C. Bartelt, Surf. Sci. Rep. 61 (2006) 1.

[11] J.G. Kushmerick, K.F. Kelly, H.P. Rust, N.J. Halas, P.S. Weiss, J. Phys. Chem. B 103 (1999) 1619.

[12] J.R. Hahn, Carbon 43 (2005) 1506-1511.

[13] H.-C. Chang, A.J. Bard, J. Am. Chem. Soc. 113 (1991) 5588-5596.

[14] F. Stevens, L.A. Kolodny, T.P. Beebe Jr., J. Phys. Chem. B 102 (1998) 10799-10804.

[15] J.D. McBride, B. Van Tassell, R.C. Jachmann, T.P. Beebe, Jr., J. Phys. Chem. 105 (2001) 3972-3980.

[16] X. Chu, L.D. Schmidt, Carbon 29 (1991) 1251-1255.

[17] K.F. Kelly, Thesis, Rice University (1996).

[18] G.M. Francis, I.M. Goldby, L. Kuipers, B. von Issendorff, R.E. Palmer, J. Chem. Soc., Dalton Trans. (1996) 665-671.

[19] I. Lopez-Salido, D.C. Lim, Y.D. Kim, Surf. Sci 588 (2005) 6-18.

[20] H. Hövel, T. Becker, A. Bettac, B. Reihl, M. Tschudy, E.J. Williams, J. App. Phys. 81 (1997) 154.

[21] H.-B.-R. Lee, S.H. Baeck, T.F. Jaramillo, S.F. Bent, Nano Lett. (2013).

[22] P. Scheier, B. Marsen, M. Lonfat, W.-D. Schneider, K. Sattler, Surf. Sci. 458 (2000) 2000.

[23] I.N. Kholmanov, L. Gavioli, M. Fanetti, M. Casella, C. Cepek, C. Mattevi, M. Sancrotti, Surface Sci. 601 (2007) 188-192.

[24] H. Xu, H. Permana, Y. Lu, K.Y.S. Ng, Surf. Sci. 325 (1995) 283-295.

[25] G.W. Clark, L.L. Kesmodel, J. Vac. Sci. Technol. B 11 (1993) 131-136.

[26] T.P. Darby, C.M. Wayman, Journal of Crystal Growth 28 (1975) 41-52.

[27] C.M. Wayman, T.P. Darby, Journal of Crystal Growth 28 (1975) 53-67.

[28] X.S. Wang, W. Xiao, S.S. Kushvaha, Z. Yan, M. Xu, Graphene and Graphite Materials (book) (2009).

[29] u.d. Huaping Lei.

[30] U.r. D.-J. Liu.

[31] J.R. Arthur, A.Y. Cho, Surface Science 36 (1973) 641-660.

[32] M. Büttner, P. Choudhury, J. Karl Johnson, J.T. Yates Jr, Carbon 49 (2011) 3937-3952.

[33] J.G. Kushmerick, K.F. Kelly, H.P. Rust, N.J. Halas, P.S. Weiss, Physical Chemistry B 103 (1999).

[34] J.R. Hahn, H. Kang, Physical Review B 60 (1999) 6007-6017.

[35] W.-T. Pong, C. Durkan, Journal of Physics D: Applied Physics 38 (2005).

[36] P.L. Bartlett, A.T. Stelbovics, Physical Review A 66 (2002) 012707.

[37] A. Lyutovich, K. Maile, A. Gusko, K. Ashurov, S. Morozov, Surface and Coatings Technology 151–152 (2002) 105-109.

[38] C. Nagl, O. Haller, E. Platzgummer, M. Schmid, P. Varga, Surface Science 321 (1994) 237-248.

[39] I. Lopez-Salido, D.C. Lim, Y.D. Kim, Surface Science 588 (2005) 6-18.

[40] R.M. Nielsen, S. Murphy, C. Strebel, M. Johansson, J.H. Nielsen, I. Chorkendorff, Surface Science 603 (2009) 3420-3430.

Tables

Table 1
Accounting table for the clean HOPG defect survey, including the atomic-resolution survey (marked with an *). Data taken from only high-quality images 500 nm x 500 nm or smaller, non-overlapping area.

	Total Defects	Total Area Sampled (nm^2)	Defect Density (nm_{-2})
ZYH	**6**	**1187500**	**5.05263E-06**
ZYA	**22**	**1337500**	**1.64486E-05**

Date/File	Image #	Tot. Visible Point Defects	Image Area (nm^2)	Pre-heat Temp (K)	Days Since Cleave	Notes
ZYH						
20120919	25	0	62500	1000	2	
20120921	9	0	250000	750-950	0	
20130222	8	0	62500	300	0	Imaged in air
20130315	12	6	250000	600-850	0	3 easy to see, 3 hard to see (faint)
20130318	15	0	62500	600-850	3	
	17	0	250000	600-850	3	
	33	0	250000	600-850	3	
ZYA						
20130424	2	1	62500	300	0	
20130505	40	0	62500	300	0	
20130511	*50-154	0	62500	450	1	atomic res survey #1

Table 1 cont.

Date/File	Image #	Tot. Visible Point Defects	Image Area (nm^2)	Pre-heat Temp (K)	Days Since Cleave	Notes
20130513	6	0	62500	950	0	Highly decorated step-edges (cauliflower)
20130517	8	3	62500	950	0	
20130522	*3-141	0	87500	500	0	atomic res. survey #2
	145	1	62500	500	0	Large intercalated defect
	148	0	62500	500	0	
20130523	8	0	62500	300	0	
	10	0	62500	300	0	
20130524	1	8	62500	500	0	Broad defects, questionable.
	7	2	62500	500	0	
	12	0	62500	500	0	
	22	0	62500	600	0	
	32	1	62500	700	0	
	41	0	62500	800	0	
	47	1	62500	800	0	
	59	0	62500	900	0	
	68	2	62500	950	0	
	81	0	62500	950	0	
	85	3	62500	950	0	

Table 2

Display of relative volumes of features ≤ 1 nm high versus > 1 nm high.

For 22W, 90 min (0.17 ML) deposition	Number of islands	% of total island volume (nm^3)
Height ≤ 1 nm	226	0.46
Height > 1 nm	212	99.54
Total	438	100.00

Figures

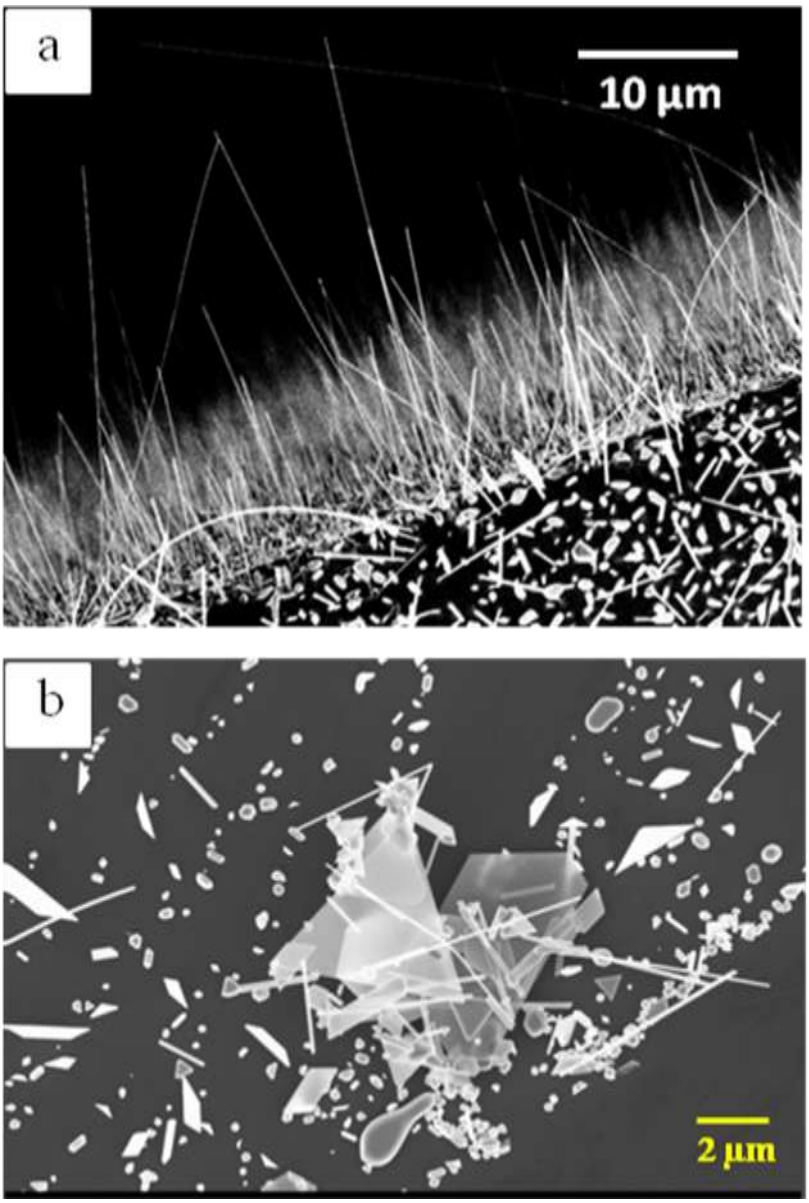

Fig. 1
SEM images of Cu nanowires grown on (a) a-C and (b) HOPG.

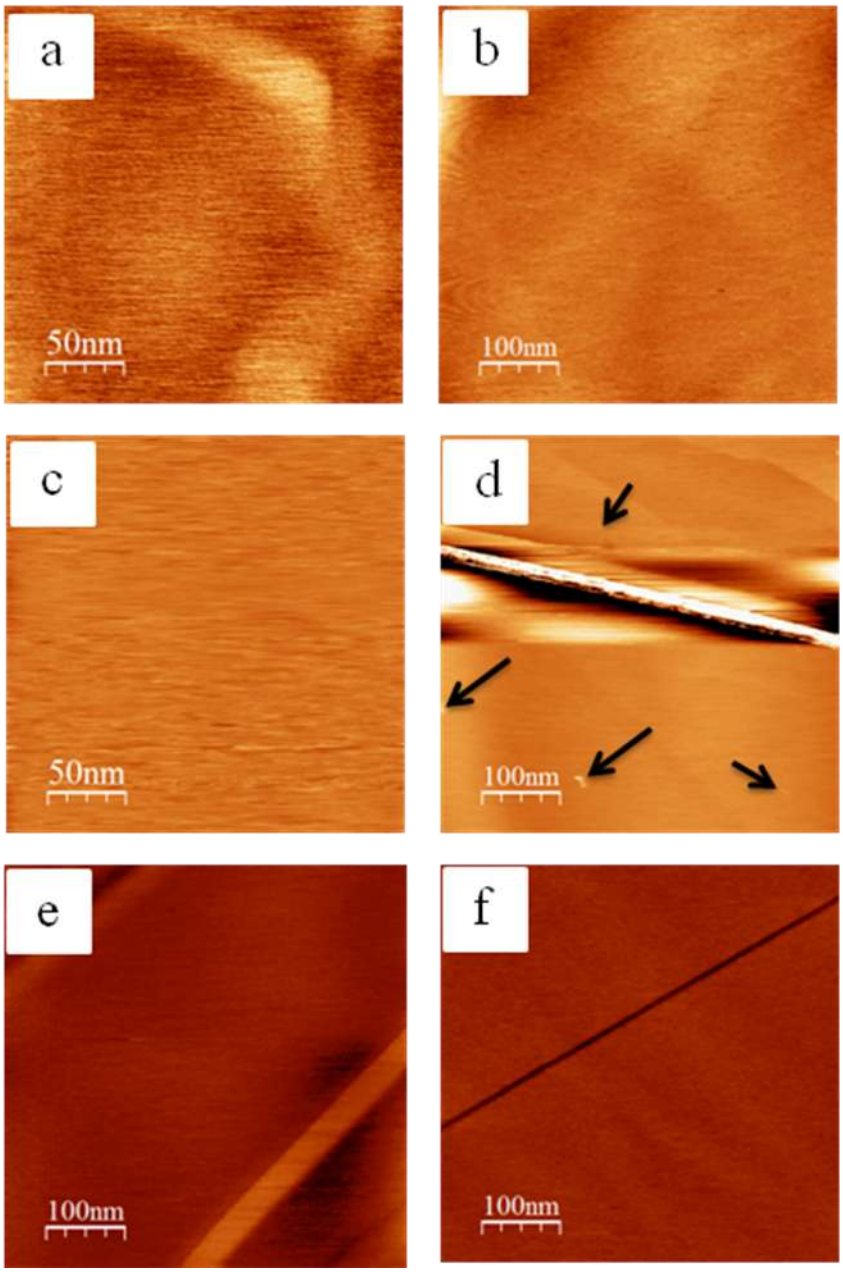

Fig. 2
Low-magnification images (constant current mode) of the clean HOPG ZYH surface. (a) 250 nm x 250 nm, V_{tip} = 0.1 V, *i* = 0.5 nA; (b) 500 nm x 500 nm, V_{tip} = 0.1 V, *i* = 0.5 nA; (c) 250 nm x 250 nm, V_{tip} = 0.1 V, *i* = 0.5 nA; (d) 500 nm x 500 nm, V_{tip} = 0.1 V, *i* = 0.3 nA, visible defects are marked with arrows; (e) 500 nm x 500 nm, V_{tip} = -0.1 V, *i* = 0.3 nA; (f) 500 nm x 500 nm, V_{tip} = -0.1 V, *i* = 0.5 nA.

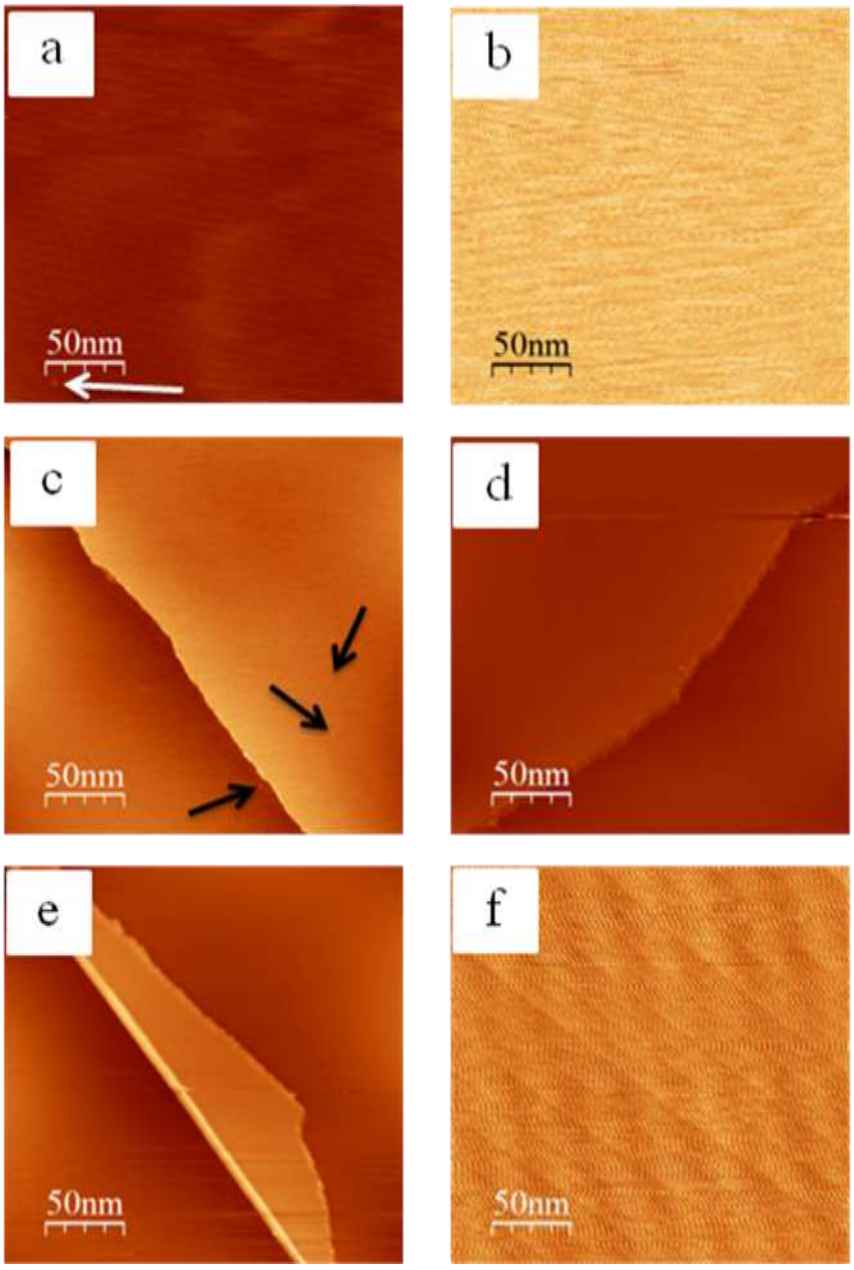

Fig. 3
Low-magnification images (constant current mode) of the clean HOPG ZYA surface. (a) 250 nm x 250 nm, V_{tip} = 0.1 V, *i* = 0.3 nA, visible defect is marked with an arrow; (b) 250 nm x 250 nm, V_{tip} = 0.2 V, *i* = 0.3 nA; (c) 250 nm x 250 nm, V_{tip} = 0.5 V, *i* = 0.1 nA, visible defects marked with arrows; (d) 250 nm x 250 nm, V_{tip} = 0.3 V, *i* = 0.3 nA; (e) 250 nm x 250 nm, V_{tip} = -0.7 V, *i* = 0.2 nA; (f) 250 nm x 250 nm, V_{tip} = 0.3 V, *i* = 0.1 nA.

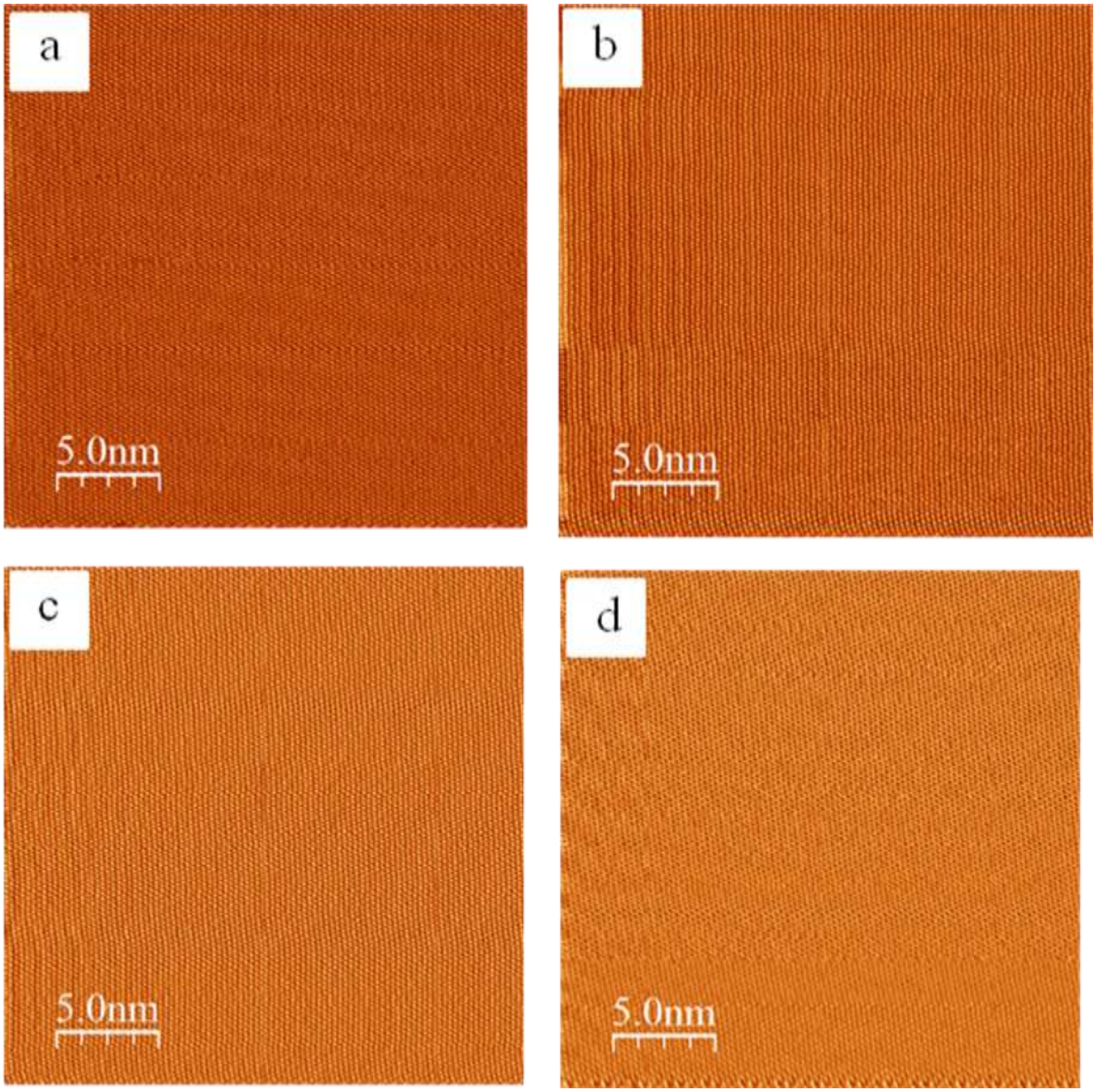

Fig. 4
(a-d) Atomic-resolution images (constant height mode) of the clean HOPG ZYA surface taken as part of a 200-image survey. The top ¾ of (d) shows an example of corrugation reversal in the imaging. All images 25 nm x 25 nm, V_{tip} = 0.05 V, i = 0.3 nA.

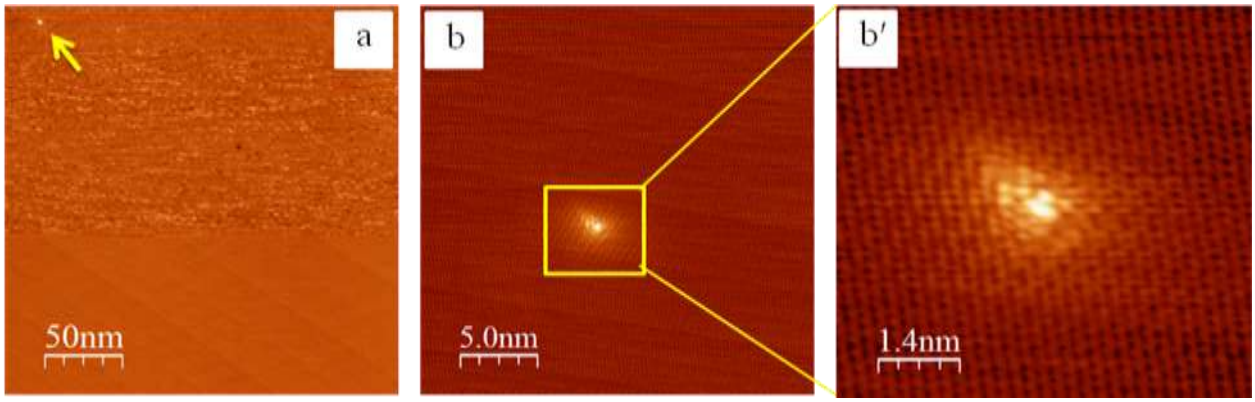

Fig. 5
(a) A typical 250 nm x 250 nm image (constant height mode) showing a point defect in the upper left (marked with an arrow); (b) 25 nm x 25 nm shows the same defect under higher magnification. The graphite lattice is visible in the background; (b′) is a zoom-in of (b). For all images V_{tip} = 0.1 V, i = 0.3 nA.

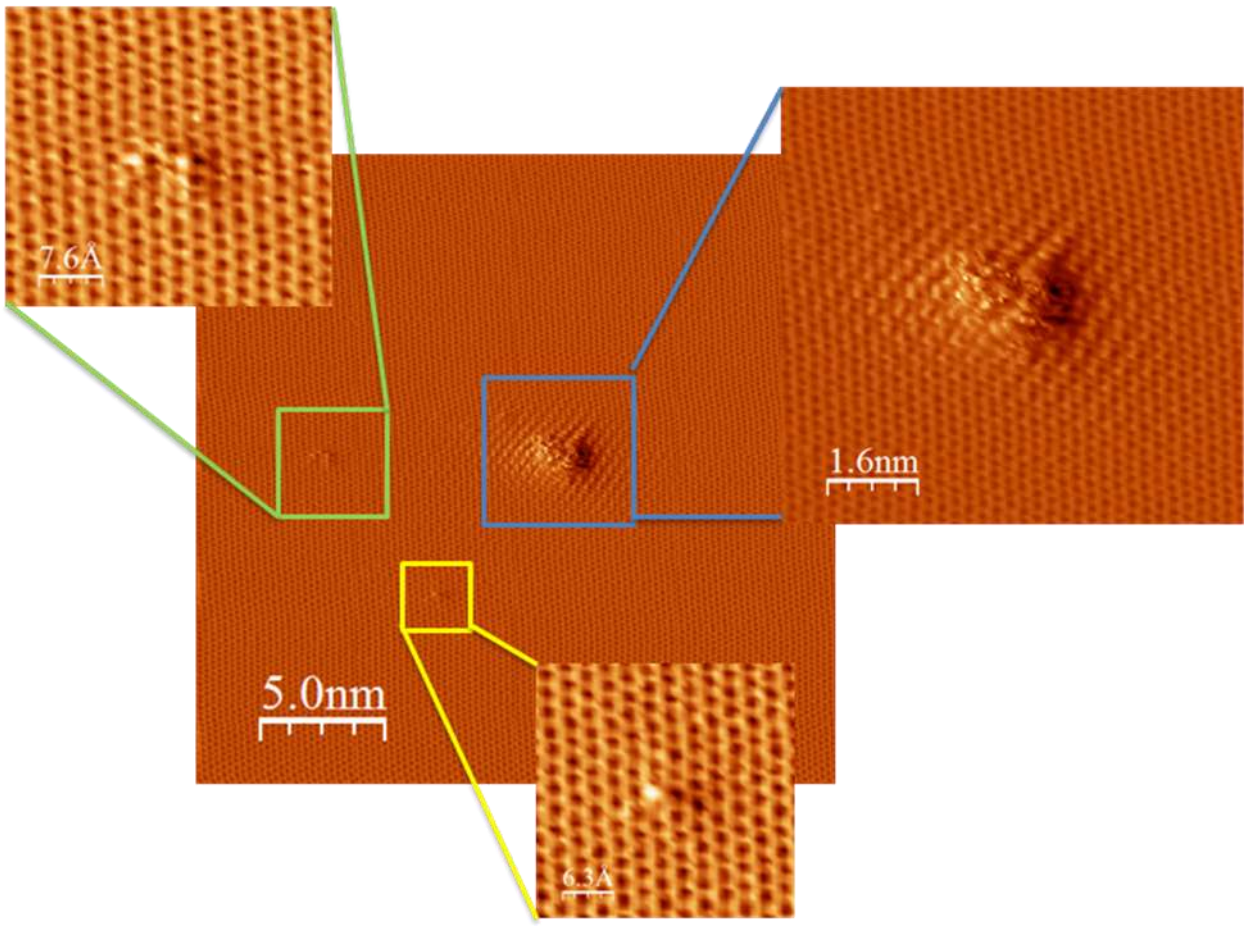

Fig. 6
STM images in const. height mode of a rare cluster of defects on the clean HOPG ZYA surface, 25 nm x 25 nm, V_{tip} = 0.1 V, *i* = 0.5 nA

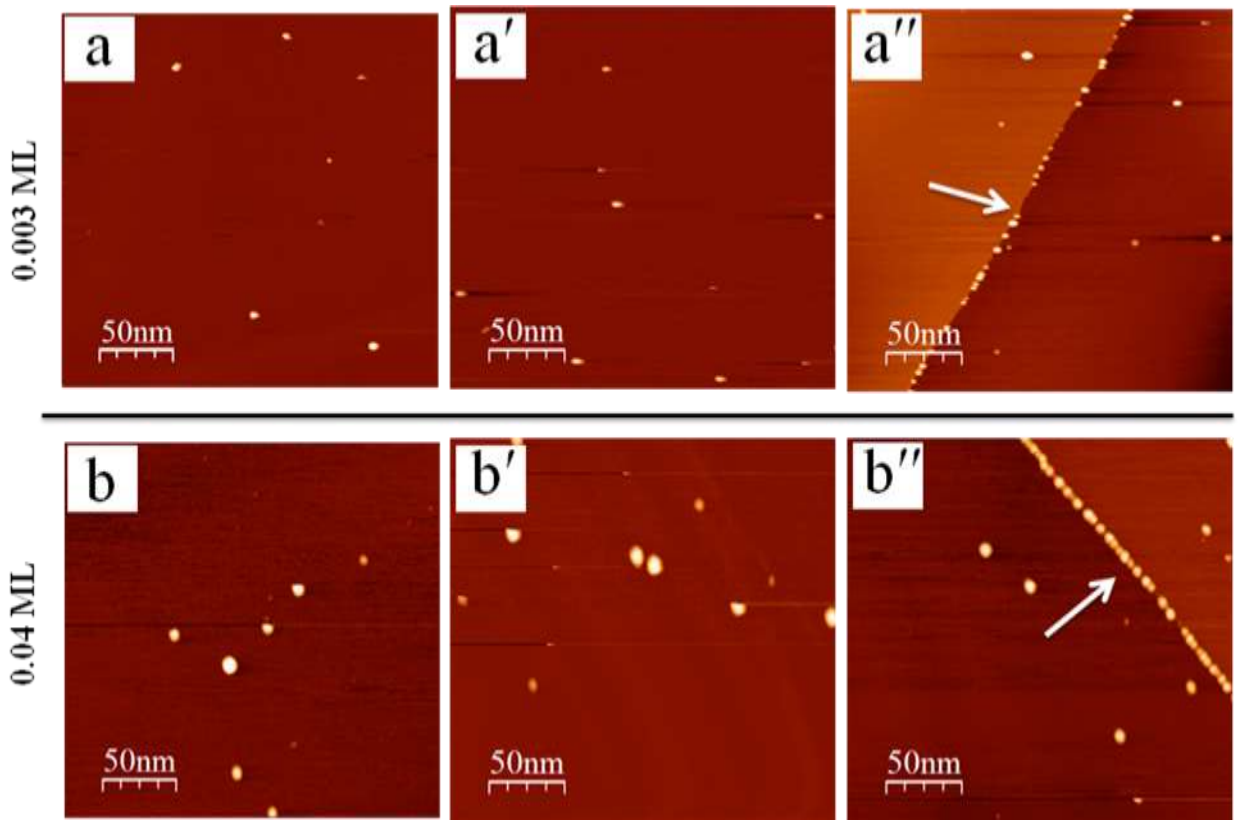

Fig. 7
STM images of Cu on HOPG at various coverages: (a-a″) 0.003 ML; (b-b″) 0.04 ML,. Step edges are marked with an arrow. All images 250 nm x 250 nm, V_{tip} = -1.0 V, *i* = 0.1 nA.

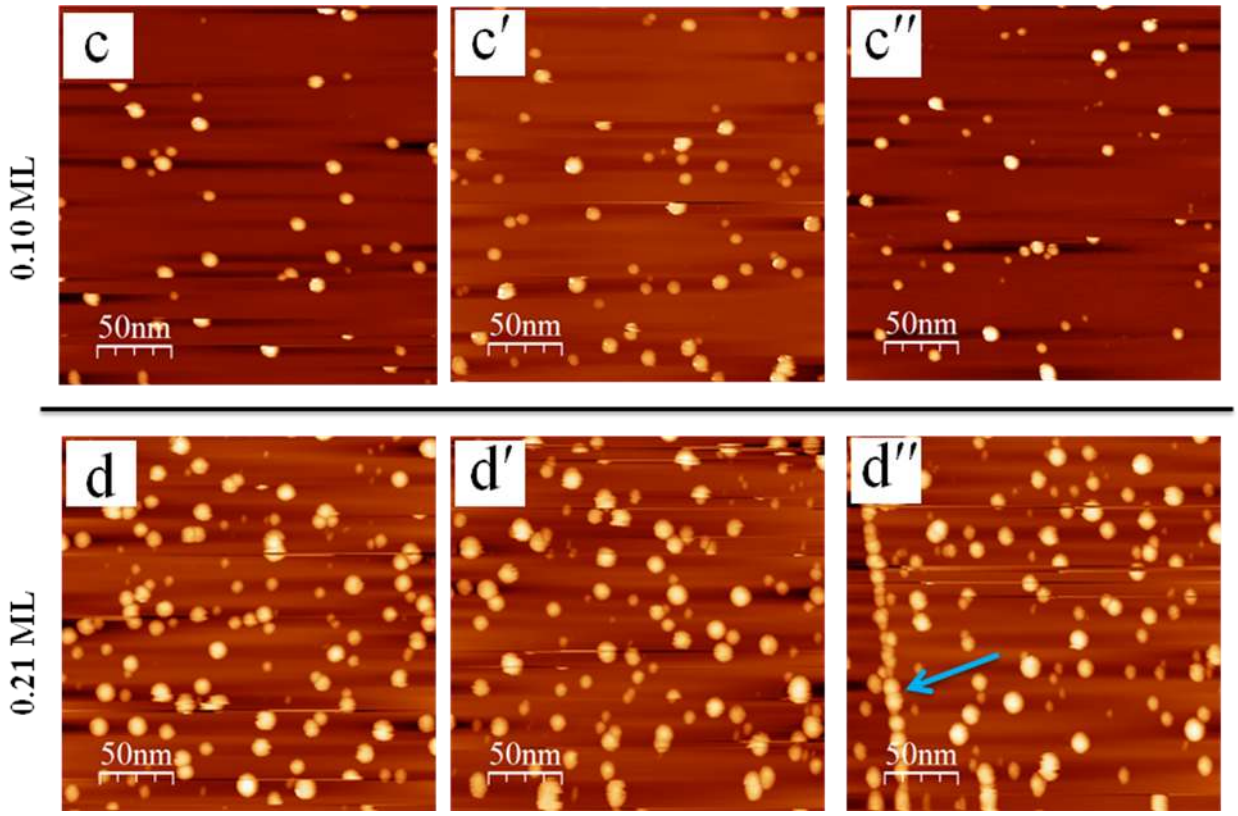

Fig. 8
STM images of Cu on HOPG at various coverages: (c-c″) 0.10 ML; (d-d″) 0.21 ML, step edges are marked with an arrow. All images 250 nm x 250 nm, V_{tip} = -0.8 V, *i* = 0.1 nA.

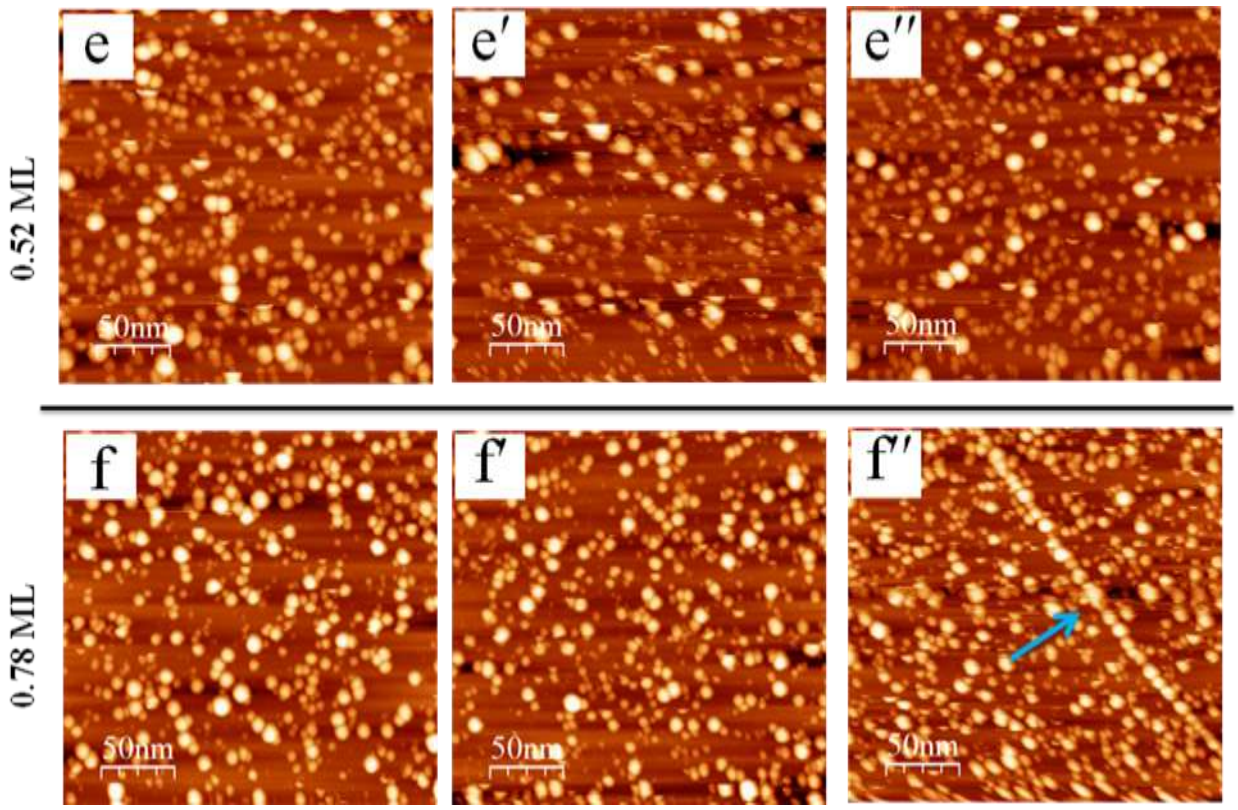

Fig. 9
STM images of Cu on HOPG at various coverages: (e-e″) 0.52 ML, V_{tip} = -1.5 V, *i* = 0.3 nA; (f-f″) 0.78 ML, V_{tip} = -1.8 V, *i* = 0.1 nA, step edges are marked with an arrow. All images 250 nm x 250 nm.

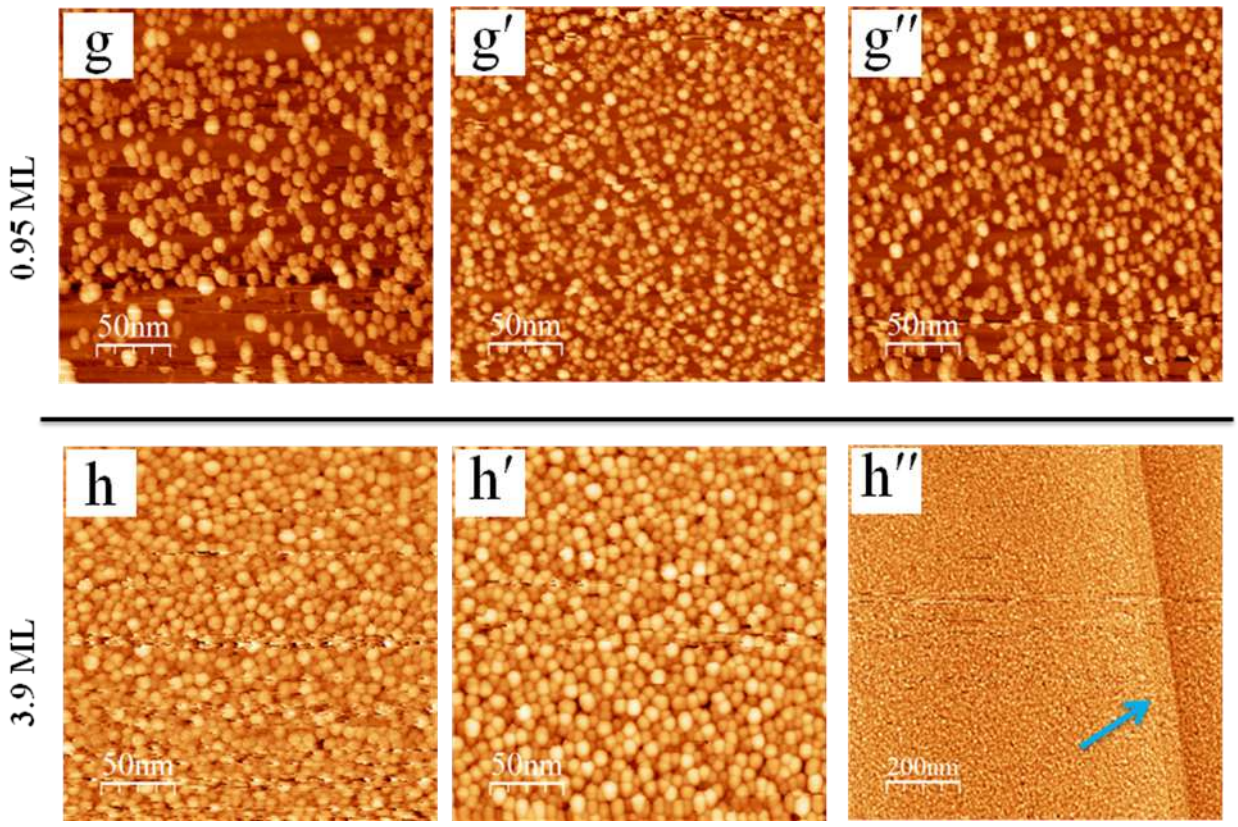

Fig. 10
STM images of Cu on HOPG at coverages of: (g-g″) 0.95 ML, V_{tip} = -0.9 V, *i* = 0.1 nA; (h-h″) 3.9 ML, V_{tip} = -1.8 V, *i* = 0.1 nA, step edges are marked with an arrow. All images 250 nm x 250 nm except (h″) 1μm x 1μm.

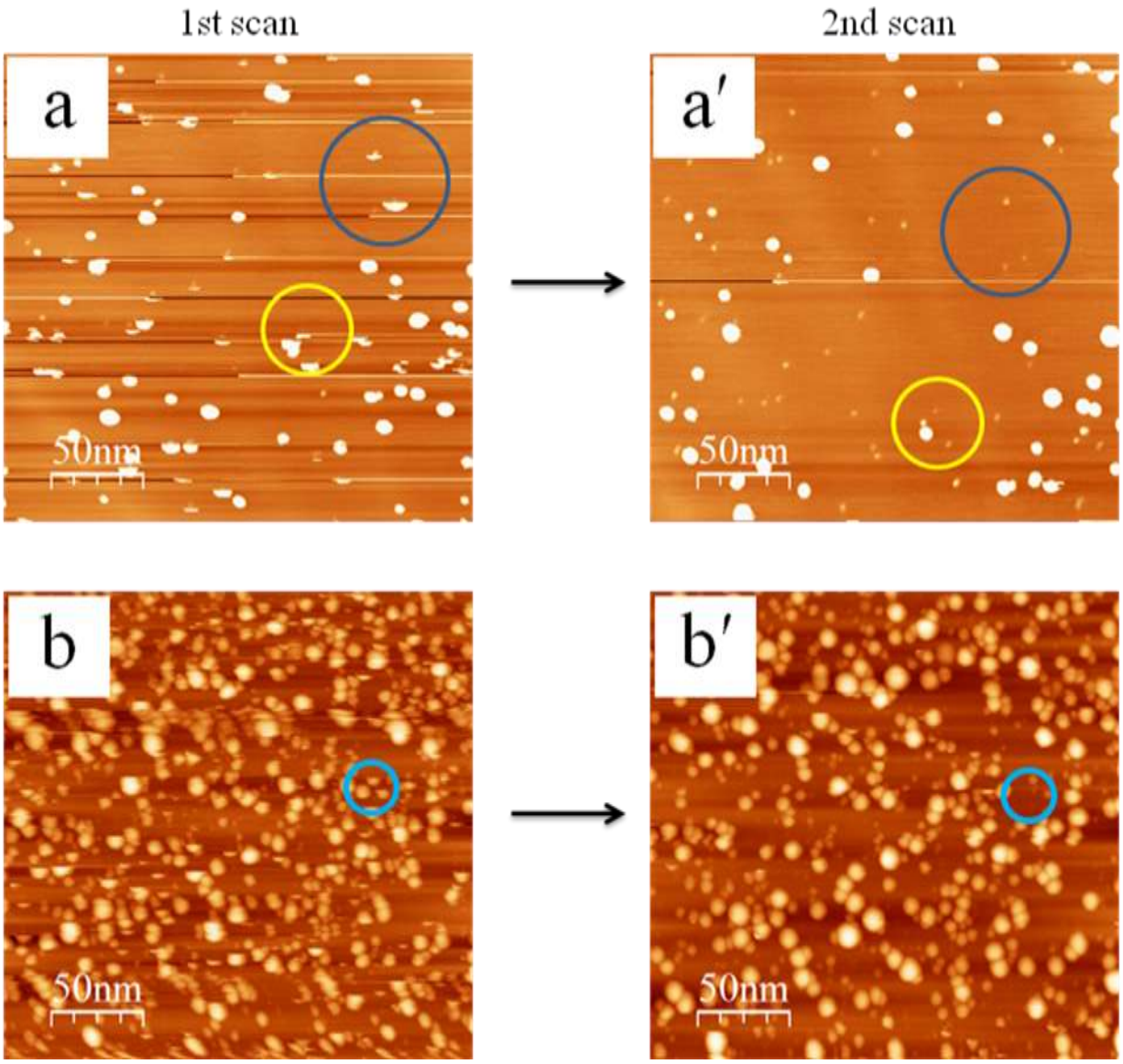

Fig. 11
STM images illustrating tip-sample interaction in the Cu-HOPG system at different Cu coverages. Horizontal pairs (for instance (a) and (a′)) are consecutive scans of the same area. The circles show areas where islands are sheared in the first image and gone in the second image. Panels (a-a′) V_{tip} = -0.8 V, i = 0.1 nA; (b-b′) V_{tip} = -1.9 V, i = 0.1 nA. All images 250 nm x 250 nm.

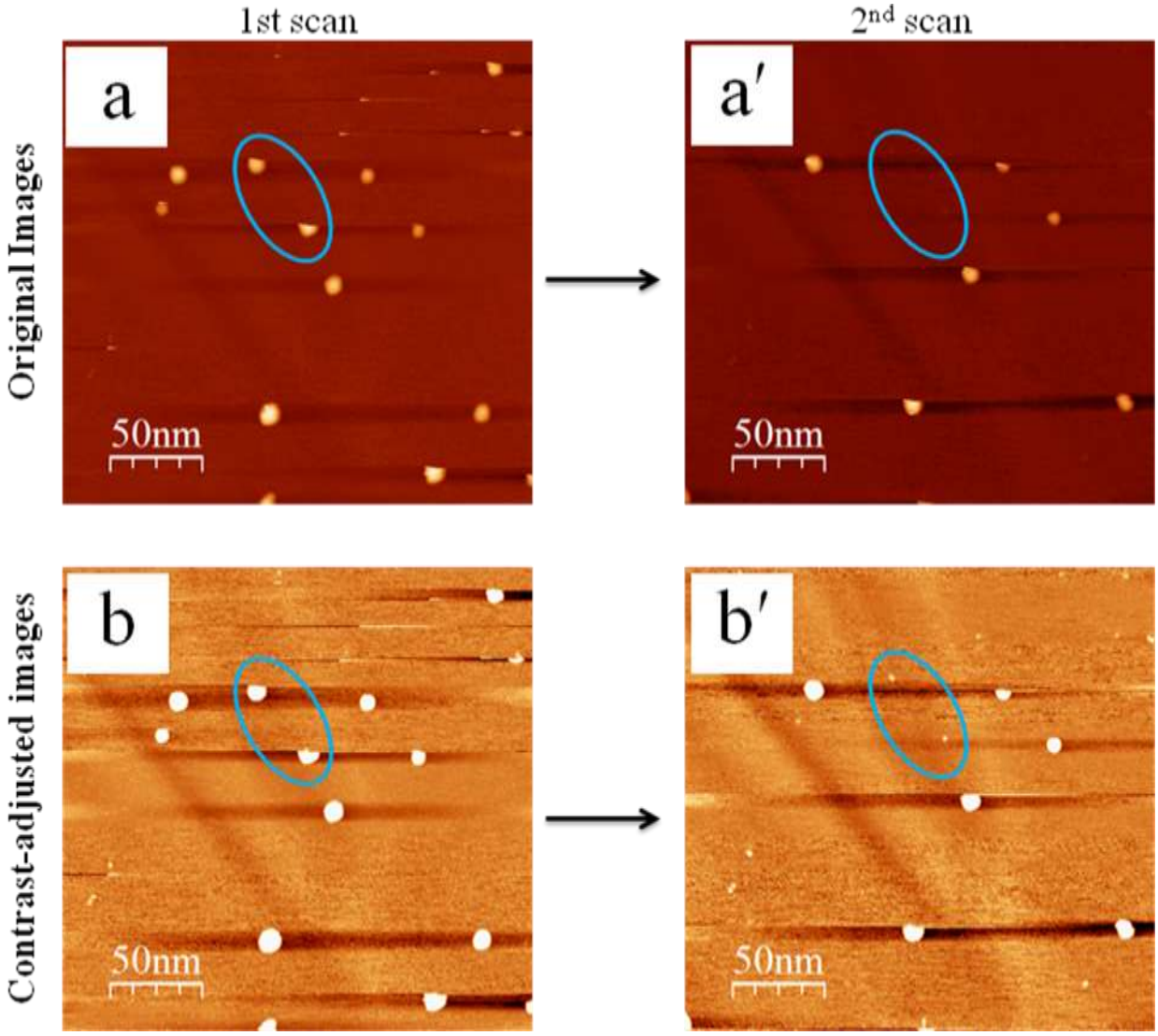

Fig. 12
STM images illustrating tip-sample interaction in the Cu-HOPG system using different post-processing contrast adjustments. Horizontal pairs (for instance (a) and (a′)) are consecutive scans of the same area. The circles show areas where islands are sheared in the first image and gone in the second image. Panels (a-a′) V_{tip} = -0.9 V, i = 0.08 nA; (b-b′) Contrast-adjusted images, V_{tip} = -0.9 V, i = 0.08 nA. All images are for 0.10 ML Cu, 250 nm x 250 nm.

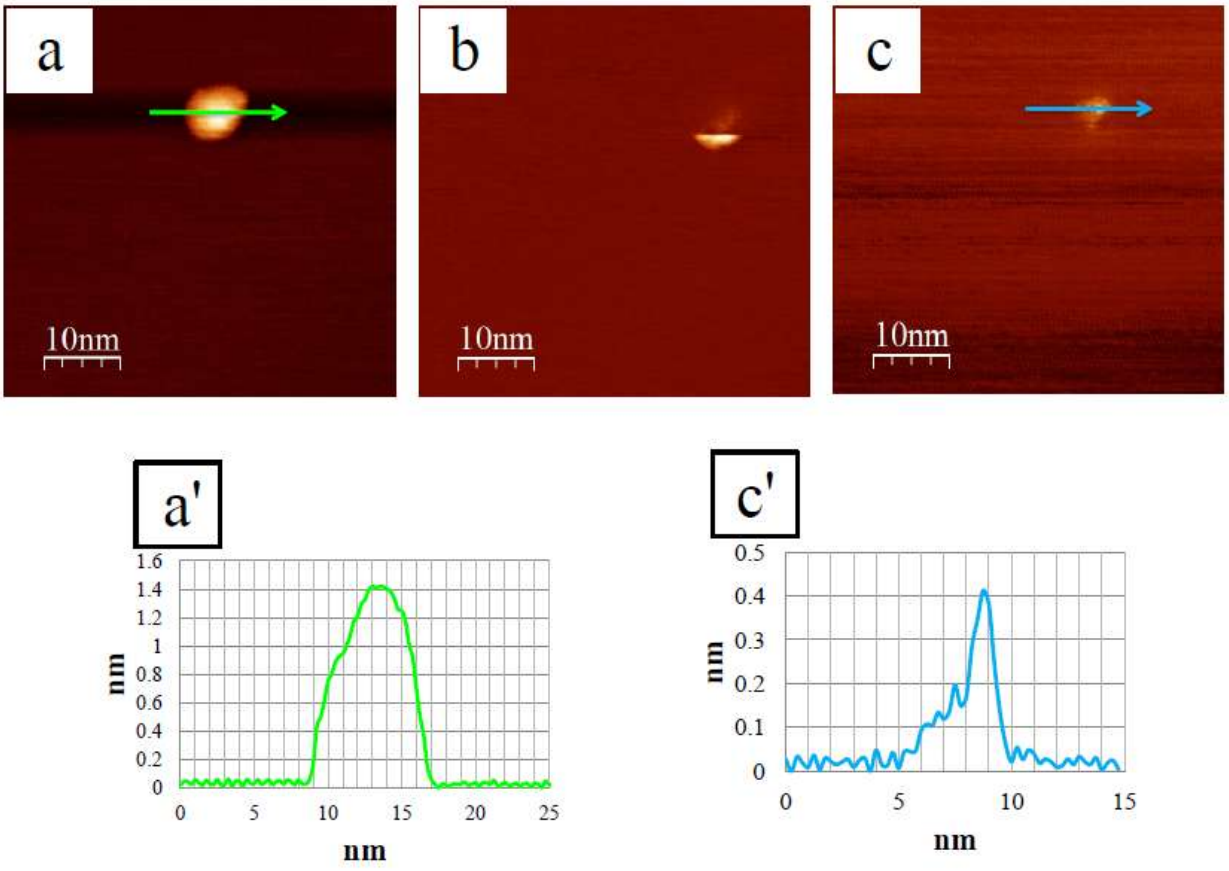

Fig. 13
Panels (a), (b), and (c), are consecutive STM images showing a Cu island being severed by the STM tip, all images 50 nm x 50 nm, V_{tip} = 0.1 V, *i* = 0.1 nA. (a') and (c') show line profiles of the unsheared island (a) and the residue left after shearing (c), respectively.

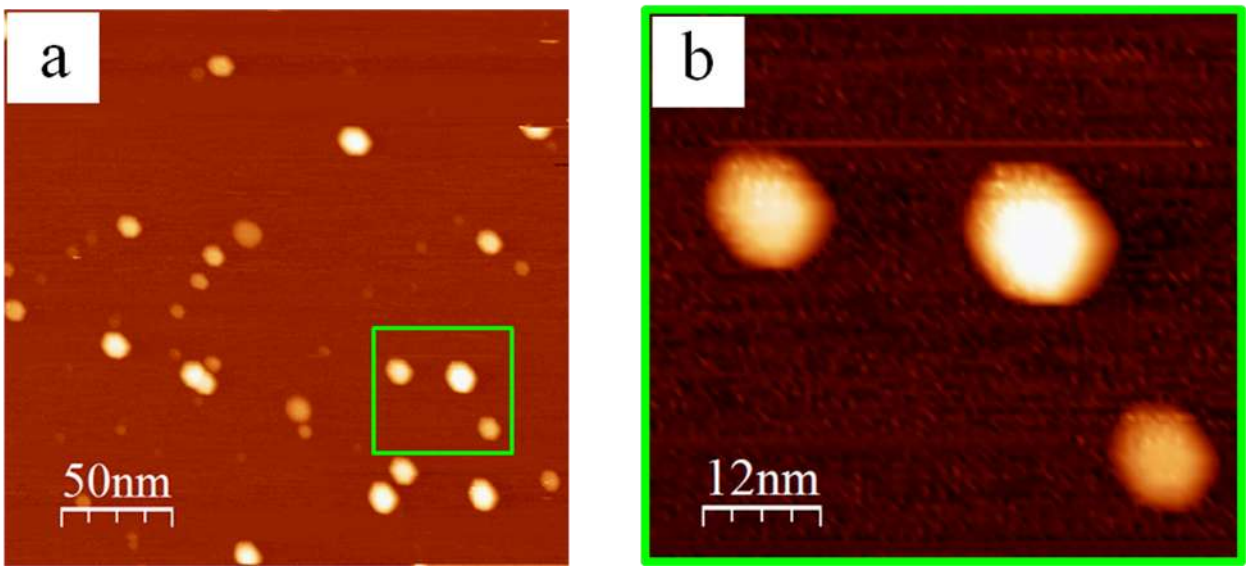

Fig. 14
(a) STM image of Cu islands displaying hexagonal geometry, 0.8 ML, 250 nm x 250 nm V_{tip} = -1.5 V, *i* = 0.3 nA; and (b) a zoom-in of (a).

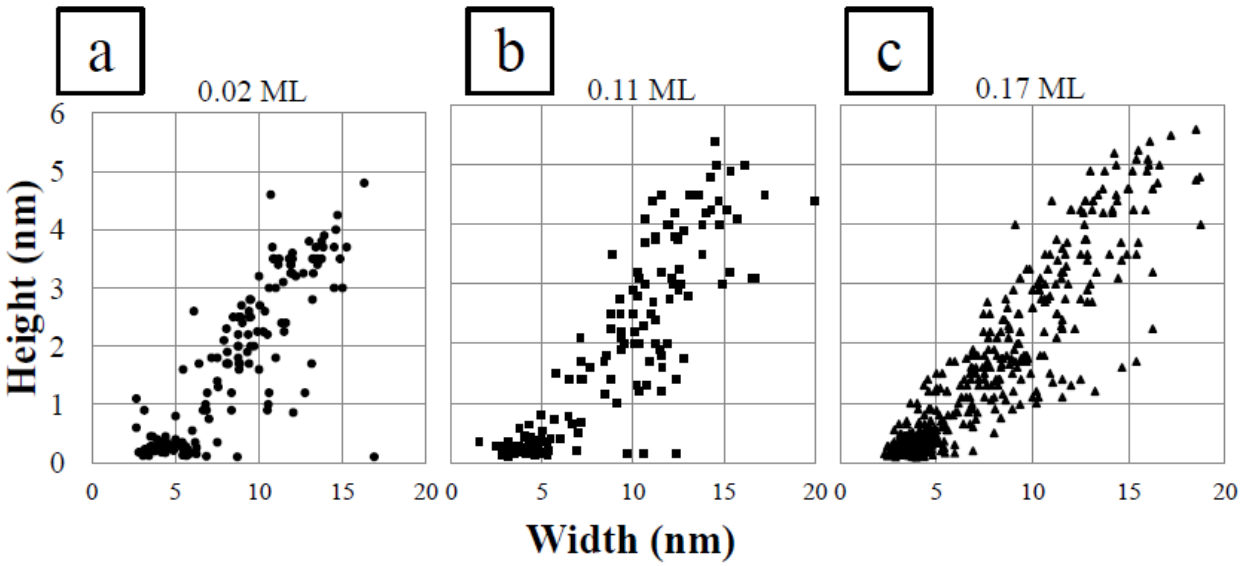

Fig. 15
Plots of H v. W for Cu island populations at (a) 0.02 ML; (b) 0.11 ML; and (c) 0.17 ML.

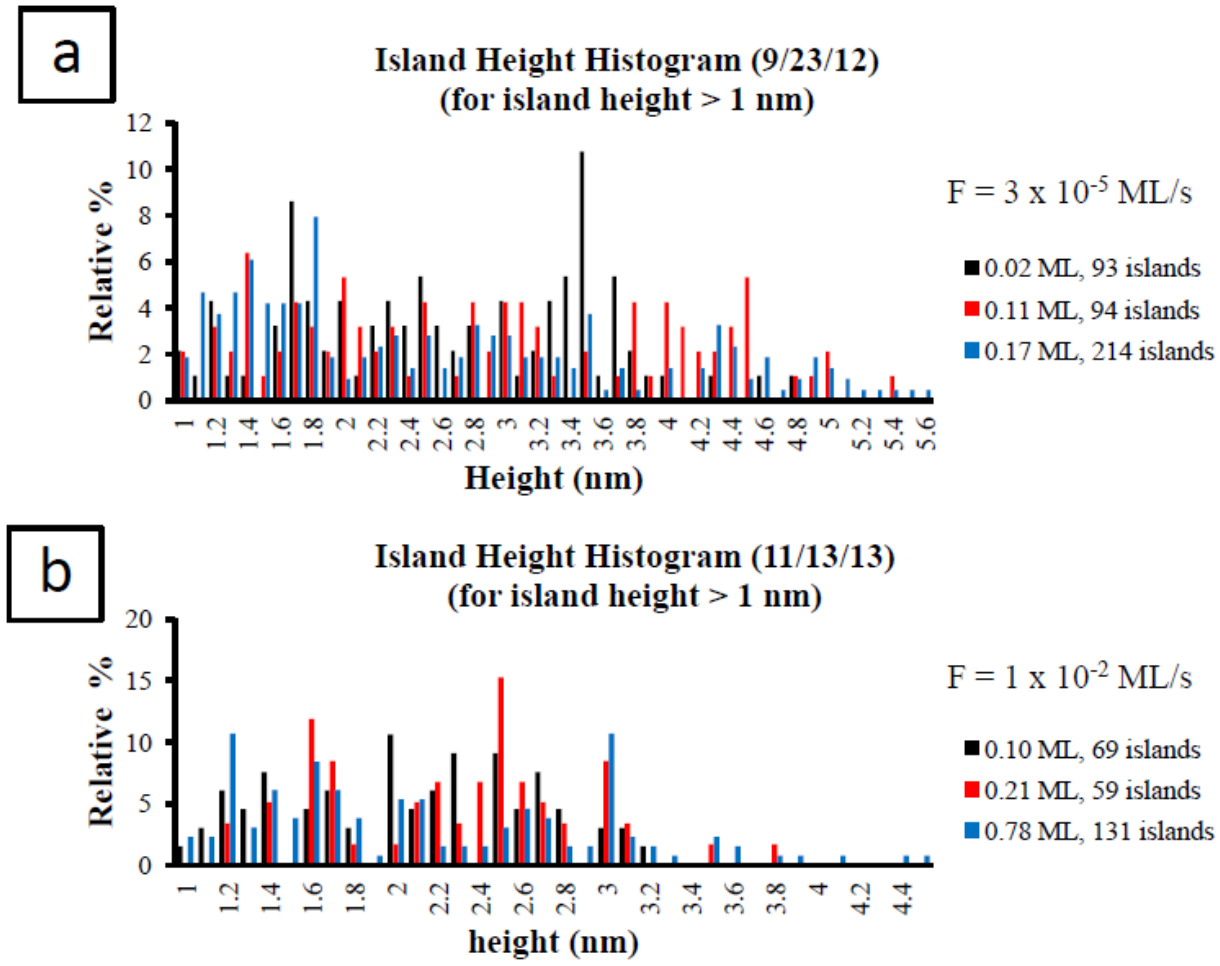

Fig. 16
Cu island height histograms for islands > 1 nm tall at various coverages (a) for F = 3 x 10^{-5} ML/s; and (b) for F = 1 x 10^{-2} ML/s.

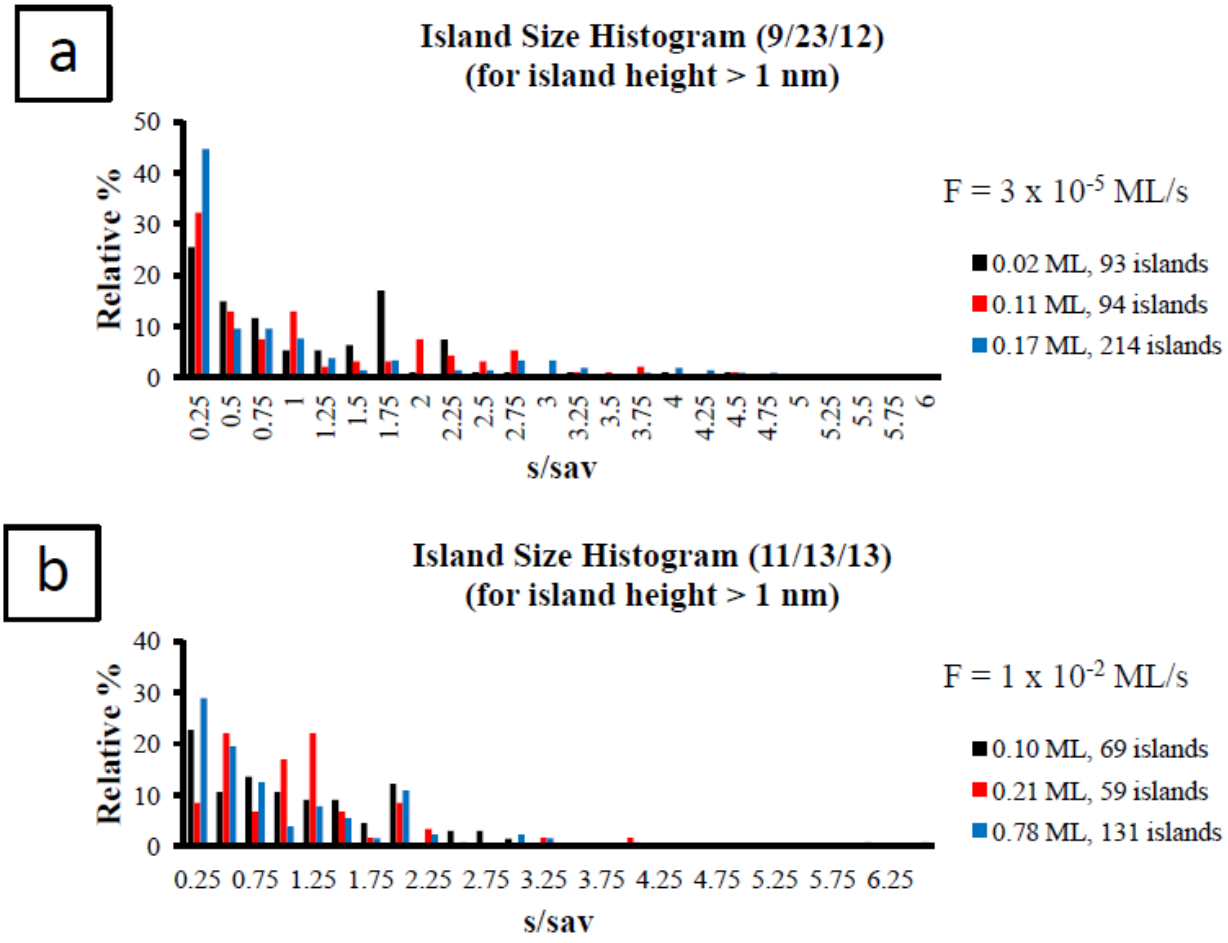

Fig. 17
Cu island size histograms (s/s_{av}) for islands > 1 nm tall at various coverages (a) for F = 3 x 10^{-5} ML/s; and (b) for F = 1 x 10^{-2} ML/s.

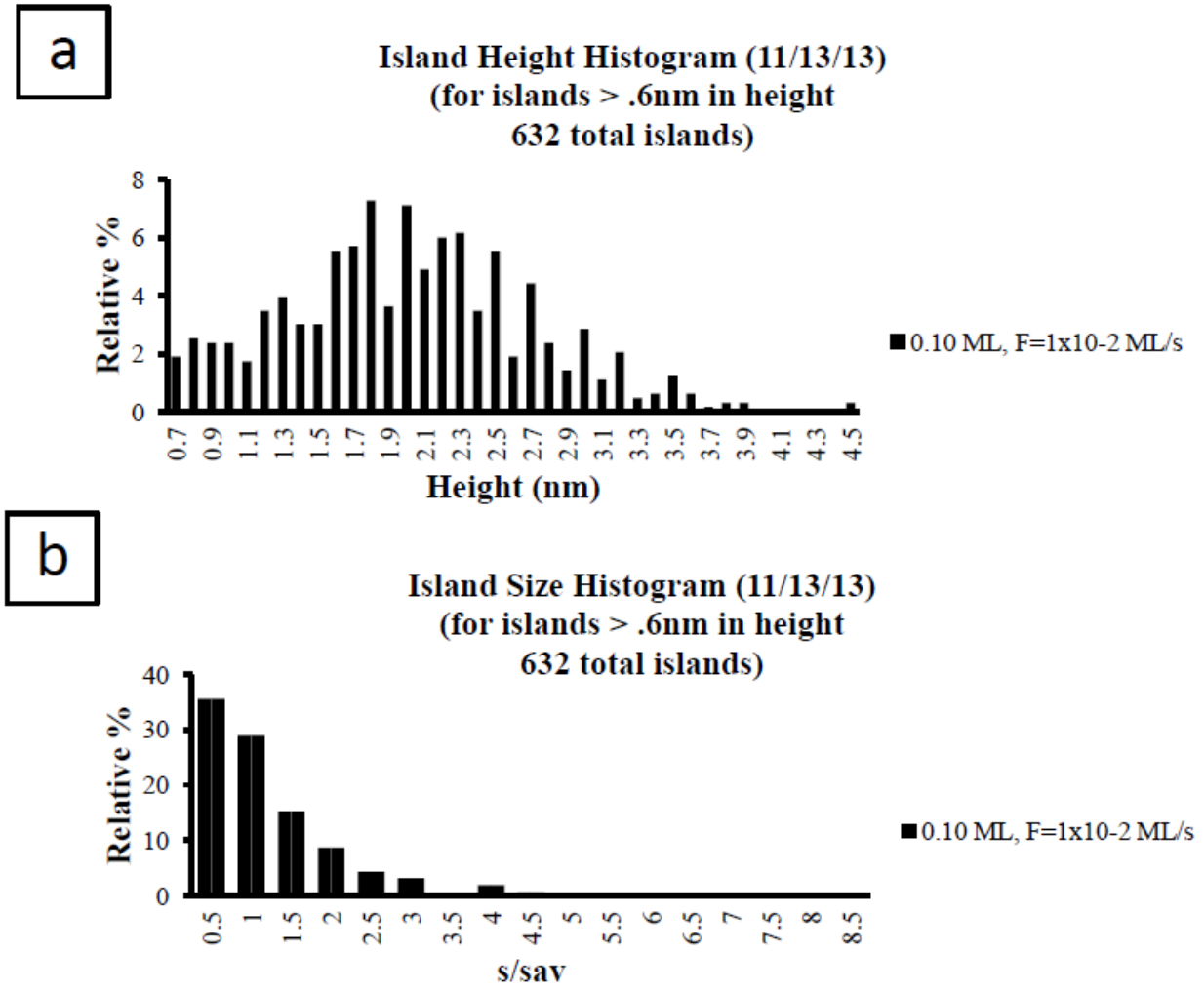

Fig. 18
Expanded island (a) height; and (b) size histograms for 0.1 ML coverage at F = 1 x 10^{-2} ML/s.

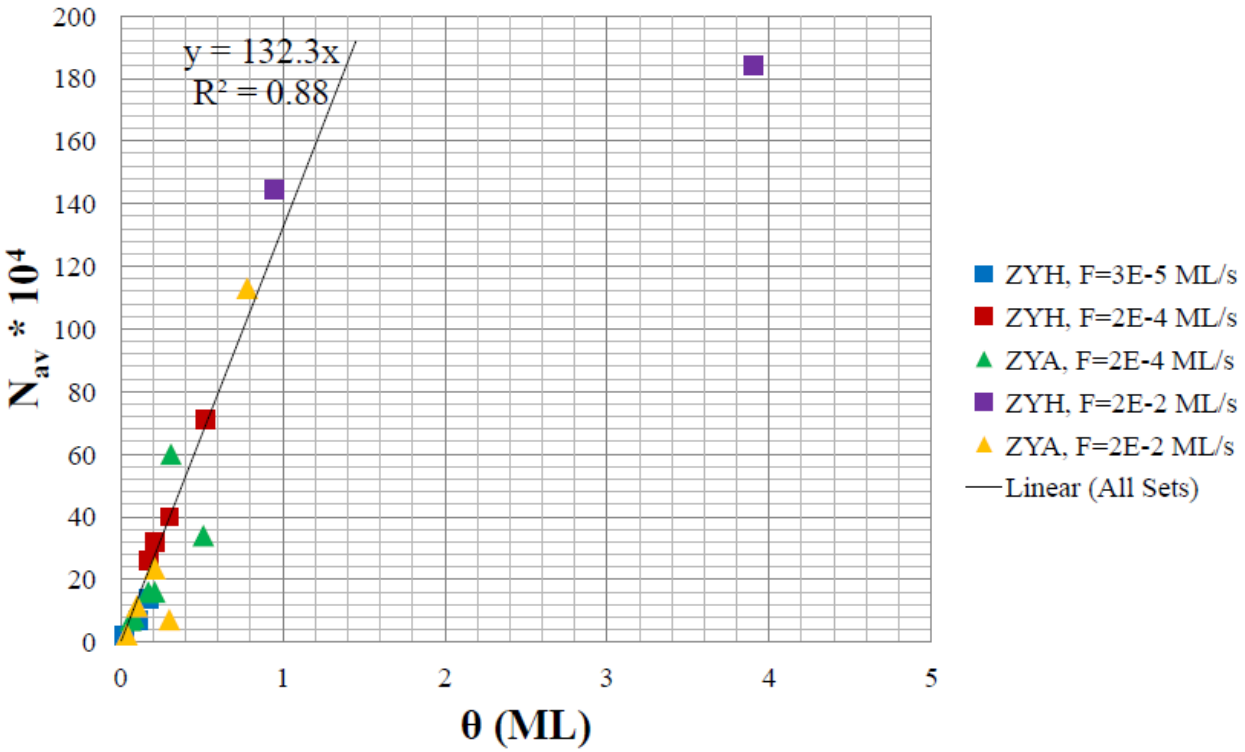

Fig. 19
Plot of N_{av} v. θ for Cu depositions at various fluxes and HOPG grades.

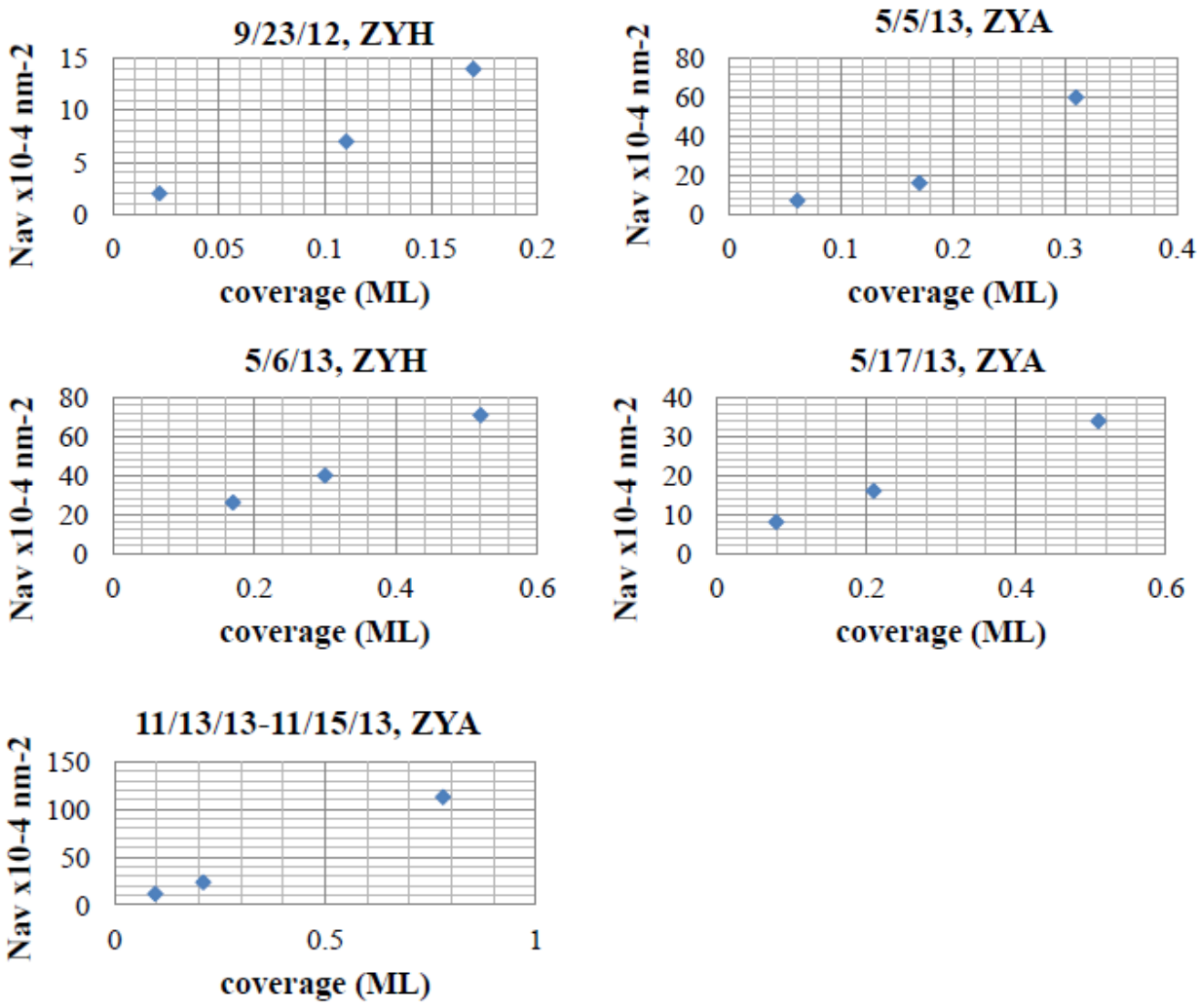

Fig. 20
Plots of N_{av} v. θ for Cu depositions at various fluxes and HOPG grades. Each plot shows a series of depositions done in the same day.

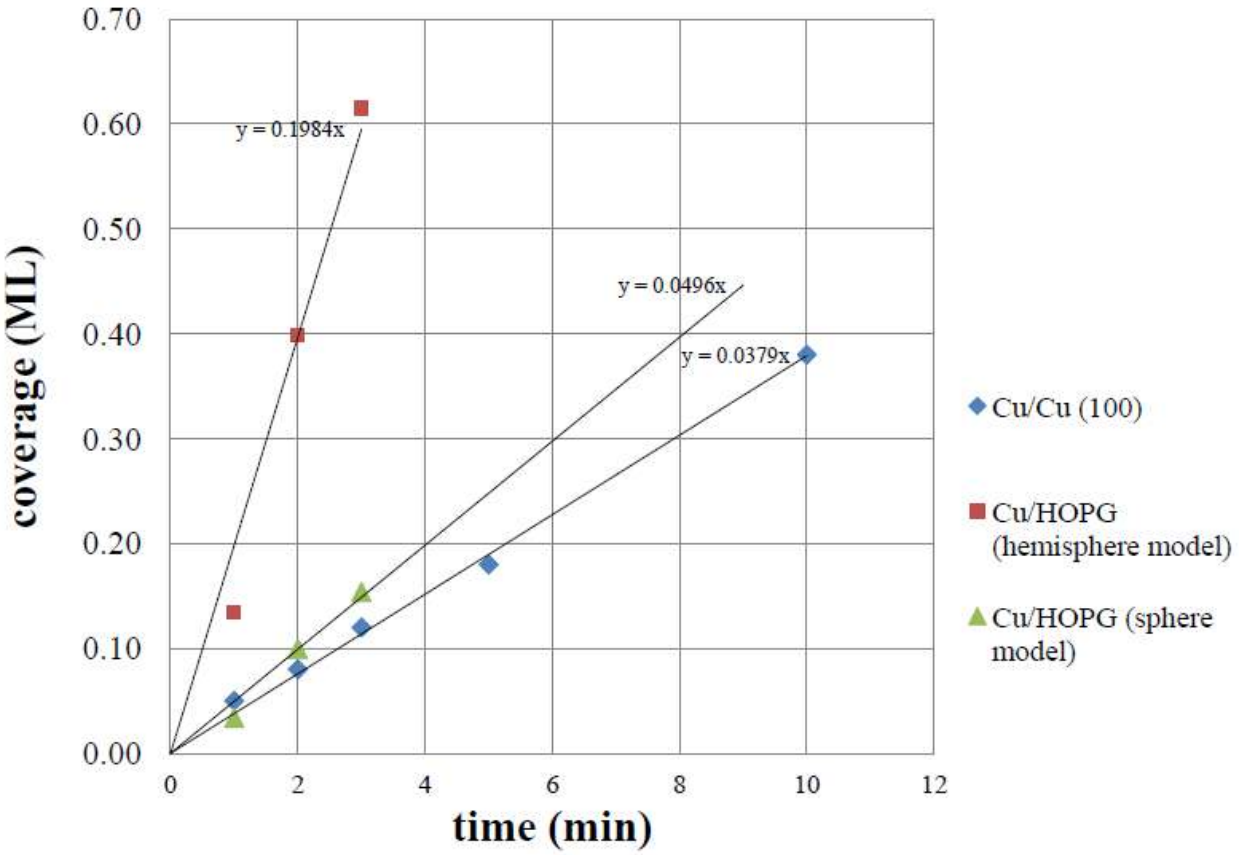

Fig. 21
Cu calibration plot comparing Cu flux on copper foil versus Cu flux on HOPG on the same day, but using different models for the shape of Cu/HOPG clusters.

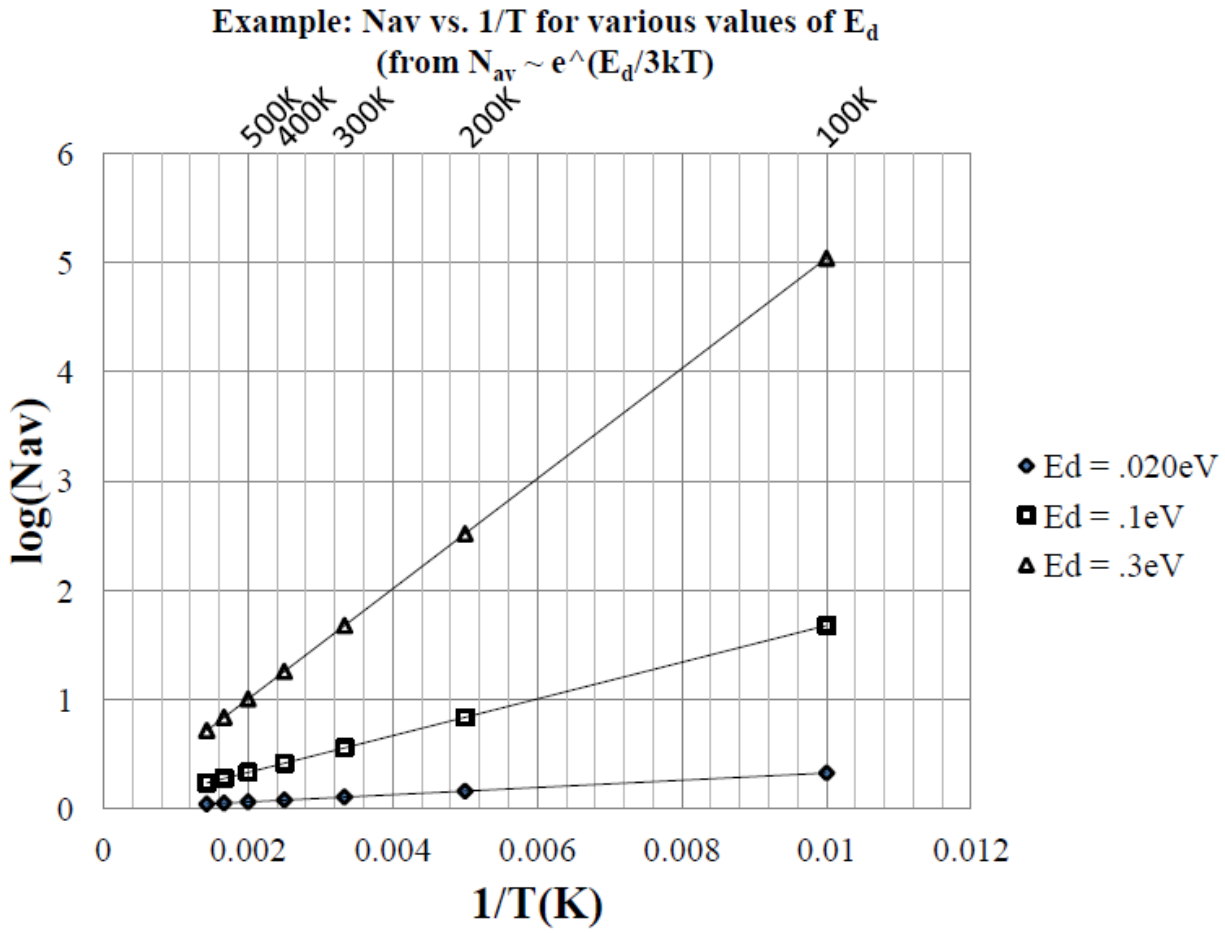

Fig. 22
Hypothetical plot of $\log(N_{av})$ v. 1/T for different values of E_d.

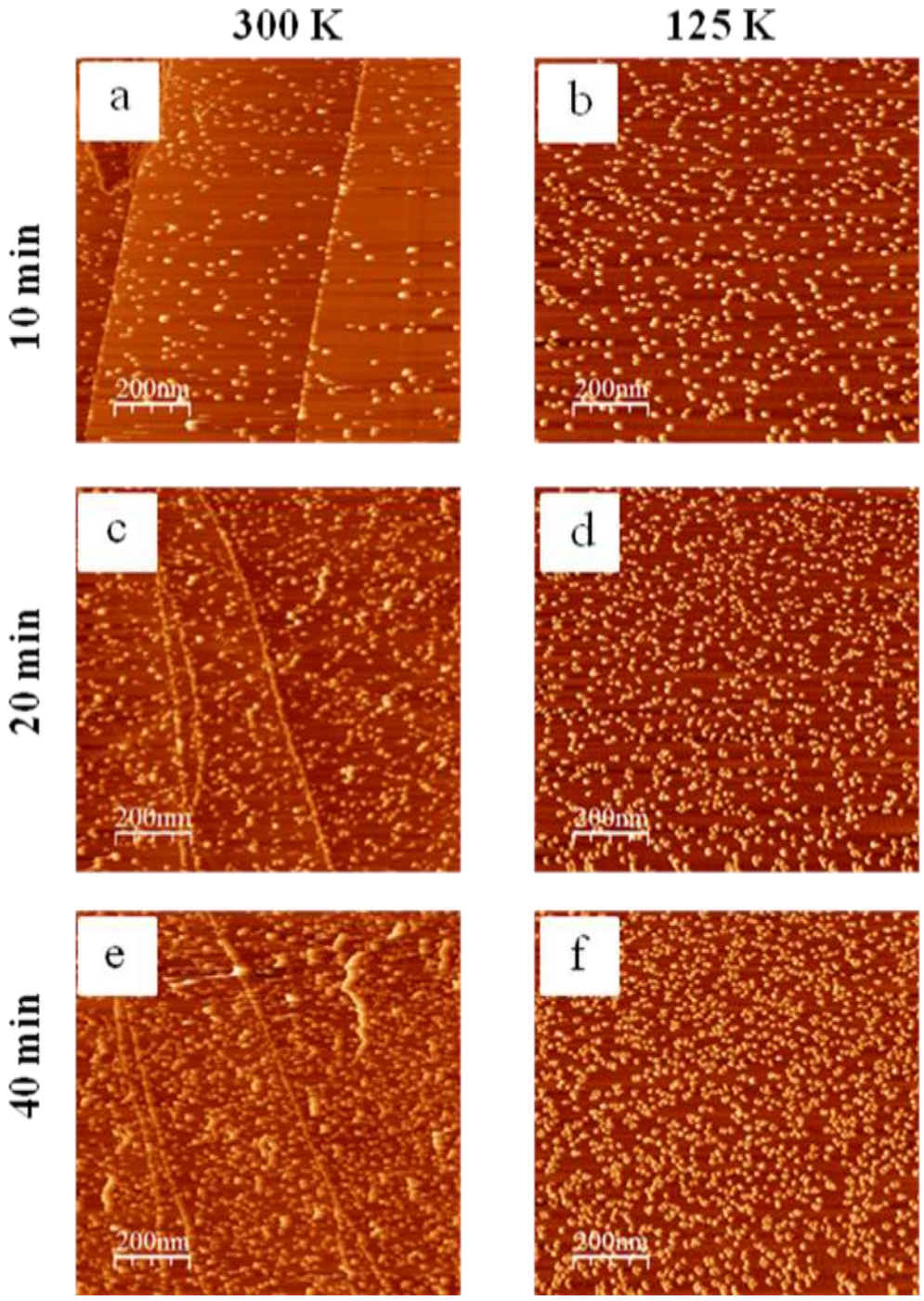

Fig. 23
STM image pairs (e.g. (a) and (b)) comparing Cu island densities between depositions at 300 K and 125 K, respectively for deposition times of (a-b) 10 minutes; (c-d) 20 minutes; and (e-f) 40 minutes. All depositions at 23.5 W power, 1 μm x 1 μm, V_{tip} = -1.0 V, i = 0.5 nA.

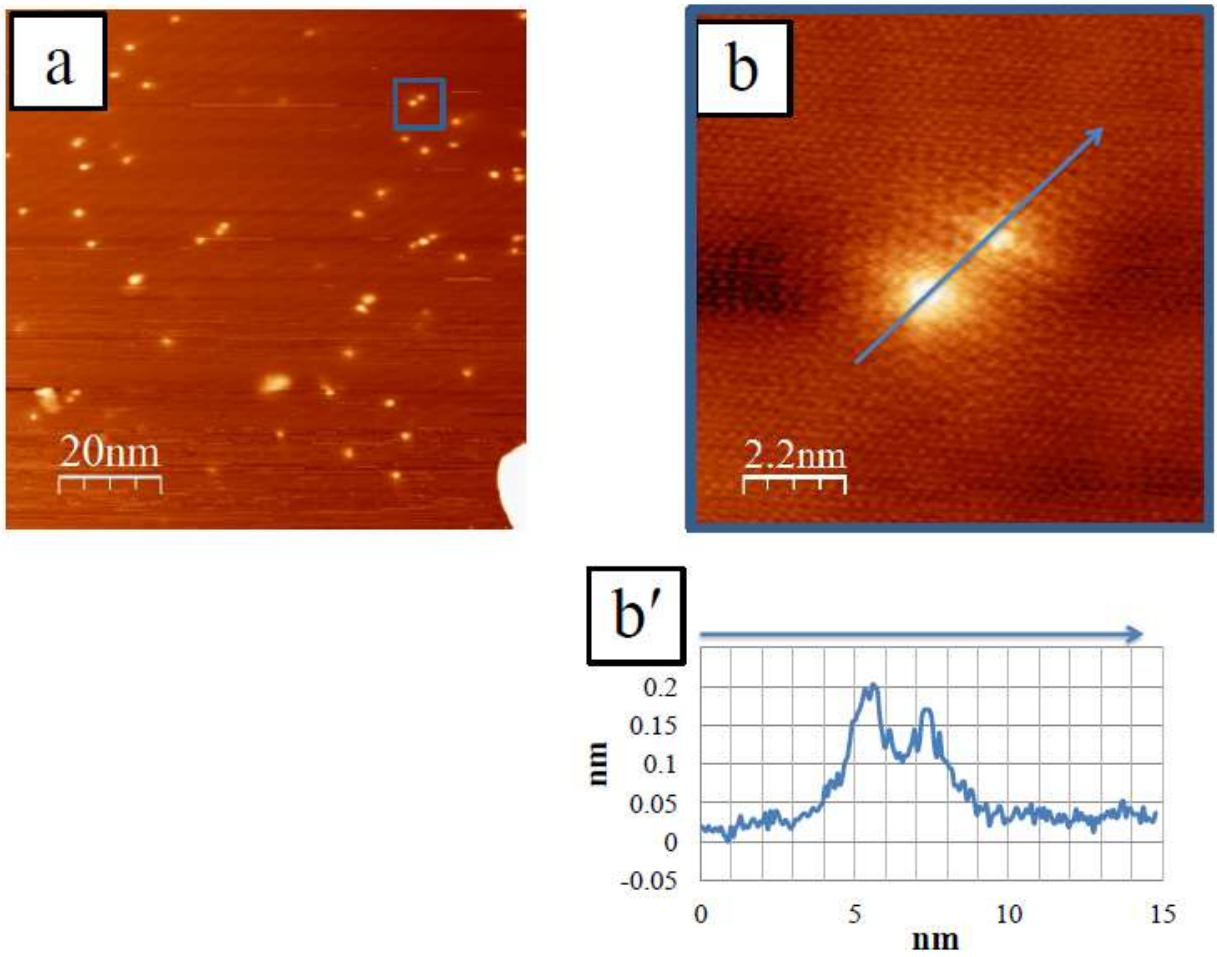

Fig. 24
(a) STM image in constant current mode of surface defects on Cu/HOPG after annealing to 700 K, 100 nm x 100 nm V_{tip} = -1.0 V, *i* = 0.1 nA; (b) a zoom-in of (a); (b′) a line profile of the feature in (b).

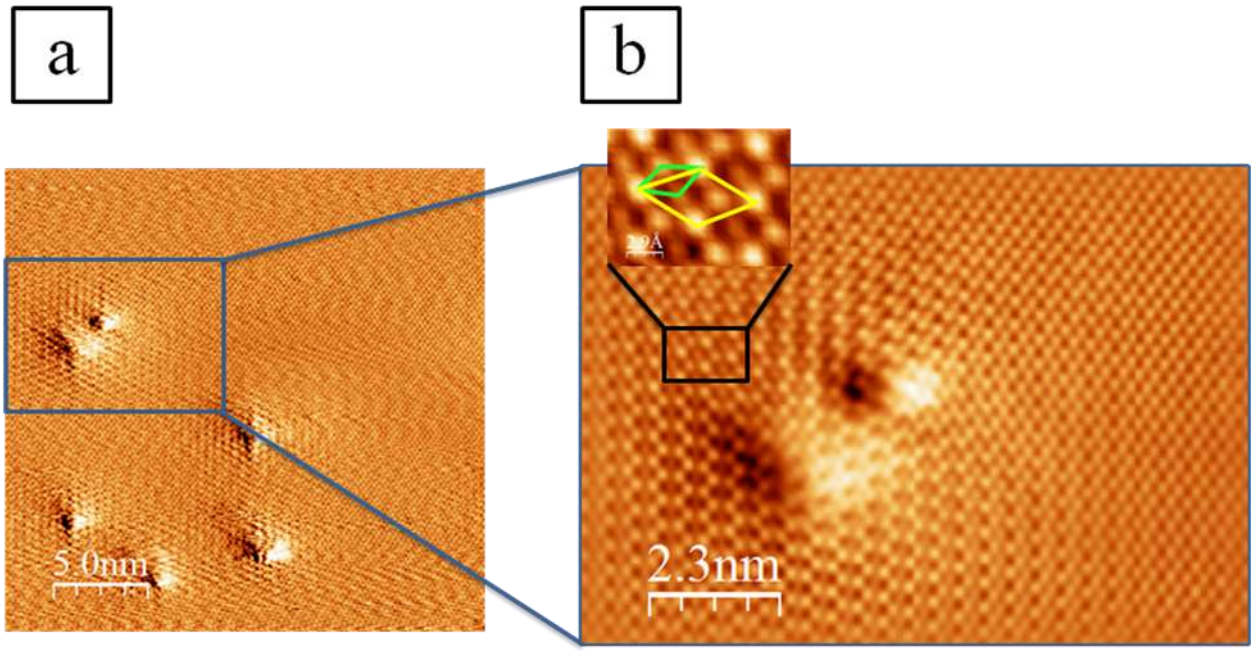

Fig. 25
(a) STM image in constant height mode of surface defects on Cu/HOPG after annealing to 700 K, 25 nm x 25 nm, V_{tip} = -1.0 V, *i* = 0.3 nA; and (b) a zoom-in of (a) with an inset showing (√3 x √3)R30° scattering.

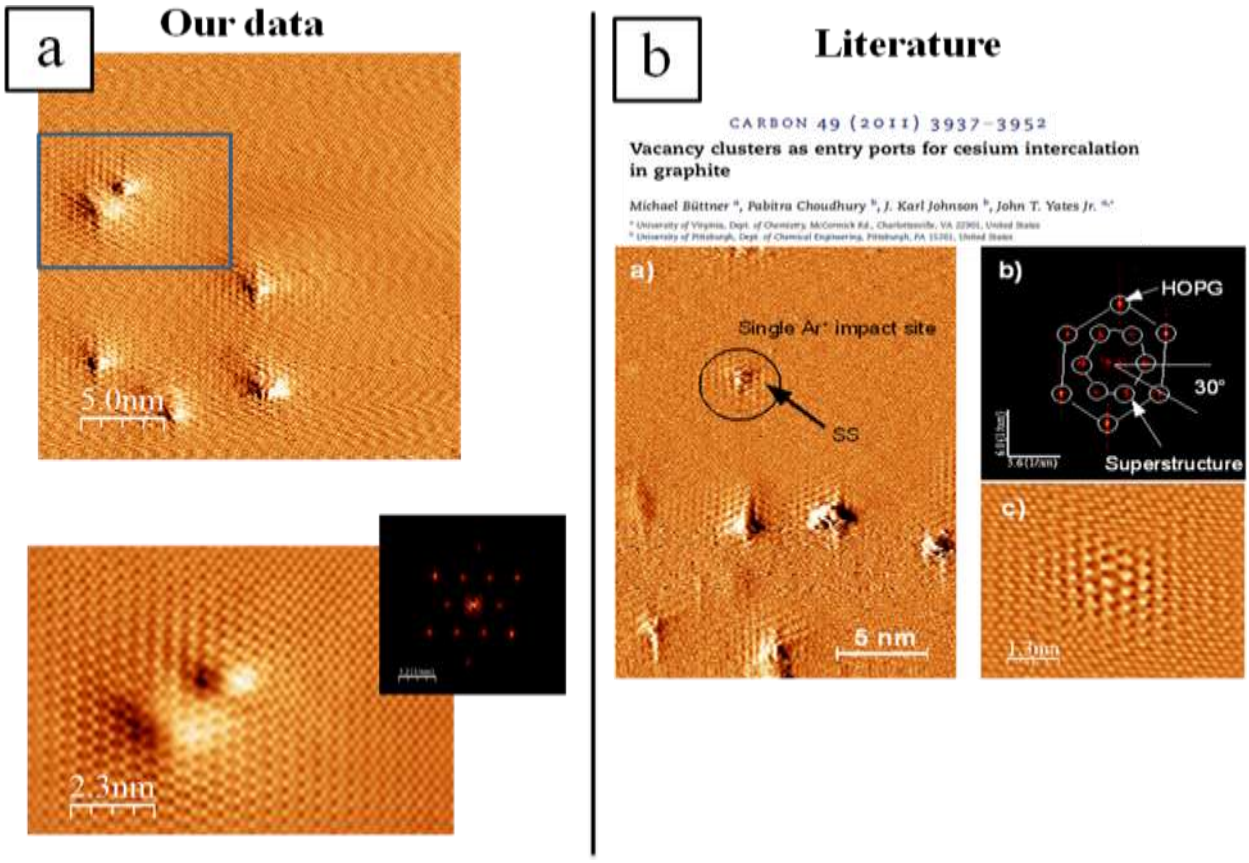

Fig. 26
A comparison of surface defects from (a) our STM data (also shown in Fig. 25); and (b) Ar^+ ion damage from Buttner et al.[32].

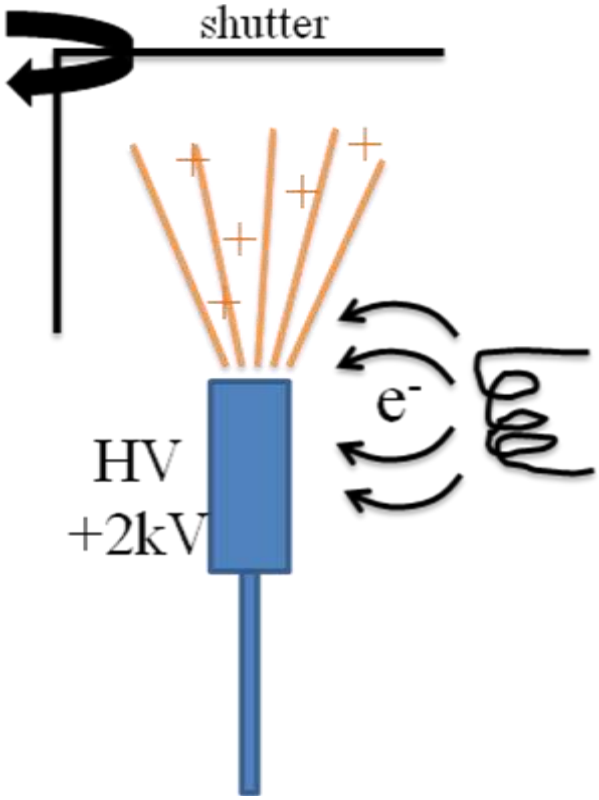

Fig. 27
Schematic diagram of our e-beam evaporator.

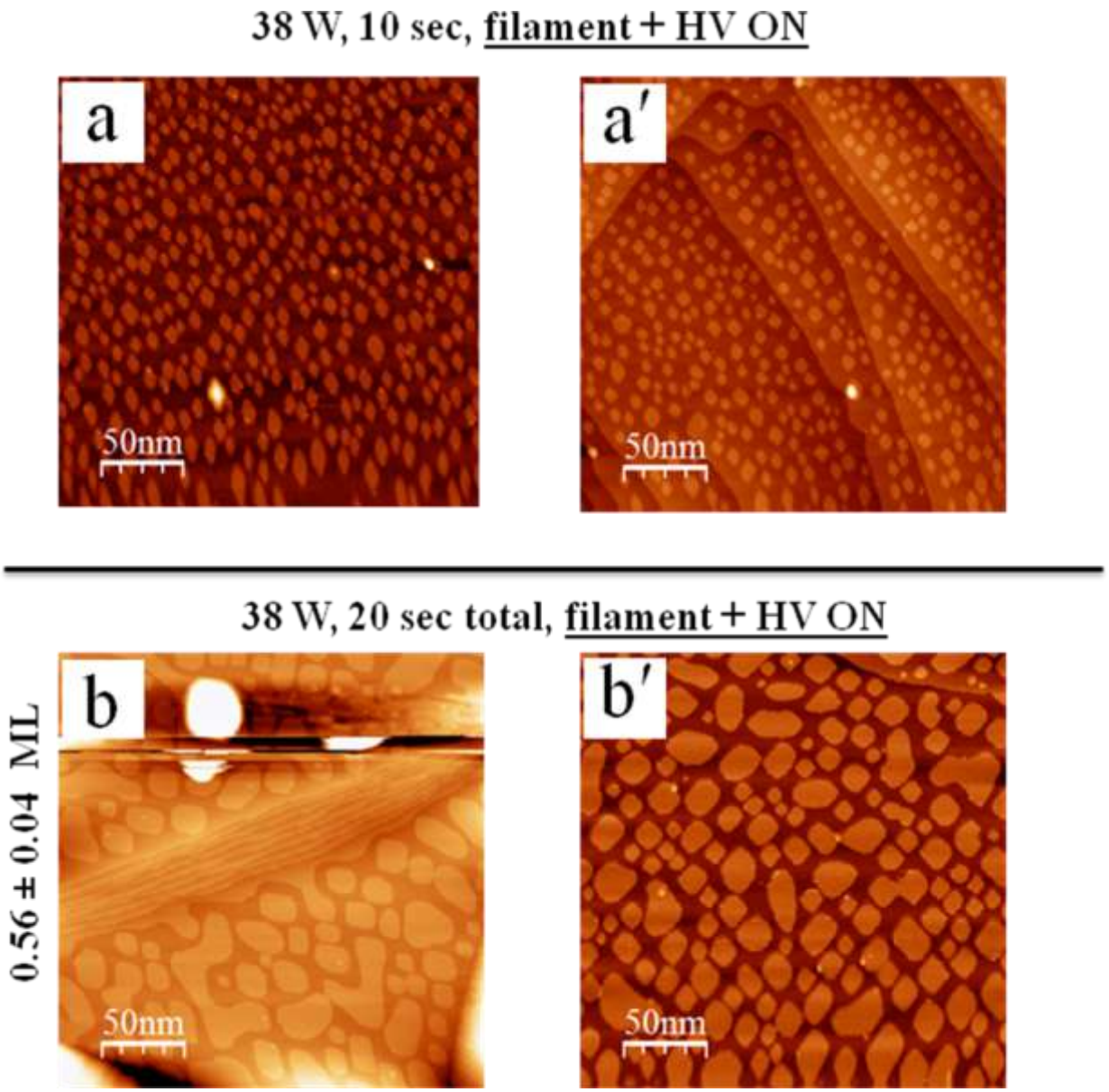

Fig. 28
STM images of the Cu/Cu(100) surface from the control run of a first flux drop experiment at 38 W power (filament + HV ON); (a-a′) after 10 seconds, giving 0.32 ± 0.02 ML, where (a) V_{tip} = -4.0 V, i = 0.1 nA and (b) V_{tip} = -3.1 V, i = 0.1 nA; and (b-b′) after 20 seconds (total) giving 0.56 ± 0.04 ML, V_{tip} = -3.5 V, i = 0.1 nA. All images are 250 nm x 250 nm.

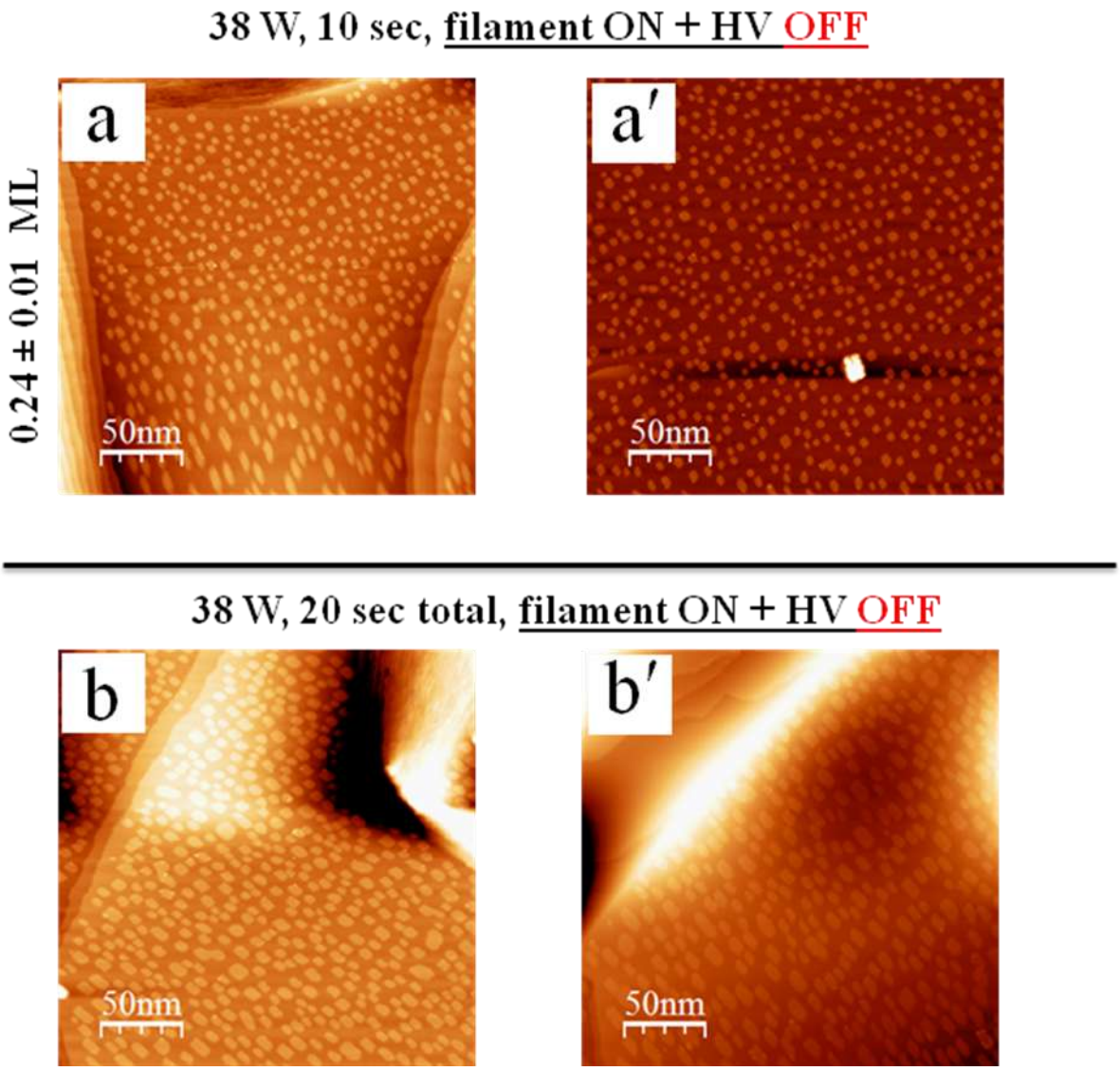

Fig. 29
STM images of the Cu/Cu(100) surface from the experimental run of a first flux drop experiment at 38 W power (filament + HV OFF); (a-a′) after 10 seconds, giving 0.24 ± 0.01 ML, V_{tip} = -3.7 V, *i* = 0.1 nA; and (b-b′) after 20 seconds (total) giving 0.40 ± 0.02 ML, V_{tip} = -3.7 V, *i* = 0.1 nA. All images are 250 nm x 250 nm.

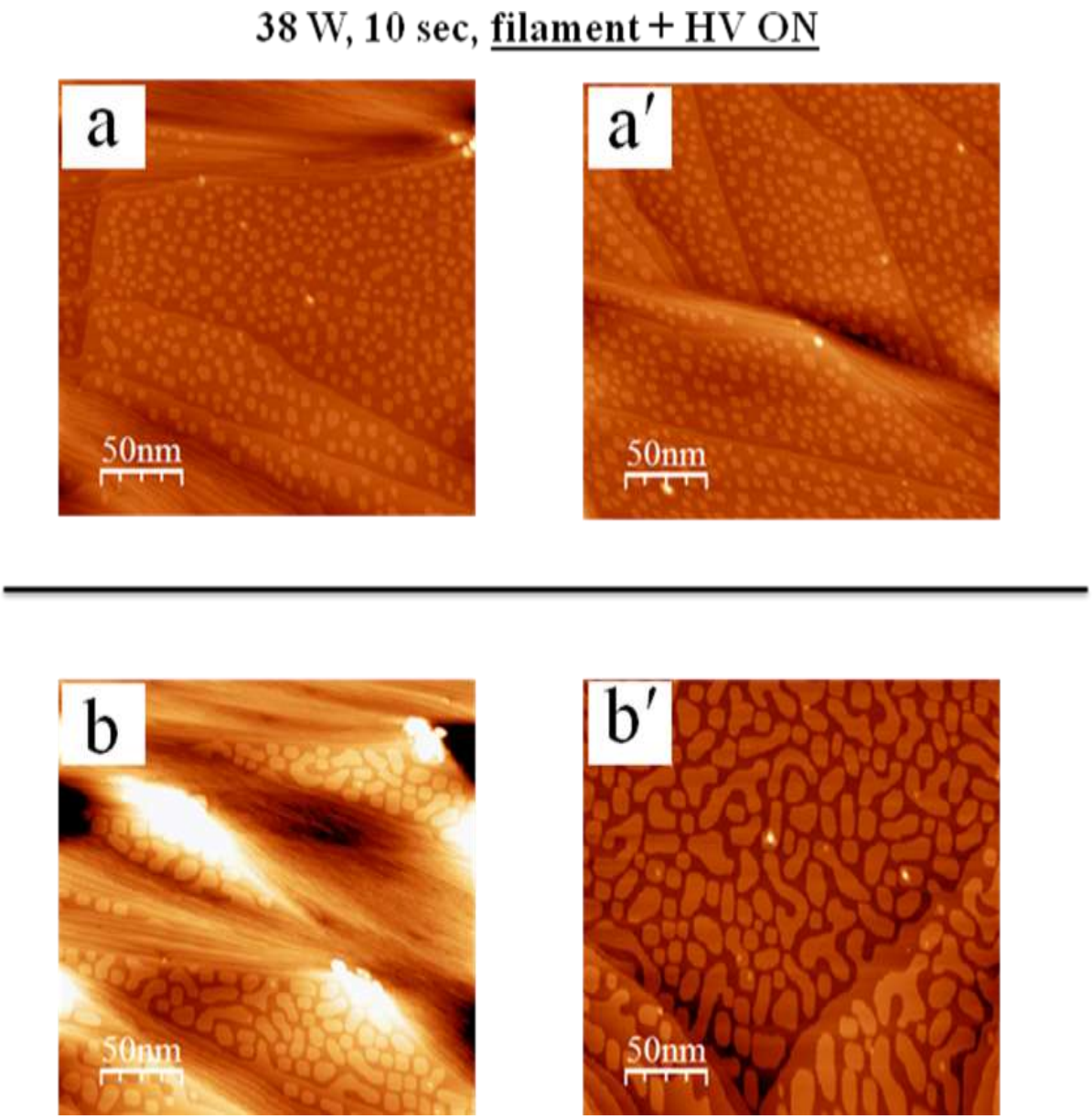

Fig. 30
STM images of the Cu/Cu(100) surface from the control run of a second flux drop experiment at 38 W power (filament + HV ON); (a-a′) after 10 seconds, giving 0.33 ± 0.01 ML, V_{tip} = -3.0 V, *i* = 0.1 nA; and (b-b′) after 20 seconds (total) giving 0.59 ± 0.01 ML, V_{tip} = -3.0 V, *i* = 0.1 nA. All images are 250 nm x 250 nm.

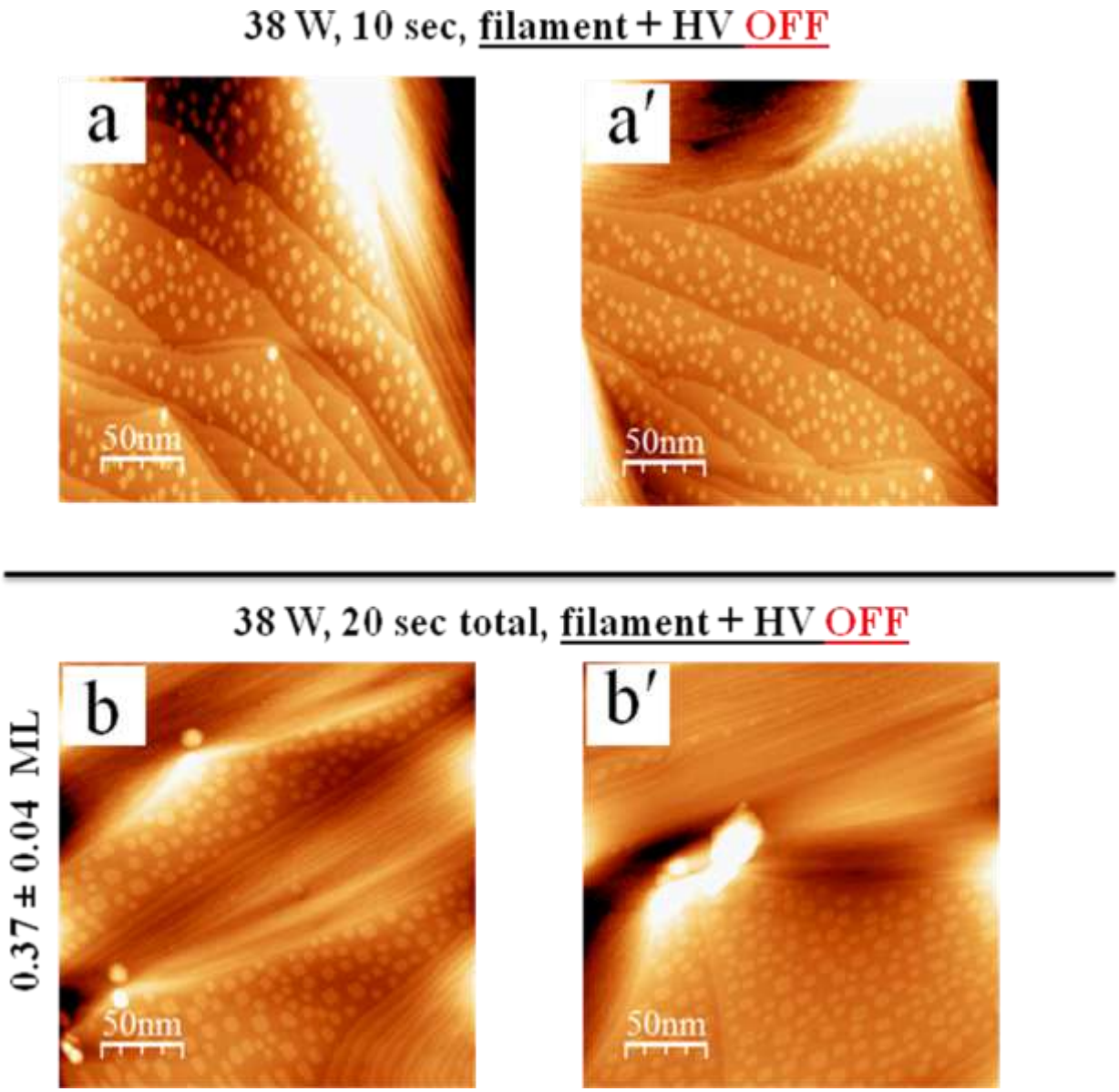

Fig. 31
STM images of the Cu/Cu(100) surface from the experimental run of a second flux drop experiment at 38 W power (filament + HV OFF); (a-a′) after 10 seconds, giving 0.28 ± 0.02 ML, where (a) V_{tip} = -3.0 V, *i* = 0.1 nA and (b) V_{tip} = -3.5 V, *i* = 0.1 nA; and (b-b′) after 20 seconds (total) giving 0.37 ± 0.04 ML, V_{tip} = -3.0 V, *i* = 0.1 nA. All images are 250 nm x 250 nm.

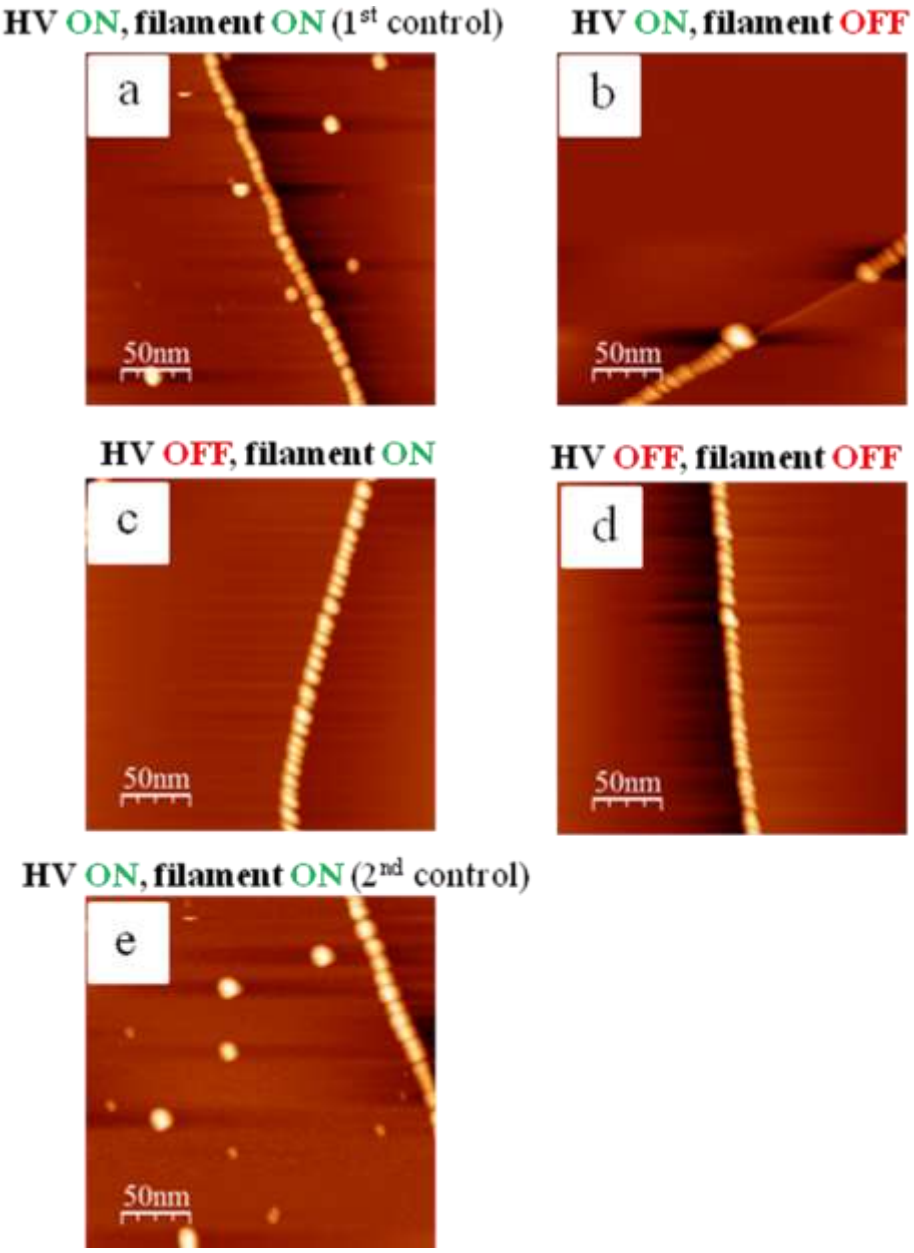

Fig. 32
Cu deposition on HOPG at 38 W power for 10 sec with (a) HV ON, filament ON (1st control); (b) HV ON, filament OFF; (c) HV OFF, filament ON; (d) HV OFF, filament OFF; (e) HV ON, filament ON (2nd control). Each frame has a step edge in view to show that Cu was actually deposited. (a-d) V_{tip} = -1.0 V, i = 0.1 nA; (e) V_{tip} = -2.0 V, i = 0.05 nA. All images are 250 nm x 250 nm.

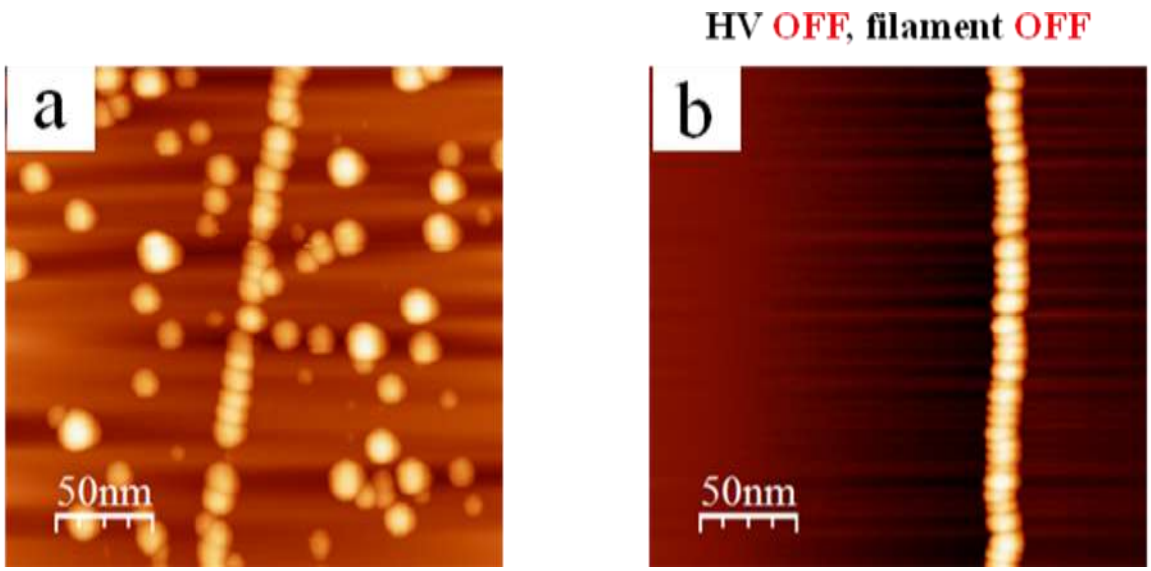

Fig. 33
Cu deposition on HOPG at 43 W power for 10 sec with (a) HV ON, filament ON, V_{tip} = -1.5 V, *i* = 0.05 nA; (b) HV OFF, filament OFF, V_{tip} = -1.5 V, *i* = 0.1 nA; Each frame has a step edge in view to show that Cu was actually deposited. Both images are 250 nm x 250 nm.

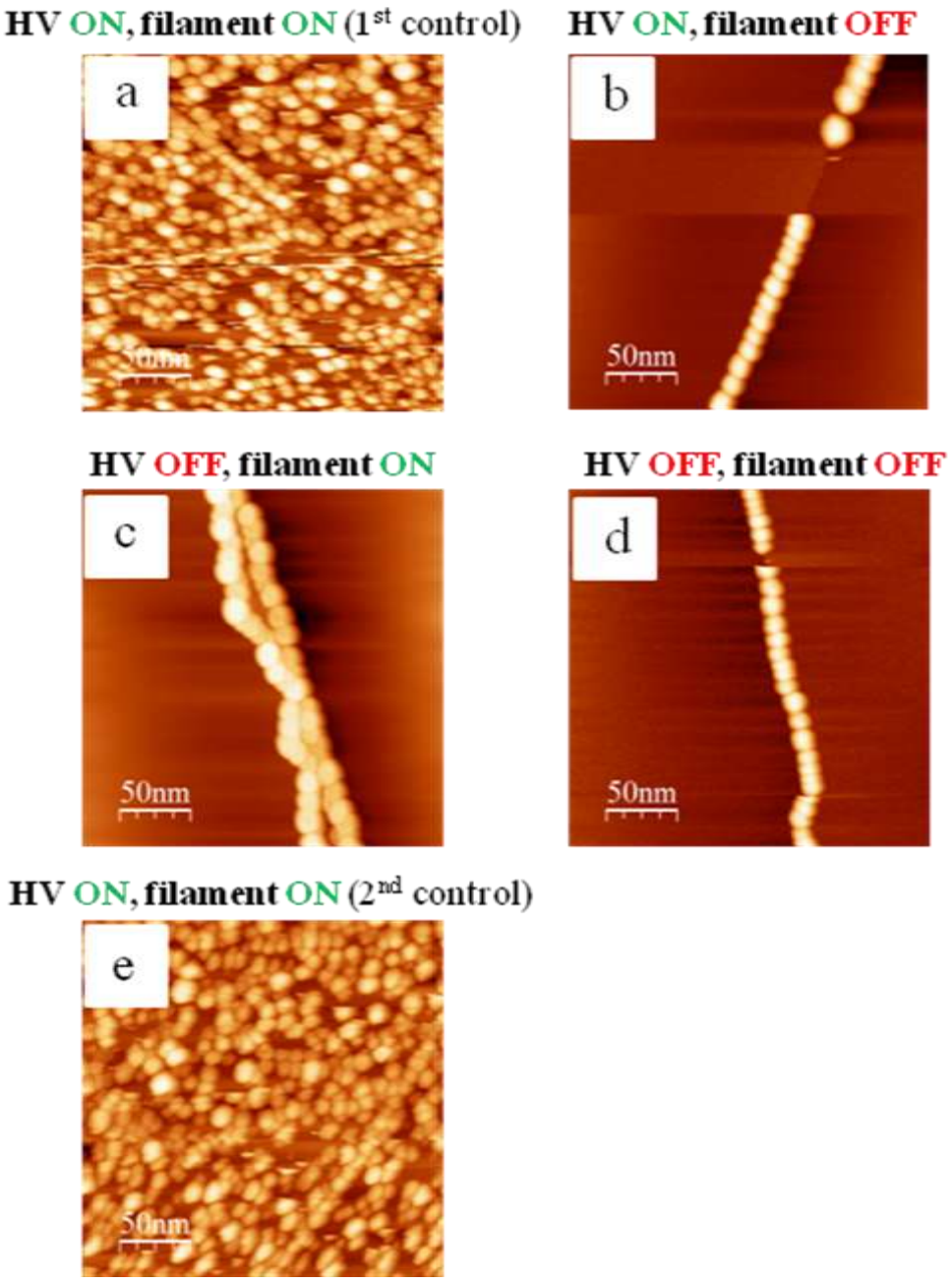

Fig. 34
Cu deposition on HOPG at 48 W power for 10 sec with (a) HV ON, filament ON (1st control); (b) HV ON, filament OFF; (c) HV OFF, filament ON; (d) HV OFF, filament OFF; (e) HV ON, filament ON (2nd control). Each frame has a step edge in view to show that Cu was actually deposited. (a-d) V_{tip} = -1.5 V, i = 0.05 nA; (e) V_{tip} = -1.3 V, i = 0.05 nA. All images are 250 nm x 250 nm.

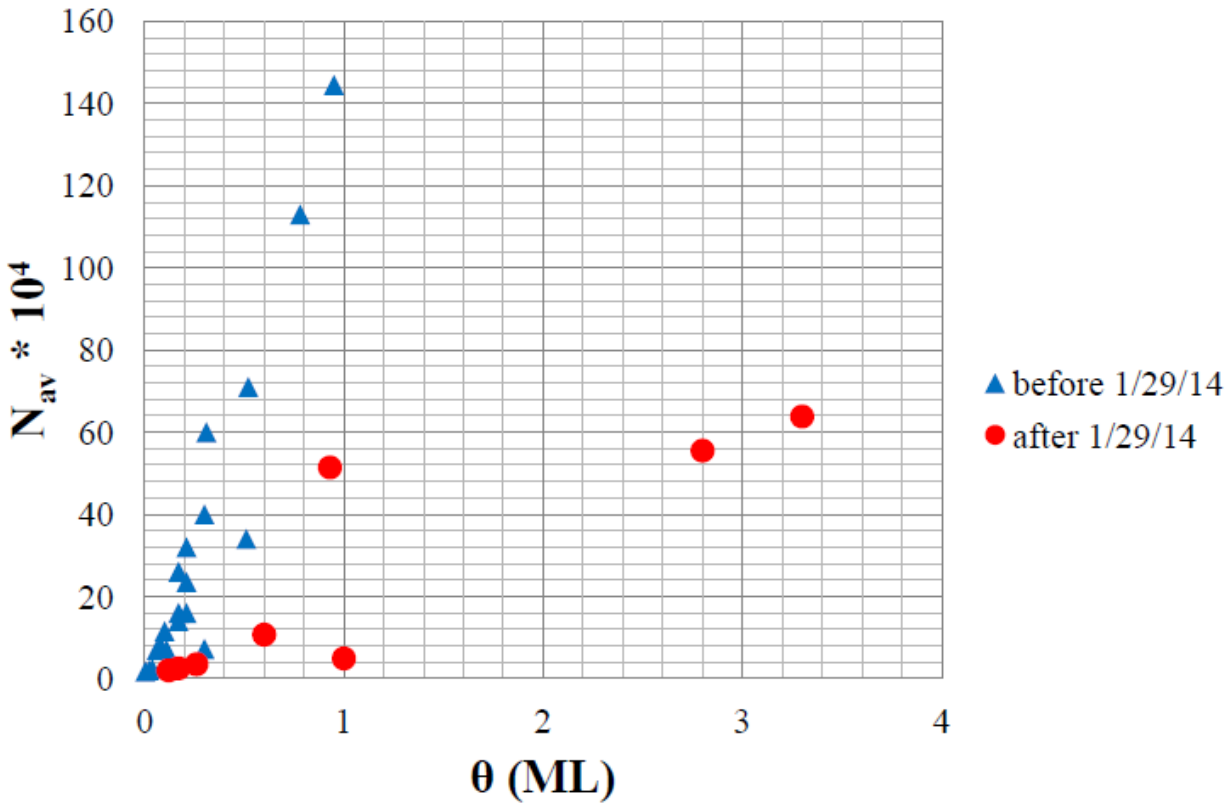

Fig. 35
Plot of Nav vs. θ comparing trials before 1/29/14 to trials after 1/29/14.

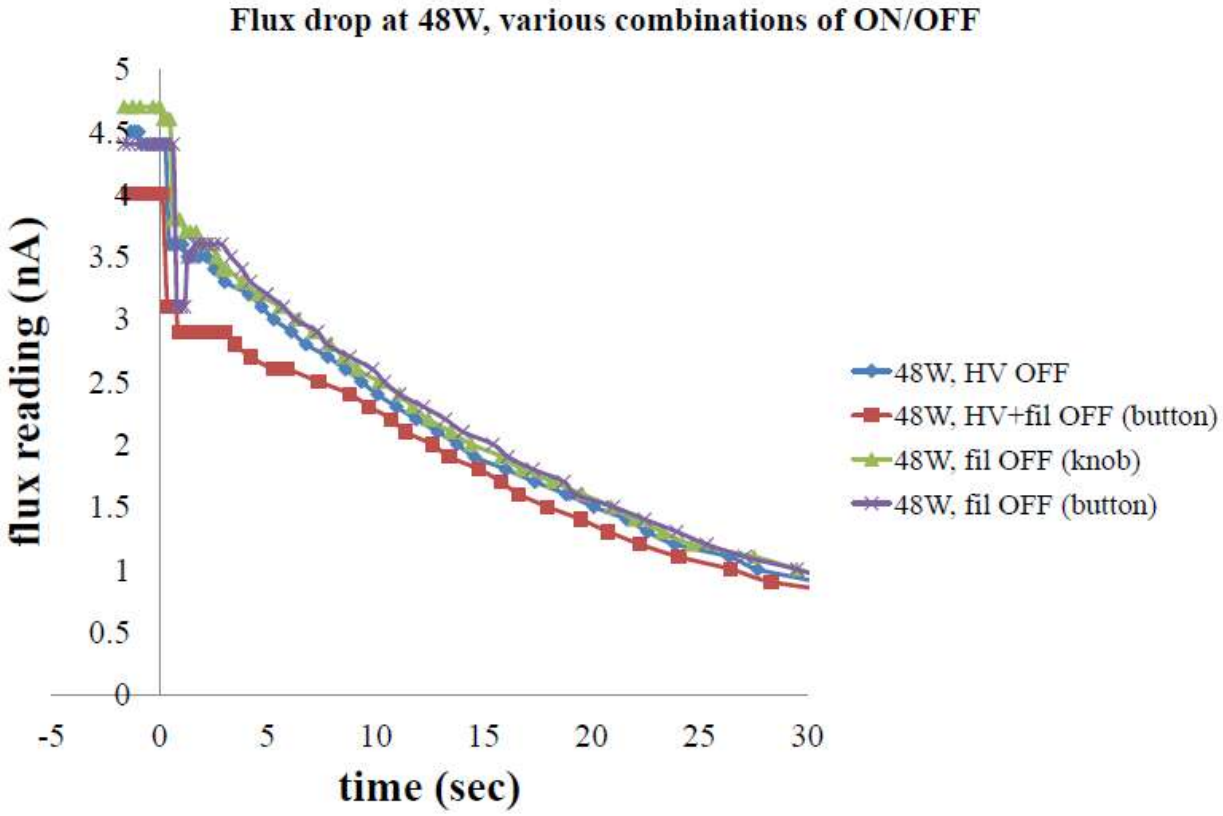

Fig. 36
Plot of the decay in displayed flux (nA) vs. time for our e-beam evaporator at an initial power of 48 W, after various combinations of components have been shut off. The shutter remained closed during all trials.

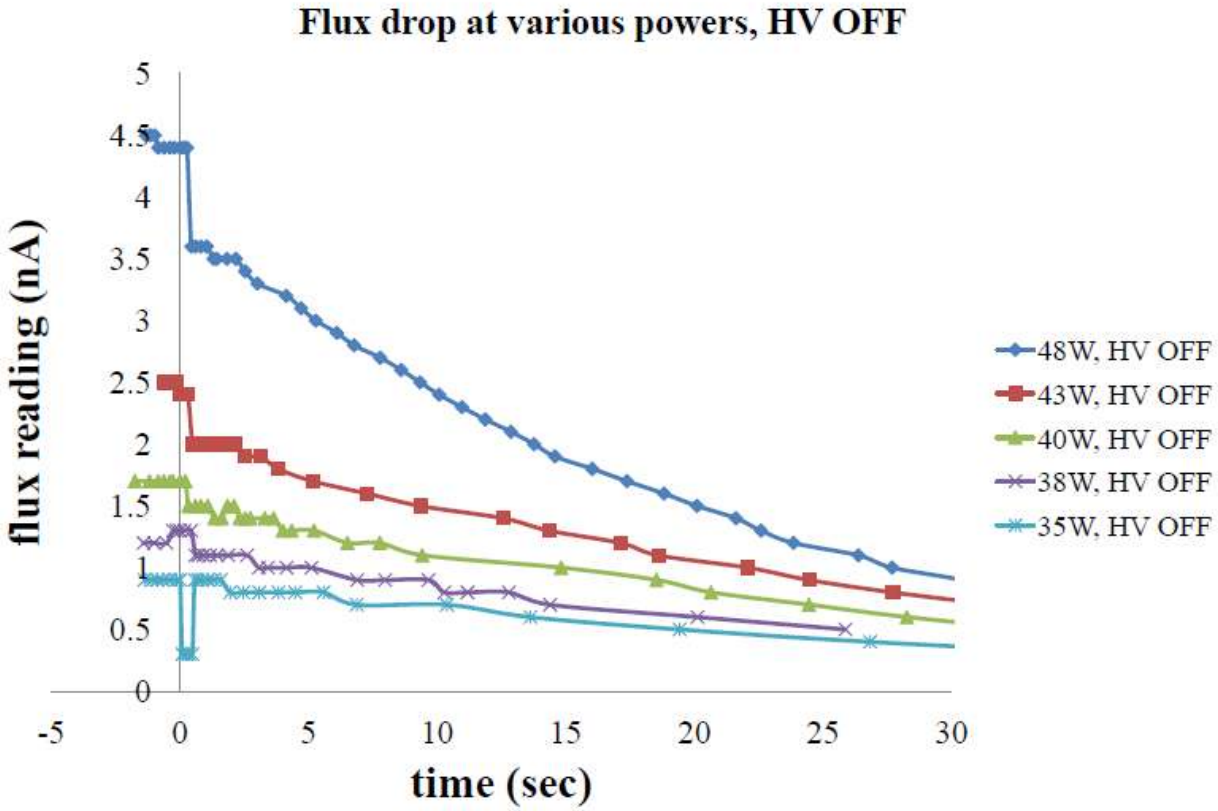

Fig. 37
Plot of the decay in displayed flux (nA) vs. time for our e-beam evaporator at various starting powers, after HV has been switched off. The shutter remained closed during all trials.

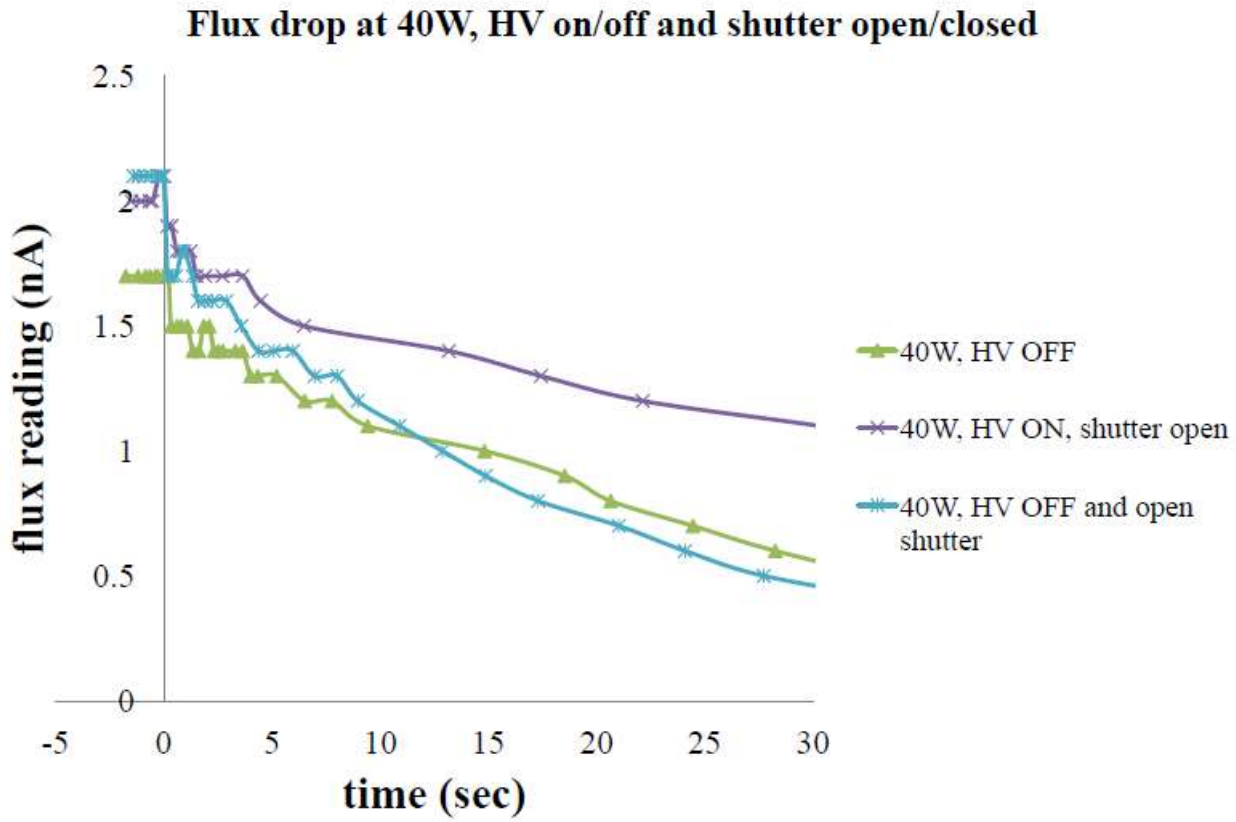

Fig. 38
Plot of the decay in displayed flux (nA) vs. time for our e-beam evaporator for various combinations of HV ON/OFF and shutter open/closed.

CHAPTER 4

CU ON HOPG AT T > 300 K

4.1 Introduction

As a continuation of our study of nucleation of Cu on the HOPG surface at 300 K, we conducted a series of experiments to investigate the behavior of this system at higher temperatures. A number of phenomena could conceivably occur, such as desorption, coarsening, and intercalation.

Arthur and Cho[1] conducted temperature programmed desorption (TPD) experiments to determine the desorption temperature of Cu on graphite. They found desorption began near 900 K, with a peak desorption temperature at 1025-1125 K, depending on coverage (0.01-0.1 ML, respectively). They modeled their desorption kinetics, and interpreted the result to mean that at high coverage (2-3 ML) Cu desorbs from bulk Cu rather than from HOPG.

Several groups have deposited metals on graphite with the substrate held at elevated temperature, e.g. for Au [2; 3], and Ag[4]. Based on these studies Au particles on graphite undergo morphological changes from 450 K[2] to 550 K[3], and Ag coarsens as low as 463 K[4]. Howells[5] conducted an XPS incremental heating study for Pt/HOPG starting at 150 K and found Pt binding peak transitions occur from 150-375 K. Nielsen[6] saw coarsening in the Ru/HOPG system at 800 K. Kholmanov[7] saw significant coarsening and desorption of Fe from HOPG at 1100 K. To the best of our knowledge there have been no coarsening studies on the Cu/HOPG system.

Intercalation is also seen for certain metal/graphite systems, most notably the alkali metals [8; 9], but also some rare earths [10-12]. We have found little evidence for intercalated graphite compounds of transition metals in the literature, although attempts have been made by reduction of intercalated metal-halide systems[13]. There are several studies showing intercalation of transition metals on supported *graphene*[14-18]. However in these systems intercalation is driven by a strong interaction between the deposited metal and the underlying graphene support, which does not apply to HOPG.

Our goals for this study are to determine the coarsening, desorption, and possible intercalation behavior of the Cu/HOPG system.

4.2 Experimental Details

In the following experiments, Cu was deposited on HOPG at 300 K, then heated incrementally in 100 K increments from 300 K to 900 K or higher for 15 minutes at each temperature, and imaged with STM after cooling from that temperature. All STM images were taken at 300 K in constant current mode unless otherwise specified. The heating parameters are discussed in detail in Chapter 2. The experiment was repeated five times at various coverages. One of the coarsening experiments was conducted on a post-heated surface (defected surface) and is discussed in section 4.5 below.

4.3 Coarsening and Desorption

Coarsening is noticeable in STM images starting around 600-700 K (see Fig. 1-12), for a range of 0.07 to 1.1 ML Cu depositions. For incremental heating experiments #2 (0.51 ML) and #5 (0.07 ML), cluster height histograms are provided to show the shift in cluster height

distribution from 300 K to the onset of substantial coarsening at 700 K (see Figs. 5, 12). It should be noted that experiment 5 is a slightly different system in that the starting surface had pre-formed defects, discussed in section 4.5. For heating experiment 2, the average cluster height changed from 2.6 nm at 300 K to 4.3 nm at 700 K. For heating experiment 5, the average cluster height changed from 1.6 nm at 300 K to 1.8 nm at 700 K. In Fig. 12, the group around 0.2-0.8 nm in the 700 K data probably represents defects on the HOPG surface which are exposed during coarsening but possibly retain a small amount of residual Cu.

Plots of coverage vs. temperature (Figs. 2(b), 4(b), 7(b), 9(b), and 11(b)) show a marked decrease in Cu coverage at 900 K, suggesting that desorption begins between 800-900 K in our system, assuming that Cu was not lost due to intercalation into the bulk. Above 900 K the HOPG terraces were mostly clean, and ion-induced defects on the surface were evident (see Figs. 1(g′), 6(g′), 8(g′) and 10(g′)). By 1200 K, desorption was essentially complete and the ion-induced defect sites were imaged more clearly (see Fig. 14). Typically, though, the contrast needed to be adjusted in post-processing to see the defects clearly, e.g. by comparing Fig. 1(g) and 1(g')) The defect sites on these high-heated surfaces were 0.1 to 0.3 nm tall, which was shorter than the range for residues seen at lower temperatures (0.1-0.8 nm). We attribute this to residual adsorbed Cu at lower temperatures. The defect density corresponded to the original cluster density as shown for a range of cluster densities in Table 1. Arthur and Cho[1] determined a desorption range of 900-1150 K for Cu on HOPG using TPD with peak desorption between 1050-1100 K depending on coverage (flash heated at 600 K/min). Our STM study used a much slower and longer heating process (60 K/min and heated incrementally for 15 minutes at each temperature), so our apparent desorption in the slightly lower range of 800-900 K is in relative agreement with Arthur and Cho.

Relative error for all data points is 3-10 % in N_{av} and ≈ 5-15 % in coverage based on the square root of the number of clusters sampled, which is one standard deviation for samples of randomly-distributed events or objects. Expressed in terms of two standard deviation (95% confidence interval), the relative error is 6-20 % in N_{av} and ≈ 10-30 % in coverage.

4.4 Morphology of the Post-Heated HOPG Surface

Heating the Cu/HOPG surface to 1200-1300 K for > 30 minutes was sufficient to desorb nearly all Cu from the surface including the step edges, as shown in Fig. 13 (in comparison to a clean surface). Fig. 14 shows an STM image of Cu/HOPG after 1200 K heating, with a 5 nm high residual Cu cluster. It was typical to find a few large, sparsely-dispersed clusters such as this one on a post-heated surface. They were presumably residual products of coarsening. An adjustment to the contrast in post-processing images reveals more subtle features on the surface. Fig. 14(a) and the accompanying line profile shows residues which were ion-induced defects from the Cu deposition process. The bare defects were typically 0.1 – 0.3 nm in height (average 0.22 nm) and several nm in apparent width (average 3.3 nm), with soft edges. A high-resolution view of a defect imaged in constant height mode is shown in Fig. 15. Most of the apparent width of these defects is the product of $(\sqrt{3} \times \sqrt{3})R30°$ scattering commonly seen with point defects on graphite [9; 19-21]. It is unclear whether these defects were caused by a missing carbon atom, an intercalated Cu atom, or combinations of both.

Heating the surface to 1300 K for > 30 minutes (large view in Fig. 16) caused a light etching at some defect sites but not others, as seen in Fig. 17 (higher magnification images from the same surface as Fig. 16). In Fig. 17 the bright spots are normal defects and the dark spots are etched holes. Oxygen-etching of graphite around defects to produce 1-layer deep pits is well-

documented in the literature [22-26], as discussed in Chapter 1. Since we work in UHV, the effect was very subtle and seen primarly after heating to 1300 K for > 20 minutes. Metal nanoparticles have also been shown induce catalytic etching of graphite if heated in a hydrogen atmosphere[27]. The apparent etching in our system is evidence that some defects have a break in the carbon sheet (allowing etching), and others do not. Another feature common to the post-heated surface is wide pancake-like features 0.3 nm high and 10-20 nm wide, present in Figs. 16-19, and shown in detail in Fig. 18. When imaged in constant current mode at low to medium magnification, these features imaged as mounds 0.3 nm high (approx. 1 atom high). At high magnification, their profile changed depending on the scanning mode used. Under constant current mode (Fig. 18(a′)) they imaged asymmetrically, as a depression 0.3 nm below the basal plane on the left (leading) edge of the scan, and as a protrusion 0.3 nm above the basal plane on the right (trailing) edge of the scan. Imaged under constant height mode (Fig. 18(a″), they were symmetrical in shape (height not measurable in this mode). From this mode it is clear that the graphite sheet is not broken, and is possibly draped over something under the surface. The feature height of 0.3 nm is consistent with a raft of Cu atoms 1 layer high intercalated under the graphite surface.

4.5 Post-Heated Surface as a Template for Small Cu Cluster Growth

The post-heated HOPG surface (especially after a heavy Cu deposition) can be used as a template for growth of large numbers of small Cu clusters (average cluster height < 2 nm). Small clusters were difficult to prepare via depositions on a pristine HOPG surface because depositing a small amount of material necessarily results in a small number of clusters, which makes gathering meaningful statistics difficult. On the post-heated surface, with defects already

present (and defect density moderately controllable by the initial Cu deposition), growing clusters of any small size is possible. One distinct advantage of studying smaller clusters is that they are much easier to image with the STM. The cluster shearing rate was consistently about 10%, compared to 10 – 50 % for a normal deposition. In general, STM images on the post-heated surface were much cleaner than for a normal deposition, which is why some of the STM literature dealing with metal-on-graphite systems uses an ion-sputtered surface (usually Ar^+)[4-7; 28; 29].

Figs. 10 and 11 show incremental heating experiment #5, conducted on the post-heated surface with small clusters (0.07 ML, average height 1.6 nm). This was a lower Cu coverage than experiments #1-4 on the clean starting surface (0.51-1.1 ML). In this experiment, coarsening was apparent at 700 K, in agreement with the experiments on the clean surface, but the change in average cluster height between 300 K and 700 K was relatively smaller (1.6 to 1.8 nm as shown in Fig. 12 compared with 2.6 to 4.3 nm for experiment #2 in Fig. 5). Surface coverage decreased in the range 800-900 K as with experiments on the clean surface.

Because the post-heated surface allows us to create Cu clusters of any size, it is a perfect system for studying the early stages of Cu cluster growth. An experiment was designed to form very small Cu clusters. To accomplish this, a post-heated surface with a defect density of 1.0×10^{-3} defects/nm^2 was exposed to a total Cu flux of 1×10^{-3} ML (based on flux calculated from a previous experiment). Based on the closed-packed surface geometry of fcc Cu with an atomic diameter of 0.255 nm, 1 ML ≈ 20 atoms/nm^2.

$(20 \text{ atoms/nm}^2)(1 \times 10^{-3})(1 \times 10^3 \text{ nm}^2/\text{defect}) \approx 20 \text{ atoms/defect} \approx 20 \text{ atoms/cluster}$

STM images of this surface are shown in Fig. 20. The Cu clusters were difficult to image, which probably indicates that the Cu atoms were arranged 3-dimensionally relative to the surface. Fig. 20(b) shows zoomed-in images of the small Cu clusters. The cluster corresponding to the line profile in Fig. 20b′ is likely 4-6 atoms high (1.2 nm) with the spike at the front edge likely a tip effect. The clusters in Fig. 20(b″) are probably 1-3 atoms (0.3-0.6 nm) high and 3-4 atoms (0.9 nm) high, respectively. The elongation of all clusters in the vertical direction is probably a tip effect which is more indicative of tip shape than cluster shape. This experiment indicates that Cu clusters assume a 3D arrangement at the earliest stages of cluster growth, contra to Ganz et al.[30], who reported STM images of 2D Au and Ag clusters on the graphite terrace, and also contra to Arthur and Cho[1], whose Cu/HOPG adsorption data fit well with an initial 2D growth model.

4.6 Conclusions

We have conducted experiments to examine the behavior of Cu on HOPG deposited at 300 K and heated incrementally up to 1300 K. Significant coarsening began between 600 K and 700 K. Desorption, marked by a decrease in surface coverage, begins between 800 K and 900 K and is substantially complete by 1200 K. The post-heated Cu/HOPG surface reveals ion-induced defects which have a number density approximately equal to the initial density of Cu clusters on the surface. Re-depositing Cu on the post-heated surface allows us to produce populations of very small Cu clusters. An experiment was conducted to image Cu clusters containing an average of 20 atoms. Based on the apparent height of these clusters (variable from 0.3 to 1.2 nm), we conclude that Cu cluster on HOPG adopt a 3D configuration even at the earliest stages of growth at defect sites.

Acknowledgements

This work was supported by the Office of Science, Basic Energy Sciences, Materials Sciences and Engineering Division of the U.S. Department of Energy (USDOE), under Contract No. DE–AC02–07CH11358 with the U.S. Department of Energy. We thank Jim Anderegg for his contribution of HOPG substrates.

References

[1] J.R. Arthur, A.Y. Cho, Surface Science 36 (1973) 641-660.

[2] C.M. Wayman, T.P. Darby, Journal of Crystal Growth 28 (1975) 53-67.

[3] R. Anton, P. Kreutzer, Physical Review B 61 (2000) 16077.

[4] A. Stabel, K. Eichhorst-Gerner, J.P. Rabe, A.R. González-Elipe, Langmuir 14 (1998) 7324-7326.

[5] A.R. Howells, L. Hung, G.S. Chottiner, D.A. Scherson, Solid State Ionics 150 (2002) 53-62.

[6] R.M. Nielsen, S. Murphy, C. Strebel, M. Johansson, J.H. Nielsen, I. Chorkendorff, Surface Science 603 (2009) 3420-3430.

[7] I.N. Kholmanov, L. Gavioli, M. Fanetti, M. Casella, C. Cepek, C. Mattevi, M. Sancrotti, Surface Science 601 (2007) 188-192.

[8] M. Caragiu, S. Finberg, Journal of Physics: Condensed Matter 17 (2005) R995.

[9] M. Büttner, P. Choudhury, J. Karl Johnson, J.T. Yates Jr, Carbon 49 (2011) 3937-3952.

[10] G.V. Prudnikova, A.G. Vjatkin, A.V. Ermakov, A.M. Shikin, V.K. Adamchuk, Journal of Electron Spectroscopy and Related Phenomena 68 (1994) 427-430.

[11] Physics and Chemistry of Materials with Layered Structures, D. Reidel Publishing Company, 1979.

[12] M.E. T. E. Weller, S. S. Saxena, R. P. Smith, N. T. Skipper, Nat Phys 1 (2005) 39.

[13] G. Sirokmán, Á. Mastalir, Á. molnár, M. Bartók, Z. Schay, L. Guczi, Carbon 28 (1990) 35-42.

[14] A.M. Shikin, G.V. Prudnikova, V.K. Adamchuk, F. Moresco, K.H. Rieder, Physical Review B 62 (2000) 13202-13208.

[15] Y.S. Dedkov, A.M. Shikin, V.K. Adamchuk, S.L. Molodtsov, C. Laubschat, A. Bauer, G. Kaindl, Physical Review B 64 (2001) 035405.

[16] A.G. Starodubov, Medvetski, icaron, M. A., A.M. Shikin, V.K. Adamchuk, Physics of the Solid State 46 (2004) 1340-1348.

[17] L. Huang, Y. Pan, M. Gao, W. Xu, Y. Que, H. Zhou, Y. Wang, S. Du, H.-J. Gao, Appl. Phys. Lett. 99 (2011).

[18] R. Addou, A. Dahal, M. Batzill, Surface Science 606 (2012) 1108-1112.

[19] J.G. Kushmerick, K.F. Kelly, H.P. Rust, N.J. Halas, P.S. Weiss, Physical Chemistry B 103 (1999).

[20] J.R. Hahn, H. Kang, Physical Review B 60 (1999) 6007-6017.

[21] W.-T. Pong, C. Durkan, Journal of Physics D: Applied Physics 38 (2005).

[22] D.L. Patrick, V.J. Cee, J. Thomas P. Beebe, Science 265 (1994).

[23] F. Stevens, L.A. Kolodny, T.P. Beebe, The Journal of Physical Chemistry B 102 (1998) 10799-10804.

[24] Y.-J. Zhu, T.A. Hansen, S. Ammermann, J.D. McBride, T.P. Beebe, The Journal of Physical Chemistry B 105 (2001) 7632-7638.

[25] Y. Zhu, J.D. McBride, T.A. Hansen, J. Thomas P. Beebe, J. Phys. Chem. B 105 (2001) 2010-2018.

[26] Y.-J. Zhu, A. Schnieders, J.D. Alexander, T.P. Beebe, Langmuir 18 (2002) 5728-5733.

[27] M. Lukas, V. Meded, A. Vijayaraghavan, L. Song, P.M. Ajayan, K. Fink, W. Wenzel, R. Krupke, Nat Commun 4 (2013) 1379.

[28] G.W. Clark, L.L. Kesmodel, Journal of Vacuum Science & Technology B: Microelectronics and Nanometer Structures 11 (1993) 131-136.

[29] I. Lopez-Salido, D.C. Lim, Y.D. Kim, Surface Science 588 (2005) 6-18.

[30] E. Ganz, K. Sattler, J. Clarke, Surface Science 219 (1989) 33-67.

Tables

Table 1
A comparison of initial Cu cluster density to final residue density after heating the Cu/HOPG surface to 1200-1300 K.

Experiment	Initial Cluster Density (nm^{-2})	Final Residue Density (nm^{-2})
1	$2.4 \pm 0.2 \quad x10^{-4}$	$1.5 \pm 0.2 \quad x10^{-4}$
2	$4.9 \pm 0.4 \quad x10^{-4}$	$3.2 \pm 0.3 \quad x10^{-4}$
3	$10.7 \pm 0.8 \quad x10^{-4}$	$6.8 \pm 0.7 \quad x10^{-4}$
4	$113.0 \pm 2.5 \quad x10^{-4}$	$100.8 \pm 1.8 \quad x10^{-4}$
5	$184.1 \pm 5.4 \quad x10^{-4}$	$191.8 \pm 5.8 \quad x10^{-4}$

Figures

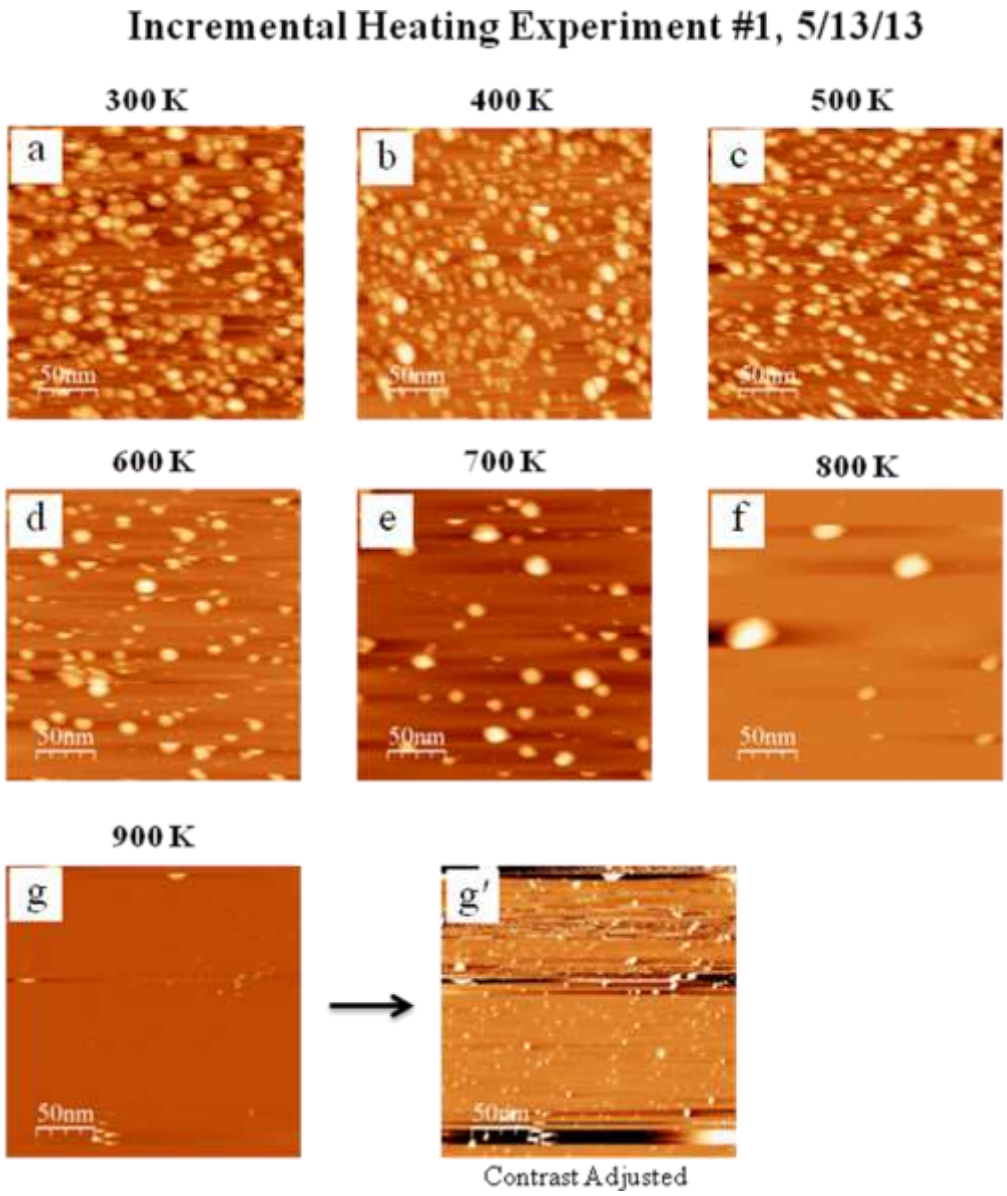

Fig. 1
STM images from incremental heating experiment #1, after initial deposition of 1.1 ML Cu on HOPG ZYA and annealing to (a) 300 K, V_{tip} = -1.5 V, *i* = 0.5 nA; (b) 400 K, V_{tip} = -1.5 V, *i* = 0.5 nA; (c) 500 K, V_{tip} = -1.5 V, *i* = 0.1 nA; (d) 600 K, V_{tip} = -1.4 V, *i* = 0.1 nA; (e) 700 K, V_{tip} = -2.0 V, *i* = 0.1 nA; (f) 800 K, V_{tip} = -2.0 V, *i* = 0.1 nA; (g) 900 K, V_{tip} = -2.0 V, *i* = 0.1 nA; and (g′) 900 K, contrast adjusted from (g). All images are 250 nm x 250 nm.

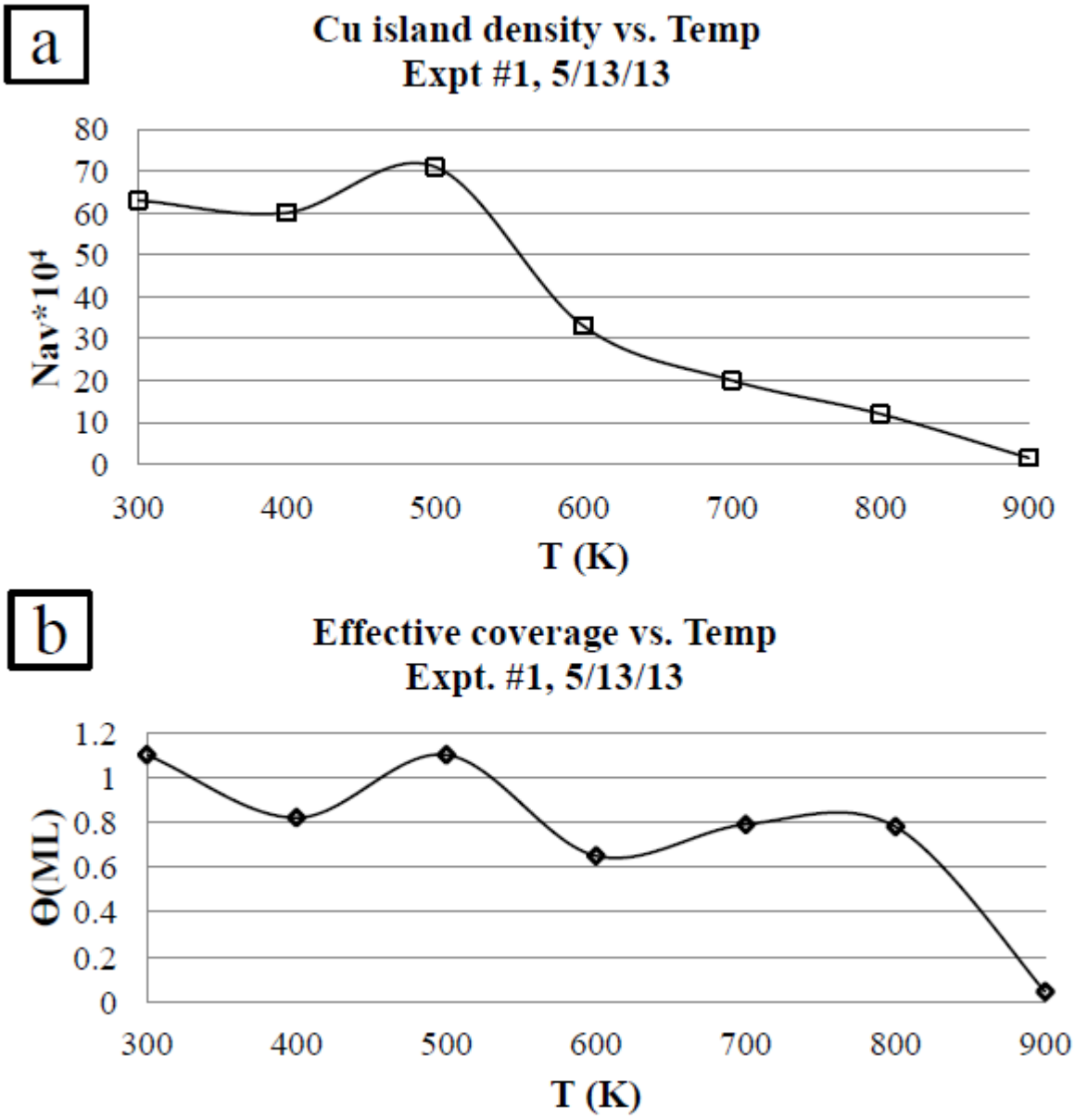

Fig. 2
Plots of (a) $N_{av.}$ vs. T; and (b) Θ vs. T for incremental heating experiment #1.

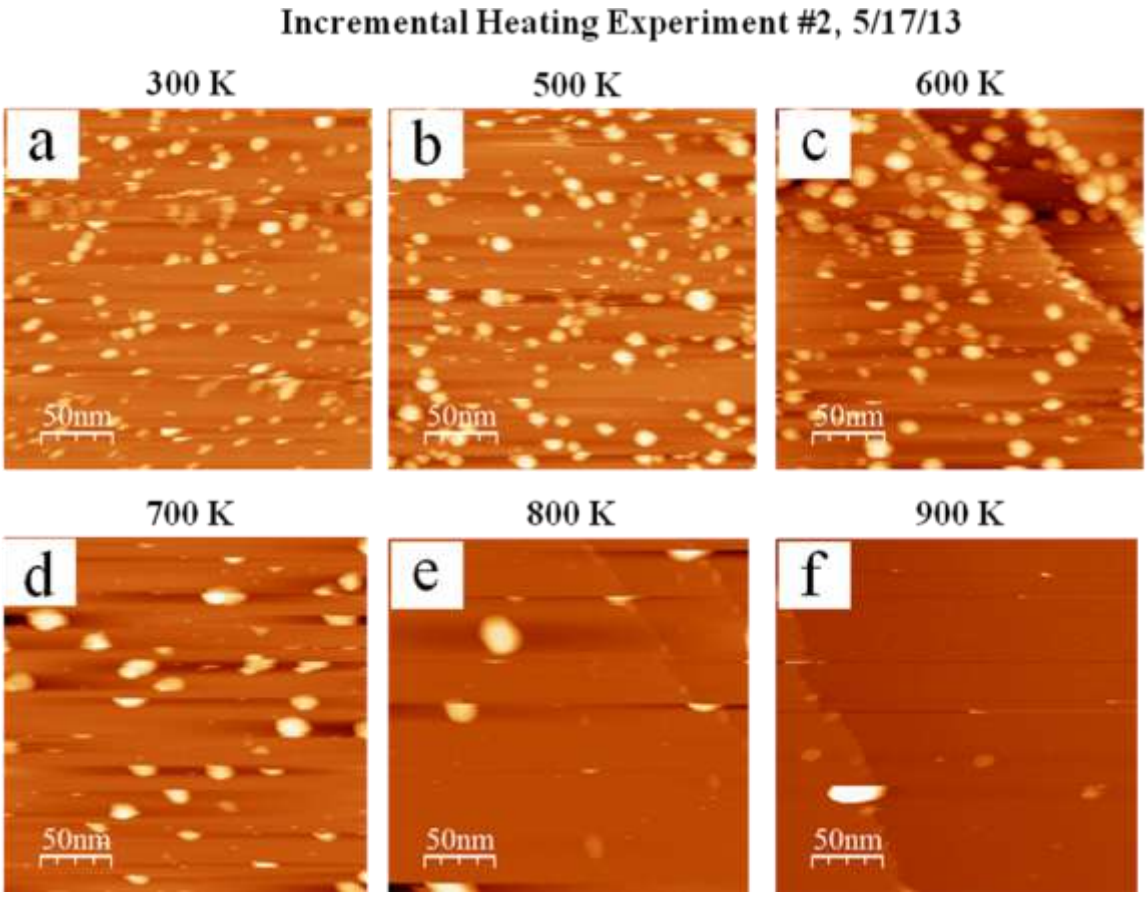

Fig. 3
STM images from incremental heating experiment #2, after initial deposition of 0.51 ML Cu on HOPG ZYA and annealing to (a) 300 K, V_{tip} = -1.5 V, *i* = 0.3 nA; (b) 500 K, V_{tip} = -1.5 V, *i* = 0.1 nA; (c) 600 K, V_{tip} = -1.5 V, *i* = 0.1 nA; (d) 700 K, V_{tip} = -1.5 V, *i* = 0.1 nA; (e) 800 K, V_{tip} = -1.5 V, *i* = 0.1 nA; and (f) 900 K, V_{tip} = -1.5 V, *i* = 0.05 nA. All images are 250 nm x 250 nm.

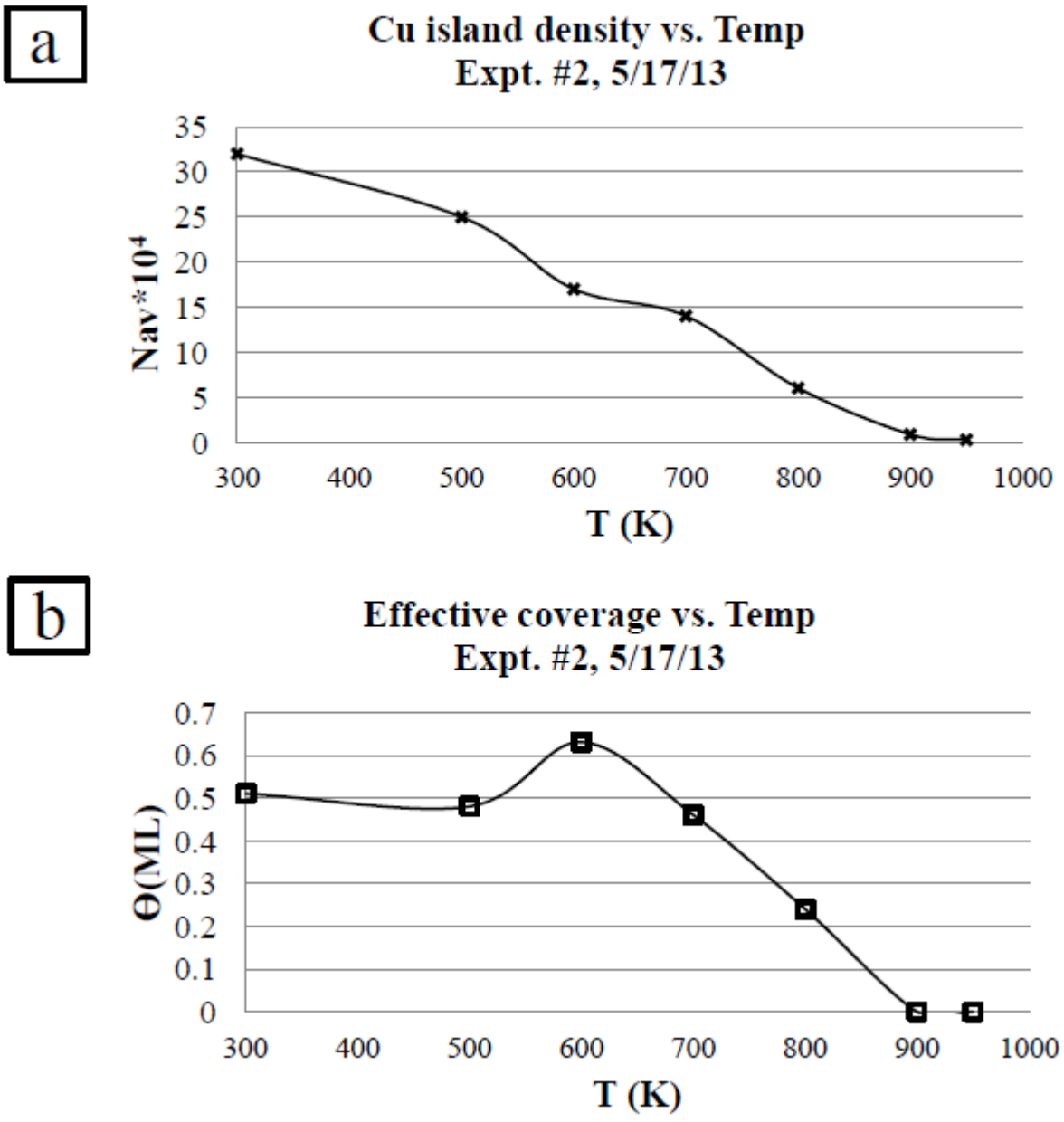

Fig. 4
Plots of (a) N_{av}. vs. T; and (b) Θ vs. T for incremental heating experiment #2.

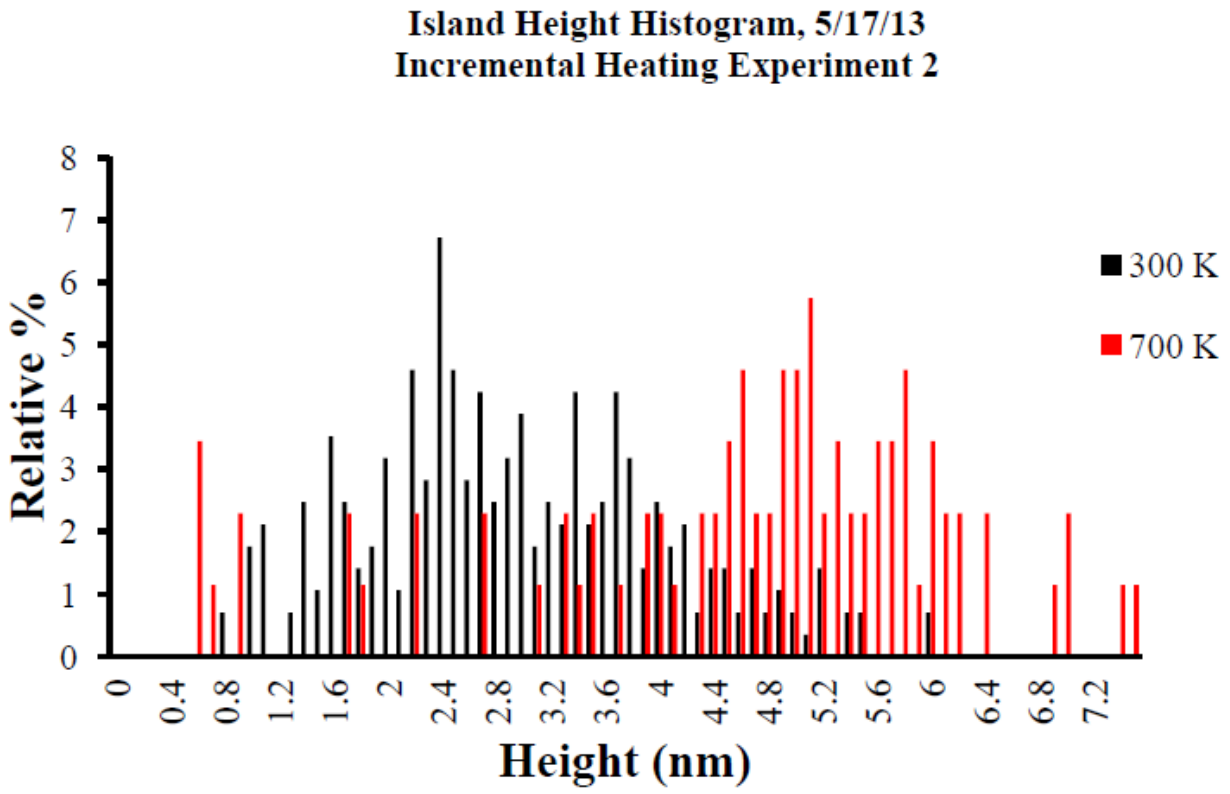

Fig. 5
Island height histogram for the 300 K and 700 K Cu island populations from heating experiment #2.

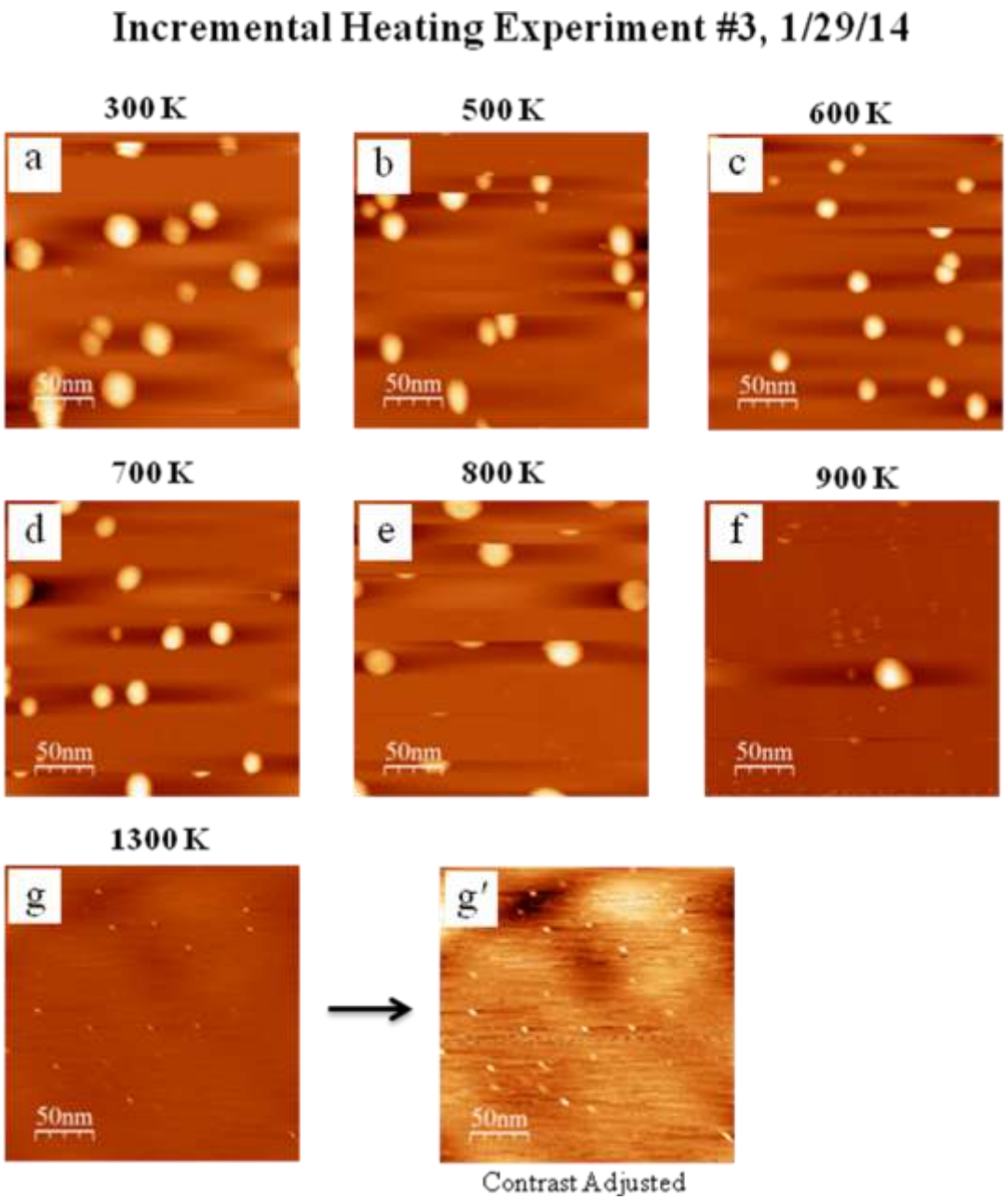

Fig. 6
STM images from incremental heating experiment #3, after initial deposition of 1.0 ML Cu on HOPG ZYA and annealing to (a) 300 K, V_{tip} = -2.0 V, i = 0.1 nA; (b) 500 K, V_{tip} = -2.0 V, i = 0.1 nA; (c) 600 K, V_{tip} = -2.0 V, i = 0.1 nA; (d) 700 K, V_{tip} = -2.0 V, i = 0.1 nA; (e) 800 K, V_{tip} = -2.0 V, i = 0.1 nA; (f) 900 K, V_{tip} = -2.0 V, i = 0.1 nA; (g) 1300 K, V_{tip} = -0.2 V, i = 0.2 nA; and (g′) 1300 K, contrast adjusted from (g). All images are 250 nm x 250 nm.

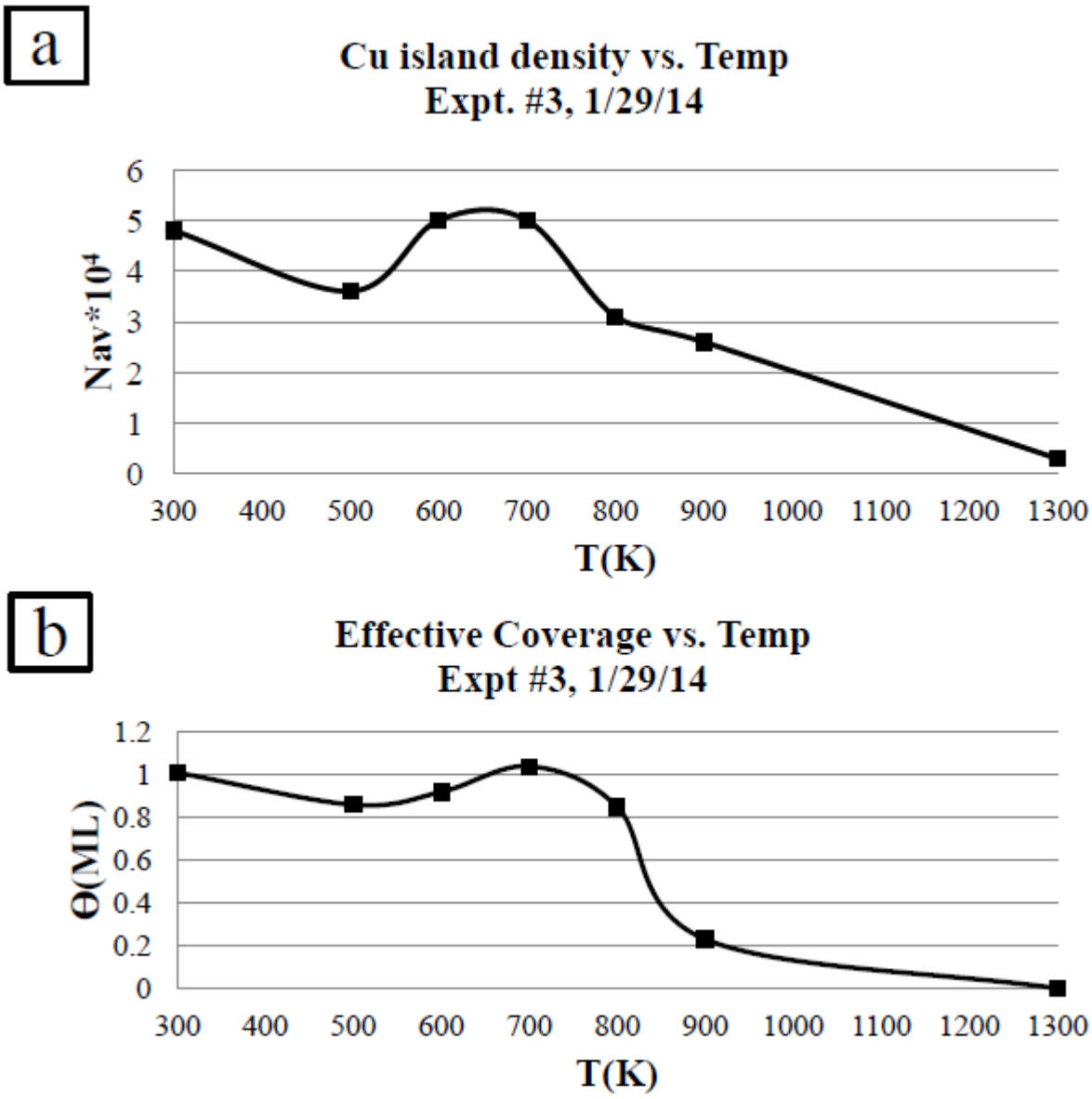

Fig. 7
Plots of (a) $N_{av.}$ vs. T; and (b) Θ vs. T for incremental heating experiment #3.

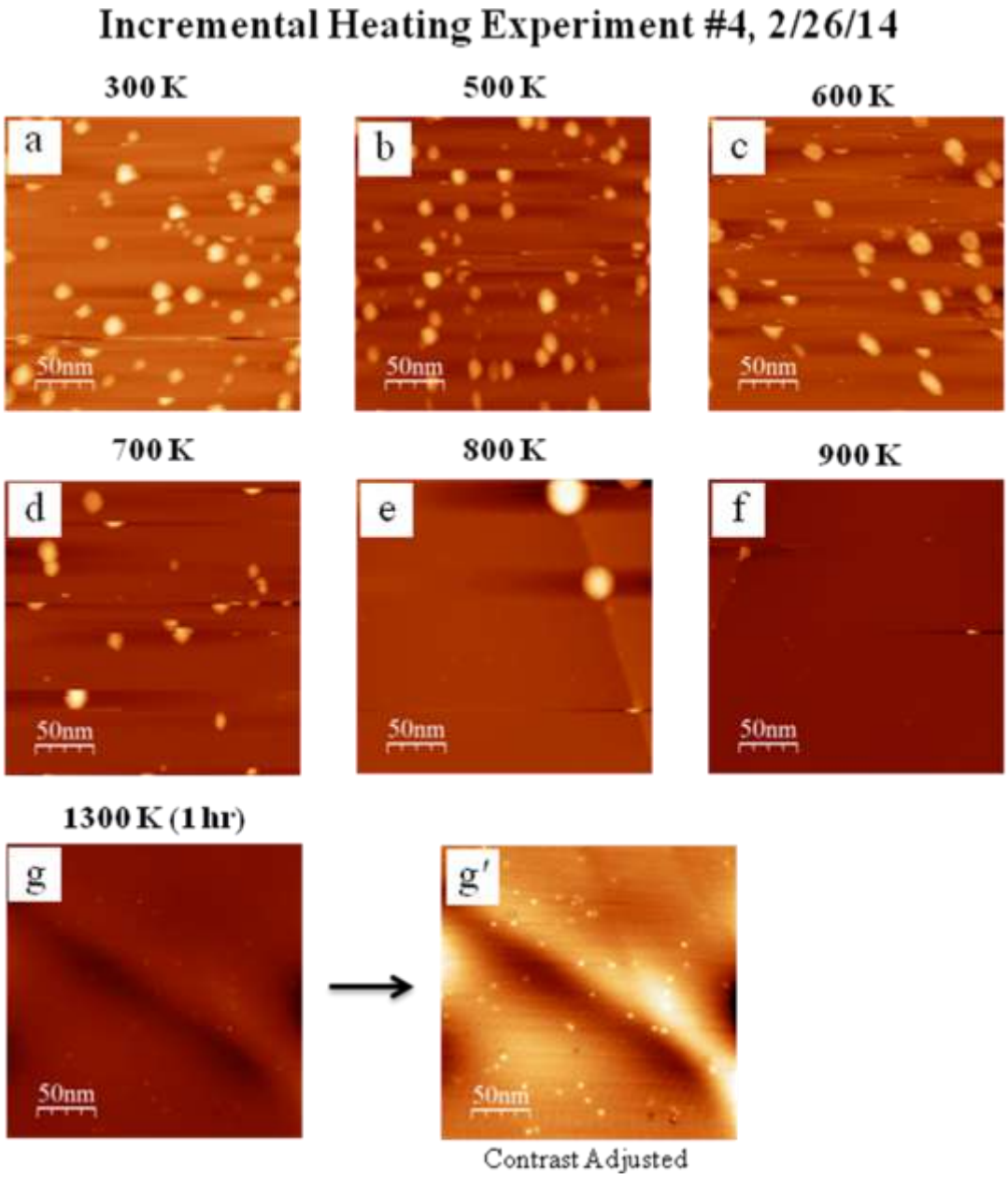

Fig. 8
STM images from incremental heating experiment #4, after initial deposition of 0.60 ML Cu on HOPG ZYA and annealing to (a) 300 K, V_{tip} = -1.5 V, *i* = 0.05 nA; (b) 500 K, V_{tip} = -1.5 V, *i* = 0.05 nA; (c) 600 K, V_{tip} = -1.5 V, *i* = 0.05 nA; (d) 700 K, V_{tip} = -1.0 V, *i* = 0.05 nA; (e) 800 K, V_{tip} = -1.5 V, *i* = 0.05 nA; (f) 900 K, V_{tip} = -1.5 V, *i* = 0.05 nA; (g) 1300 K (1 hr), V_{tip} = -0.6 V, *i* = 0.3 nA; and (g′) 1300 K, contrast adjusted from (g). All images are 250 nm x 250 nm.

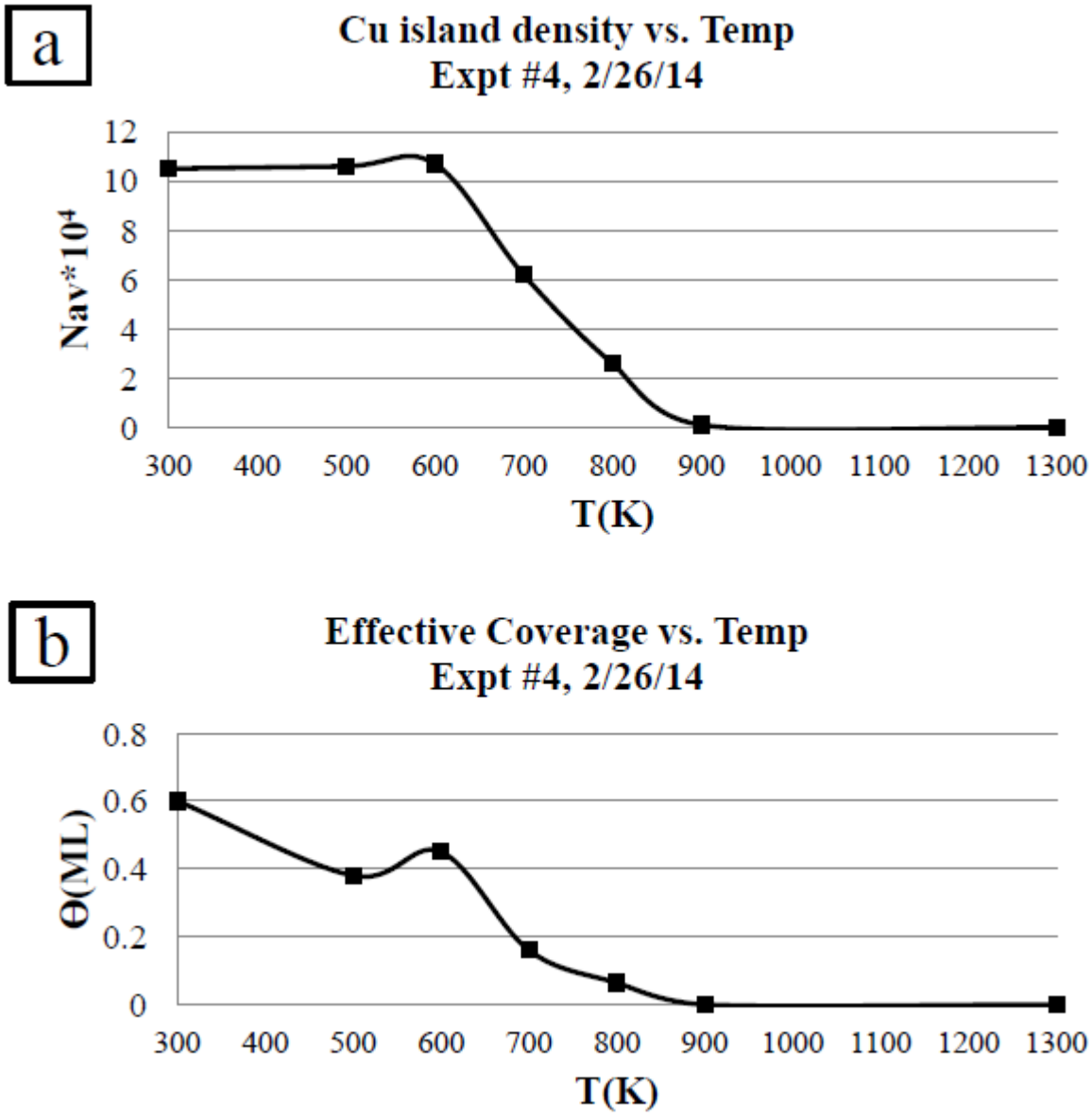

Fig. 9
Plots of (a) $N_{av.}$ vs. T; and (b) Θ vs. T for incremental heating experiment #4.

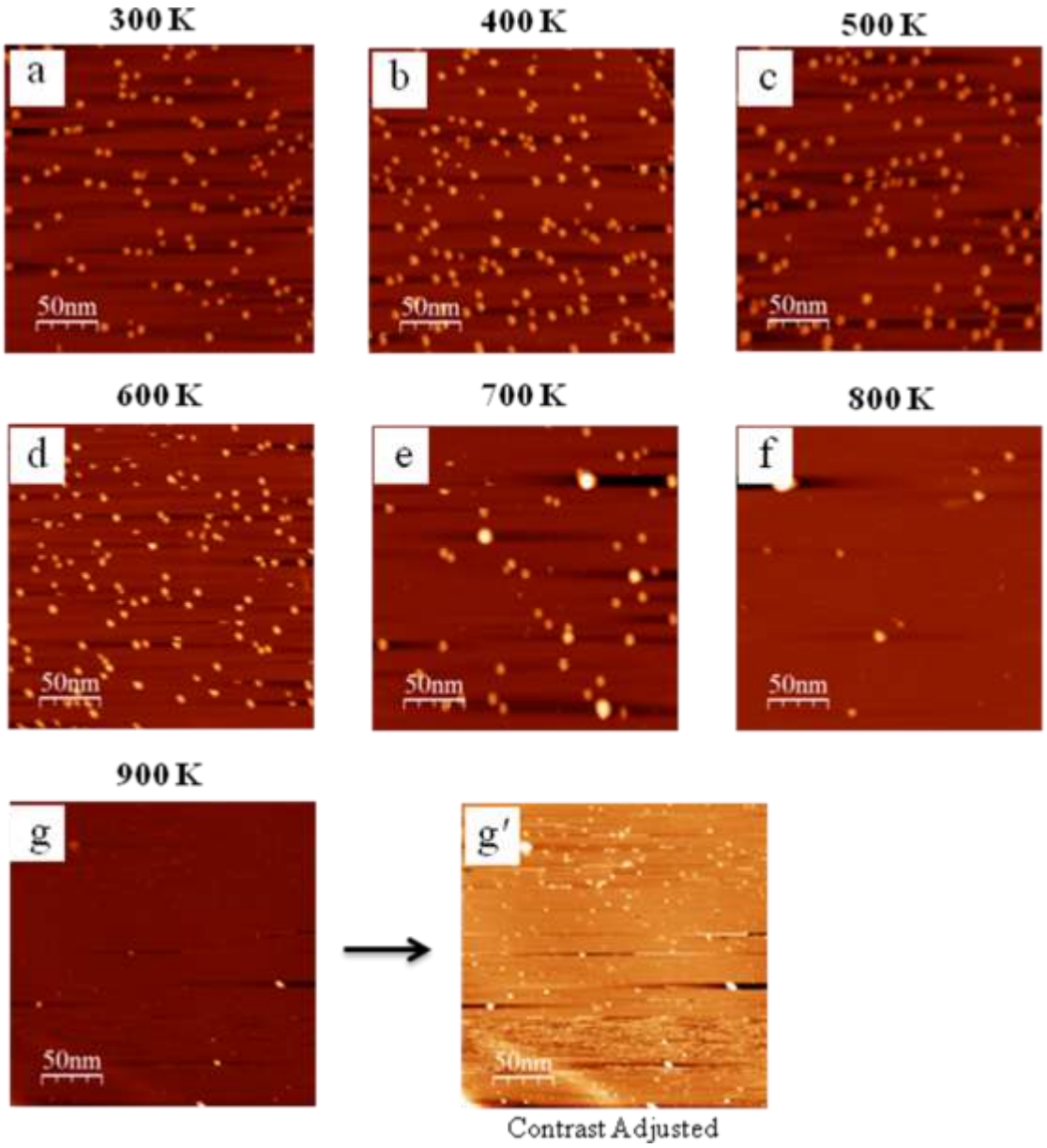

Fig. 10
STM images from incremental heating experiment #5, after initial deposition of 0.07 ML Cu on HOPG ZYA (post-heated surface) and annealing to (a) 300 K, V_{tip} = -1.5 V, *i* = 0.05 nA; (b) 400 K, V_{tip} = -1.5 V, *i* = 0.05 nA; (c) 500 K, V_{tip} = -1.5 V, *i* = 0.05 nA; (d) 600 K, V_{tip} = -1.5 V, *i* = 0.05 nA; (e) 700 K, V_{tip} = -1.5 V, *i* = 0.05 nA; (f) 800 K, V_{tip} = -2.5 V, *i* = 0.02 nA; (g) 900 K, V_{tip} = -2.5 V, *i* = 0.05 nA; and (g′) 900 K, contrast adjusted from (g). All images are 250 nm x 250 nm.

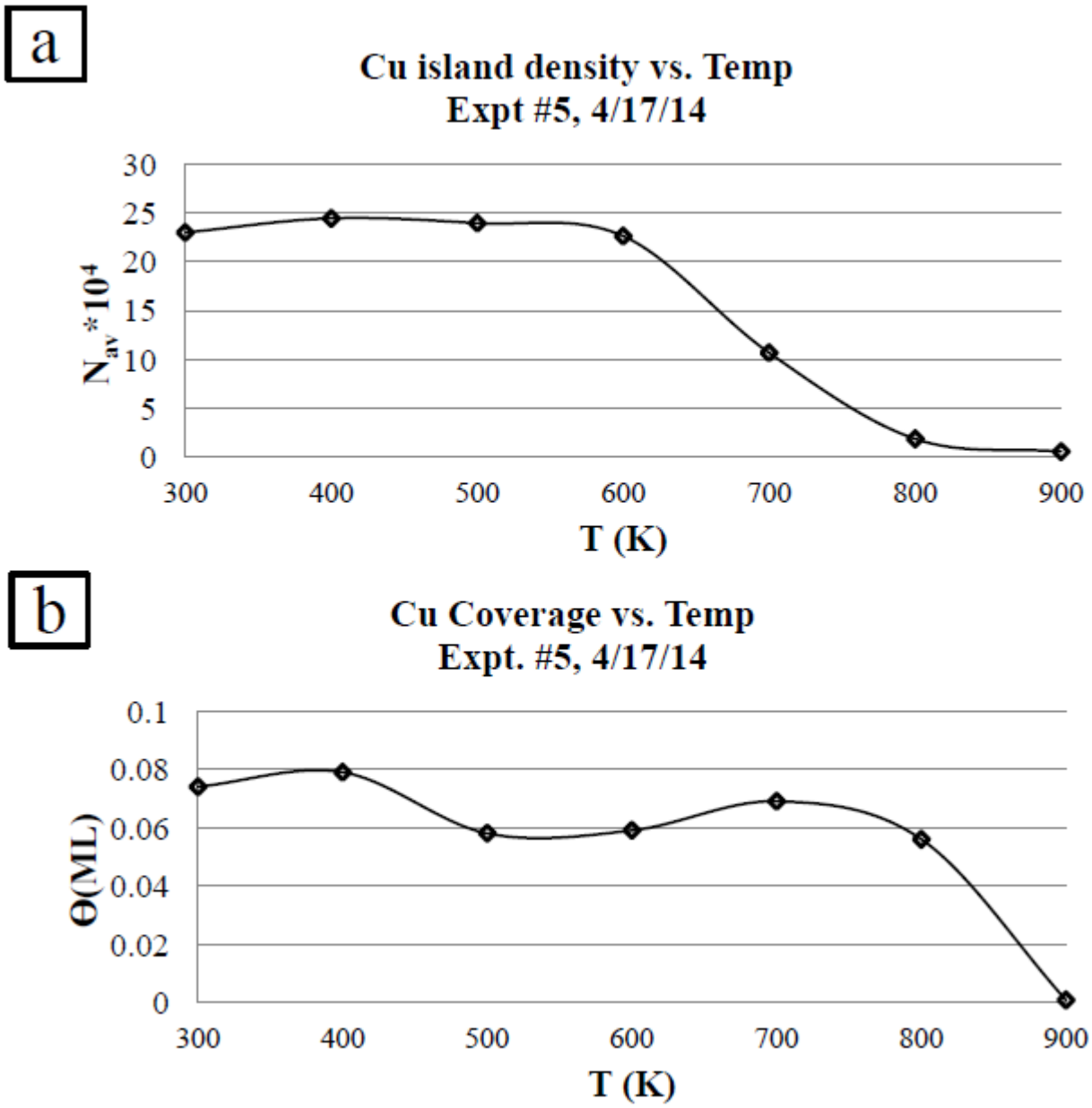

Fig. 11
Plots of (a) N_{av}. vs. T; and (b) Θ vs. T for incremental heating experiment #5.

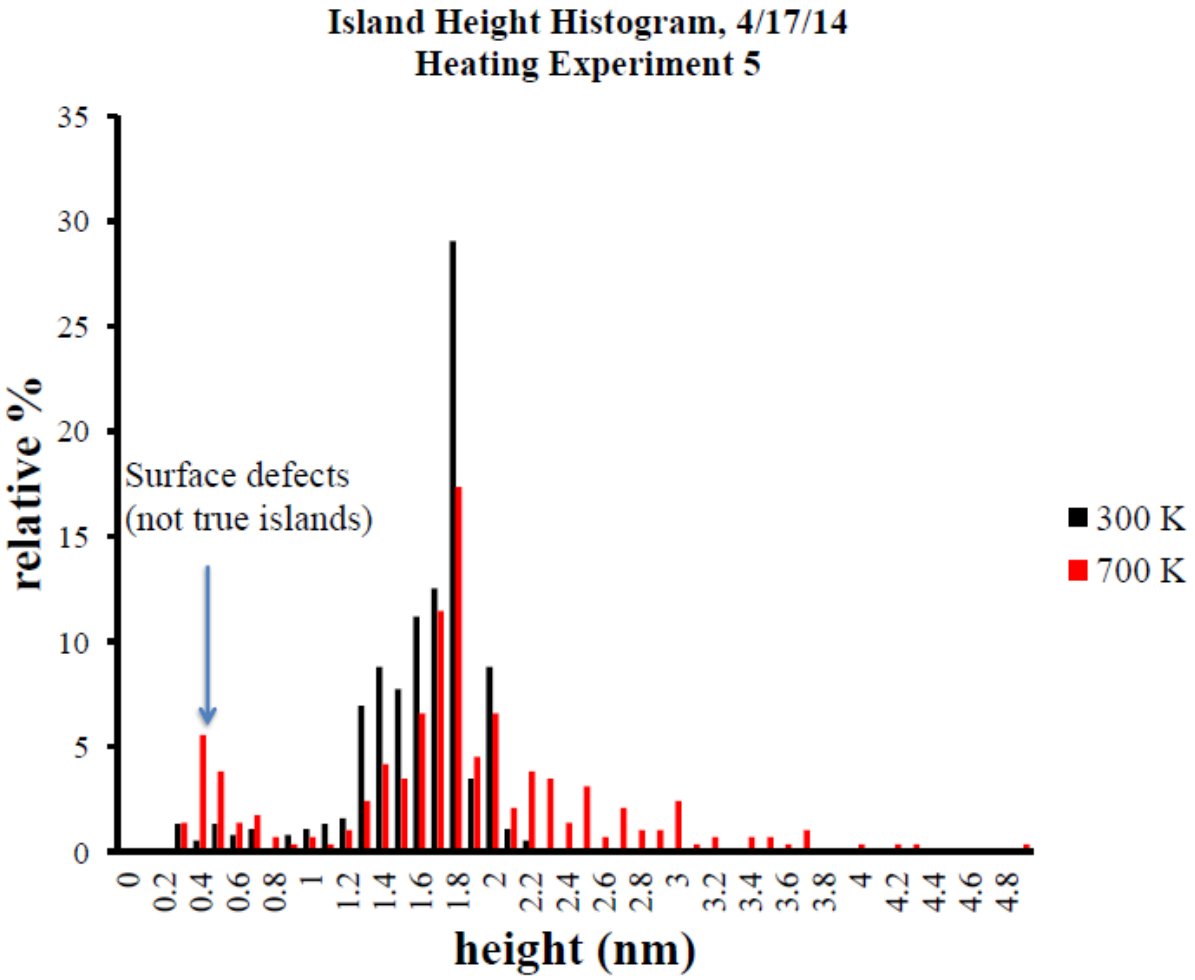

Fig. 12
Island height histogram for the 300 K and 700 K Cu island populations from heating experiment #5.

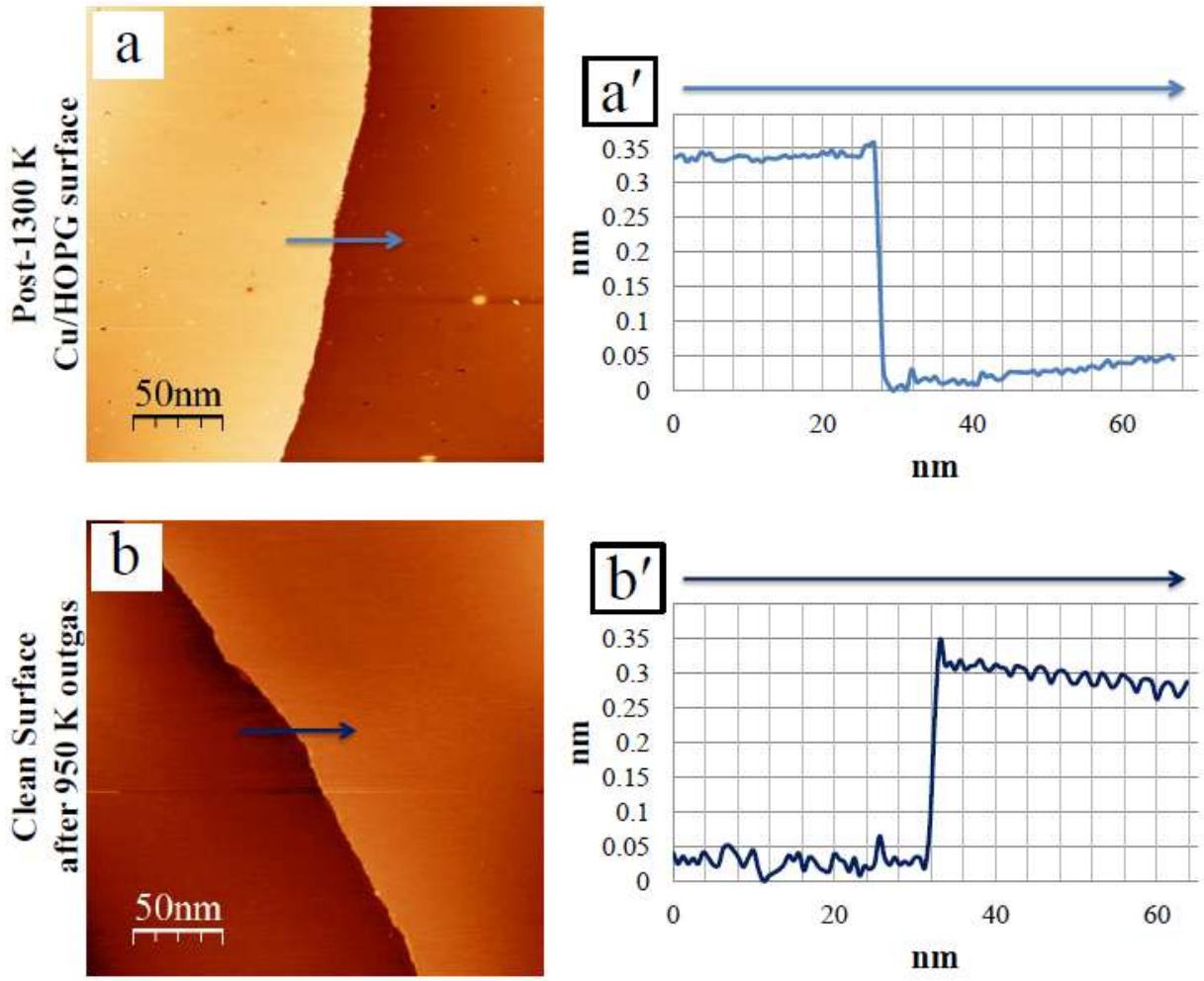

Fig. 13
STM images comparing step edge decoration between (a) a Cu/HOPG surface after heating to 1300 K for 1 hour, V_{tip} = -0.6 V, i = 0.2 nA; and (b) a clean HOPG surface after outgassing at 950 K, V_{tip} = -0.5 V, i = 0.2 nA. The respective line profiles are shown in (a′) and (b′). All images are 250 nm x 250 nm.

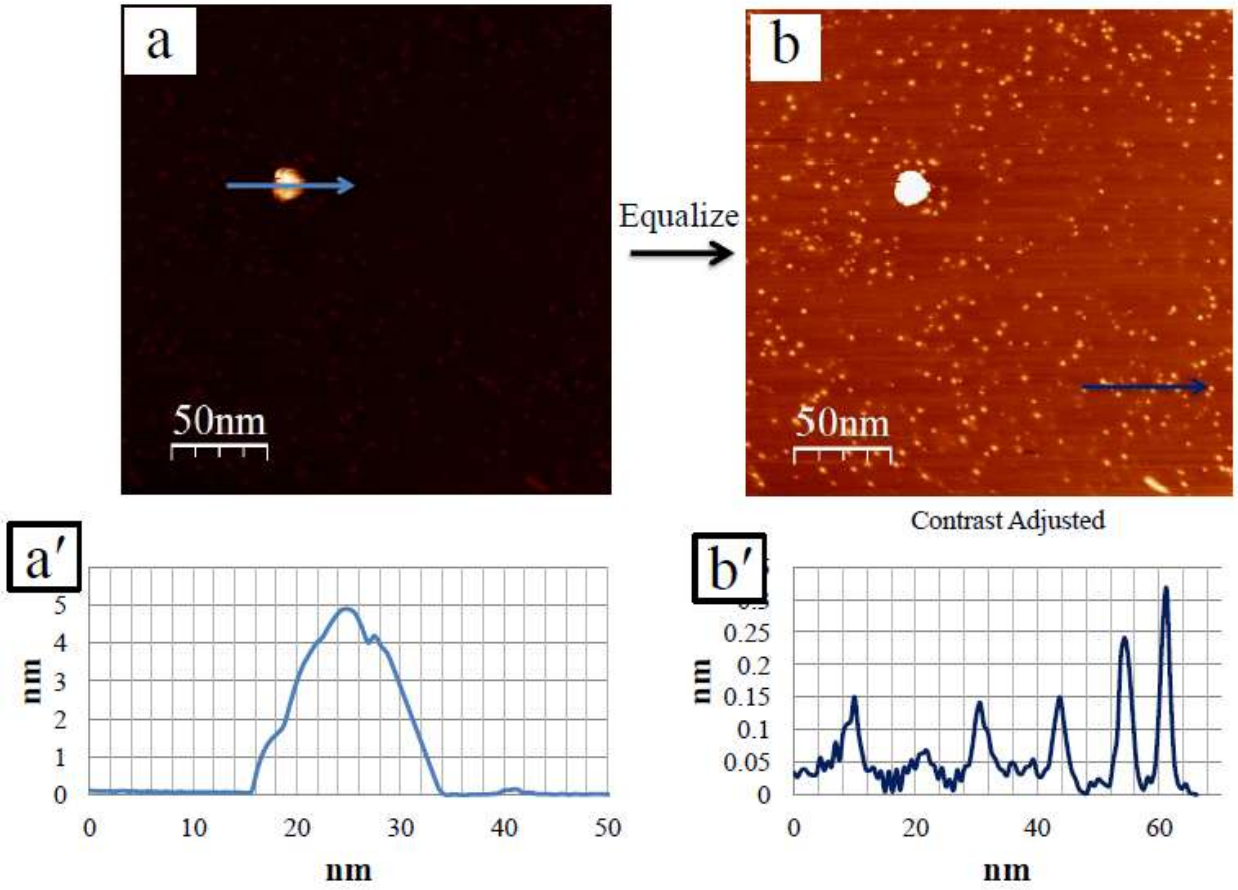

Fig. 14
(a) STM image of the Cu/HOPG post-heated surface after heating to 1200 K for 1.5 hours, V_{tip} = -0.2 V, *i* = 0.2 nA; (a′) line profile of a residual copper cluster from (a). (b) The same STM image, but contrast adjusted so that ion-induced defects are visible; and (b′) line profile from (b). All images are 250 nm x 250 nm.

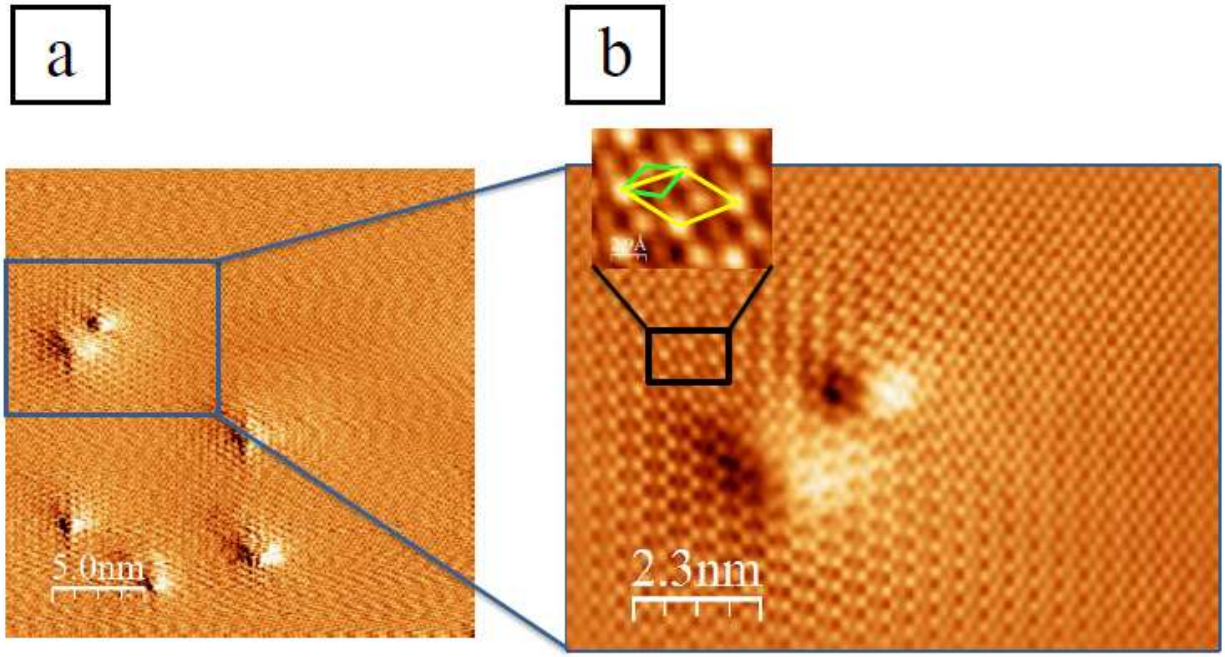

Fig. 15
(a) STM image in constant height mode of a cluster of ion-induced defects on the post-heated HOPG surface, 25 nm x 25 nm, V_{tip} = -0.1 V, *i* = 0.3 nA; and (b) zoom-in of a defect in (a), with inset showing √3 x √3 R30° scattering.

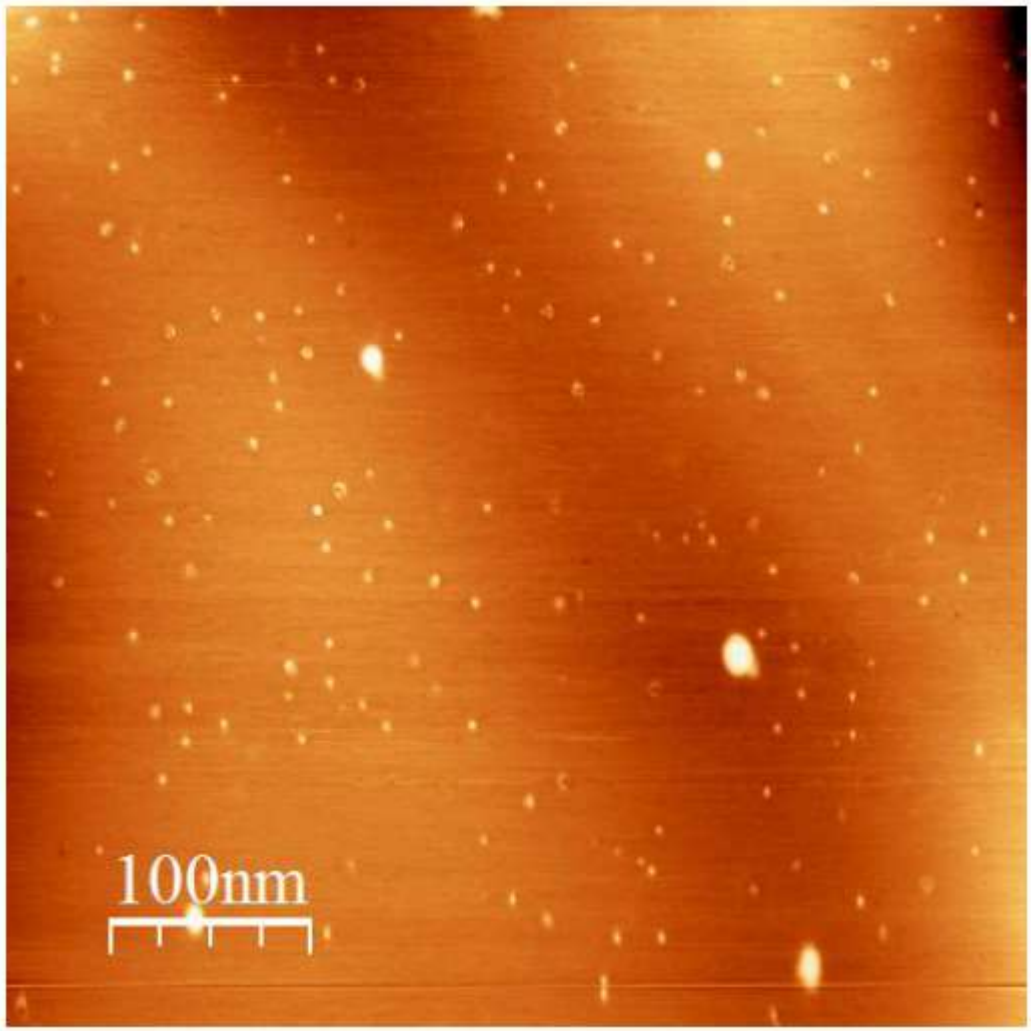

Fig. 16
STM image of the Cu/HOPG post-heated surface after heating to 1300 K for 1 hour, 500 nm x 500 nm, V_{tip} = -0.2 V, *i* = 0.3 nA.

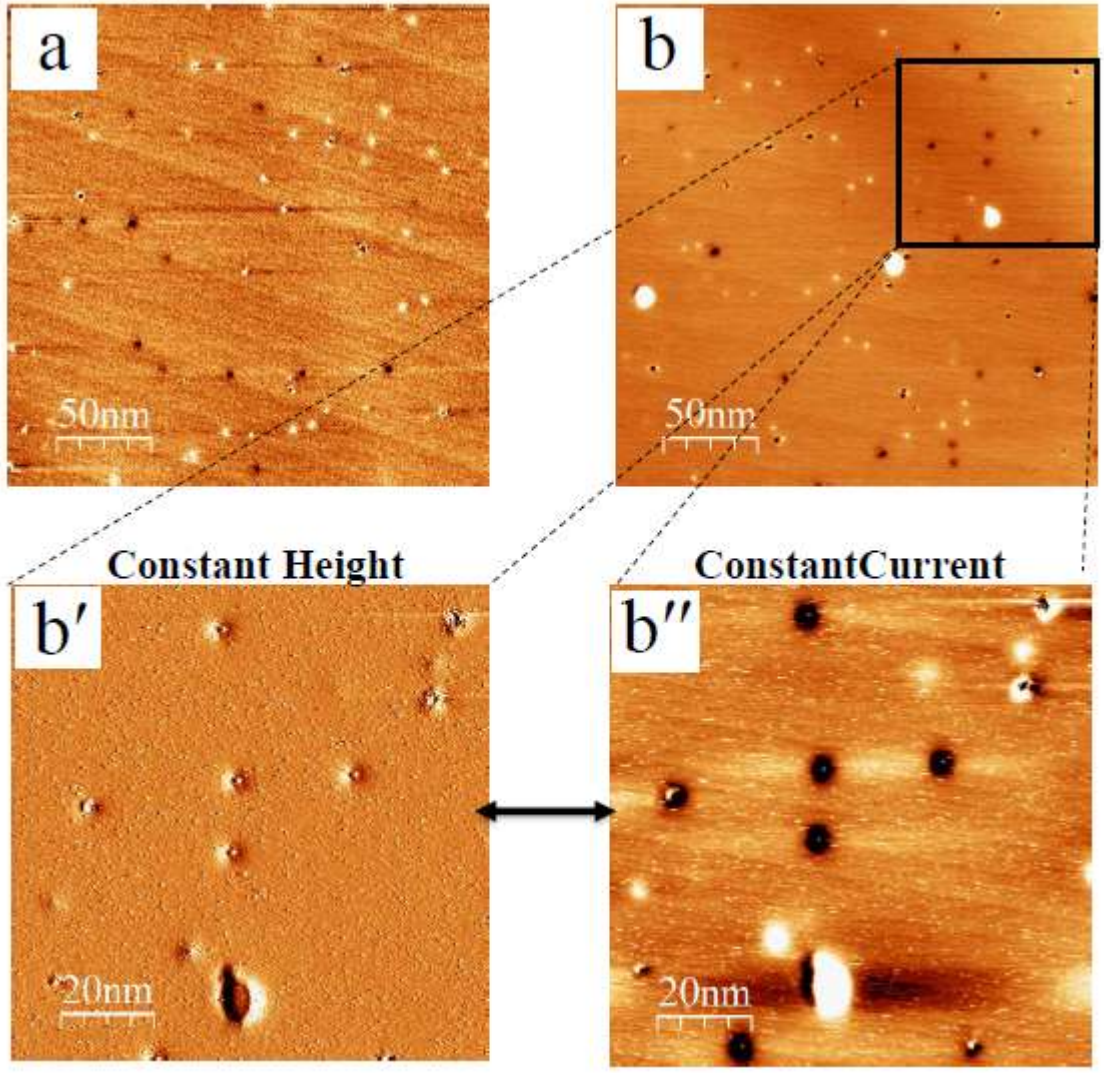

Fig. 17
STM images of the Cu/HOPG post-heated surface (1300 K); (a) 250 nm x 250 nm, V_{tip} = -0.5 V, i = 0.5 nA; (b) 250 nm x 250 nm, V_{tip} = -0.5 V, i = 0.3 nA; (b′) higher magnification of the area in (b) in constant height mode, 100 nm x 100 nm, V_{tip} = -0.5 V, i = 0.4 nA; and (b″) the same area as in (b′) but imaged in constant current mode.

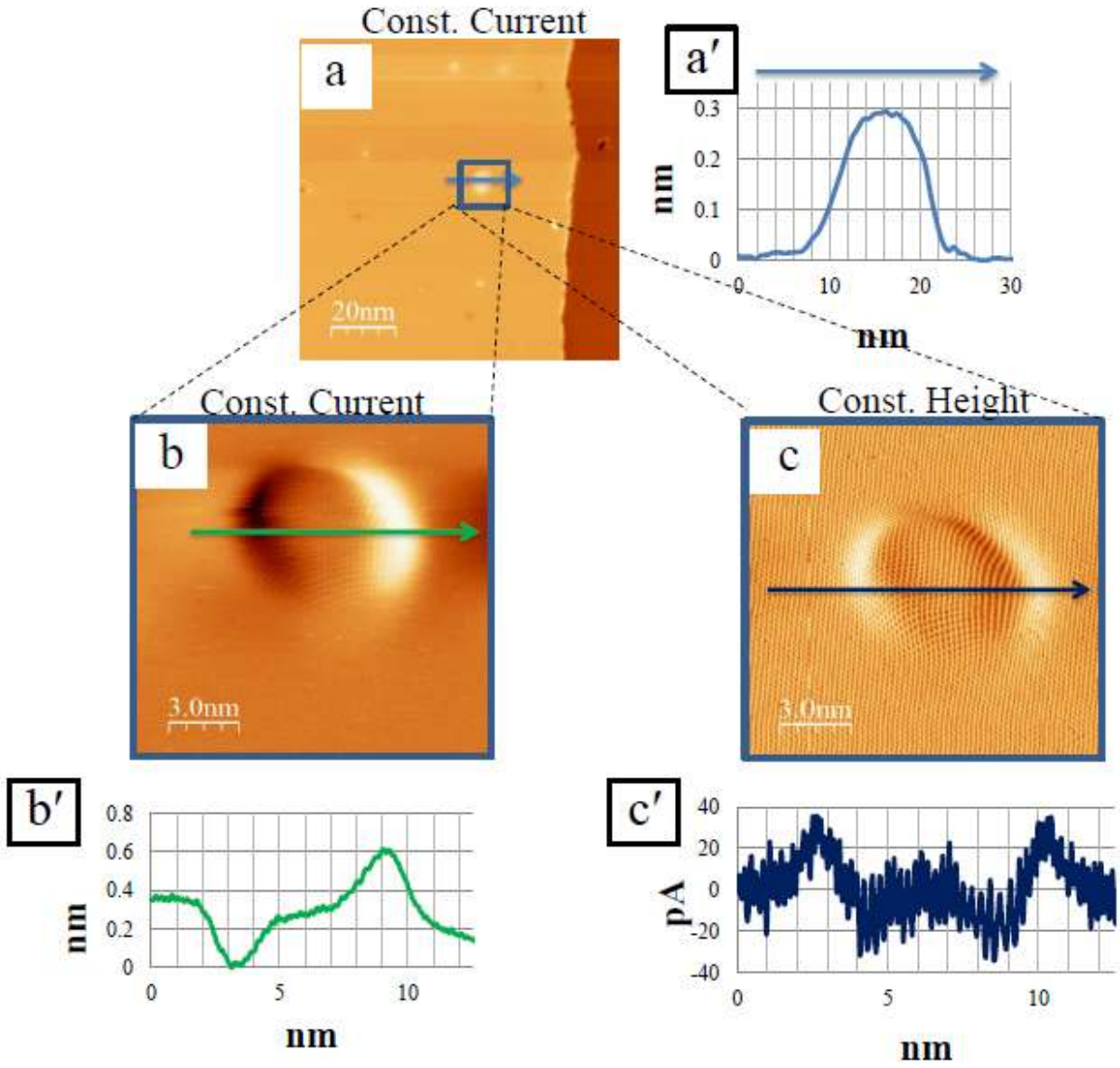

Fig. 18
(a) STM image of the Cu/HOPG post-heated surface (1300 K) taken in constant current mode, 100 nm x 100 nm, V_{tip} = -0.5 V, i = 0.2 nA; (a′) line profile of a pancake feature from (a); (b) higher-magnification image of the same pancake feature taken in constant current mode, 15 nm x 15 nm, V_{tip} = -0.4 V, i = 0.5 nA; (b′) line profile of the pancake feature from (b); (c) image of the same pancake feature as (b) taken in constant height mode, 15 nm x 15 nm, V_{tip} = -0.4 V, i = 0.5 nA; and (c′) line profile of the pancake feature from (c).

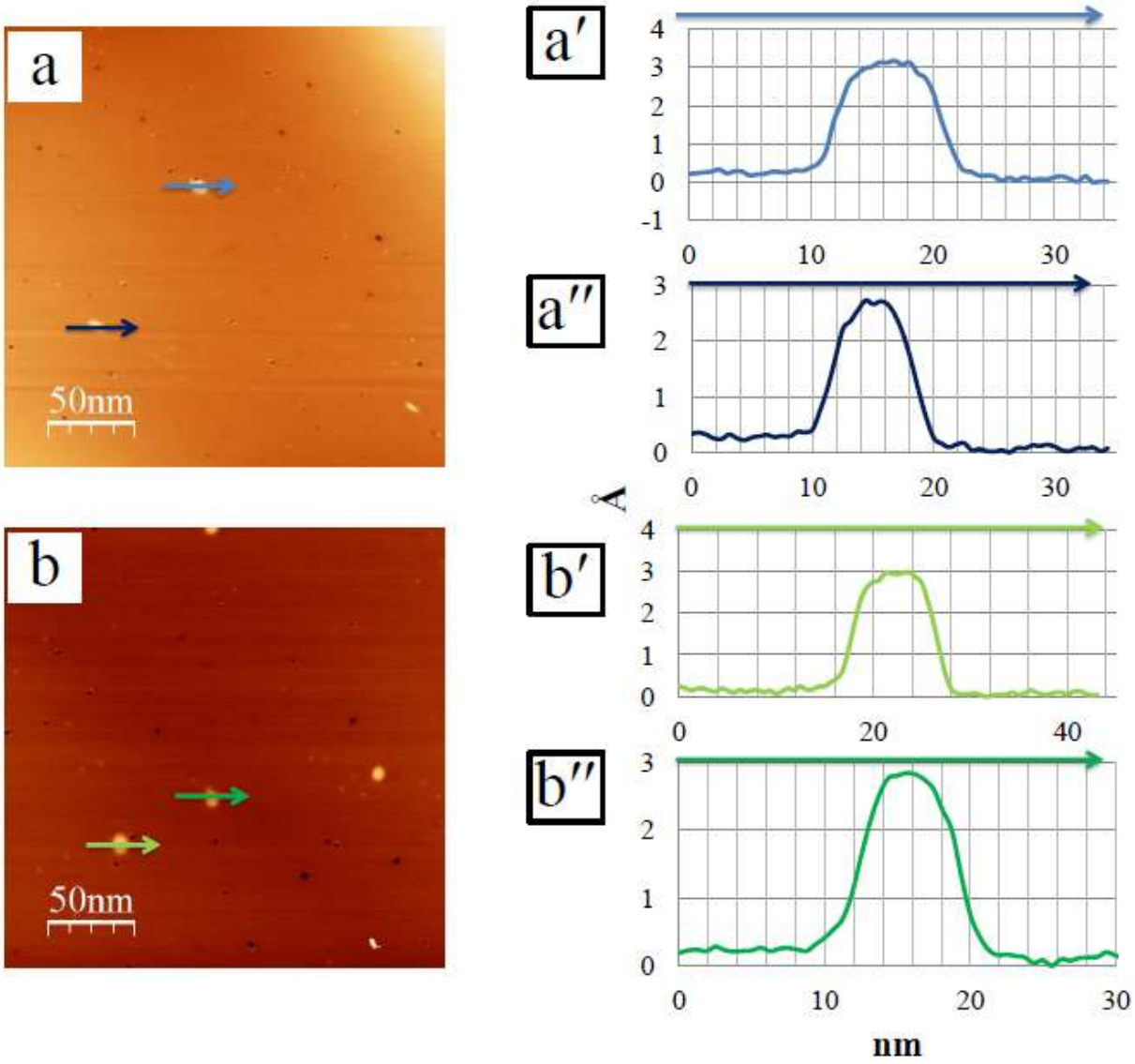

Fig. 19
STM images of the Cu/HOPG post-heated surface (1300 K) and associated line profiles of pancake features, (a) V_{tip} = -0.5 V, i = 0.4 nA; (a′-a′) line profiles from (a); (b) V_{tip} = -0.6 V, i = 0.2 nA; and (b′-b″) line profiles from (b). Both STM images are 250 nm x 250 nm.

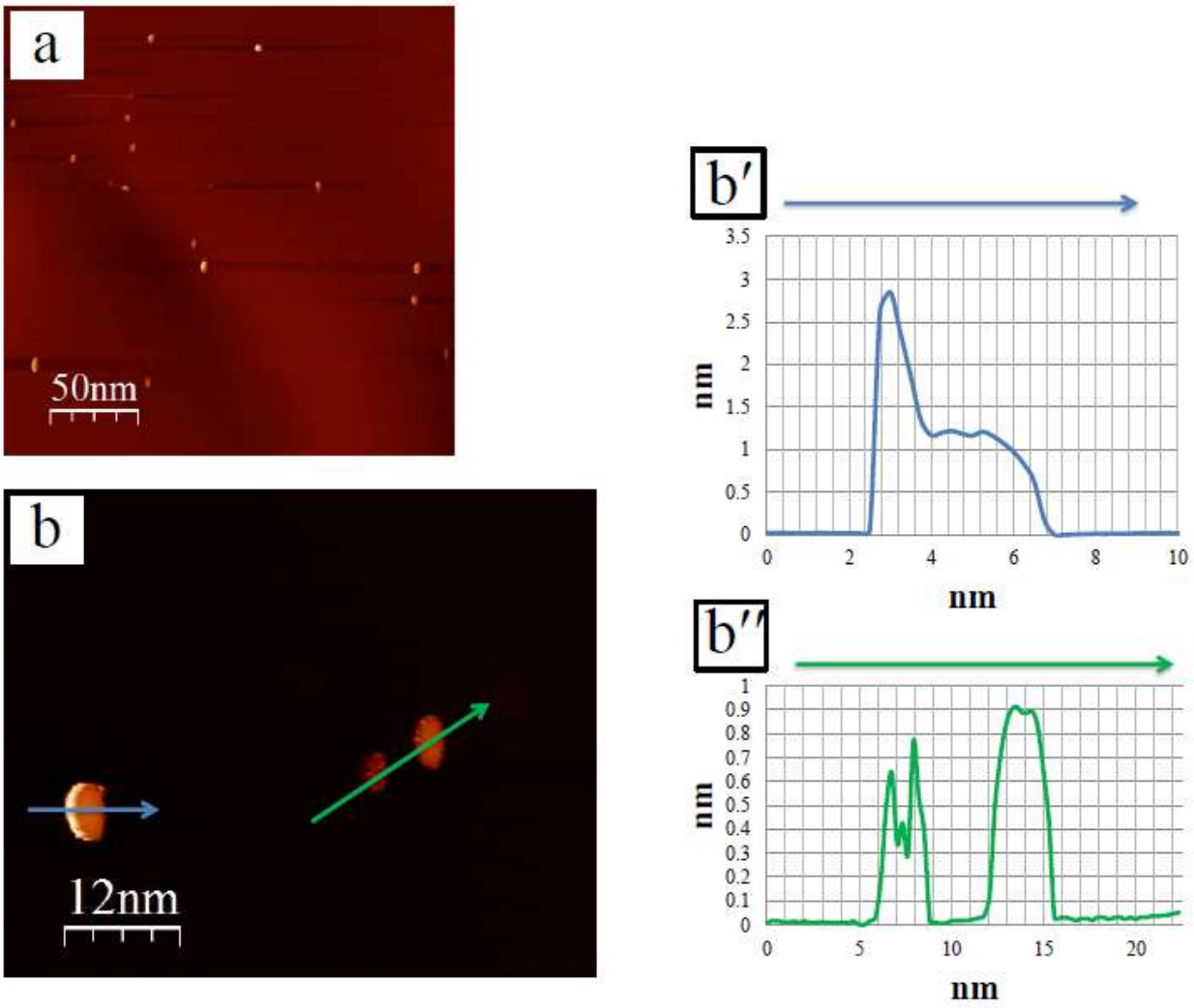

Fig. 20
(a) STM image of Cu clusters estimated to contain on average 20 atoms each, 250 nm x 250 nm, V_{tip} = -0.6 V, *i* = 0.3 nA; (b) higher magnification image of Cu clusters, 60 nm x 50 nm, V_{tip} = -0.6 V, *i* = 0.3 nA; (b′) and (b″) are line profiles from Cu clusters in (b).

CHAPTER 5

AMORPHOUS CARBON AS A SUBSTRATE FOR NANOWIRE GROWTH

5.1 Introduction – Substrate for Nanowire Growth

Our work with amorphous carbon, and metals on amorphous carbon, was motivated by the discovery of a family of metal nanowires (NW's) which grow as single crystals protruding substantially perpendicular to a substrate, as shown in Fig. 1.[1; 2] These wires are grown by physical vapor deposition (PVD) (which includes molecular beam epitaxy (MBE) as well as magnetron sputtering) of metal onto a substrate surface, with the substrate surface held at an elevated temperature ranging from 800-1100K, depending on the metal. The fabrication and properties of these wires have been pioneered by our collaborator, Dr. Gunther Richter, at the Max Planck Institute (MPI) for Intelligent Systems in Stuttgart, Germany.[1; 2] These wires have exceptional tensile strength compared with their respective bulk materials due to their pristine single crystalline nature.[3] They have potential uses in nanoscale mechanical/electrical devices, as chemical/optical sensors and, in the case of magnetic wires, non-rare-earth permanent magnets and high density magnetic storage media.[4] Chapters 5 and 6 of this thesis present a group of experiments aimed at developing an understanding of the nucleation and growth of these structures, with the ultimate goal of fine-tuning their growth with respect to aspect ratio, density, and orientation.

The most prolific nanowire growth occurs for copper deposited on Si coated with amorphous carbon (a-C). In this chapter we analyze a-C films produced by magnetron sputtering with STM and XPS.

5.2 Fabrication of the Various a-C Samples

For this study we used a-C samples produced at MPI Stuttgart by the group of Dr. Gunther Richter, as well as a-C samples produced at the Ames laboratory by Ryan Ott and Matt Besser. All a-C samples were produced by magnetron sputtering. A detailed table of the preparation and resulting a-C thickness for all samples is shown in Table 1. Methods for determining film thickness are described in Section 5.2.3, below. The preparation of the MPI samples, which were the main focus of our early STM experiments, is described graphically in Fig. 5.

5.2.1 Fabrication by magnetron sputtering

Amorphous carbon substrates in this study were formed by magnetron sputtering from a graphite target onto a silicon wafer as shown schematically in Fig. 2. Magnetron sputtering involves bombarding a target material (the material to be sputtered) with Ar^+ ions from a plasma generated above the target and sustained by magnetic confinement of electrons. A fraction of the target material is ejected as a result of the ion bombardment and condenses on the substrate.

Fig. 3 shows a schematic view of the magnetron target area. Ar plasma is ignited by applying a high voltage between the target (cathode (-)) and a surrounding shield (ground). Electrons generated in the plasma are confined above the target in a donut-shaped track by a magnetic field (generated by magnets underneath the target). The confined electrons sustain and enhance the plasma, as Ar^+ ions are accelerated toward the target. The magnetron is powered either by direct current (DC), or by a radio-frequency bias (RF). DC mode is used for conducting targets and RF mode is used for insulating or semi-conducting targets. The RF bias

quickly switches the bias on the target between (-) and ground to prevent build-up of charge. The graphite targets used for a-C fabrication in this study were powered by RF bias at 75-100 W (see Table 1). Additionally, for Ames a-C samples the substrate itself was RF biased under light power (6 W) to energize adatoms and provide them additional mobility on the substrate surface.

The MPI Stuttgart group used an ATC 1500 F magnetron system (AJA International Inc http://www.ajaint.com/systems_atc.htm) with 2" carbon targets. The Ames Laboratory group used a Kurt J. Lesker magnetron system with 3" carbon targets also purchased from Kurt J. Lesker. The base pressure in these systems is in the 10^{-8} mbar range.

5.2.2 Nature and history of the silicon substrate

The properties of the silicon wafer itself were non-critical to NW growth, or at least, the effect of Si orientation, thickness, doping, and degree of oxidation on NW character made no difference in experiments performed thus far (both at MPI Stuttgart and in Ames). Both (111) and (100) Si wafers of 0.30-0.60 nm thickness were used. Commercially purchased Si wafers were typically doped either positively (p-type) with boron, or negatively (n-type) with phosphorus. In the present study p-type Si was used. Optionally, the Si wafers were plasma etched in the magnetron chamber before a-C sputtering to remove the native oxide layer. The plasma etching was done by applying a negative RF bias to the sample in the presence of an Ar^+ plasma. The plasma etching was typically done at 10 W for 15 minutes.

5.2.3 Thickness of the carbon

Producing an a-C layer of a pre-specified thickness is very difficult according to the magnetron operators at MPI Stuttgart and in the Ames Laboratory. Sputter rates are highly

instrument-dependent, and also inconsistent trial-to-trial for a given instrument. Although the deposition rates (for a given set of parameters) are well known for commonly sputtered substances like Cu, Ag, and Au, the sputter rate of carbon is something that must be explored by trial and error. The difficulty in sputtering carbon targets may arise from poor mass transfer between the Ar^+ ions and the carbon atoms in the target.

a-C substrates made at MPI were produced using an RF bias (0 to -200 V) and a target-to-substrate distance of 7 cm. The power used and actual sputter rate were highly variable. Thicknesses of a-C films made at MPI were measured using a profilometer on a section of the sample where the a-C had been removed. This was done by selectively preparing a section of a-C for profilometer measurement by marking the Si substrate with a Sharpie marker prior to carbon sputtering. After sputtering, the section of a-C atop the marker was dissolved away with ethanol or similar solvent. Using this approach, we found that MPI-1 and MPI-2 both had a 100 nm carbon layer, and MPI-3 had a 30 nm carbon layer.

a-C substrates produced in Ames were made in three batches. Details of the fabrication process for each batch are listed in Table 1. The thickness of the first batch (Ames-1) was measured with AFM against a section of the substrate which was masked with a coverslip during sputtering. The thickness of Ames-1 samples as measured by AFM was 8-12 nm. AFM measurements and data post-processing were done by Gilson Lomboy in the research group of Dr. Sriram Sundararajan. AFM was run in contact mode using a silicon nitride probe with a stiffness of 0.24 N/m. The data post-processing was done with Nanoscope v.5.31r1 Software. Sample Ames-2 was prepared using the same parameters as Ames-1 except for 4 times the sputter duration with the expectation of producing a film that was 30-50 nm in thickness (ideal for NW growth as suggested by the Richter Group). However, Ames-2 ended up having a very

thick black film visible to the naked eye, which means its thickness was probably >> 100 nm (based on comparison with the 100 nm a-C films which were barely visible to the naked eye). Ames-3 was produced using a sputter time intermediate between Ames-1 and Ames-2, and with the sample moved farther back from the sputter gun. We roughly estimate the thickness of Ames-3 to be 10-100 nm.

5.2.4 Whether used for NW growth or not

All but one of the a-C samples used in this study were "clean surfaces", meaning that they were never subjected to metal deposition, with the exception being MPI-3. MPI-3 was subjected to Ag NW growth conditions (180 nm Ag at 1100 K substrate temp), but then the heater was left at 1100 K for 30 minutes too long by accident, presumably causing the Ag to desorb. This substrate provided an early testing ground for the effect that NW growth would have on the a-C substrate. The sample history of MPI-3 was conveyed to us by Dr. Richter, but because the Ag was annealed away immediately after deposition, we do not have SEM images or other evidence of the Ag nanostructures grown thereon.

Our results, discussed in the sections below, show that MPI-3 had no scarring from Ag NW growth, which was surprising given the TEM image in Fig. 1(b), which clearly shows metal NW's (and other nanostructures, which we can generically call "features") protruding through the a-C film to the Si substrate below. Therefore we consider the possibility that holes existed on the surface, but we did not encounter them in our scans. Figs. 6(a) and (b) show Cu NW's on MPI-3 a-C and Ag NW's on Ames-2 a-C, with feature densities of approximately 1 μm^{-2} and 0.01 μm^{-2}, respectively. These samples represent approximate upper and lower bounds of feature

densities for metals on a-C substrates (at least for Cu and Ag). The probability of failing to encounter a feature from a population of randomly-distributed features is given by

$$P_{fail} = e^{-A/A_o} \quad (1)$$

where A is the scan area in μm^2, $A_o = 1/n_o$, where n_o is the mean feature density in μm^{-2}. Assuming that we scan a total area of 20 μm^2, the probability that the scan area is too small to reveal a hole that exists on the surface is $2x10^{-9}$ for the high-density limit and 0.82 for the low-density limit. Therefore it is entirely plausible that the scan area we used was simply inadequate to reveal features left by nanowire growth for this sample, if the density of Ag NW's was toward the lower end of the considered density range. Table 2 shows the probability of failing to find holes for samples with feature densities in the range of 1-0.01 μm^{-2}.

In Chapter 6 we explore further experiments which indicate that the a-C substrate *is* disturbed by NW growth, which means that either we did not find holes on MPI-3 due to insufficient scan area (which is a likely scenario), or that growth of features on this surface had not proceeded as expected based on the experimental conditions.

5.3 Characterization of a-C Substrates

5.3.1 STM – nature of the carbon, overall roughness, and tip effects

a-C is challenging to image with STM due to the roughness of the surface and also the lack of conductivity of some films[5] (not an issue with our films, but more common with high sp3-content films). As a result, AFM is a more common technique for studying large areas (micron-scale) of amorphous carbon films.[6; 7] Although there are a few works which study

the fine surface structure of a-C films with STM[5; 8; 9], and at least one which shows STM images at the 100 nm-scale[10], to the best of our knowledge there are no micron-sized surveys of a-C surfaces using STM.

Fig. 6 shows micron sized STM images of a-C samples MPI1-3 and Ames-3. It should be noted that Ames-3 was the only Ames a-C sample studied with STM, and we have a very limited number of images of it. Despite their roughness, all of the MPI a-C samples showed a surprising uniformity at the micron scale over tens of square microns sampled (and also at different areas of the sample separated by millimeters). The Ames a-C was slightly less uniform in that it had local protrusions (bright spots in Fig. 6, also see Fig. 14).

The appearance of the a-C surface in STM depended strongly on tunneling parameters. Figs. 8 and 9 show multiple images of sample MPI-2 using different tunneling parameters. At low magnification (> 100 nm x 100 nm, as in Fig. 7) a high tip bias allowed more effective imaging of surface contours, whereas a low tip bias produced repeating patterns of the tip. For instance, in Figs. 8(d-f), the tip was pear-shaped. At high magnification (Fig. 8, especially at 25 nm x 25 nm), a low tip bias allowed imaging of fine structure on the surface.

For atomically flat surfaces, the image seen is an approximately true representation of the surface. For rougher surfaces, however, convolution between surface and tip becomes more pronounced. A general rule of thumb is that the sharper object will image the smoother object. More examples of tip effects are shown in Fig. 9, with the repeating shape of the STM tip outlined in each panel. Tip apex shape changed substantially between sessions, and sometimes within the same session.

A low bias produced tip effects at low magnification, but at high magnification it revealed fine structure of the sample. Figs. 11-13 show fine structure on the MPI a-C films.

Fine structure could not be resolved on the Ames a-C films. The MPI a-C samples all displayed patches of scale-like features, shown at higher magnification in the lower right of each Figure. The features had separations of 0.27-0.35 nm. Similar scale-like features have been seen by Ivanov-Omskii[8], but with a smaller separation (0.25 nm). The scale-like feature separation in our images is larger than the graphite lattice constant (0.246 nm), and their arrangement is not hexagonal as in the graphite basal plane.

It is possible that the fine structures are layers of graphite sheets in an edge-on arrangement (see Fig. 13). The distance between carbon sheets in graphite is 0.334 nm, which is within the range of the width of our scale features (0.27-0.35 nm). The length of the scaled features is highly variable (0.4-0.9) nm, and not always easily defined in the images. In the image in Fig. 13, the length of the scaled features is 0.48 nm, which corresponds roughly to the distance between adjacent rings in edge-on-graphite of 0.426 nm. Panel (d) of Fig. 13 shows a hypothetical cluster of stacked graphite sheets (in blue) overlaid with a cartoon representation of the a-C scaled features (in red).

Moving back to larger scale images (250 nm x 250 nm or greater) the MPI a-C samples have deeper surface contours than do the Ames a-C samples as seen in Fig. 14 (with the caveat that only Ames-3 was imaged with STM, with marginal image quality). The standard way of expressing roughness (R) is given by the equation:

$$R_q = \sqrt{\frac{1}{n}\sum_{i=1}^{n} y_i^2} \qquad (2)$$

Where *R* is the root mean squared (rms) roughness, *n* is the number of points measured, and *y* is the vertical distance from the mean at each point. We analyzed R using the "roughness" analysis in the WSxM post-processing software package (available free online). Based on our highest

quality images, R = 1.0-1.2 nm for the MPI a-C samples , while R = 0.3 nm for Ames-3 (see Table 1).

The apparent roughness of the a-C samples changed depending on tunneling conditions and image size. Fig. 15 shows variation in R as a function of image dimensions for images taken under similar tunneling conditions. Based on this graph, images of 250 nm x 250 nm or larger provide the most accurate gauge of R. In general, all measurements of R based on STM images are a lower bound of the true R due to the limitations of the STM tip in probing the true depth of pits on the surface.

5.3.2 XPS – nature of the carbon: sp^2 vs. sp^3

X-ray photoelectron spectroscopy was used to probe the chemical nature of our a-C substrates. The XPS study was conducted at MPI-Stuttgart using amorphous carbon from their standard batch (not shown in Table 1, but prepared similarly), and using sample Ames-2, which was shipped to us from the Ames Laboratory. The purpose of the experiment was to determine the relative percentage of sp^2 carbon (graphitic) versus sp^3 carbon (diamond-like carbon, or DLC) in the samples. The chemical nature of a-C substrates depends on deposition method[11]. Magnetron-sputtered carbon films are typically 70-95% sp^2 in character[11].

As a pure-sp^2 reference we used HOPG, and as a pure-sp^3 reference we used diamond microparticles precipitated out from a polishing emulsion and dried initially at 400 K in an oven to remove solvent. All samples were heated at 800 K for 30 minutes in UHV and allowed to cool prior to measurement. Chamber pressure was 1.4×10^{-8} mbar, and an Al anode was used (K-alpha x-ray excitation energy = 1486.7 eV). Spectrum processing was done using Casa XPS software. All peaks were fitted with a Shirley background in the energy range 280-295 eV

(binding energy). The sp^2 (graphite) reference gave a C1s binding energy peak at 284.7 eV, and the sp^3 (diamond) reference gave a C1s binding energy peak at 285.4 eV (see Fig. 16). Amorphous carbon from MPI and Ames gave C1s binding energy peaks at 284.6 and 284.8 eV, respectively, and were slightly wider than either of the reference peaks (see Fig. 17). The reference peaks were fitted underneath the a-C peaks using a customized peak-fitting algorithm (see Fig. 18). By taking the resulting ratio of areas under the reference peaks, the MPI a-C was determined to be 81 % sp^2, and the Ames a-C was 87 % sp^2, with the remaining fraction being sp^3. This result is consistent with the range of 70-95 % sp^2 character of a-C films found in the literature[11].

5.4 Conclusions

Amorphous carbon samples from MPI Stuttgart and Ames both have high sp^2 content (81-87%) based on XPS measurement. The MPI a-C surfaces all show a rough but uniform surface at the micron scale, with rms roughness of 1.0-1.2 nm, regardless of film thickness or pre-treatment of the Si substrate. The Ames a-C sample has shallower surface contours and therefore a lower rms roughness than the MPI samples, but is also less uniform in appearance at the micron scale. In some regions, the MPI samples exhibit a scale-like fine structure which could be graphitic clusters arranged in an edge-on fashion. Our search for remnants of scarring or holes on MPI-3, which was subjected to Ag NW growth conditions followed by annealing, was negative. We do not know the initial feature density on the sample. However, if we assume that it fell within a range of densities established for other samples, then it is plausible that we failed to scan a large enough area to find the holes. The question of whether a-C is scarred from NW growth is explored further in Chapter 6, where we perform experiments on Ag/a-C NW

samples to definitively show that NW growth (at least for Ag) *does* affect the morphology of the a-C substrate.

Acknowledgements

This work was supported by the Office of Science, Basic Energy Sciences, Materials Sciences and Engineering Division of the U.S. Department of Energy (USDOE), under Contract No. DE–AC02–07CH11358 with the U.S. Department of Energy. We thank Jim Anderegg for his contribution of HOPG substrates. We thank Dr. Gunther Richter for his generous collaboration on this study, and his donation of amorphous carbon and nanowire samples. We thank Gilson Lomboy and Dr. Sriram Sundararajan for performing the AFM measurements. We thank Ryan Ott and Matt Besser of Ames Laboratory for preparation of magnetron sputtered a-C substrates.

References

[1] M. Kolb, G. Richter, AIP Conference Proceedings 1300 (2010) 98-105.

[2] M. Schamel, C. Schopf, D. Linsler, S.T. Haag, L. Hofacker, C. Kappel, H.P. Strunk, G. Richter, Int. J. Mat. Res. 102 (2011).

[3] G. Richter, K. Hillerich, D.S. Gianola, R. Mönig, O. Kraft, C.A. Volkert, Nano Letters 9 (2009) 3048-3052.

[4] M. Dresselhaus, Y.-M. Lin, O. Rabin, M. Black, J. Kong, G. Dresselhaus, in: B. Bhushan (Ed.), Springer Handbook of Nanotechnology, Springer Berlin Heidelberg, 2007, pp. 113-160.

[5] B. Marchon, M. Salmeron, W. Siekhaus, Physical Review B 39 (1989) 12907-12910.

[6] S.B. W. Mróz, A. Prokopiuk, M. Jedynski, B. Budner, a.M.L. Korwin-Pawlowskib, Proceedings of the III National Conference on Nanotechnology NANO 2009 116 (2009).

[7] N. Paik, Applied Surface Science 226 (2004) 412-421.

[8] V. Ivanov-Omskii, A. Lodygin, S. Yastrebov, Semiconductors 34 (2000) 1355-1362.

[9] N.H. Cho, D.K. Veirs, J.W. Ager, M.D. Rubin, C.B. Hopper, Journal of Applied Physics 71 (1992).

[10] I. Rusman, L. Klibanov, L. Burstein, Y. Rosenberg, V. Weinstein, E. Ben-Jacob, N. Croitoru, A. Seidman, Thin Solid Films 287 (1996) 36-44.

[11] J. Robertson, Materials Science and Engineering: R: Reports 37 (2002) 129-281.

Tables

Table 1
Parameters for a-C samples fabricated at MPI Stuttgart and the Ames Laboratory.

a-C Sample	Date Made	Substrate	Ar^+ etch Si?	Est. a-C Thickness (nm)	RMS Roughness (nm)	Misc. Notes	Deposition Parameters
MPI-1	10/12/11	Si(100) p-type	no	100	1.0	-	4 mTorr Ar, 300 K, target RF bias (100 W), no sample rotation, 8 cm target-sample distance
MPI-2	~10/12/11	Si(100) p-type	yes, 10 min	100	1.2	Conditions should have produced Ag NW's, then removed by annealing (not verified by observation)	4 mTorr Ar, 300 K, target RF bias (100 W), no sample rotation, 8 cm target-sample distance
MPI-3	10/12/11	Si(100) p-type	yes, 10 min	30	1.0	-	4 mTorr Ar, 300 K, target RF bias (100 W), no sample rotation, 8 cm target-sample distance
Ames-1	7/21/11	Si(111) p-type	yes, 15 min	8-12	-	-	5 mTorr Ar, 300 K, target RF bias (75 W), sample RF bais (6 W), 40 min, 15 rpm sample rotation
Ames-2	6/13/12	Si(111) p-type	yes, 15 min	>>100	-	Film visible and non-uniform	5 mTorr Ar, 300 K, target RF bias (75 W), sample RF bais (6 W), 160 min, 15 rpm sample rotation

Table 1 cont…

a-C Sample	Date Made	Substrate	Ar^+ etch Si?	Est. a-C Thickness (nm)	RMS Roughness (nm)	Misc. Notes	Deposition Parameters
Ames-3	10/23/12	Si(111) p-type	yes, 15 min	10-100	0.3	-	5 mTorr Ar, 300 K, target RF bias (75 W), sample RF bais (6 W), 60 min, 15 rpm sample rotation, target-sample distance 1 inch farther

Table 2
The probability of failing to find a feature on a surface with a mean feature density of n_0, given a scan size of 20 μm^2.

n_0 (μm^{-2})	P_{fail}
1	$2x10^{-9}$
.25	$6.7x10^{-3}$
.1	.14
.01	.82

Figures

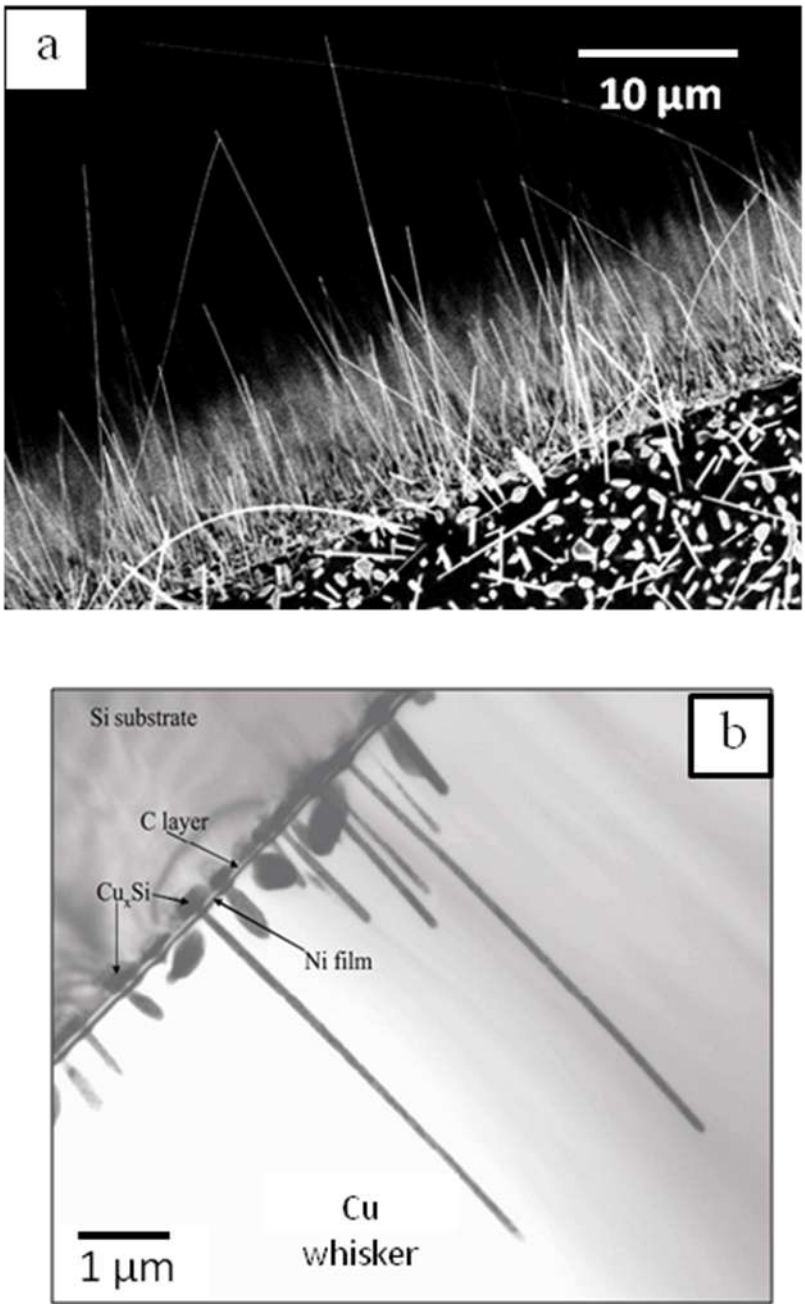

Fig. 1
(a) SEM image of Cu nanowires grown on a-C/Si; (b) TEM cross-section of Cu wires grown on a-C/Si and coated with a thin Ni film (figure reproduced with permission from ref. [3])

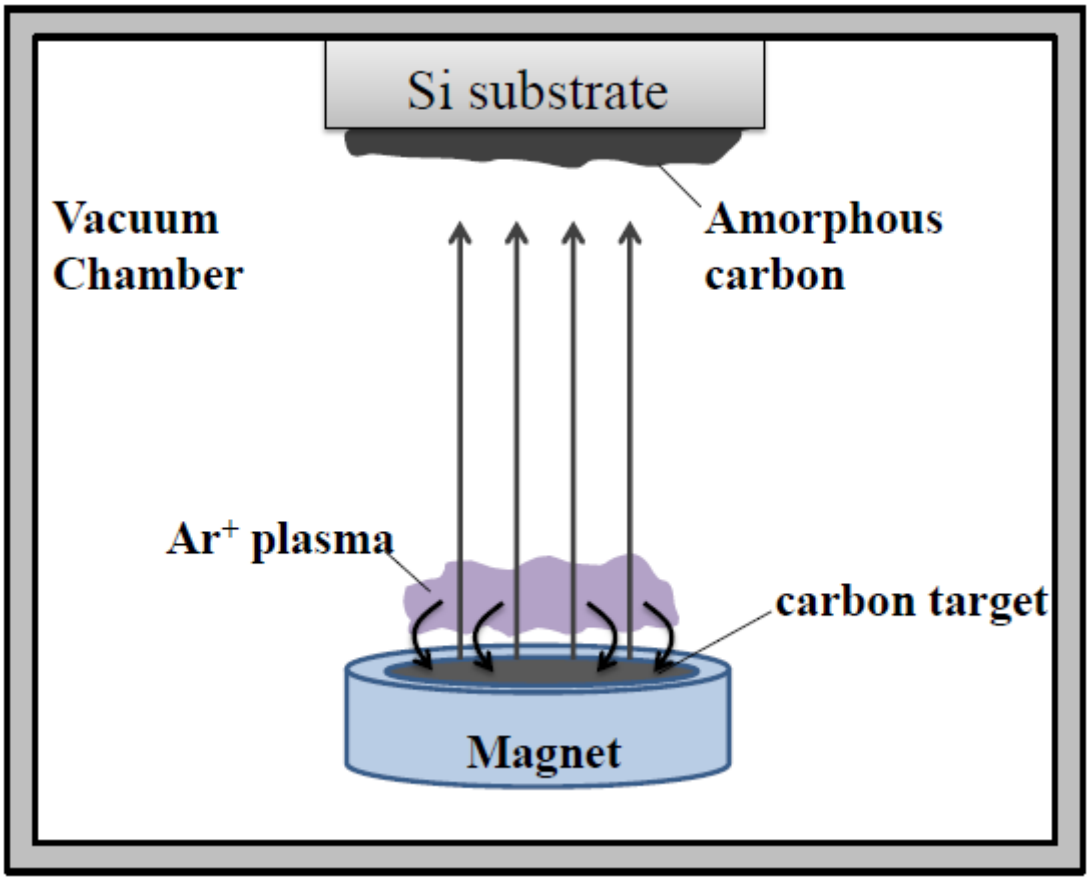

Fig. 2
Schematic diagram of a magnetron sputter system for fabricating a-C substrates.

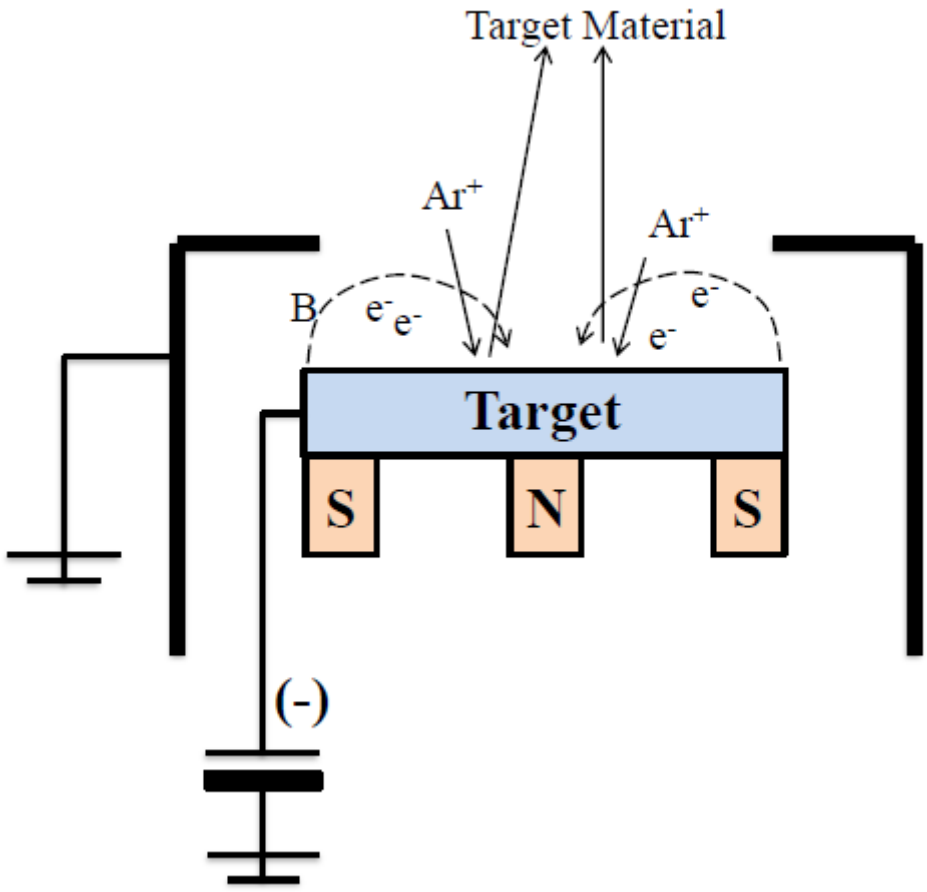

Fig. 3
Schematic diagram of the method of ion bombardment at the magnetron target.

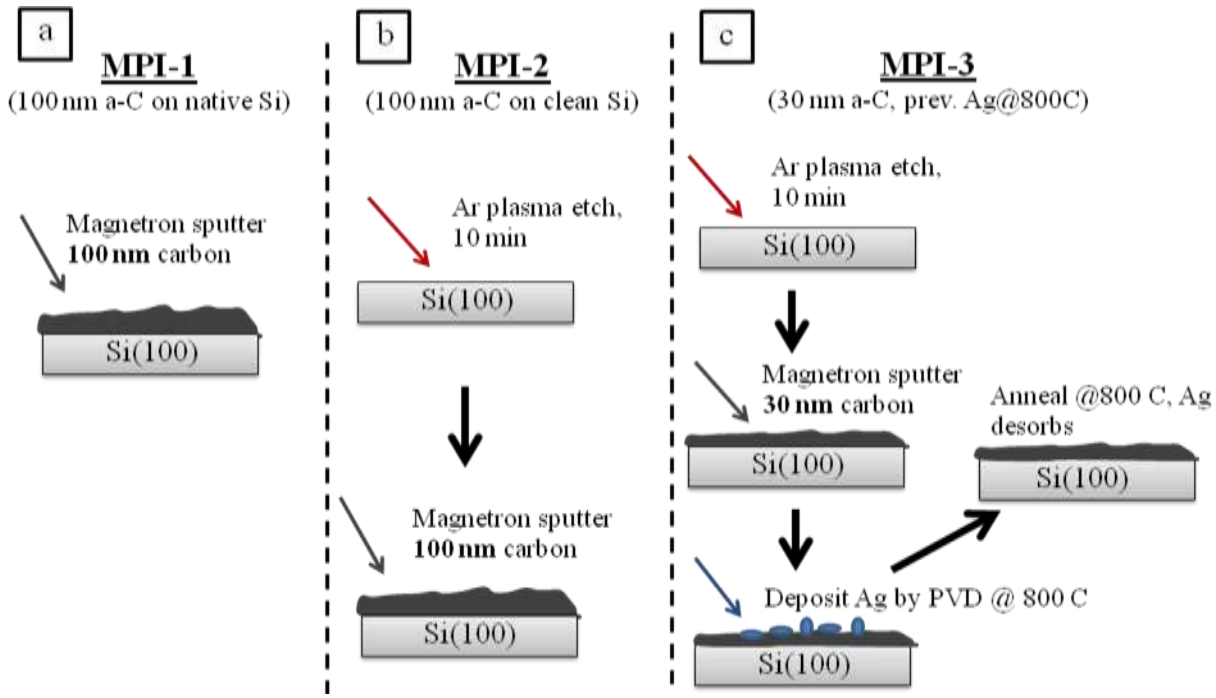

Fig. 4
Sample prep/composition of a-C samples (a) MPI-1; (b) MPI-2; and (c) MPI-3.

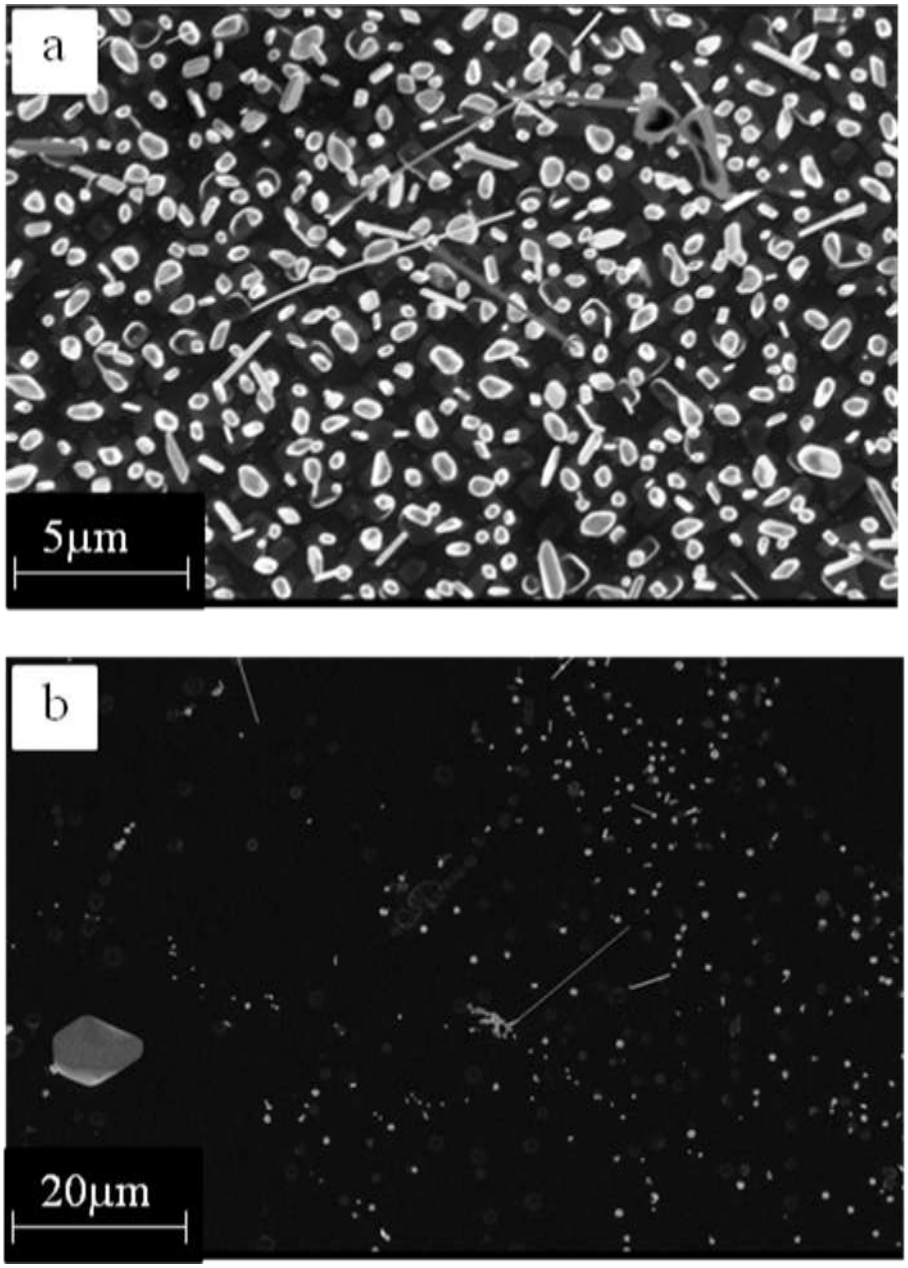

Fig. 5
SEM images of (a) Cu nanostructures on MPI-3 a-C with a feature density of 1 μm^{-2}; and (b) Ag nanostructures on Ames-2 a-C with a feature density of 0.01 μm^{-2}.

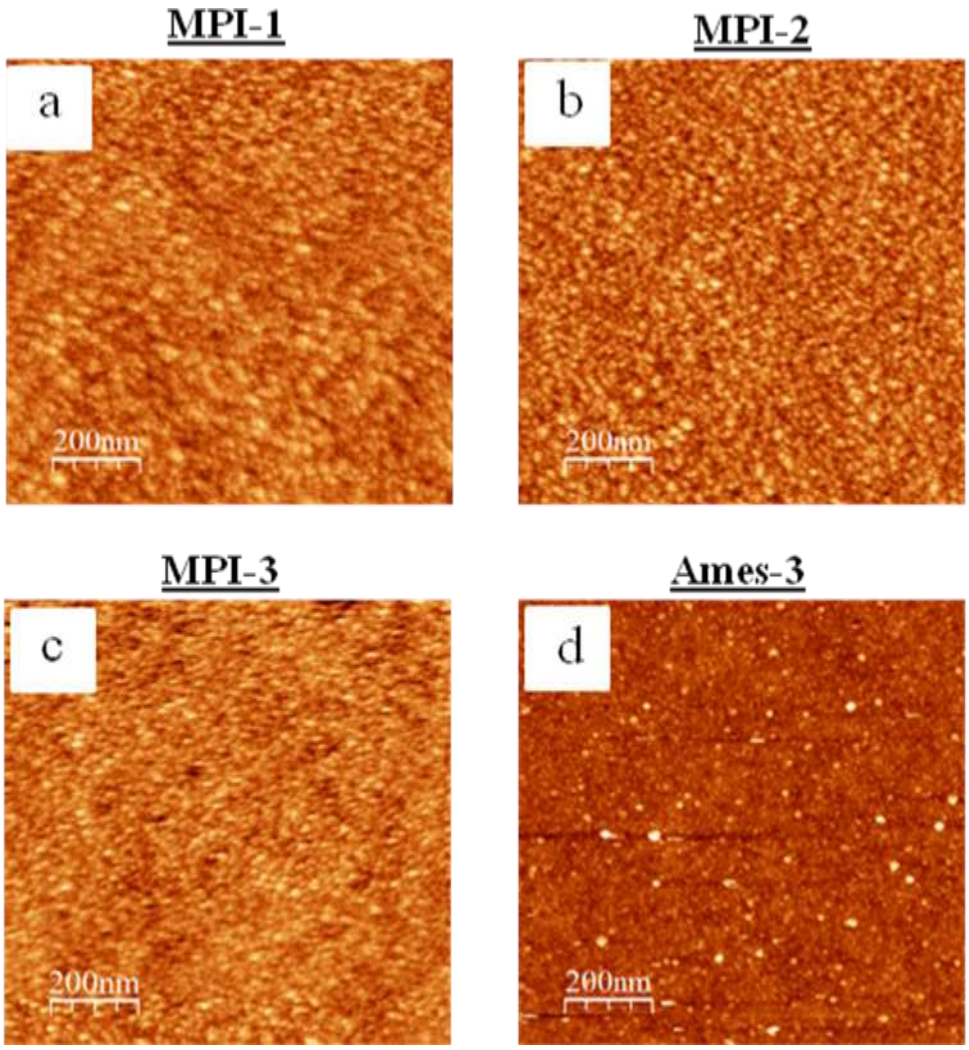

Fig. 6
STM images of a-C substrates (a) MPI-1, V_{tip} = -3.9 V, *i* = 1.8 nA; (b) MPI-2, V_{tip} = -6.0 V, *i* = 3.0 nA; (c) MPI-3, V_{tip} = -1.2 V, *i* = 1.5 nA; and (d) Ames-3, V_{tip} = -2.5 V, *i* = 0.05 nA. All images 1 μm x 1 μm.

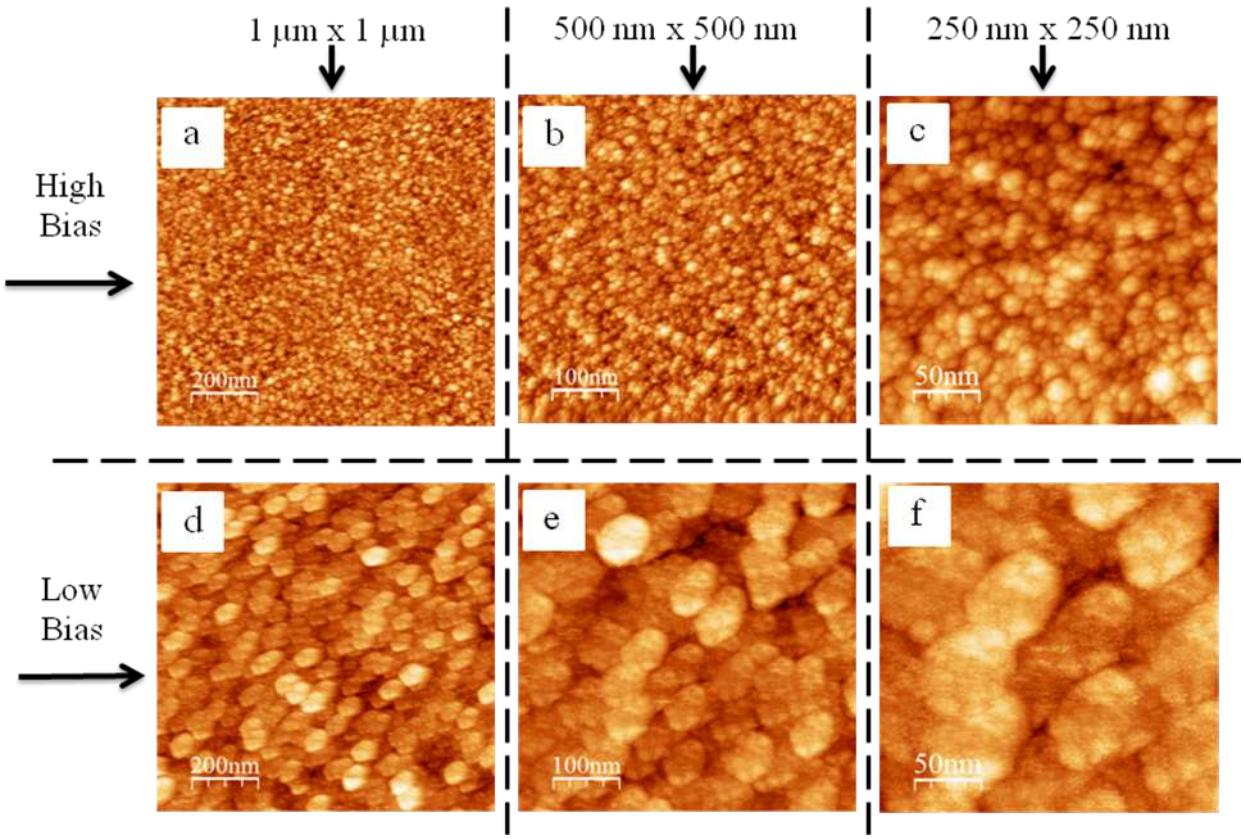

Fig. 7
A series of low-magnification STM images of a-C sample MPI-2 showing the effects of tip bias on image appearance using high bias (a-c) versus low bias (d-f). (a) 1 µm x 1 µm, V_{tip} = -6.0 V, *i* = 3.0 nA; (b) 500 nm x 500 nm, V_{tip} = -5.1 V, *i* = 2.4 nA; (c) 250 nm x 250 nm, V_{tip} = -5.1 V, *i* = 2.4 nA; (d) 1 µm x 1 µm, V_{tip} = -0.02 V, *i* = 1.8 nA; (e) 500 nm x 500 nm, V_{tip} = -0.02 V, *i* = 1.8 nA; and (f) 250 nm x 250 nm, V_{tip} = -0.02 V, *i* = 1.8 nA.

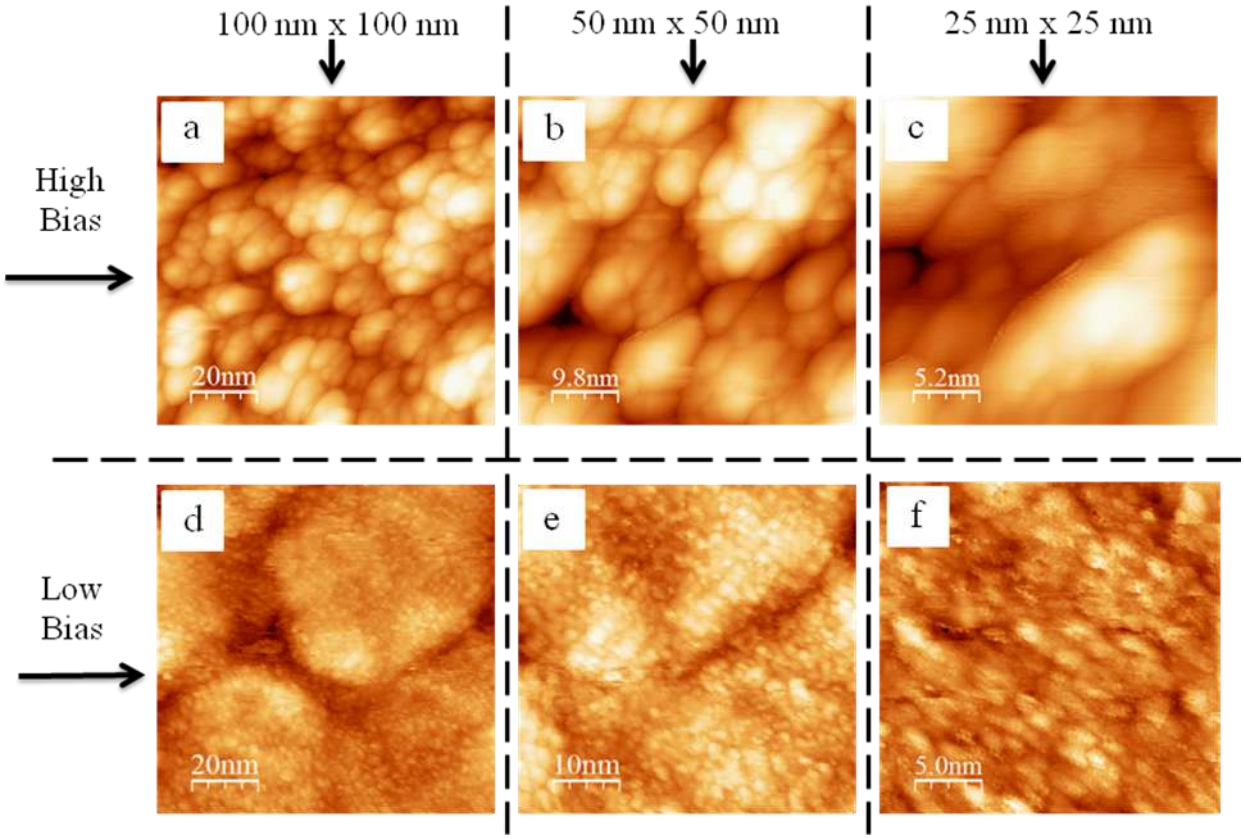

Fig. 8
A series of high-magnification STM images of a-C sample MPI-2 showing the effects of tip bias on image appearance using high bias (a-c) versus low bias (d-f). (a) 100 nm x 100 nm, V_{tip} = -3.4 V, *i* = 1.7 nA; (b) 50 nm x 50 nm, V_{tip} = -2.1 V, *i* = 1.0 nA; (c) 25 nm x 25 nm, V_{tip} = -0.51 V, *i* = 0.07 nA; (d) 100 nm x 100 nm, V_{tip} = -0.02 V, *i* = 1.8 nA; (e) 50 nm x 50 nm, V_{tip} = -0.02 V, *i* = 1.8 nA; and (f) 25 nm x 25 nm, V_{tip} = -0.02 V, *i* = 1.8 nA.

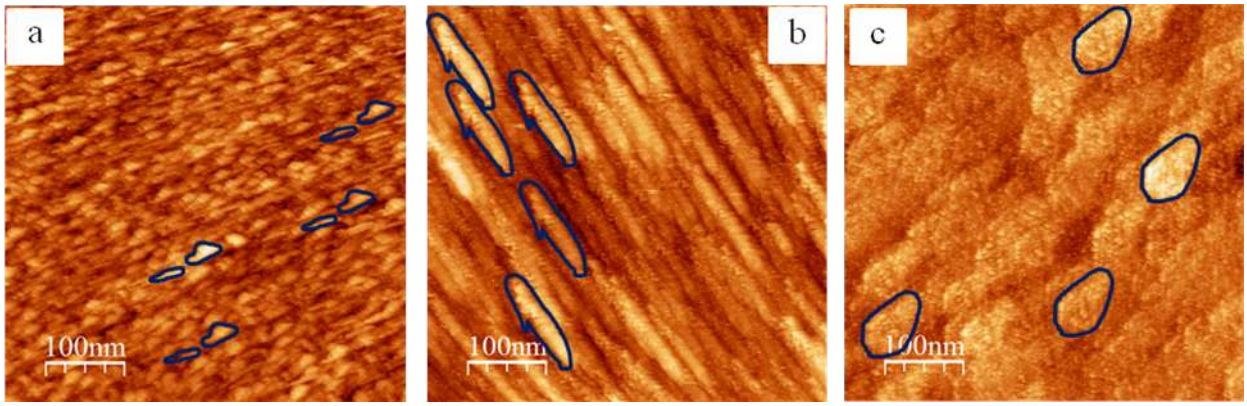

Fig. 9
STM images of a-C substrate MPI-3 showing a tip effect on different days. The shape of the tip is outlined in each image. All images are 500 nm x 500 nm with V_{tip} = -0.02 V, *i* = 1.8 nA.

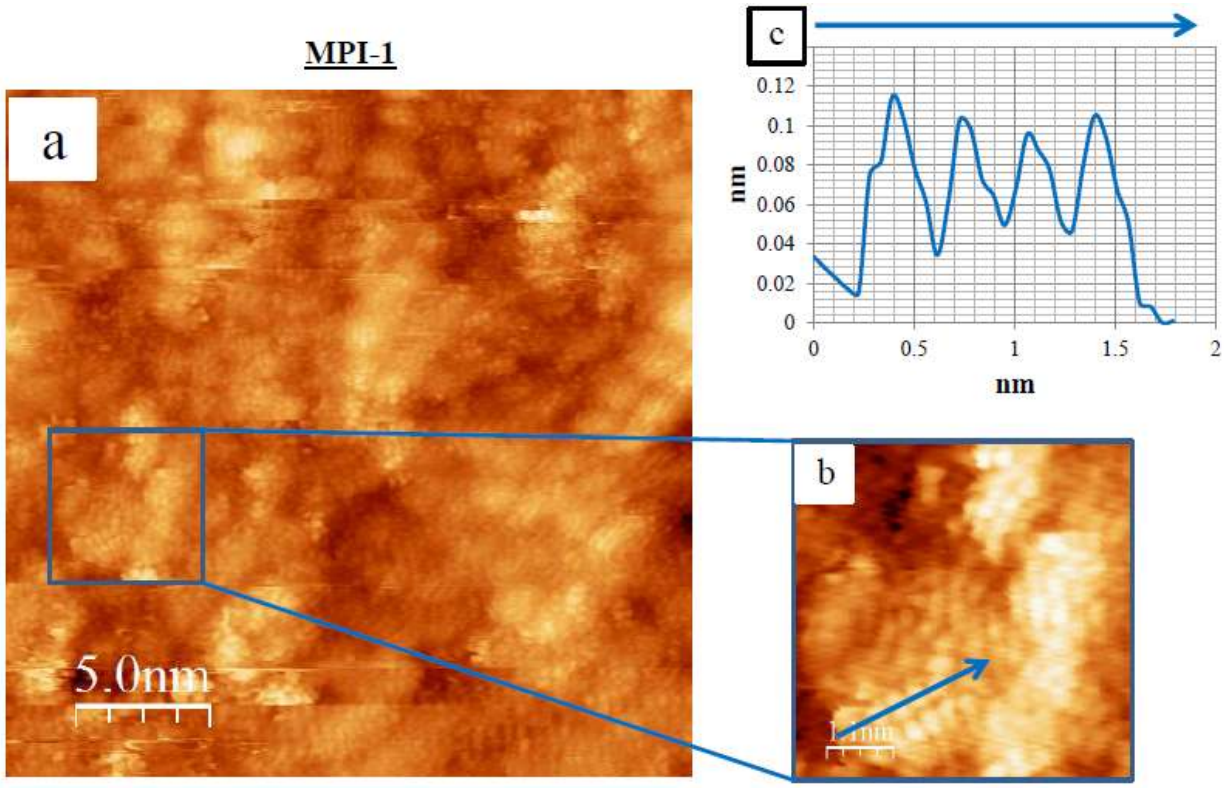

Fig. 10
(a) High-magnification image of the MPI-1 surface showing fine structure, 25 nm x 25 nm, V_{tip} = -0.02 V, *i* = 1.8 nA; (b) zoom-in from (a); (c) line profile of the scale-like features from (b).

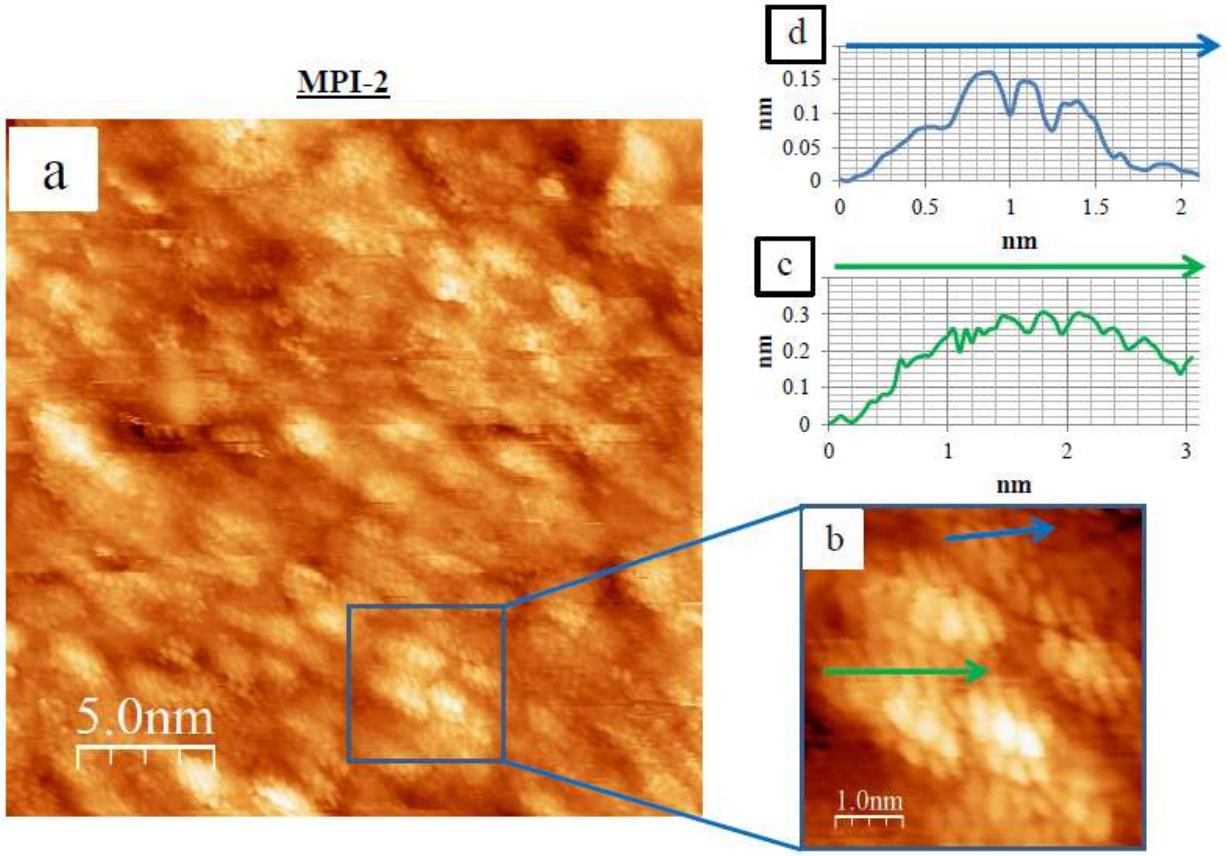

Fig. 11
(a) High-magnification image of the MPI-2 surface showing fine structure, 25 nm x 25 nm, V_{tip} = -0.02 V, *i* = 1.8 nA; (b) zoom-in from (a); (c-d) line profiles of the scale-like features from (b).

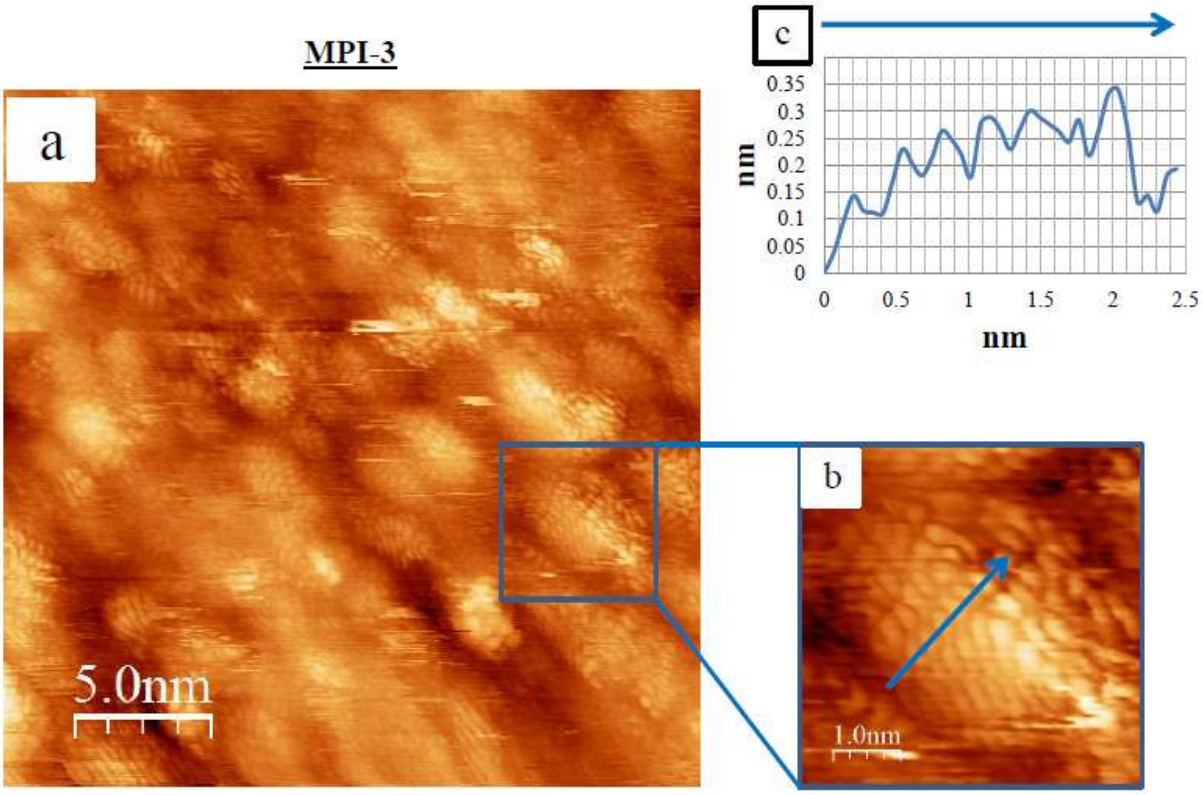

Fig. 12
(a) High-magnification image of the MPI-3 surface showing fine structure, 25 nm x 25 nm, V_{tip} = -0.02 V, *i* = 1.8 nA; (b) zoom-in from (a); (c) line profile of the scale-like features from (b).

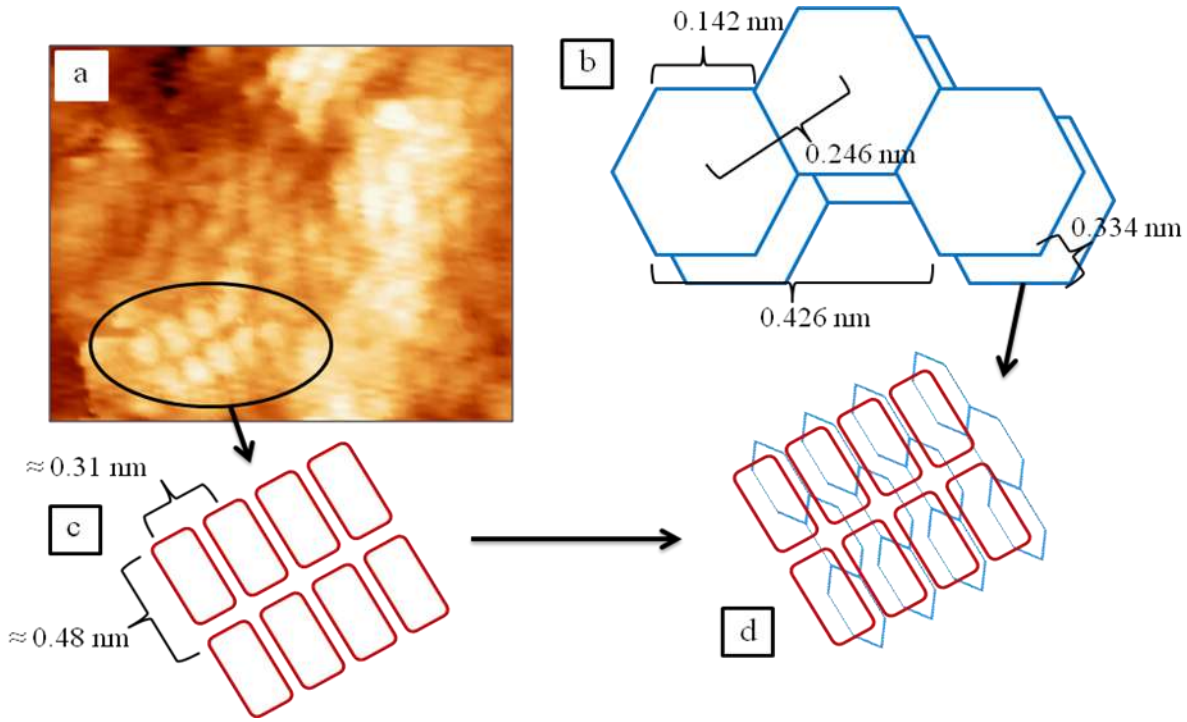

Fig. 13
(a) STM image of fine structure from MPI-1, 5 nm x 5 nm, V_{tip} = -0.02 V, *i* = 1.8 nA; (b) line representation of two stacked graphite clusters, with relevant distances shown; (c) cartoon outline of the scaled features in (a); (d) overlay of the scaled features with stacked graphite layers, giving a hypothesis for the nature of the features.

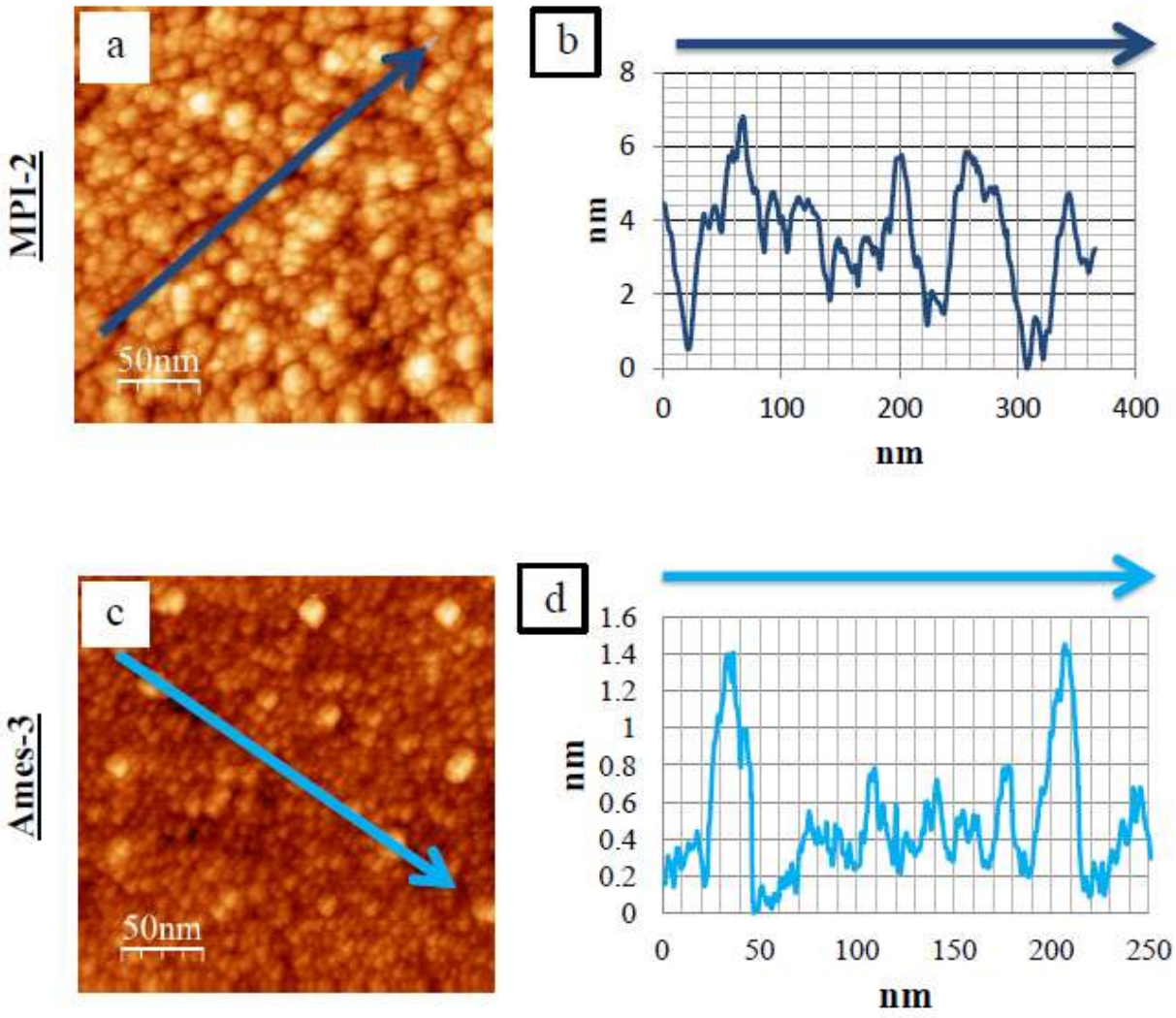

Fig. 14
STM comparison of surface contours of MPI-2 and Ames-3 a-C. (a) 250 nm x 250 nm V_{tip} = -5.1 V, *i* = 2.4 nA; (b) linen profile from (a); (c) 250 nm x 250 nm V_{tip} = -5.1 V, *i* = 2/4 nA; and (d) line profile from (c).

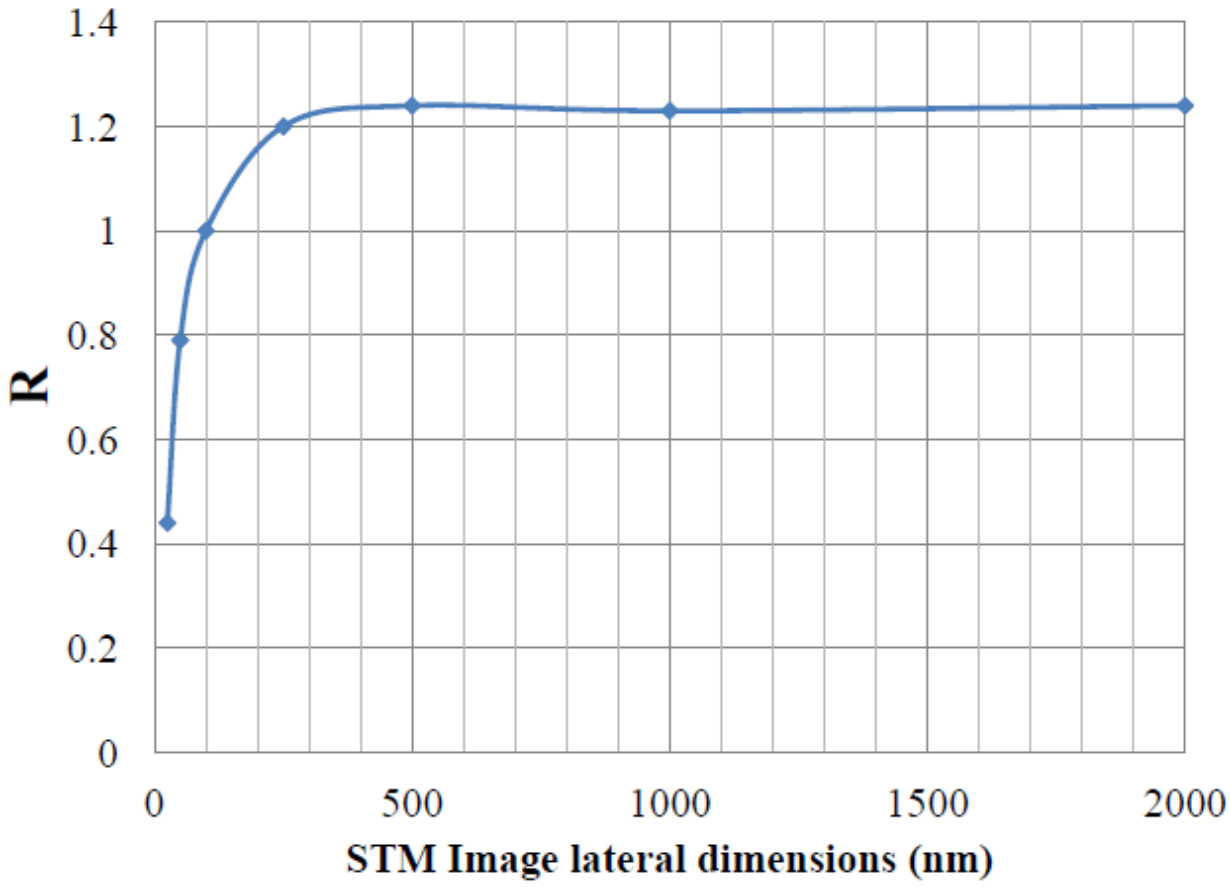

Fig. 15
Plot of measured rms roughness (R) vs. STM image size for a-C sample MPI-3.

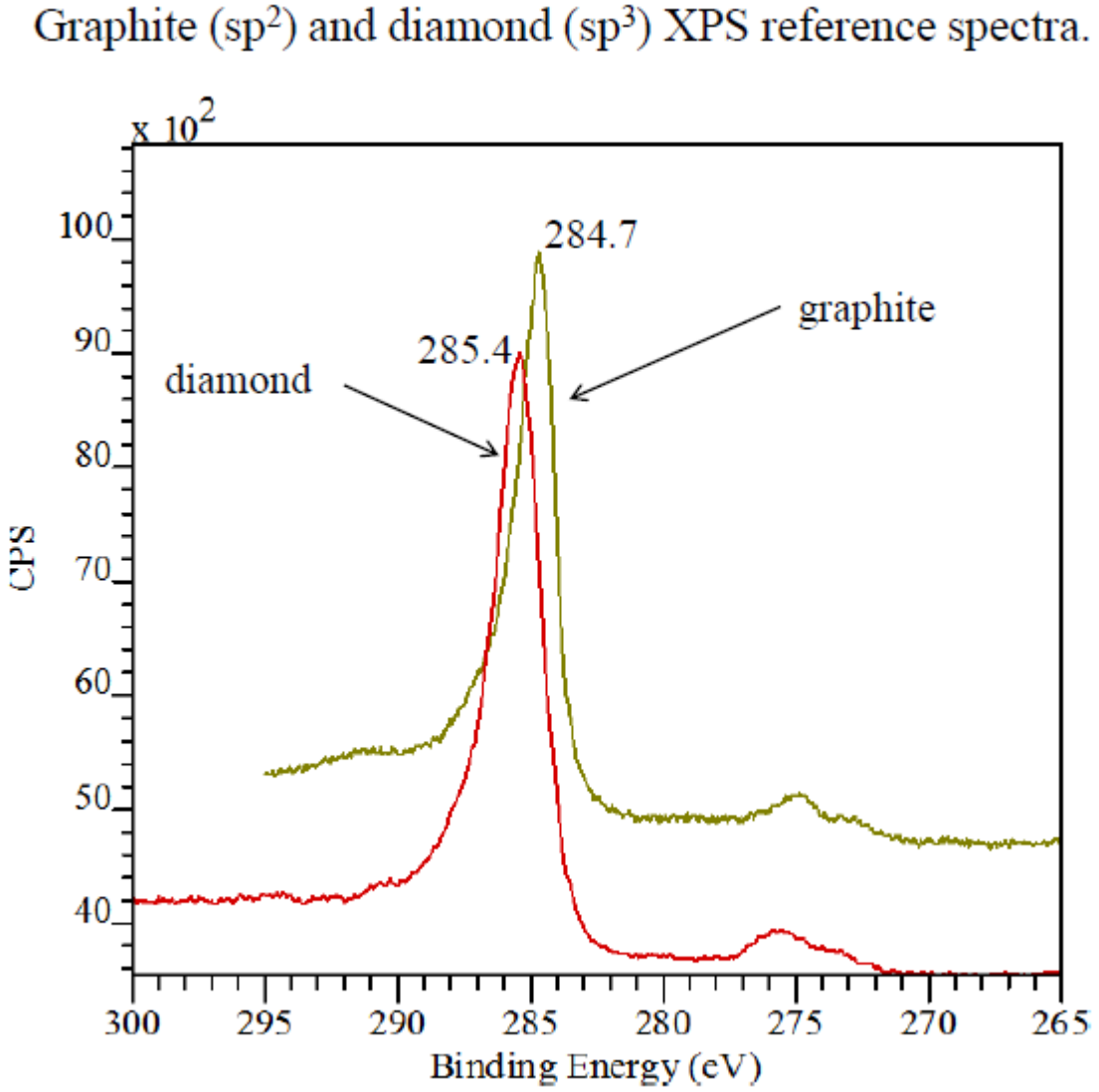

Fig. 16
XPS data showing C1s binding energy peaks for sp^3 (diamond) and sp^2 (graphite) reference peaks.

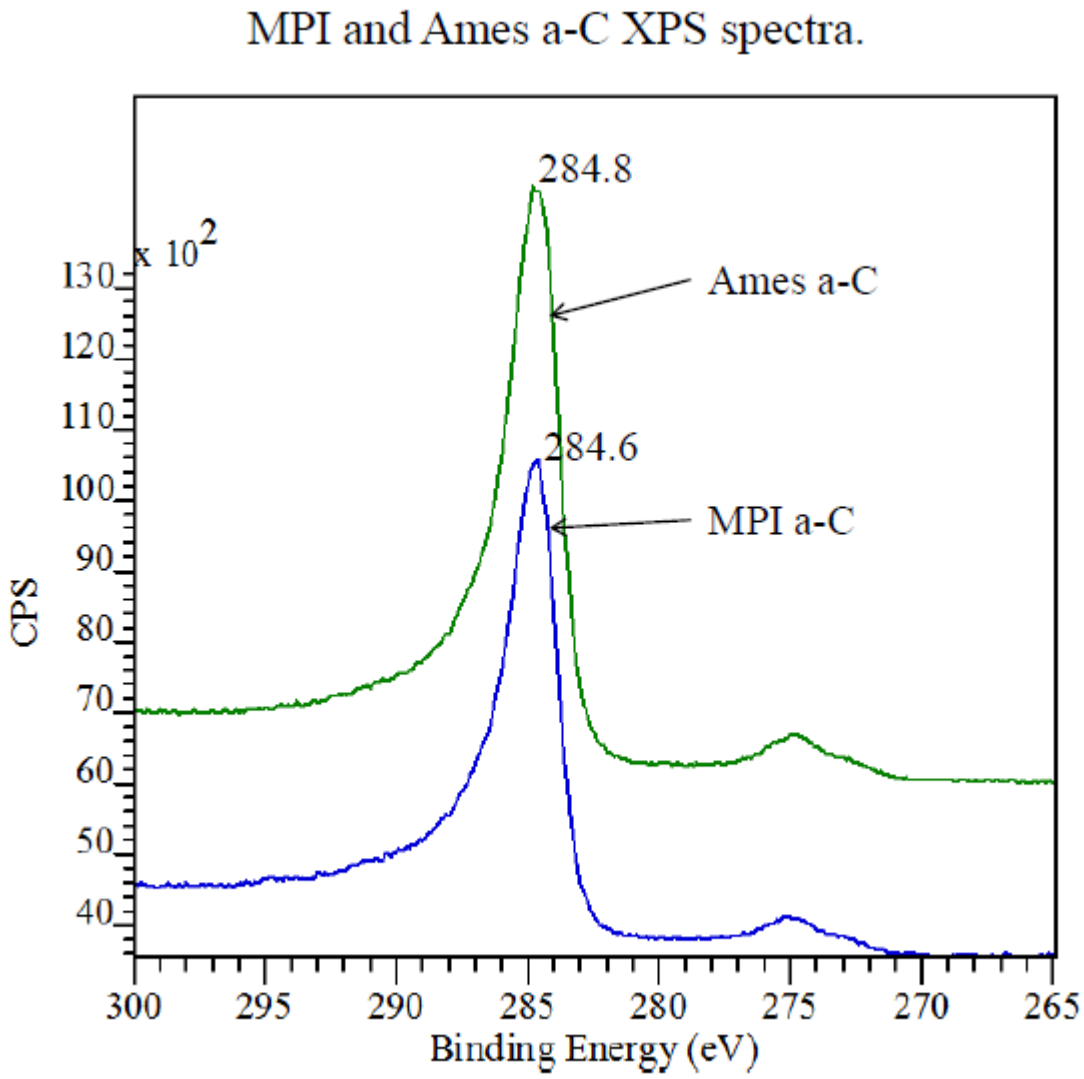

Fig. 17
XPS data showing C1s binding energy peaks for MPI and Ames a-C samples..

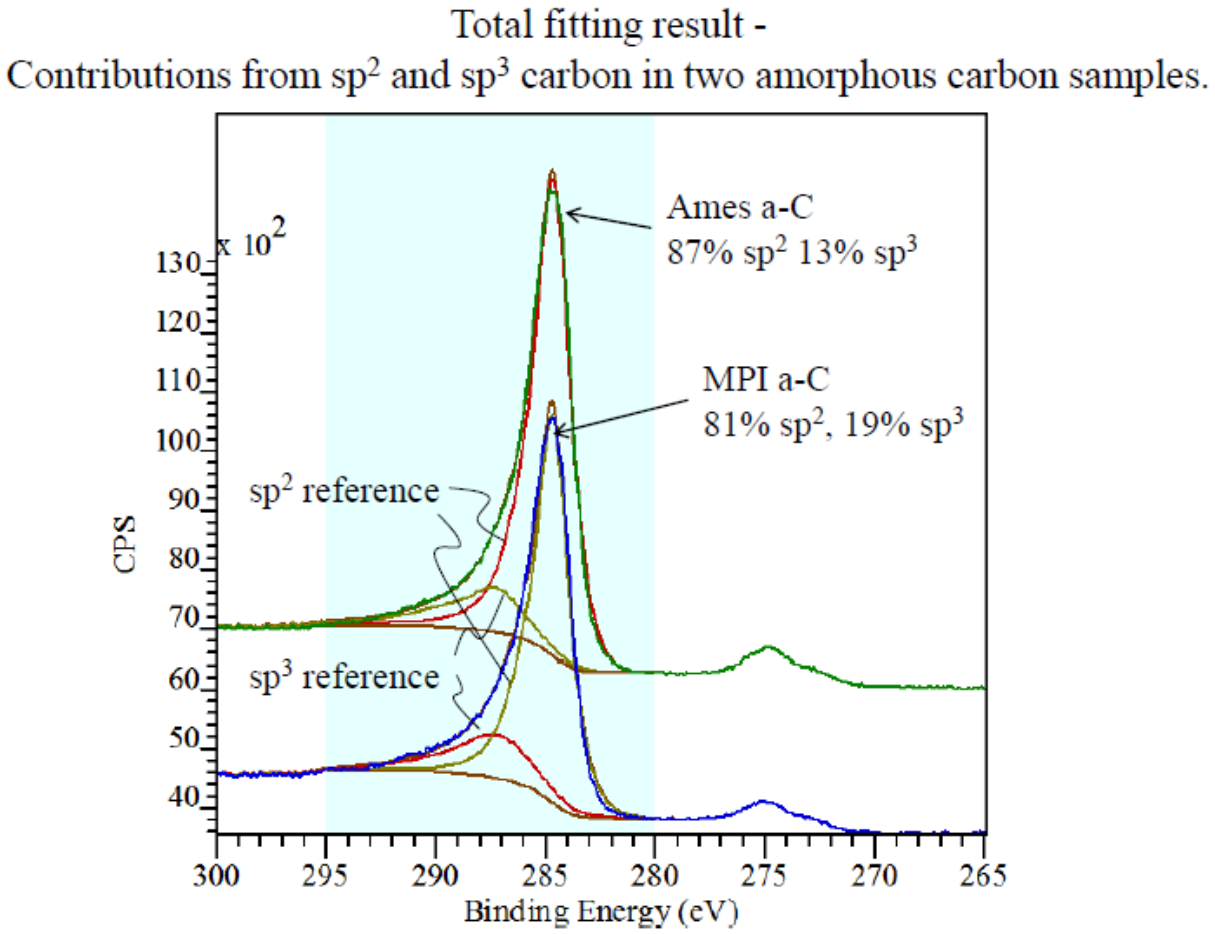

Fig. 18
XPS data showing contributions from sp^2 and sp^3 carbon in Ames a-C and MPI a-C. Diamond and graphite reference peaks are fitted underneath each curve.

CHAPTER 6

INTERACTION OF AG AND CU WITH A-C, INCLUDING NANOWIRE GROWTH

6.1 Introduction

Chapter 5 presented analysis of amorphous carbon substrates used for the growth of metal nanowires, as pioneered by our collaborator, Dr. Gunther Richter, at MPI, Stuttgart.[1; 2] In this chapter we explore the basic interaction of Cu and Ag with a-C surfaces. We have also grown metal nanowires from Cu, Ag, Fe, and Ni, and using substrates other than a-C such as graphite, diamond, and tungsten. Fe and Ni nanowires are of particular interest for their potential use in magnetic storage media[3]. We also present a table of nanowire recipes which include the nanowires grown as part of this thesis work in addition to recipes shared with us by the Richter group. The nanowire growth experiments presented here were conducted at MPI Stuttgart and at the Ames Laboratory. The wires were grown by either MBE or magnetron sputtering, both of which are discussed in detail.

6.2 Cu on a-C at 300 K – Basic Interaction

The a-C film used for this study was produced in the Ames Laboratory and was previously referred to (in Chapter 5) as sample Ames-3. In this section, we refer to it generically as a-C. The objective of this experiment was to obtain STM images of Cu on the a-C surface at 300 K as a function of coverage, and if successful, to obtain further images after annealing the sample (e.g. 800 K, see Fig. 1). Cu coverage was calibrated by comparison to a similar deposition on HOPG, and assuming the Cu islands to be spherical.

Fig. 1(a-d) shows a comparison of the clean Ames a-C surface, the same surface after 0.22 ML of Cu, after 1.3 ML, and after heating the 1.3 ML surface to 800 K for 15 minutes. The clean a-C surface in Fig. 1(a) had an apparent rms roughness (R) of 0.19 nm, which represents a lower bound for the true R, especially since there was a slight tip effect as evidenced by the streakiness of all features (tailing off to the upper right). At 0.22 ML Cu (Fig. 1(b)) there was a noticeable difference in the surface appearance. The surface contours appeared more like beads than on the clean surface. This could either be due to the presence of Cu on the surface, or due to a change in tip condition. At 1.3 ML Cu (Fig. 1(c)), the surface was markedly changed, nearly indistinguishable from the saturated Cu/HOPG surface at 3.9 ML (see Fig. 5 for comparison). Both surfaces have a cluster density of 0.15-0.2 nm^{-2}. However, since only 1.3 ML of Cu was deposited on the a-C, the apparent clusters on the 1.3 ML Cu/a-C surface are probably not solid Cu clusters, but rather a near single-layer Cu coating of the a-C surface. This lends support for an initial layer-by-layer growth mode for Cu on a-C at 300K, which is in contrast to the 3D growth mode of Cu/HOPG.

XPS supplemented the STM data. These XPS experiments were performed at the Ames Laboratory. The Cu $2p_{3/2}$ peak was monitored for Cu and the C1s peak was monitored for carbon. None of our samples showed any detectable oxygen (~532 eV), either before or after Cu deposition. Survey spectra of each surface are shown in Fig. 8, with a zoomed-in view of the Cu 2p family of peaks in Fig. 9. The relative ratio of areas between the Cu $2p_{3/2}$ peaks for the 0.22 ML and 1.3 ML depositions was 1/4.4, in moderate agreement with our estimation of relative total flux (0.22/1.3 = 1/6).

6.3 Subsequent Annealing to 800 K

After annealing the 1.3 ML surface to 800 K, coarsening was evident (See Fig. 1 and Figs. 6-7). The surface was now spotted with Cu islands extending 3-6 nm above the a-C substrate. In addition, the morphology of the substrate itself had changed from closely-spaced sharp features ~1 nm high to a rolling terrain with undulations 1-3 nm high and 25-50 nm wide.

After annealing, the XPS Cu signal dropped to 4% of the 1.3 ML case. It should be mentioned that XPS signal intensity depends not only on the amount of material on the surface, but also on its distribution. For the post-800 K case, the Cu was concentrated in Cu clusters, which would produce a lower XPS signal than an equivalent dispersed film. Attenuation of the Cu signal due to the change in surface distribution alone would be 23% of the initial signal intensity, assuming 4 nm high islands and no intercalation. This attenuation can be calculated from the equation:

$$I = I_o A_f \Sigma e^{(-\Delta x/\lambda)} \quad (1)$$

Where I_o and I are the initial and final signal intensity, A_f is the fractional area covered by Cu, Δx is the depth of a particular Cu layer in the cluster, and λ is the mean free path of electrons through Cu at a given energy, taken from [4]. The calculated attenuated signal of 23% is considerably higher than the actual intensity measured (4%). This strongly suggests that most of the initially deposited Cu is no longer on the surface.

As additional evidence, we can also estimate surface coverage on the 800 K surface based on the heights of the Cu islands in STM images. This yields 0.02 ML (if spherical) and 0.08 ML (if hemispherical), which correspond to 1.5% and 6% of the 1.3 ML case, respectively. The calculated relative coverages from STM images (1.5% - 6%) are in agreement with the

measured signal attenuations (4%), in that they show that most of the initial Cu is no longer present on the surface.

We expect minimal desorption in the Cu/a-C system at 800 K based on previous experiments with Cu/HOPG. In the Cu/HOPG system there was a decrease in the Cu surface coverage between 800 and 900 K. This was attributed to desorption assuming that Cu had not diffused into the bulk. Because the Cu on HOPG is in 3D clusters, desorption is primarily Cu-Cu desorption rather than Cu-C desorption. In the Cu/a-C system we also saw 3D morphology at elevated temperature, and therefore conclude that desorption is also a Cu-Cu phenomenon. Therefore we expect a similar desorption temperature for Cu/a-C as with Cu/HOPG. The fact that we only see a small fraction of the initial 1.3 ML of Cu on the surface after 800 K in the Cu/a-C system indicates that a substantial amount of the material has diffused into the bulk, which is consistent with the idea of NW's anchoring themselves into the Si substrate below the a-C surface.

6.4 Removal of Ag Nanowires by Annealing – STM of Holes

Chapter 5 described a comparison between a-C samples from MPI-Stuttgart, where one of the samples (MPI-3) had been subjected to Ag NW growth. We were unable to find any evidence of scarring on the MPI-3 surface, which could lead to one of two conclusions: 1) that NW growth does not disturb the a-C surface; or 2) that the initial growth of nanostructures on this surface did not proceed as expected given the experimental conditions. Our findings for Cu/a-C deposited at 300 K and annealed to 800 K (described above) showed that the a-C surface was altered by the presence of metal, and we expect that the a-C substrate would also be altered by Ag, based on the similarity between the behavior of Cu and Ag on HOPG[5].

We had two Ag/a-C NW samples (or more correctly, "nanostructure" samples, since only a small fraction of the features were actually wires). The samples were grown by MBE at MPI-Stuttgart and had known Ag feature densities, as imaged with SEM and shown in Figs. 10 and 14. For both samples, Ag was deposited by MBE with the substrate held at 1073 K. The MPI Ag NW sample was grown on MPI a-C of film thickness 30-50 nm. The Ag feature density on this sample was 0.1-1 μm^{-2} depending on the region, with an average density of 0.3 μm^{-2}. The second Ag NW sample was grown on Ames-2 a-C, which had a very thick a-C layer (>> 100 nm). The Ag feature density on this sample was 0.01-0.1 μm^{-2} and highly non-uniform, with an average feature density of ~ 0.05 μm^{-2}. Both samples were annealed in UHV for 2 hours at 1050 K to desorb the Ag nanostructures. The Ames-2 sample was annealed for an additional 3 hours after difficulty imaging with STM. For both samples, 3 areas were imaged on different regions of the sample.

Results for the holes experiment are summarized in Table 1. On the MPI a-C sample, a total of 33 holes were found over an area of 50 μm^2, for a total hole density of 0.7 μm^{-2}, which is within the range of the initial nanostructure density (0.1-1 μm^{-2}). The holes were 10-40 nm deep (see Figs. 11-13), but the measurable depth was possibly limited by the width of the STM tip. Many of the holes appeared oblong in shape and oriented in the same direction, which may be a tip effect, as the original Ag features were not particularly oblong or oriented in the same direction (see Fig. 10). The holes were several hundreds of nm's in length and 50-200 nm in width, in reasonable agreement with the size of Ag features on the surface: Metal NW's have diameters on the order of 100 nm[1]. Unscarred regions of the surface appeared to retain a similar texture to the clean a-C surface, as shown comparatively in Fig. 13. This result is in

contrast with the deformation of the a-C surface that we saw with Cu on a-C at 800 K, which may have been caused by intercalated Cu.

The Ames-2 sample was more difficult to image with STM than the MPI sample. Because the initial Ag feature density on this surface was so low (0.01-0.1 μm^{-2}), a large area of 280 μm^2 was scanned with STM. An unusually wide image frame of 4 μm x 4 μm was used for much of the survey to cover more area. Eventually an area was found which contained 2 holes, marked with arrows in Fig. 15(c). Based on this limited finding, the overall hole density on this surface is 0.007 μm^{-2}, which was close to the lower end of the pre-heat feature density of 0.01-0.1 μm^{-2}. The appearance of the hole in the upper right of Fig. 15(c) looks very much like the donut-shaped features in Fig. 14(b) and is comparable in lateral dimensions (~ 1 μm). The two holes had depths of 15 and 30 nm, respectively, below the a-C plane, as shown in Fig. 16. The areas of unadorned a-C terrace showed normal clean a-C morphology, as shown in Fig. 17 in comparison with a clean Ames-3 a-C sample.

6.5 Fabrication of Metal Nanowires

In this part of the study, metal NW's were fabricated by PVD (either MBE or magnetron sputtering) on a variety of substrates held at elevated temperatures during deposition. The NW's were typically 50 to several hundred nm's in diameter and microns in length. Nanowire length and width both increased as a function of deposition time[1]. A full accounting of the types of NW grown, their growth parameters, quality, stability, and density (both NW density and as a fraction of total feature density) are detailed in Table 2. Figs. 20-34 show SEM and TEM images of the nanowires produced as part of this thesis work, and are referenced in Table 2 for convenience. As can be seen from the figures, there were a variety of nanostructures produced

on these surfaces besides NW's, including compact faceted structures, platelets, bar-bells, and other hybrid structures (see Fig. 25 for best example). The relative NW yield was at best 1/3 of the total nanostructure yield.

6.5.1 General methods

6.5.1.1 MBE

Molecular Beam Epitaxy (MBE) is synonymous with thermal evaporation of the target material onto the substrate (see Fig. 18). Metal adatoms deposited by thermal evaporation have very low kinetic energy. NW growth by MBE have produced arrays of high-quality single-crystalline wire, especially for Cu as seen in Figs. 20-22. A case study of Cu nanowires grown on a-C is described in section 6.5.3, below. Standard deposition conditions for MBE growth was with an effusion cell (crucible) with its orifice angled at 45° to the substrate normal. The substrates were clipped to a sample stage rotating at 20 rpm during deposition. Chamber base pressure was 10^{-8} – 10^{-9} mbar. Typical deposition rate is 0.5 Å/s for 1 hr (180 nm nominal thickness). a-C substrate films were magnetron sputtered to a thickness of 10-100 nm, with a preferred thickness of 30-50 nm. For Ni, an electron beam was used to heat the target material directly. NW growth by MBE was performed at MPI Stuttgart.

6.5.1.2 Magnetron sputtering

Magnetron sputtering is a form of physical vapor deposition where a target material (the material to be sputtered) is bombarded with Ar^+ ions from a plasma generated above the target and sustained by magnetic confinement of electrons. The bombardment causes particles of the

target material to be ejected toward the substrate. Magnetron sputtering is an interesting candidate for NW growth because the energy of metal adatoms can be controlled by changing sputter power as well as vapor pressure of the background gas (typically Ar)[6; 7], with pressure being the dominant factor. Controlling adatom energy is of great importance for controlling stress in thin film deposition. For NW growth, magnetron sputtering generally produces wires of less-pristine quality than MBE deposition. Not surprisingly, the magnetron parameters which have been most successful are those which minimize adatom energy, i.e., those which mimic thermal deposition. In general, this is $\approx 5 \times 10^{-3}$ mbar Ar and a very low sputter power (7 W or less). Sputter rates differ by material and by instrument. Magnetic materials (Fe in this thesis work) are particularly difficult to sputter because the magnetic field of the target shunts the magnetic field produced by the instrument magnet, which interferes with electron confinement over the target. To mitigate this, a stronger magnet and thinner target were used. NW's were produced by magnetron sputtering at both MPI-Stuttgart and at the Ames Laboratory. Both facilities used Kurt J. Lesker magnetron chambers for the depositions.

Nanowires produced by magnetron sputtering showed a wide range of morphologies. Single crystalline Ag NW's resulted from magnetron sputtering (see Figs. 28-29), with fcc(111) facets as shown by HRTEM in Fig. 30 (close-packed hexagonal structure shown in panel (b)). However, our attempts to grow Cu NW's by magnetron sputtering resulted in irregular wires having globular features, as in Fig. 23-24. Similar variation in morphology has been seen for Fe NW's, described below.

6.5.2 Specific results: magnetic NW's

Fabricating NW's from magnetic materials such as Ni and Fe is of particular interest for their potential use in magnetic storage media[3]. SEM images of Ni and Fe wires produced in this study are shown in Figs. 31-32, and 34. Ni NW's were produced in low yield by MBE on a-C, graphite and diamond (Fig. 31). Possibly single-crystal Fe NW's were grown in low yield by magnetron sputtering at MPI-Stuttgart on Ni and W substrates, as shown in Fig. 32. TEM images of the Fe NW's are shown in Fig. 33. Fe NW's produced by magnetron sputtering in Ames had a segmented shape, as shown in Fig. 34.

6.5.3 Specific results: Cu NW on MPI a-C

The most prolific NW growth has been seen for Cu on a-C by MBE. This case study compares Cu nanowires grown on a-C substrates MPI-1 (100 nm a-C on native Si), MPI-2 (100 nm a-C on etched Si), and MPI-3 (30 nm a-C on etched Si, with possible previous Ag growth). These three substrates appear similar in STM, as discussed in Chapter 5. Cu NW's were grown on these substrates in the same deposition. The substrates were mounted at equivalent radial distance from the center of a rotating sample stage in the MBE chamber. Each sample was subject to the same Cu flux at the same range of angles.

SEM images of Cu/MPI-1 – MPI-3 are shown in Figs. 20-22, respectively. There was a surprising diversity in NW morphology and overall feature density between the three samples. Samples MPI-2 and MPI-3 (100 nm and 30 nm a-C films, respectively) had a total feature density approximately an order of magnitude higher than sample MPI-1 (100 nm a-C film). Based on this, there is no apparent correlation between feature density and thickness of the a-C film. There was a far lower total feature density on the sample which had a native oxide layer

present on the underlying Si (MPI-1). However, the Richter group has seen no correlation between feature density and the presence of a native oxide layer in their studies. The ratio of NW density to total feature density is 1/4 for both MPI-1 and MPI-2, and 1/8 for MPI-3. We cannot assign a reason for these differences based on this data.

6.5.4 Support for a wagging wire hypothesis

Sample MPI-1 produced particularly long NW's which were bundled together (see Fig. 20). The bundling may be indicative of the growth mechanism of these wires. Because the spacing of these wires is very far compared to the diameter of an individual wire (they are effectively lines extending in space), it is highly unlikely that any two wires growing in a straight line will meet. The long wires on this sample, however, were consistently bundled together. This suggests that the wires rotate or "wag" during growth, and stick together when they touch. If this is true, it implies that the wires are growing at least in part from the base. Since the width of the nanowires also changes as a function of time[1], we can conclude that they also grow in part due to direct impingement of material on the wire or due to diffusion of material from the base up the sides of the wire.

6.6 Conclusions

We have investigated the behavior of Cu on a-C at 300 K. Cu conforms to the contours of the a-C surface and forms an initial monolayer on the surface, in contrast to the 3D growth of Cu/HOPG. Upon annealing to 800 K, coarsening occurs, with some of the Cu consolidating into large islands on the surface. A calculation of surface coverage based on STM images shows that apparent Cu coverage has significantly decreased. We interpret this result to mean that Cu has

diffused into the bulk, which is consistent with TEM images of NW's protruding through a-C and anchored into the underlying Si substrate.

We have also grown metal nanowires by MBE as well as magnetron sputtering from a variety of starting mateirals. NW quality and density is highly variable, even for samples grown on similar substrates within the same deposition chamber. Annealing away Ag NW's (and other nanostructures) from the a-C substrate reveals holes with roughly the same density as the initial metal nanostructures.

Acknowledgements

This work was supported by the Office of Science, Basic Energy Sciences, Materials Sciences and Engineering Division of the U.S. Department of Energy (USDOE), under Contract No. DE–AC02–07CH11358 with the U.S. Department of Energy. We thank Jim Anderegg for his contribution of HOPG substrates. We thank Dr. Gunther Richter for his generous collaboration on this study, and his donation of amorphous carbon and nanowire samples. We thank Ryan Ott and Matt Besser of Ames Laboratory for their work with magnetron sputtering amorphous carbon and nanowire samples.

References

[1] M. Kolb, G. Richter, AIP Conference Proceedings 1300 (2010) 98-105.

[2] M. Schamel, C. Schopf, D. Linsler, S.T. Haag, L. Hofacker, C. Kappel, H.P. Strunk, G. Richter, Int. J. Mat. Res. 102 (2011).

[3] S.D. Bader, S.S.P. Parkin, Annual Review of Condensed Matter Physics 1 (2010) 71-88.

[4] S. Tanuma, C.J. Powell, D.R. Penn, Surface and Interface Analysis 43 (2011) 689-713.

[5] I. Lopez-Salido, D.C. Lim, Y.D. Kim, Surface Science 588 (2005) 6-18.

[6] M. Ohring, Material Science of Thin Films, Elsevier, 2001.

[7] http://en.wikipedia.org/wiki/Sputter_deposition.

Tables

Table 1
Results for the search for holes in a-C substrates after annealing away Ag nanostructures at 1050 K for 2+ hours.

Substrate	**Feature density pre-heat (SEM)**	**Scanned area post-heat (STM, over 3 areas each sample)**	**# of holes**	**Hole density post-heat**
MPI a-C (30-50 nm thick)	0.1 – 1 μm^{-2}	$\approx$ 50 um^2	33	0.7 ± 0.1 holes/um^2
Ames-2 a-C (>> 100 nm thick)	0.01 – 0.1 μm^{-2}	$\approx$ 280 um^2	2	0.007 ± 0.004 holes/um^2

Table 2
Growth parameters for metal nanowire (or nanostructure) growth. Standard deposition conditions for MBE of the metal is with an effusion cell angled 45° to substrate normal rotating at 20 rpm. See Fig. XXX. Typical deposition rate of the metal is 0.5 Å/s for 1 hr (180 nm nominal thickness). a-C substrate films are magnetron sputtered to a thickness of 10-100 nm, with a preferred thickness of 30-50 nm.

Material	**Substrate**	**Deposition Type**	**Deposition Parameters**	**NW Density /Total feature density (μm^{-2}), by substrate**	**Location/Notes**	**Stability**	**Figure #**
Cu	sputtered a-C on Si	MBE (effusion cell)	T_s = 823-973 K, 953 K preferred	MPI-1: 0.01/0.04 (very long) MPI-2: 0.15/0.6 MPI-3: 0.13/1	@MPI: use 30-50 nm thick a-C for most whiskers.	5-10nm oxidation immediately, then slow oxidation (10-20nm after 6 months), on ~100nm wide whisker	20-23
		magnetron	T_s = 953 K, 12 W, .8 Å/s, 45 min	Ames-1: unknown Ames-3: ≈ 0.02/0.05	@Ames: Irregular, i.e. not single crystal. @MPI: none		
	HOPG	MBE (effusion cell)	T_s = 953 K	0.1/1	@MPI: Several classes of features (NW's, platelets, barbells)		25
		Magnetron	T_s = 953 K, 12 W, .8 Å/s, 45 min	0	@Ames		23-24
	Ti-C	MBE (effusion cell)	T_s = 923-973 K		@MPI: Limited success		

Table 2 cont.

Material	Substrate	Deposition Type	Deposition Parameters	NW Density /Total feature density (μm^{-2}), by substrate	Location/Notes	Stability	Figure #
Ag	a-C on Si	MBE (effusion cell)	T_s = 973 K	MPI a-C: 0.06.0.5 Ames-2: 0.005/0.05	@MPI: 923-1073 K has been tried with varying success.	5-10nm oxidation immediately, then slow oxidation (10-20nm after 6 months), on ~100nm wide whisker	26-27
		magnetron	T_s = 923 K, 7 W, 120 min (MPI), Ts = 923 K, 8 W, .9 Å/s, 42 min (Ames)	MPI a-C (30 nm): very low	@Ames: shown, wires on edges only @MPI: unsuccessful		28
	W foil	MBE (effusion cell)	T_s = 973 K		@MPI: not reproducible		
		magnetron	T_s = 923 K	0.05/substrate covered	@MPI: many		29-30
	Nb wire	magnetron			@MPI: some		
	Ni wire	magnetron			@MPI: some		
Au	a-C or W (substrate unknown)	MBE (effusion cell)	T_s = 953 K		@MPI		
Ni	a-C on Si	MBE (e-beam)	T_s = 933 K	MPI a-C: none Ames-2: 0.05/5	@MPI		31
	graphite			0.01/1	@MPI		31
	diamond			0.1	@MPI		31
	sputtered W on Si (400nm)				@MPI: a few wires laying down. Mostly negative result		
		magnetron	T_s = 973 K, 4.2x10^-3 mbar Ar, 150 W, 30 min, 300 nm Ni thickness		@MPI: didn't work		
	W foil						
	W wire						
	a-C on Si						

Table 2 cont.

Material	Substrate	Deposition Type	Deposition Parameters	NW Density /Total feature density (μm^{-2}), by substrate	Location/Notes	Stability	Figure #
Fe	W	MBE (e-beam)			Very messy	fast, continuous oxidation	
Co	Ti-C	magnetron	T_s = 1073 K, 100 W, 1hr, 7x10^-3 mbar Ar (MPI), Ts = 1073 K, 5x10^-3 torr, 125 W (Ames)	@MPI: 0.001 @Ames: 0.1	@MPI: a few small ones, possibly single crystal @Ames: better yield but tapered/segmented	fast, continuous oxidation	32-34
Pd	TiO_2 on Si	magnetron MBE (e-beam)	T_s = 1073 K, 100 W, 1hr, 7x10^-3 mbar Ar (MPI), Ts = 1073 K, 5x10^-3 torr, 125 W (Ames) T_s = 973 K		@MPI: rough, can't tell		
		magnetron MBE (e-beam) MBE (e-beam)	T_s = 1073 K, 100 W, 1hr, 7x10^-3 mbar Ar (MPI), Ts = 1073 K, 5x10^-3 torr, 125 W (Ames) T_s = 973 K T_s = 1083 K		@MPI: none		
	Zr				@MPI: none		
	Ni			Very low	@MPI: found one at low mag, need SEM		32
	a-C on Si				@MPI: none		
	CaF w/copper islands?				@MPI: not reproducible		
					@MPI		
Al	Ti-C, sapphire, W	MBE (e-beam)	T_s = 673-798 K		@MPI		
Si	Si	VLS (on accident)	T_s = 1073 K		@MPI: Trying to grow Au, but instead grew Si by VLS		
Co(oxide)	high-purity Co wire	oven (in air)			@MPI		

Table 2 cont.

Material	Substrate	Deposition Type	Deposition Parameters	NW Density /Total feature density (μm^{-2}), by substrate	Location/Notes	Stability	Figure #
NaCl	a-C on Ge, Si, and Al2O3	thermal boat	T_s = 573 K		@MPI		
KBr	a-C on Ge, Si, and Al2O3	thermal boat	T_s = 573 K		@MPI		
Dy					@MPI: didn't work		

Figures

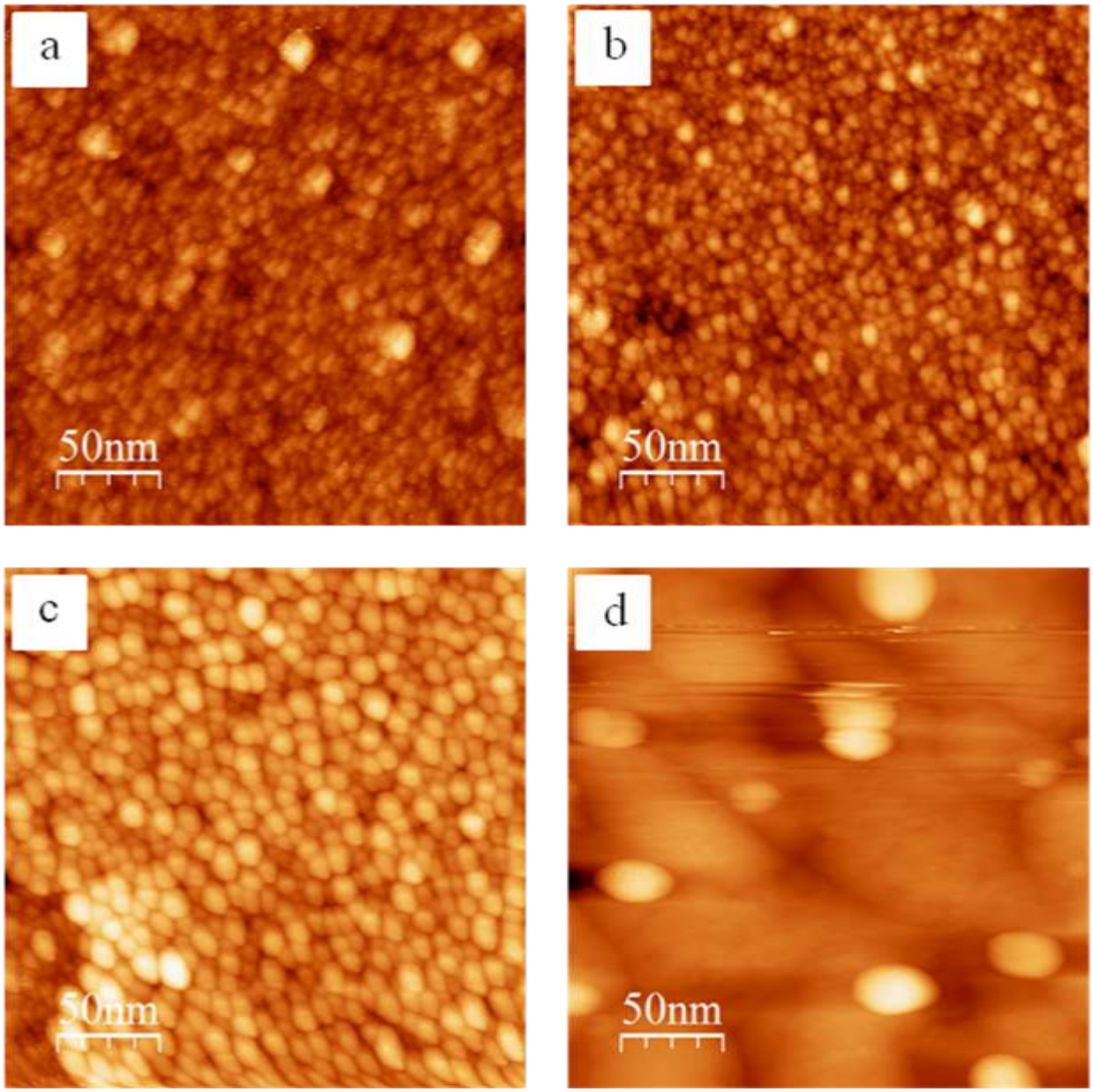

Fig. 1
STM images of the Ames-3 a-C/Si substrate (a) clean surface; (b) after 0.22 ML Cu deposited at 300 K; (c) after 1.3 ML Cu deposited at 300 K; (d) after heating the 1.3 ML Cu surface to 800 K. All images 250 nm x 250 nm, V_{tip} = -2.5 V, i = 0.05 nA.

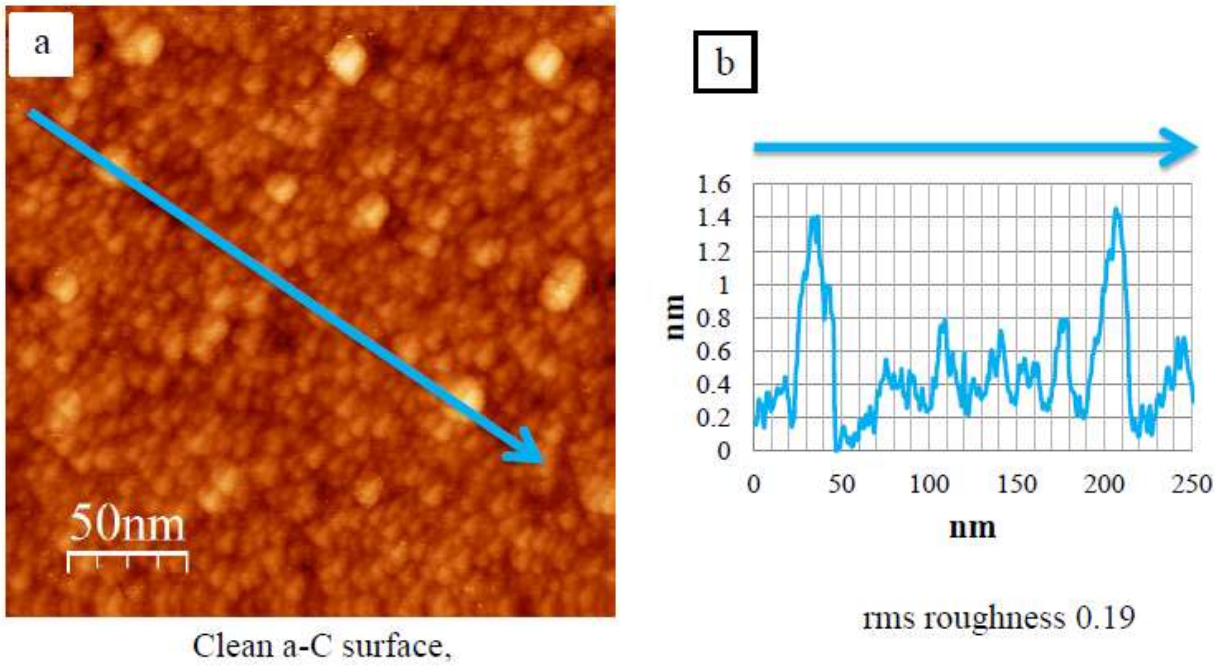

Fig. 2
(a) STM image of the clean Ames-3 a-C surface, 250 nm x 250 nm, V_{tip} = -2.5 V, *i* = 0.05 nA; and (b) line profile from (a).

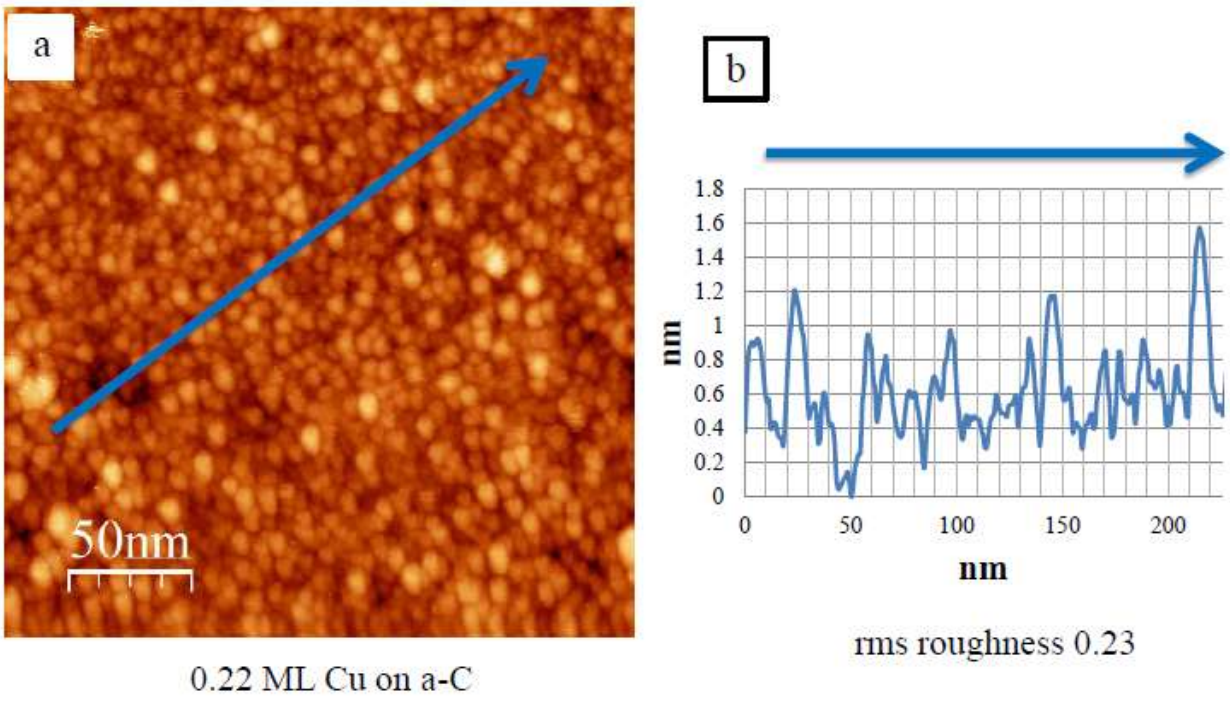

Fig. 3
(a) STM image of the Ames-3 a-C surface after 0.22 ML Cu deposited at 300 K, 250 nm x 250 nm, V_{tip} = -2.5 V, i = 0.05 nA; and (b) line profile from (a).

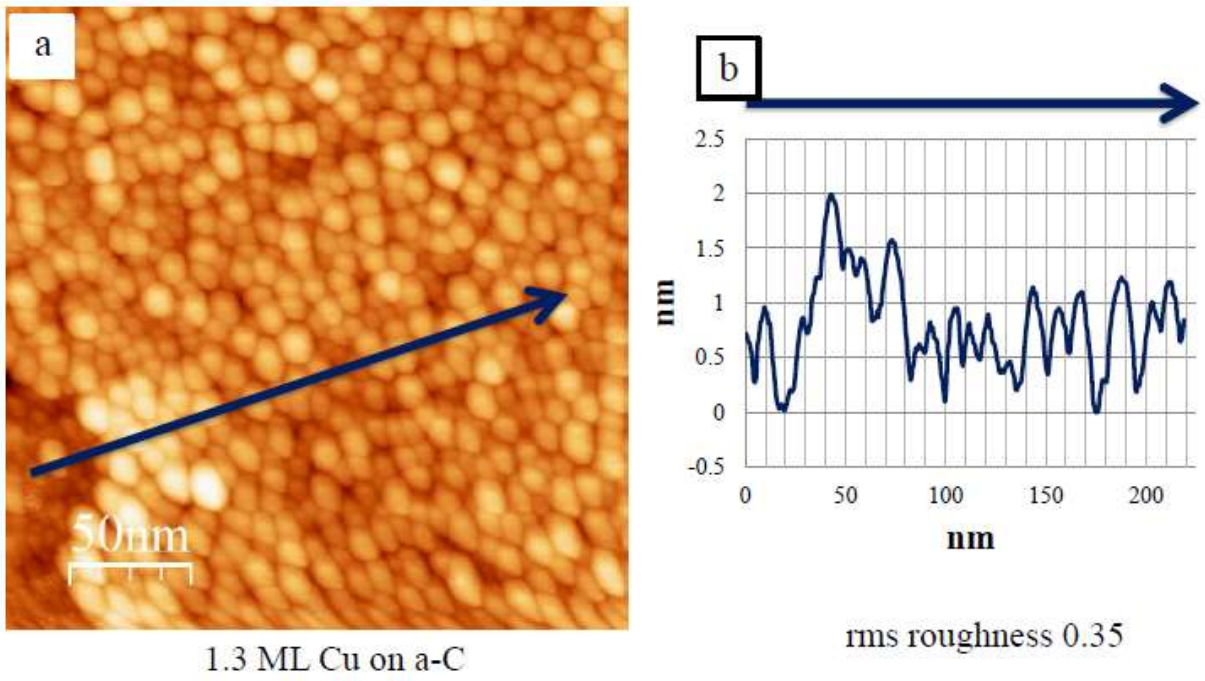

Fig. 4
(a) STM image of the Ames-3 a-C surface after 1.3 ML Cu deposited at 300 K, 250 nm x 250 nm, V_{tip} = -2.5 V, i = 0.05 nA; and (b) line profile from (a).

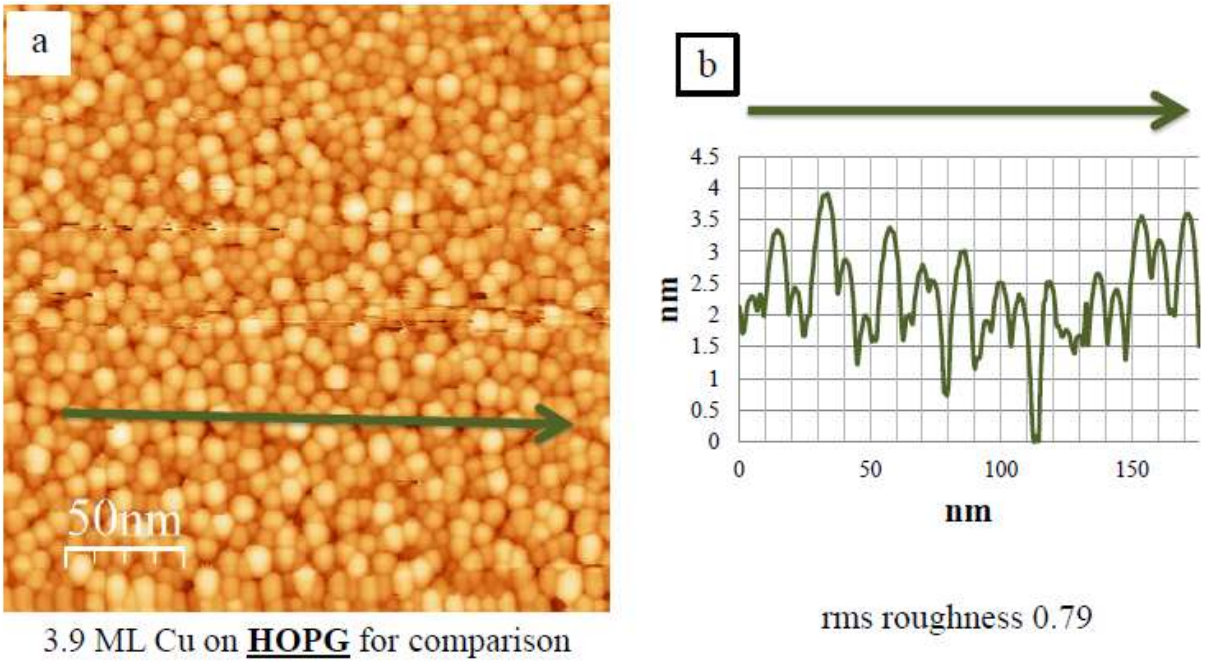

Fig. 5
(a) STM image of 3.9 ML Cu on HOPG deposited at 300 K, 250 nm x 250 nm, V_{tip} = -1.8 V, *i* = 0.1 nA; and (b) line profile from (a).

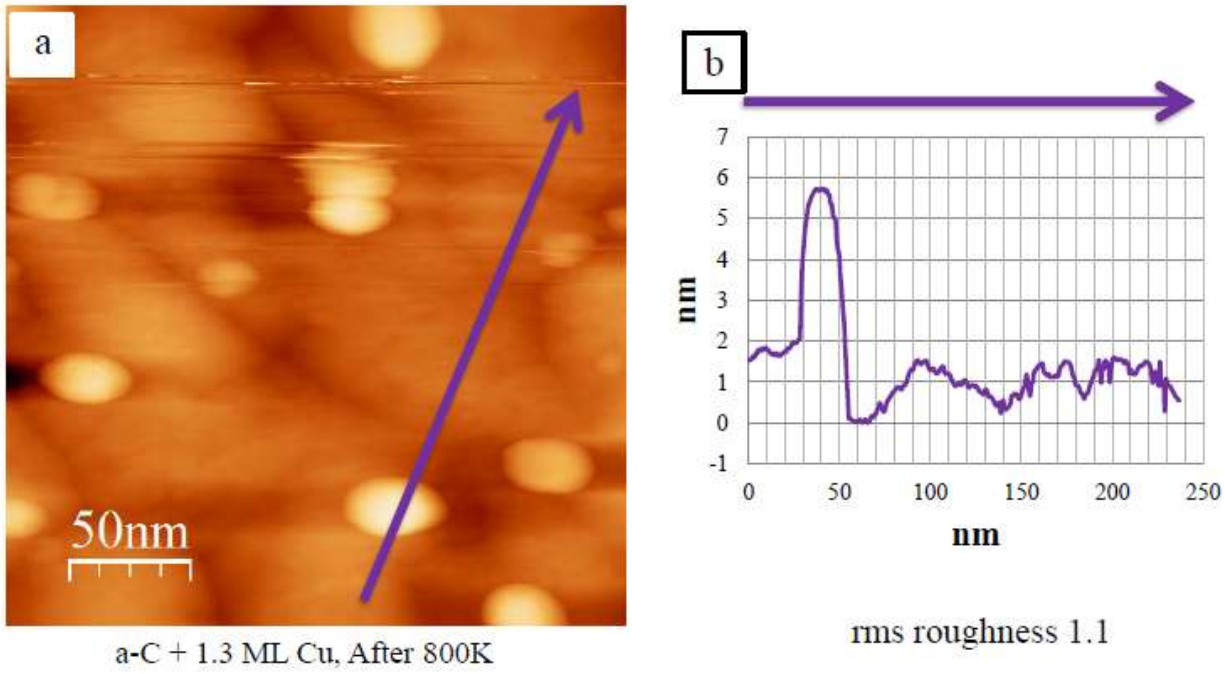

Fig. 6
(a) STM image of the Ames-3 a-C surface after 1.3 ML Cu deposited at 300 K and subsequent heating to 800 K, 250 nm x 250 nm, V_{tip} = -2.5 V, *i* = 0.05 nA; and (b) line profile from (a).

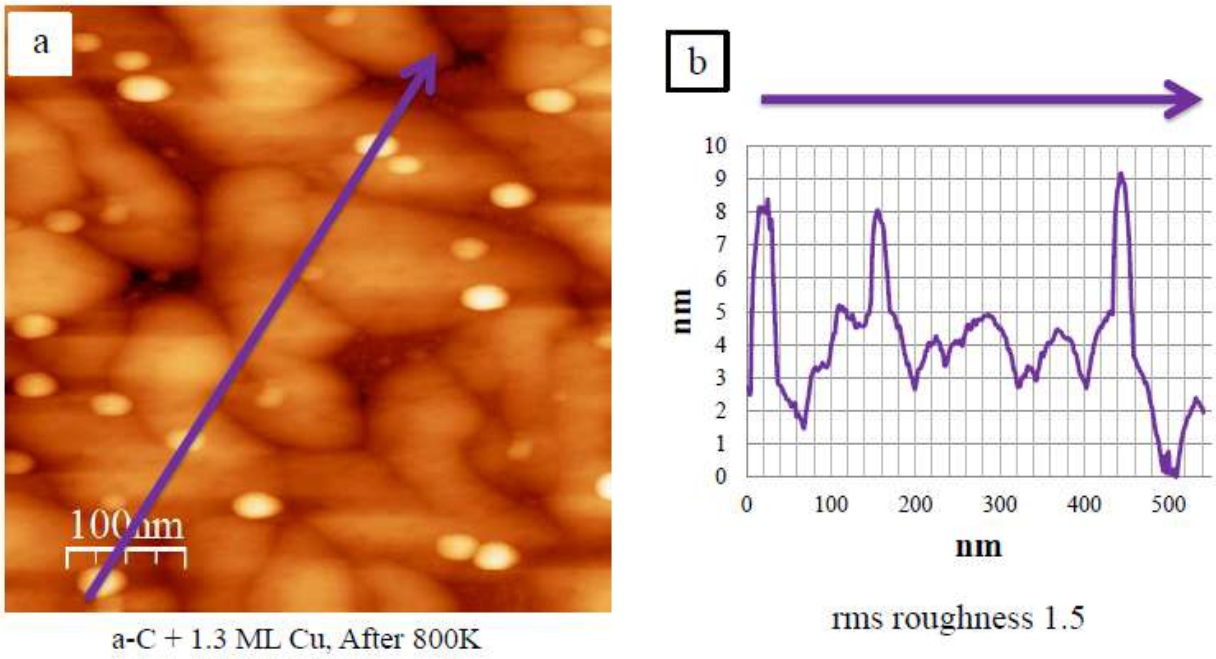

Fig. 7
(a) STM image of the Ames-3 a-C surface after 1.3 ML Cu deposited at 300 K and subsequent heating to 800 K, 500 nm x 500 nm, V_{tip} = -2.5 V, *i* = 0.05 nA; and (b) line profile from (a).

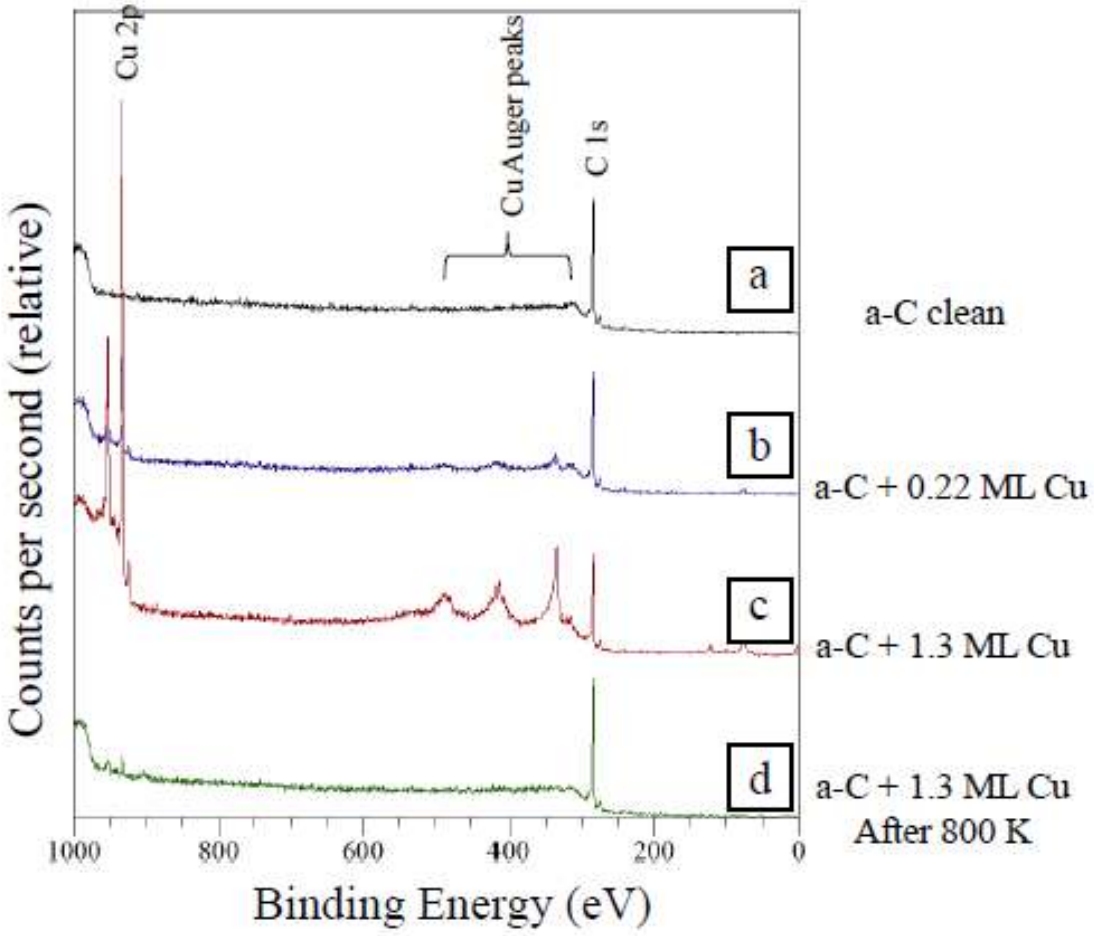

Fig. 8
XPS survey spectra of the Ames-3 a-C/Si substrate (a) clean surface; (b) after 0.22 ML Cu deposited at 300 K; (c) after 1.3 ML Cu deposited at 300 K; (d) after heating the 1.3 ML Cu surface to 800 K.

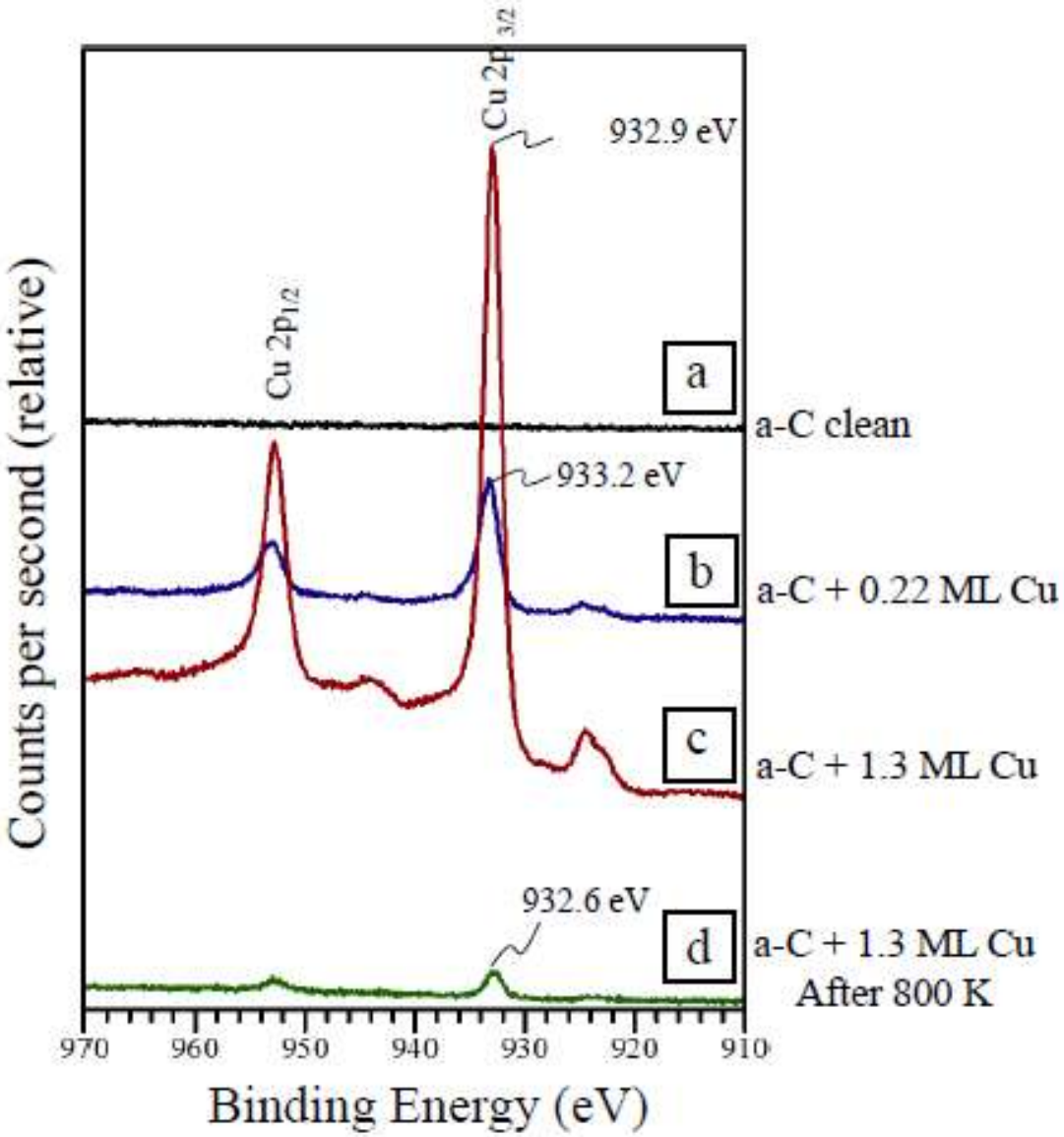

Fig. 9
XPS spectra of the Cu 2p region of the Ames-3 a-C/Si substrate (a) clean surface; (b) after 0.22 ML Cu deposited at 300 K; (c) after 1.3 ML Cu deposited at 300 K; (d) after heating the 1.3 ML Cu surface to 800 K.

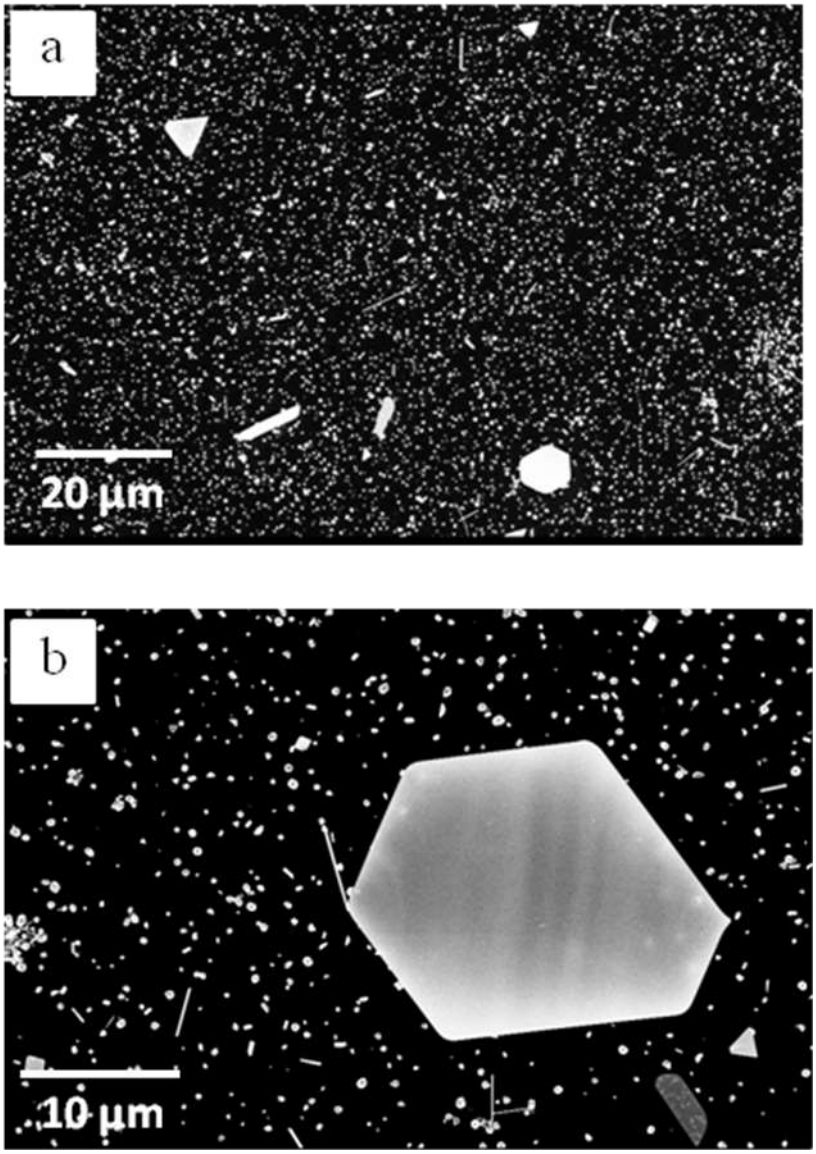

Fig. 10
(a-b) SEM images of Ag NW's (and other structures) on MPI a-C. Average feature density ≈ 0.3 μm^{-2}.

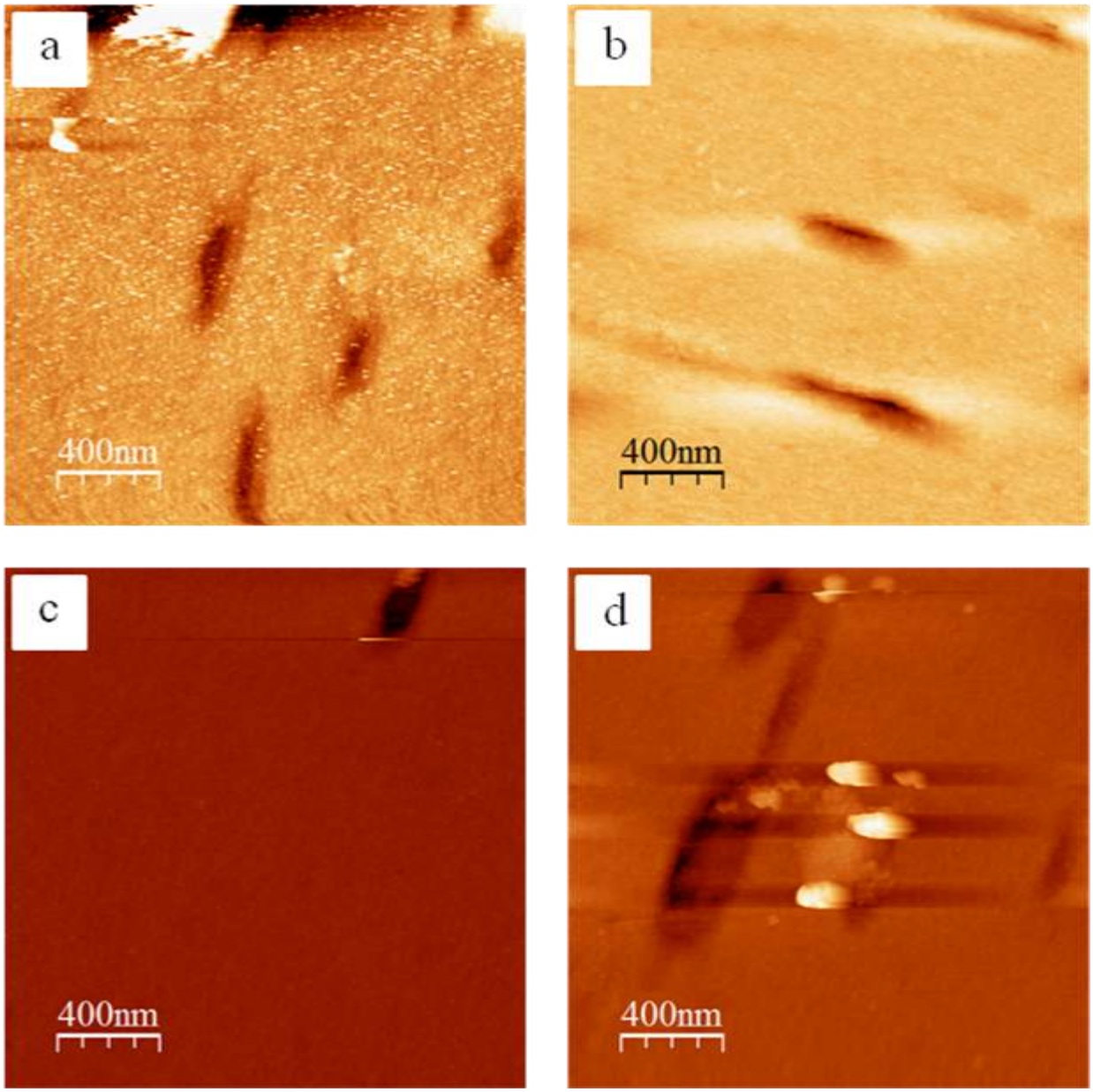

Fig. 11
(a-d) STM images of holes on MPI a-C after annealing away Ag nanostructures; (a) V_{tip} = -1.0 V, *i* = 0.1 nA; (b-d) V_{tip} = -5.0 V, *i* = 0.1 nA. All images are 2 μm x 2 μm.

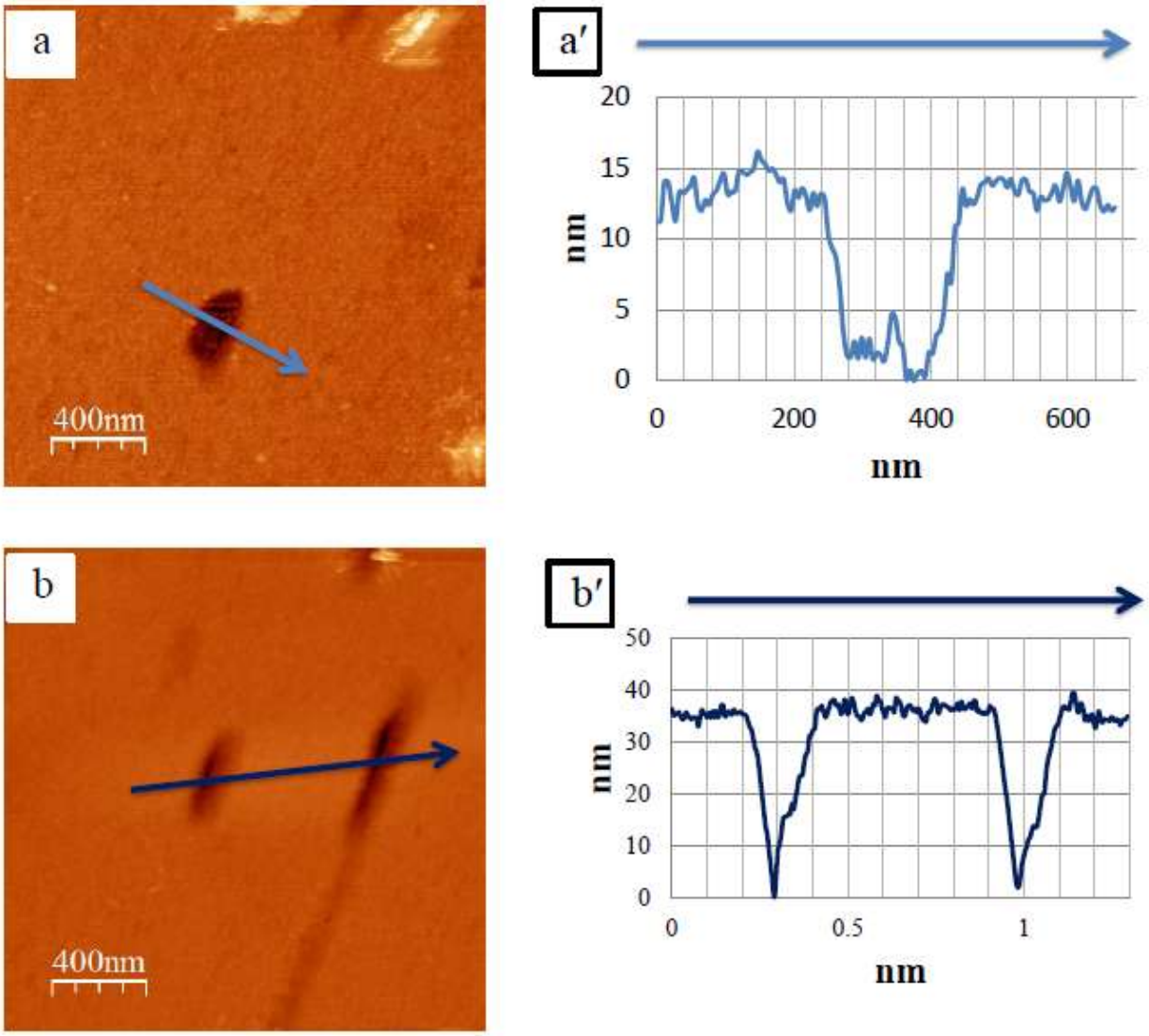

Fig. 12
(a-b) STM images and (a′-b′) respective line profile of holes on MPI a-C after annealing away Ag nanostructures. Both images 2 μm x 2 μm, V_{tip} = -5.0 V, i = 0.1 nA.

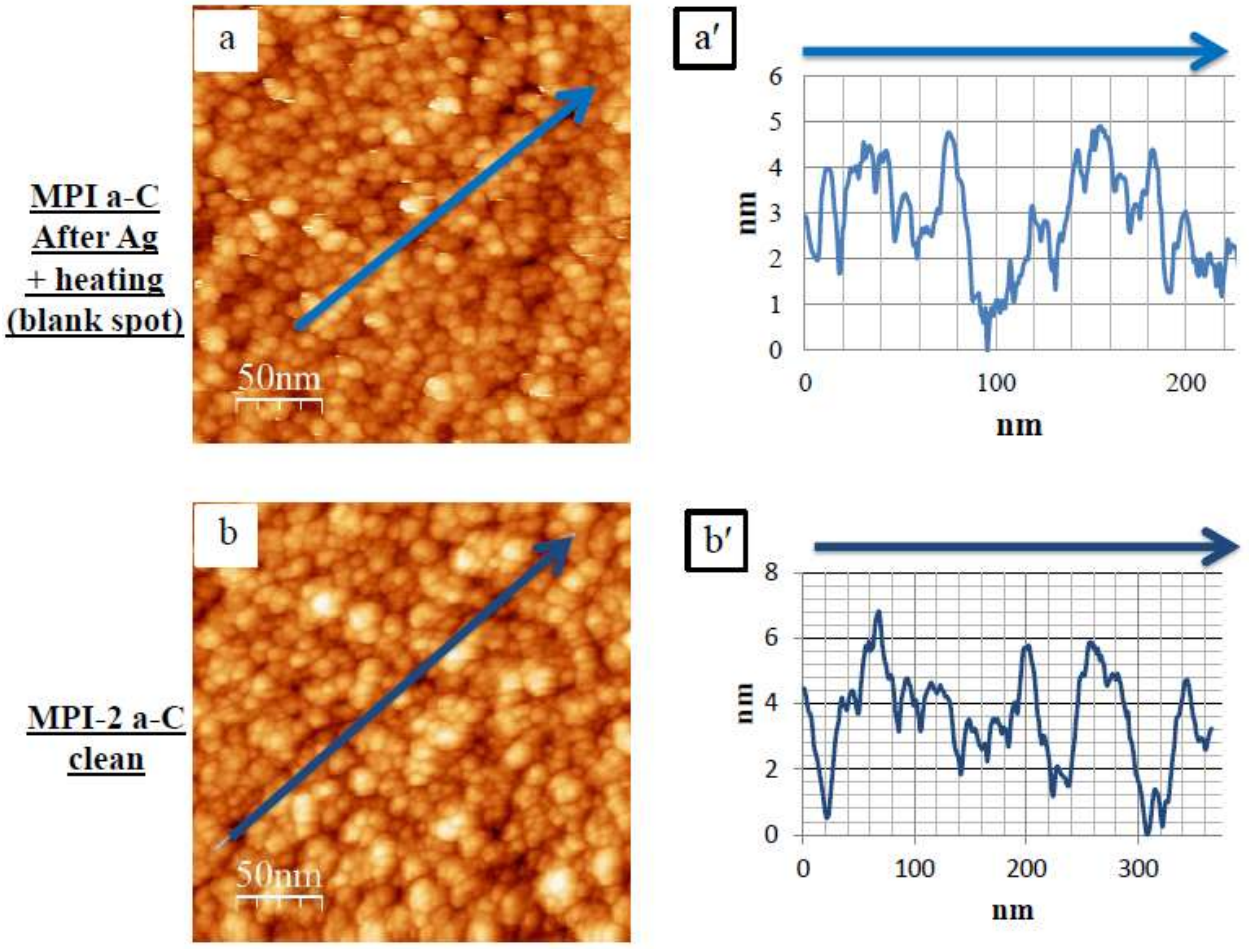

Fig. 13
(a-a′) STM image of a blank area from MPI a-C after annealing away Ag nanostructures with line profile; and (b-b′) STM image of a the clean MPI-2 a-C surface with line profile for comparison. (a) V_{tip} = -1.0 V, *i* = 0.2 nA; (b) V_{tip} = -5.1 V, *i* = 2.4 nA. Both images are 250 nm x 250 nm.

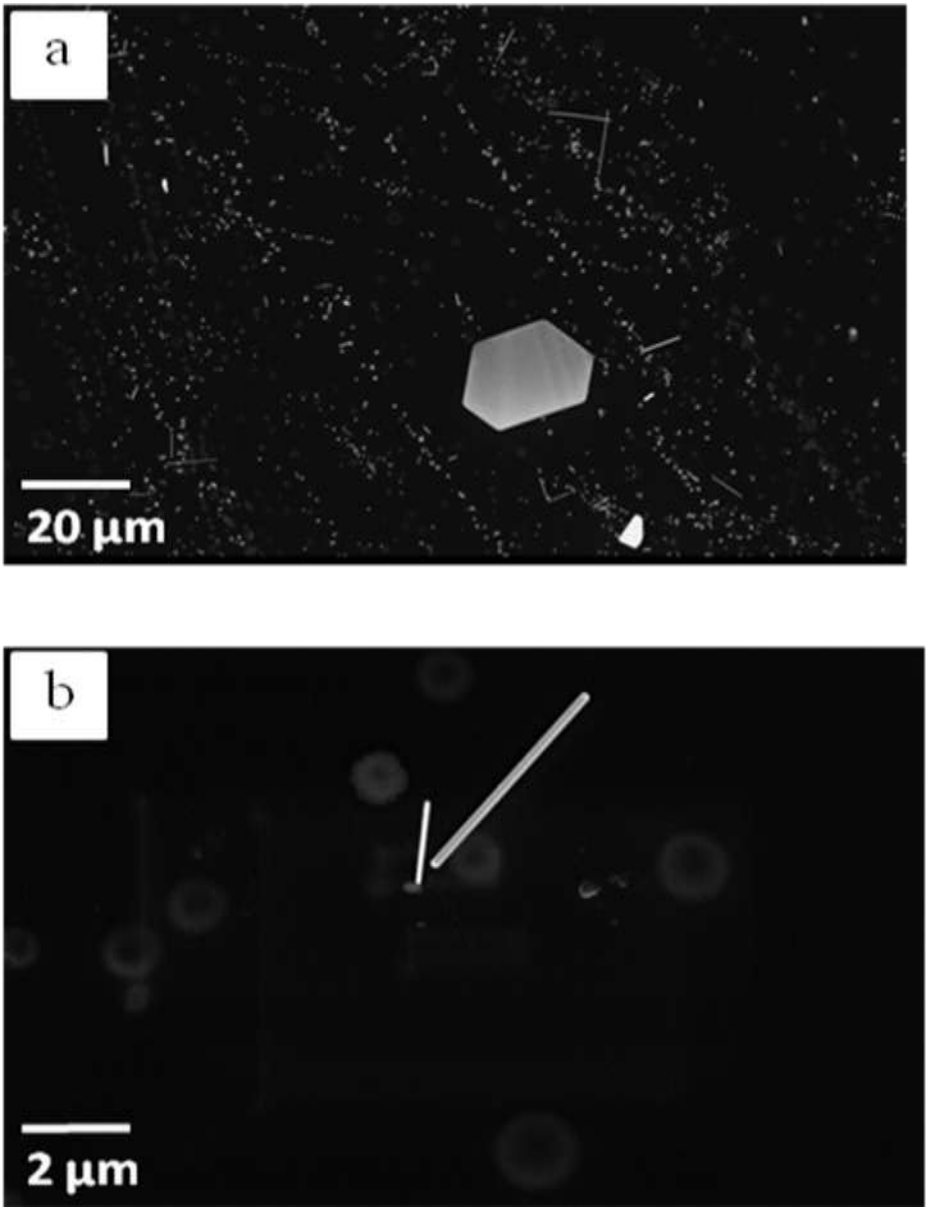

Fig. 14
(a-b) SEM images of Ag NW's (and other structures) on Ames-2 a-C. Average feature density ≈ 0.05 μm^{-2}.

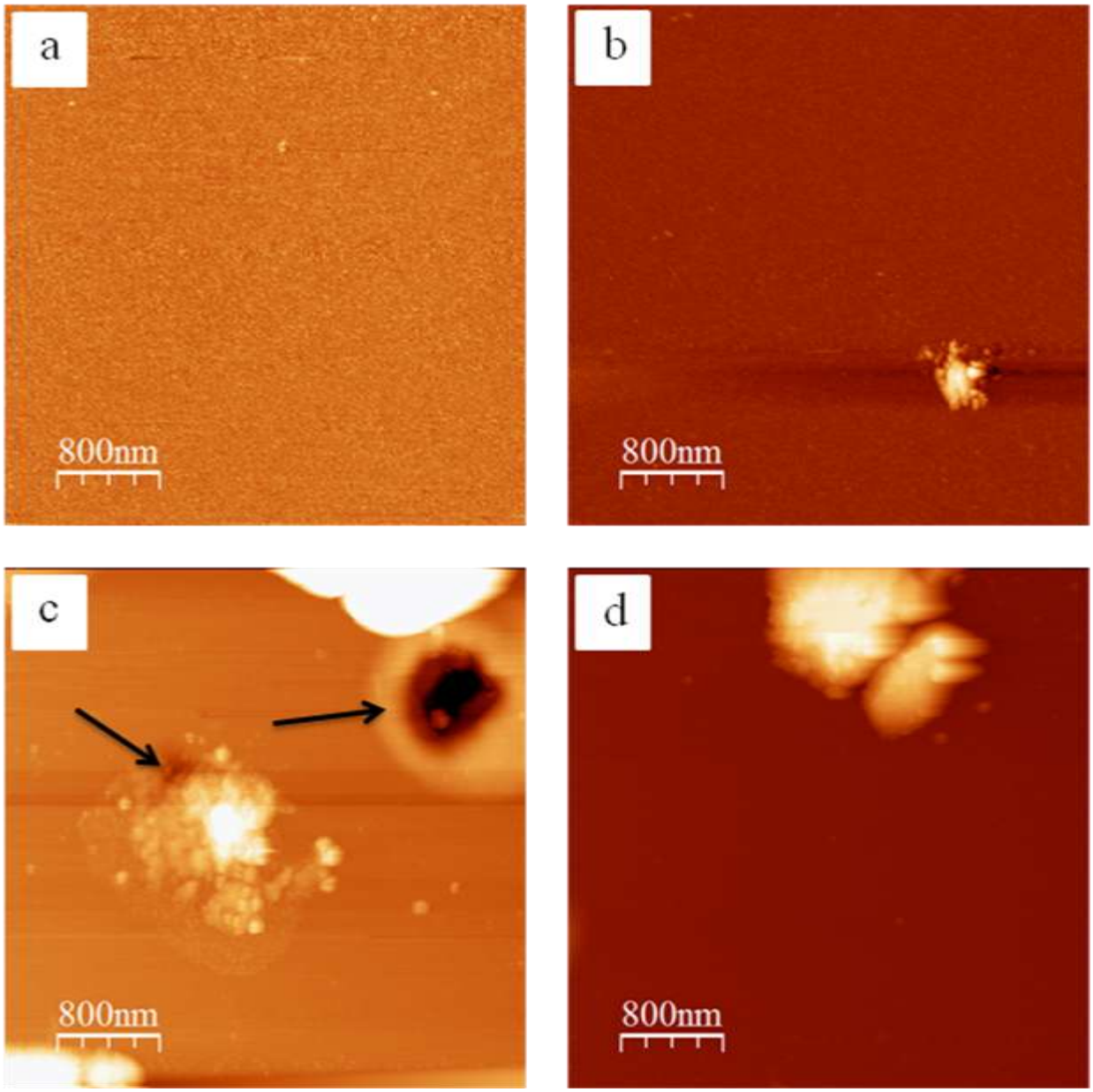

Fig. 15
STM images of Ames-2 a-C after annealing away Ag nanostructures. Residual Ag structures are present in (b-d), and two holes are marked in (c) with arrows. (a-b) V_{tip} = 5.0 V, *i* = 0.1 nA; (c-d) V_{tip} = 7.0 V, *i* = 0.1 nA. All images are 4 μm x 4 μm.

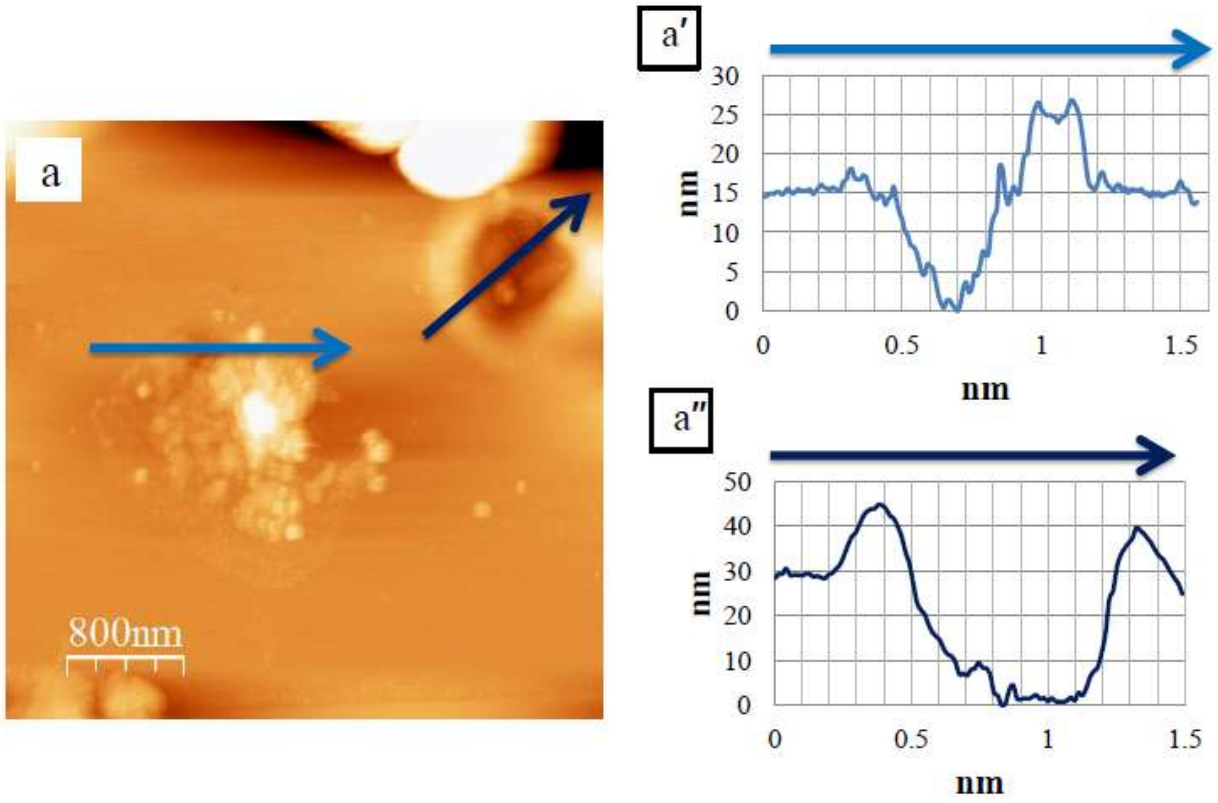

Fig. 16
(a) STM image of Ames-2 after annealing away Ag nanostructures, 4 μm x 4 μm, V_{tip} = 7.0 V, *i* = 0.1 nA; and (a′-a″) line profiles of the holes.

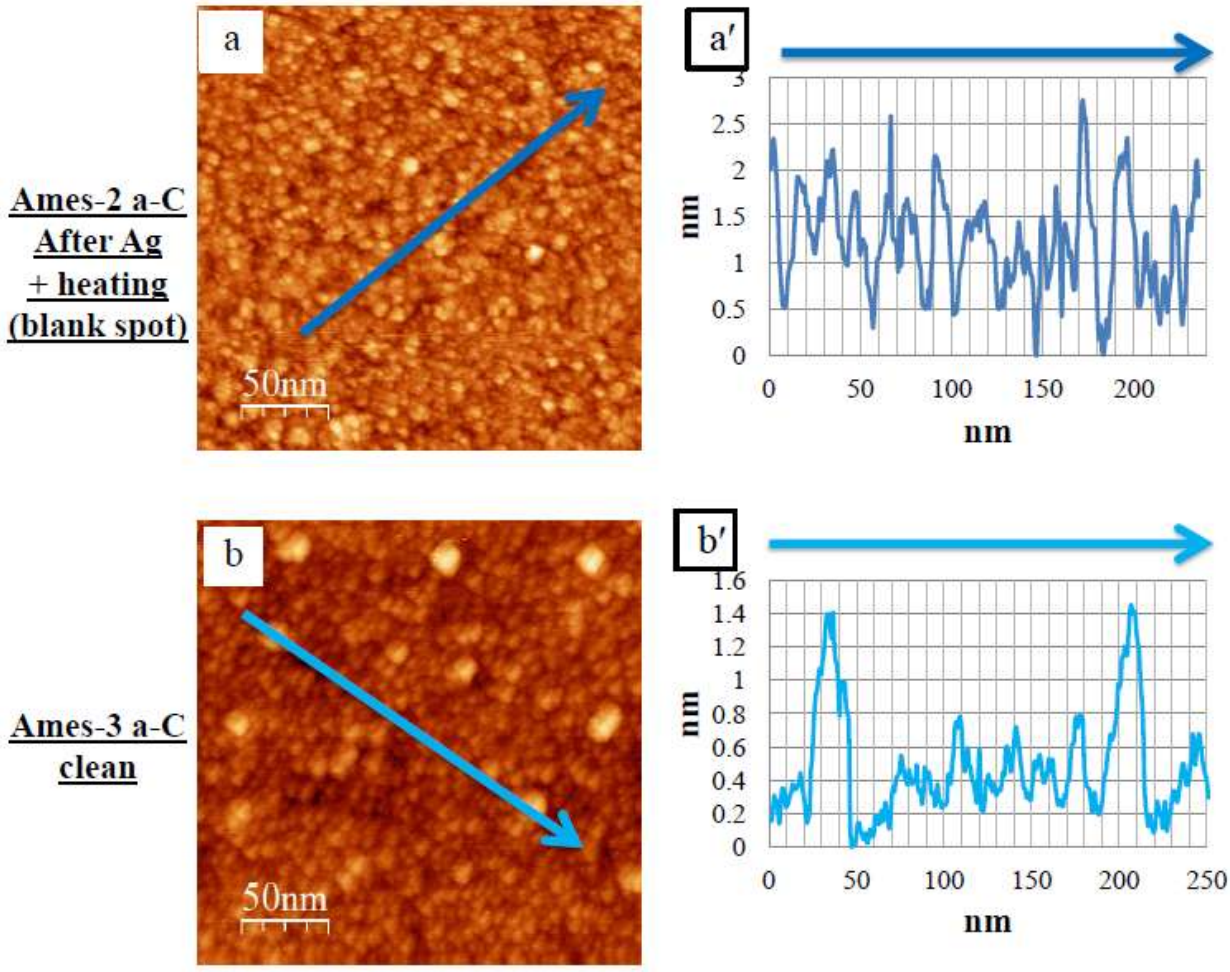

Fig. 17
(a) STM image of a blank area from Ames-2 a-C after annealing away Ag nanostructures, V_{tip} = 5.0 V, i = 0.1 nA; (a′) line profile from (a); (b) STM image of a the clean Ames-3 a-C surface, V_{tip} = -5.1 V, i = 2.4 nA; and (b′) line profile for comparison. Both images are 250 nm x 250 nm.

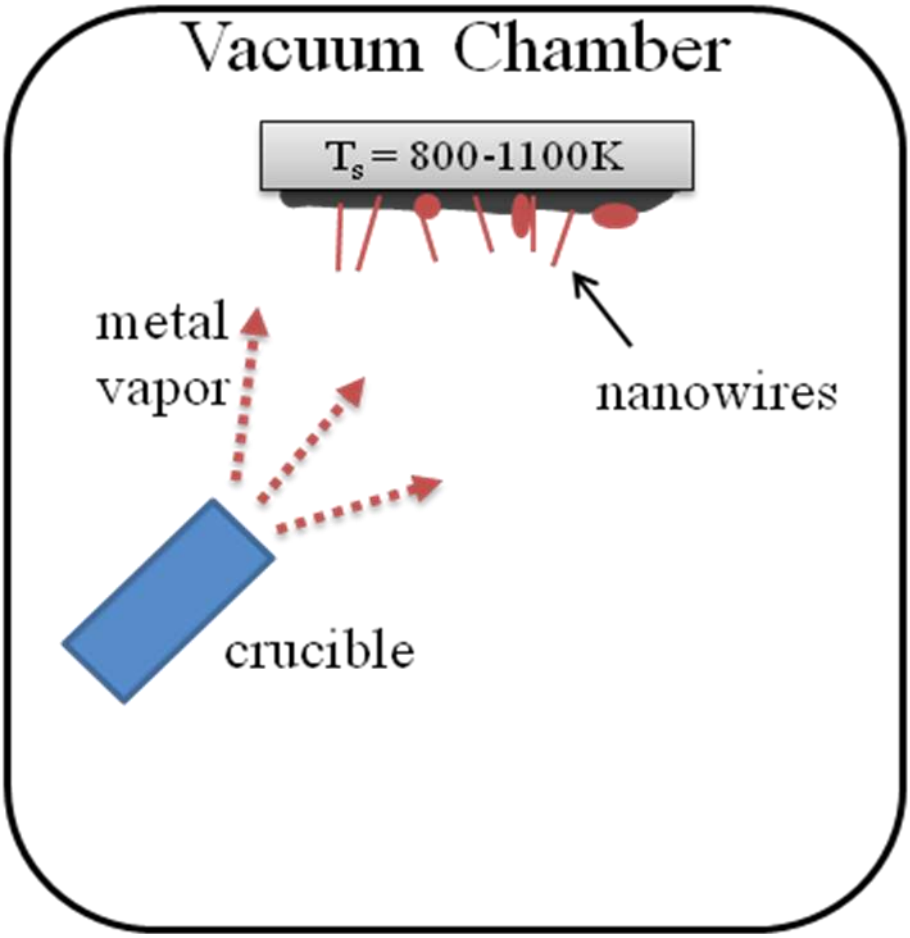

Fig. 18
Schematic diagram of a MBE deposition system for producing metal nanowires.

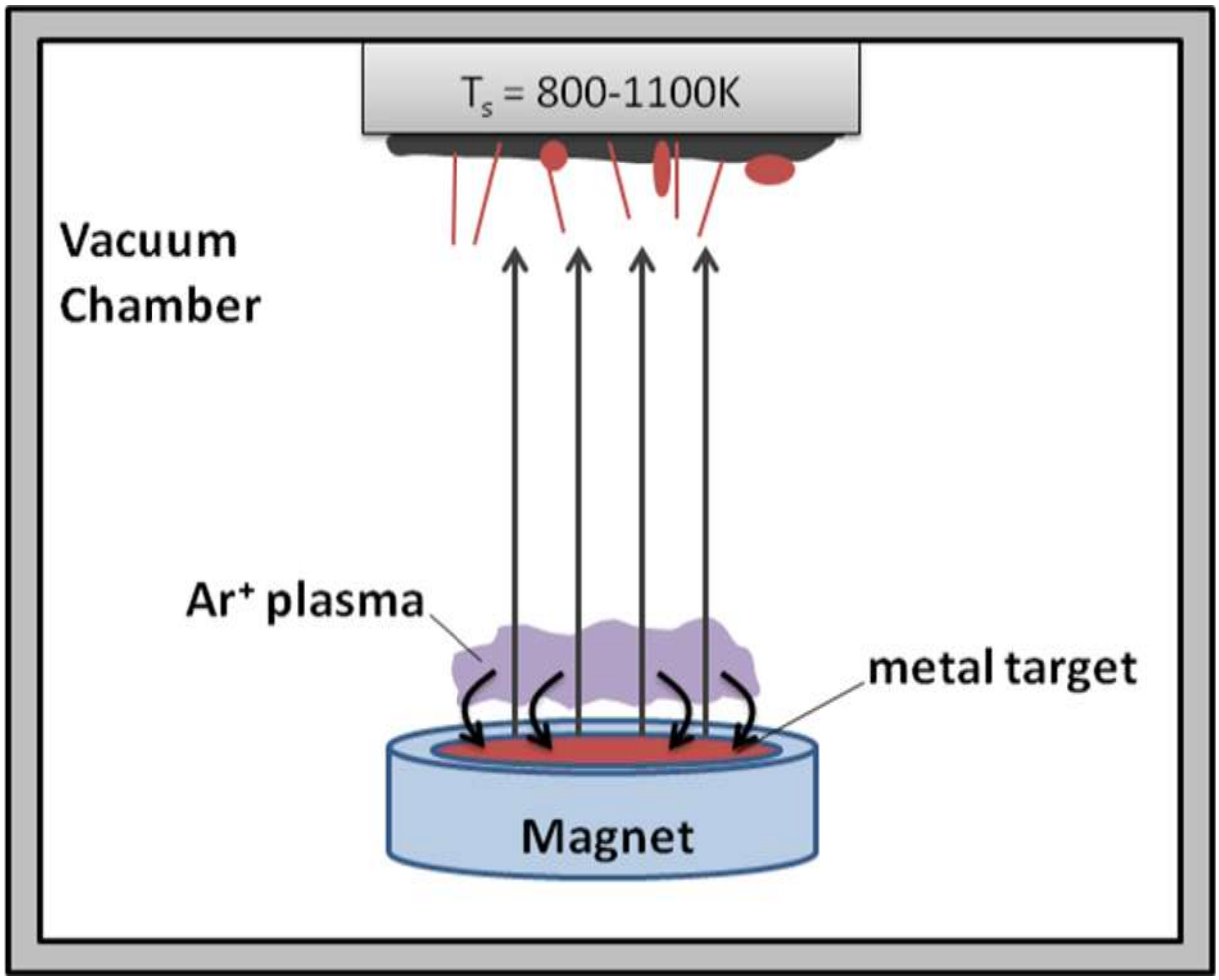

Fig. 19
Schematic diagram of a magnetron sputter system for producing metal nanowires.

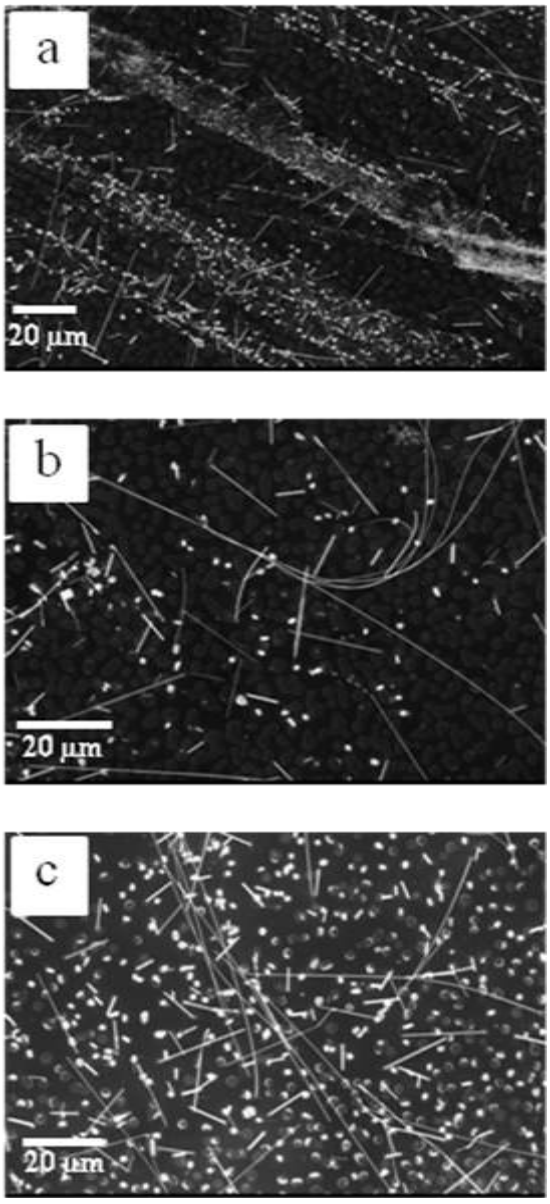

Fig. 20
(a-c) SEM images of Cu NW's (and other nanostructures) grown on MPI-1 a-C by MBE.

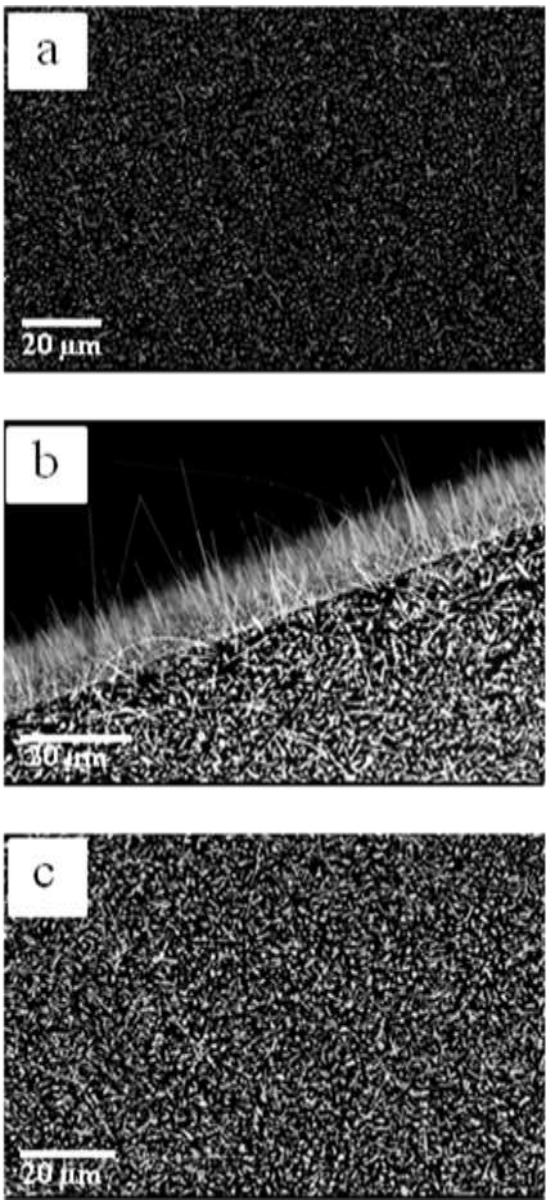

Fig. 21
(a-c) SEM images of Cu NW's (and other nanostructures) grown on MPI-2 a-C by MBE.

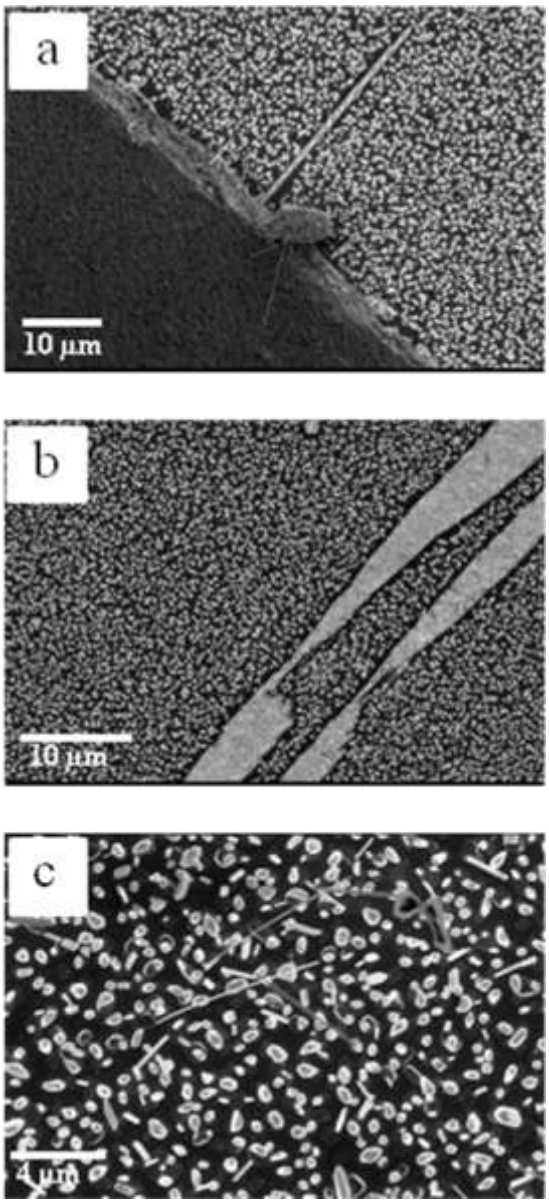

Fig. 22
(a-c) SEM images of Cu NW's (and other nanostructures) grown on MPI-3 a-C by MBE.

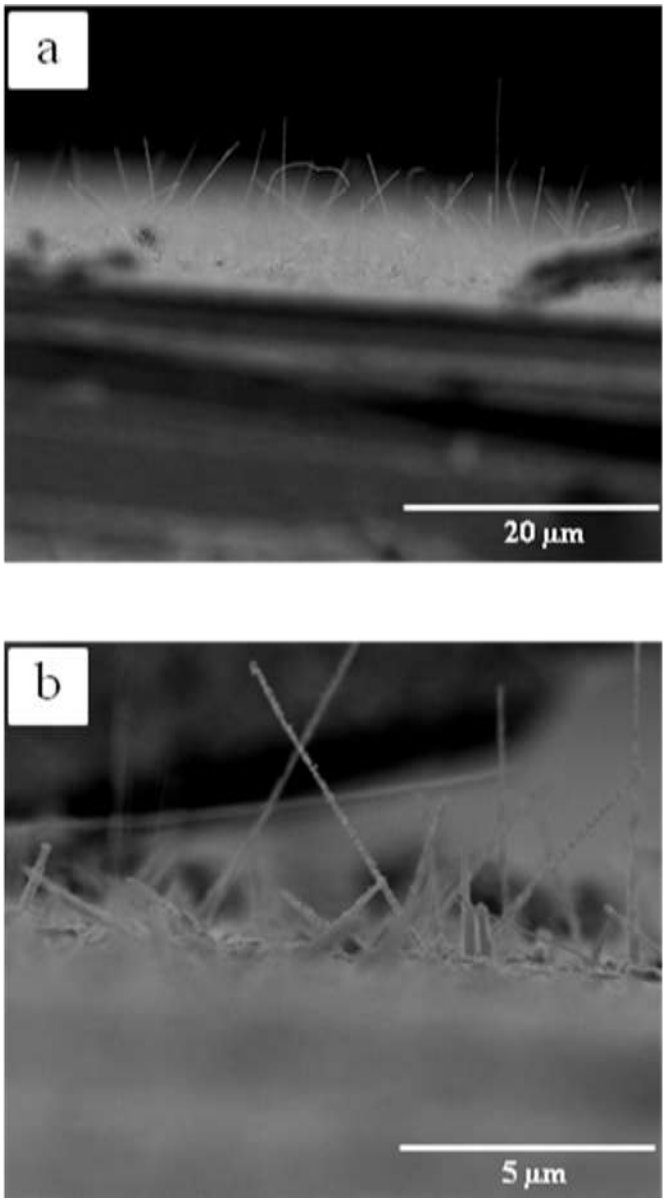

Fig. 23
(a-b) SEM images of Cu NW's (and other nanostructures) grown on Ames-1 a-C by magnetron sputtering.

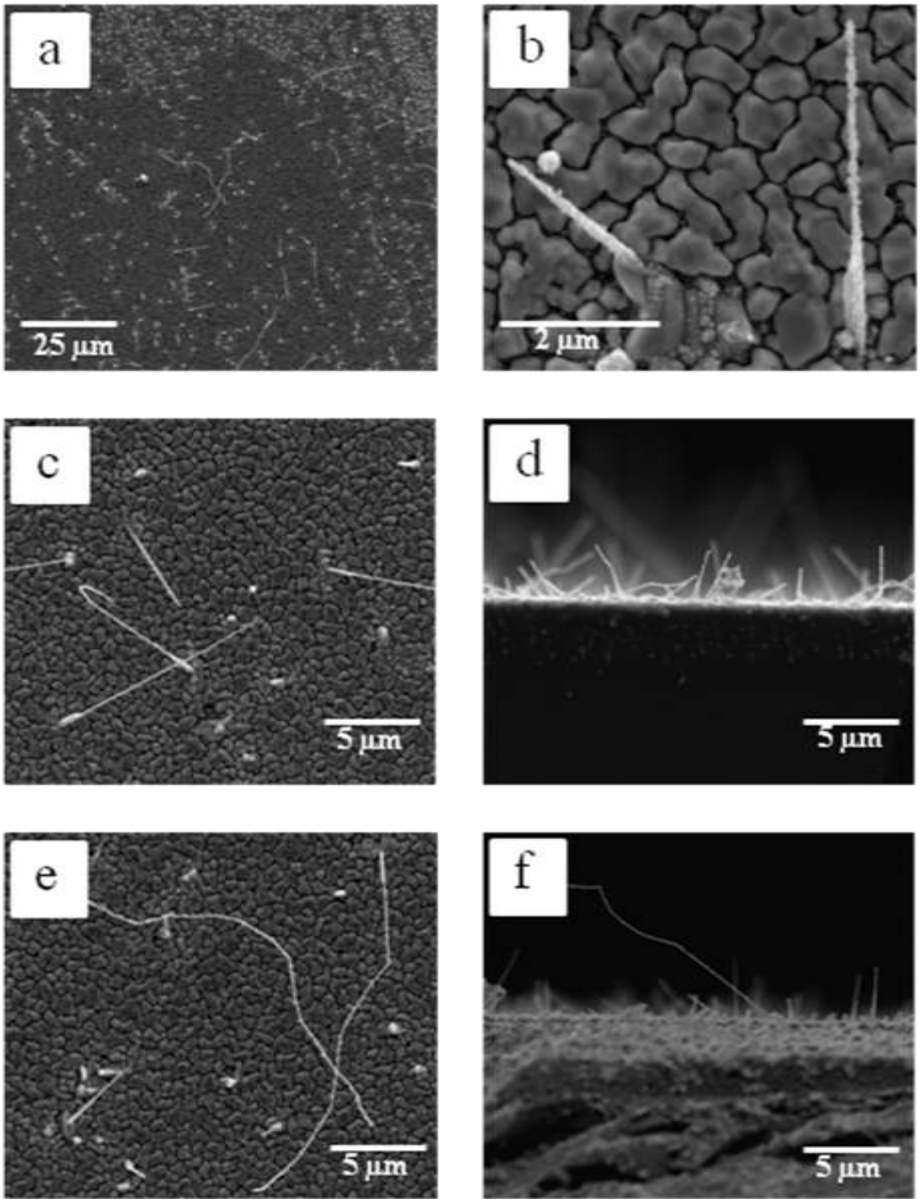

Fig. 24
(a-f) SEM images of Cu NW's (and other nanostructures) grown on Ames-3 a-C by magnetron sputtering.

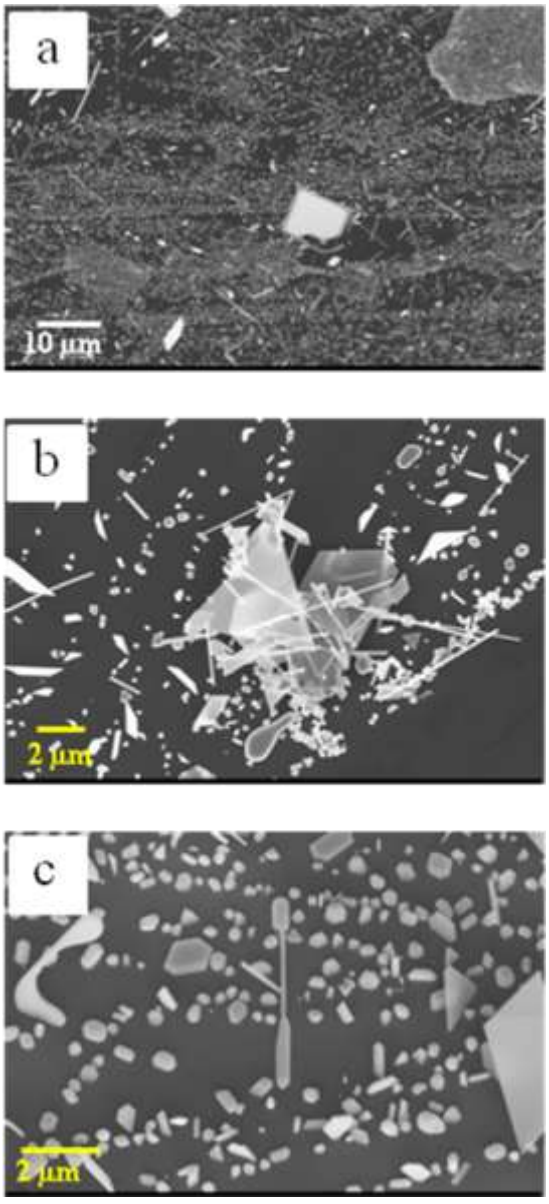

Fig. 25
(a-c) SEM images of Cu NW's (and other nanostructures) grown on HOPG by MBE.

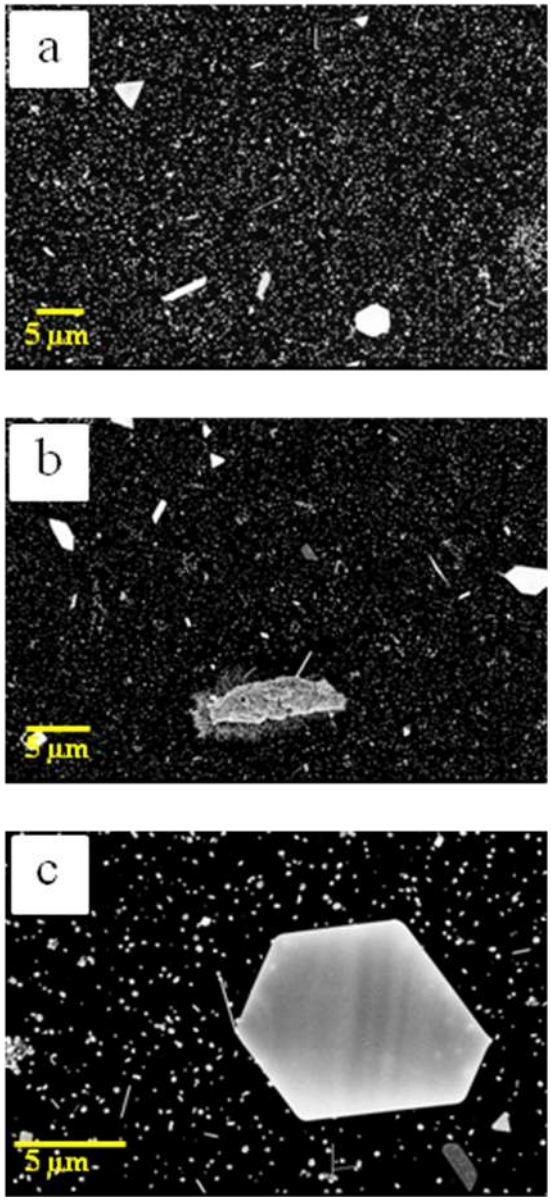

Fig. 26
(a-c) SEM images of Ag NW's (and other nanostructures) grown on MPI a-C by MBE.

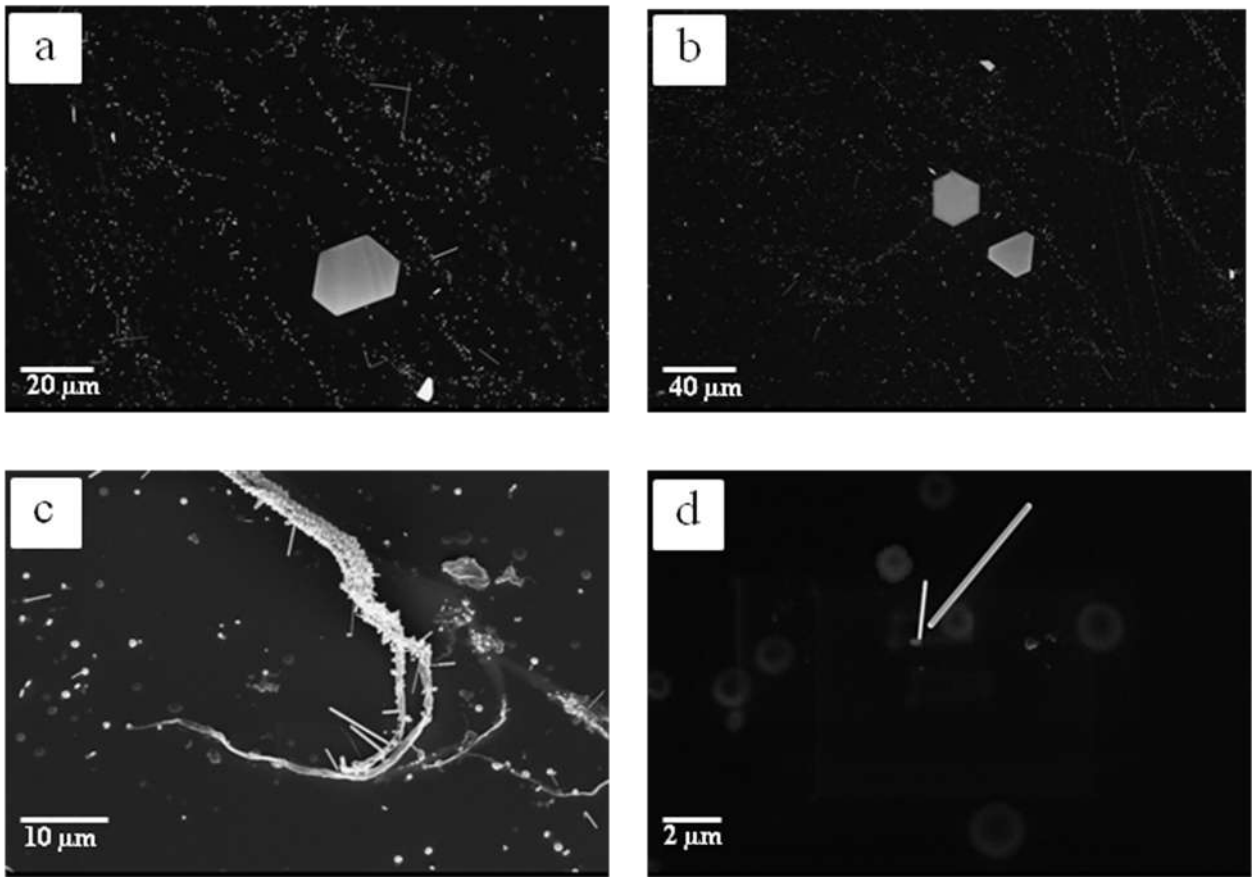

Fig. 27
(a-d) SEM images of Ag NW's (and other nanostructures) grown on Ames-2 a-C by MBE.

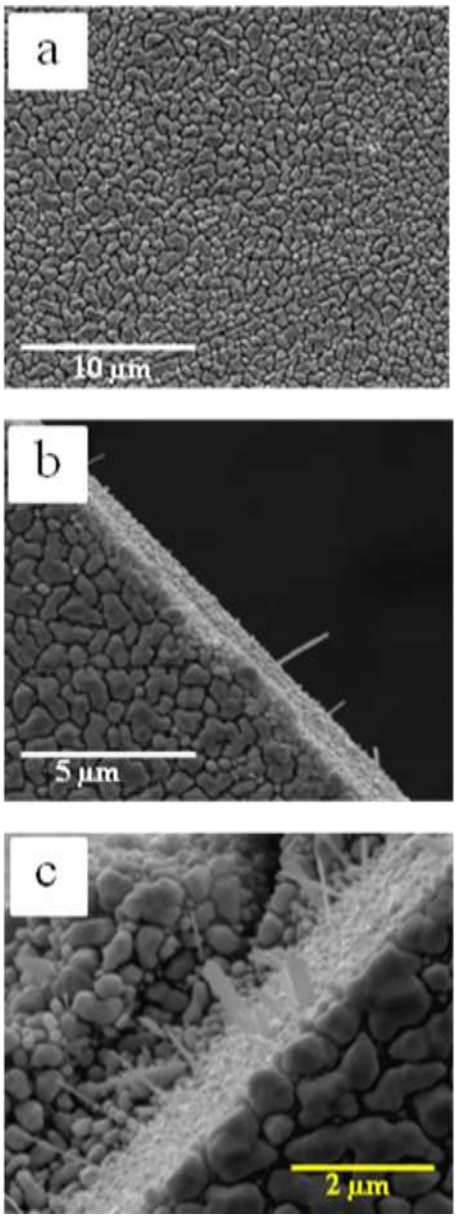

Fig. 28
(a-d) SEM images of Ag NW's (and other nanostructures) grown on MPI a-C by magnetron sputtering. (a) is an image taken from the face of the foil, and (b, c) are images taken from the edge.

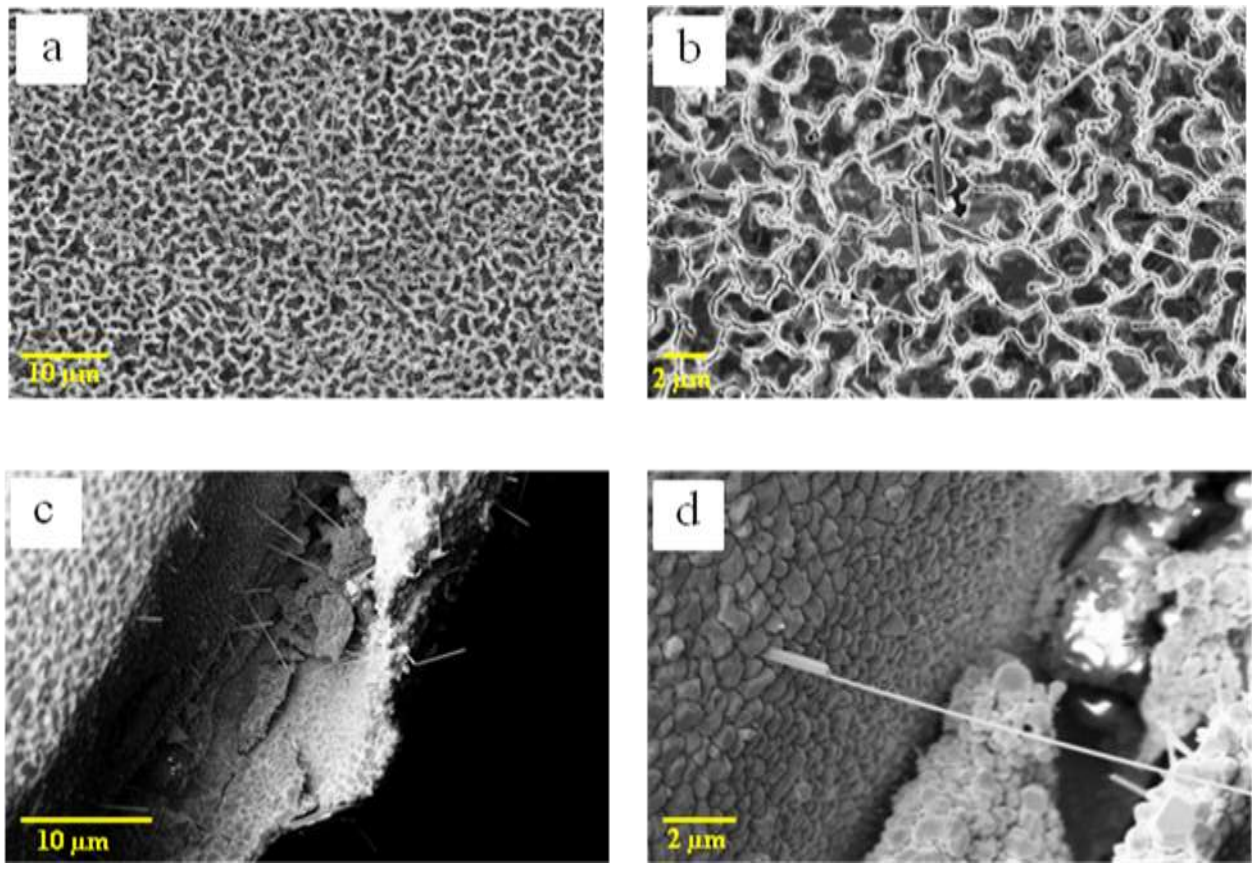

Fig. 29
(a-d) SEM images of Ag NW's (and other nanostructures) grown on W foil by magnetron sputtering. (a, b) are images of the face of the foil, and (c, d) are images taken of the edge.

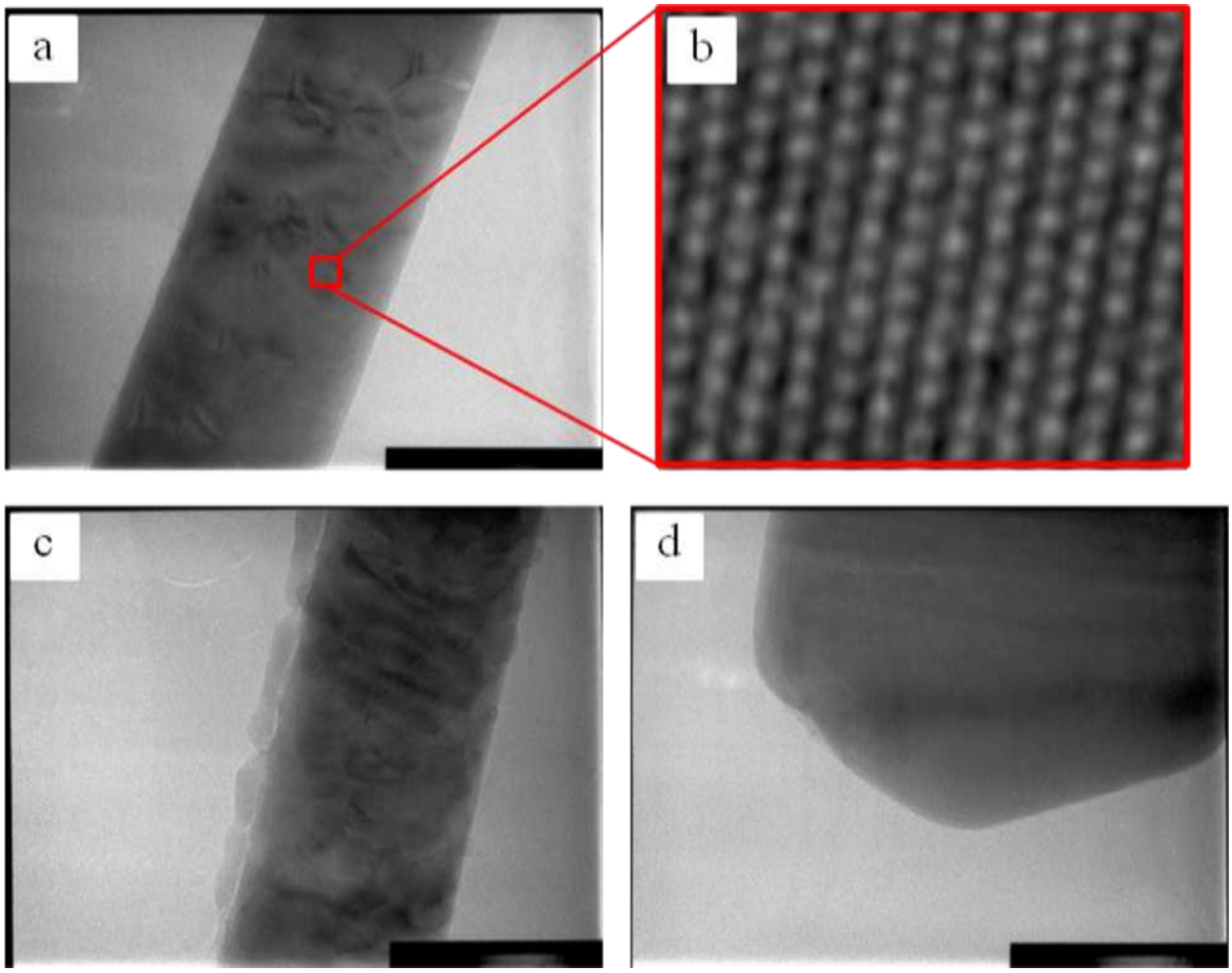

Fig. 30
TEM images of single crystal Ag NW's grown on W foil by magnetron sputtering. (a) Ag NW with (b) atomic resolution showing a close-packed hexagonal structure; (c) a different section of the same wire, showing the formation of an oxide layer around the wire surface; and (d) the tip of a wire, showing facets.

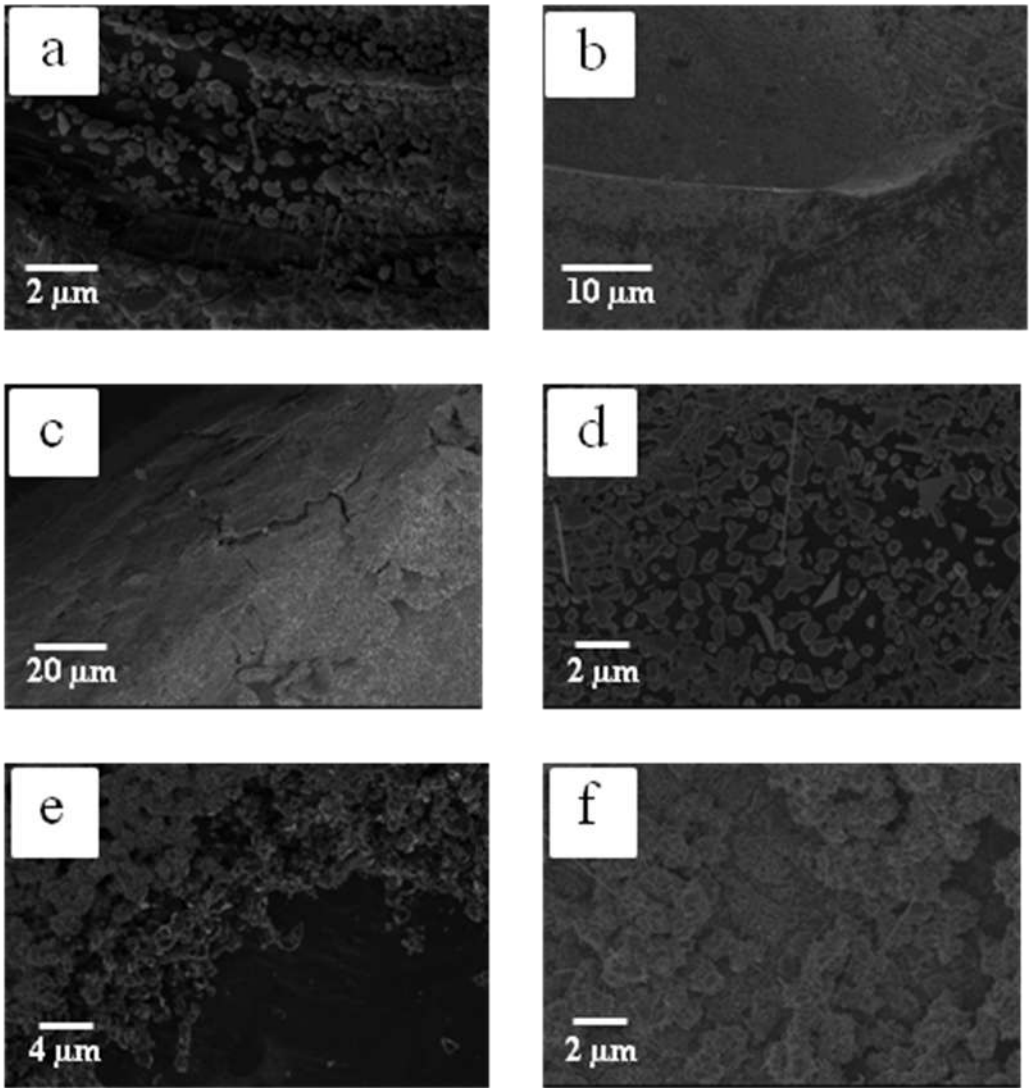

Fig. 31
SEM images of Ni NW's grown on various substrates by MBE; substrates (a) Ames-2 a-C; (b) MPI a-C; (c-d) graphite (HOPG); and (e-f) diamond microparticles.

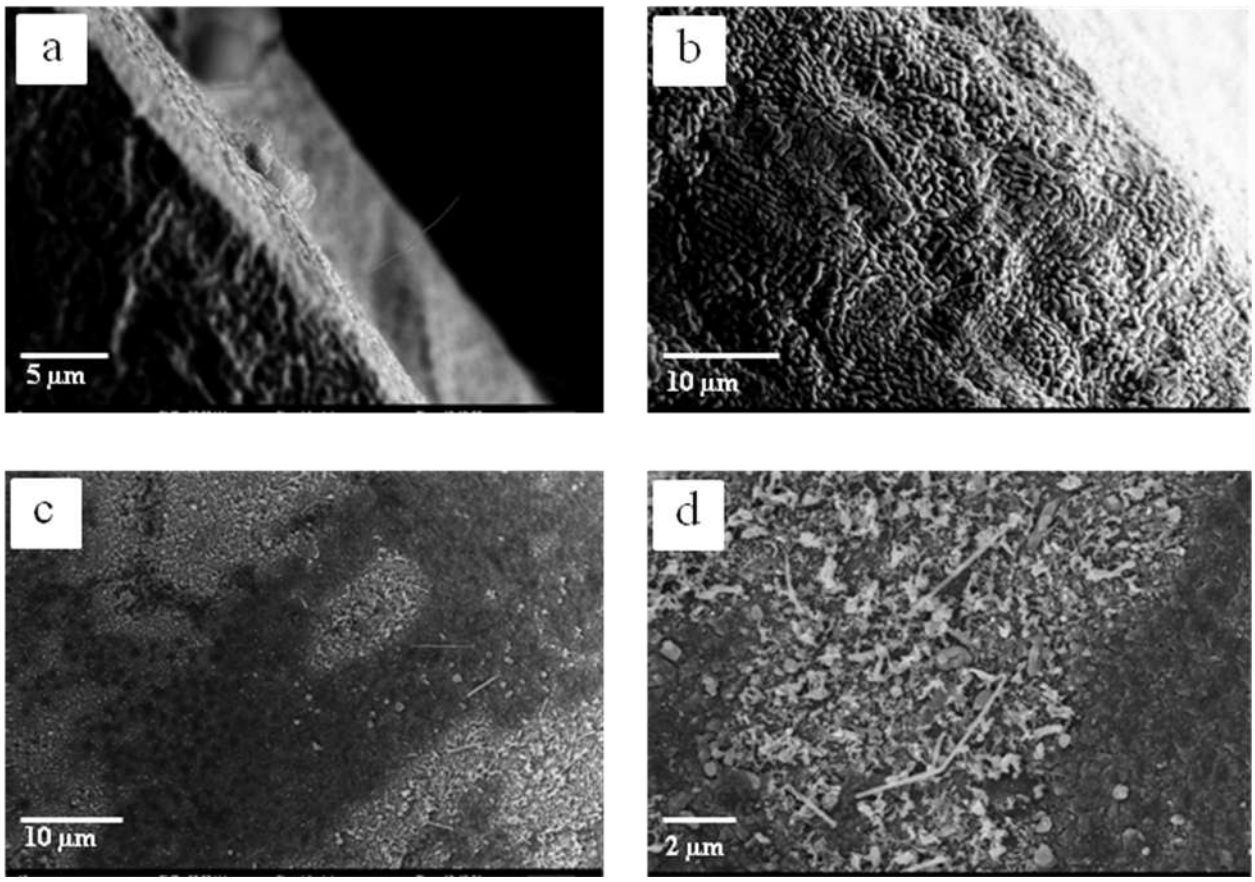

Fig. 32
SEM images of Fe NW's grown on various substrates by magnetron sputtering at MPI Stuttgart; substrates (a-b) Ni foil; and (c-d) W foil.

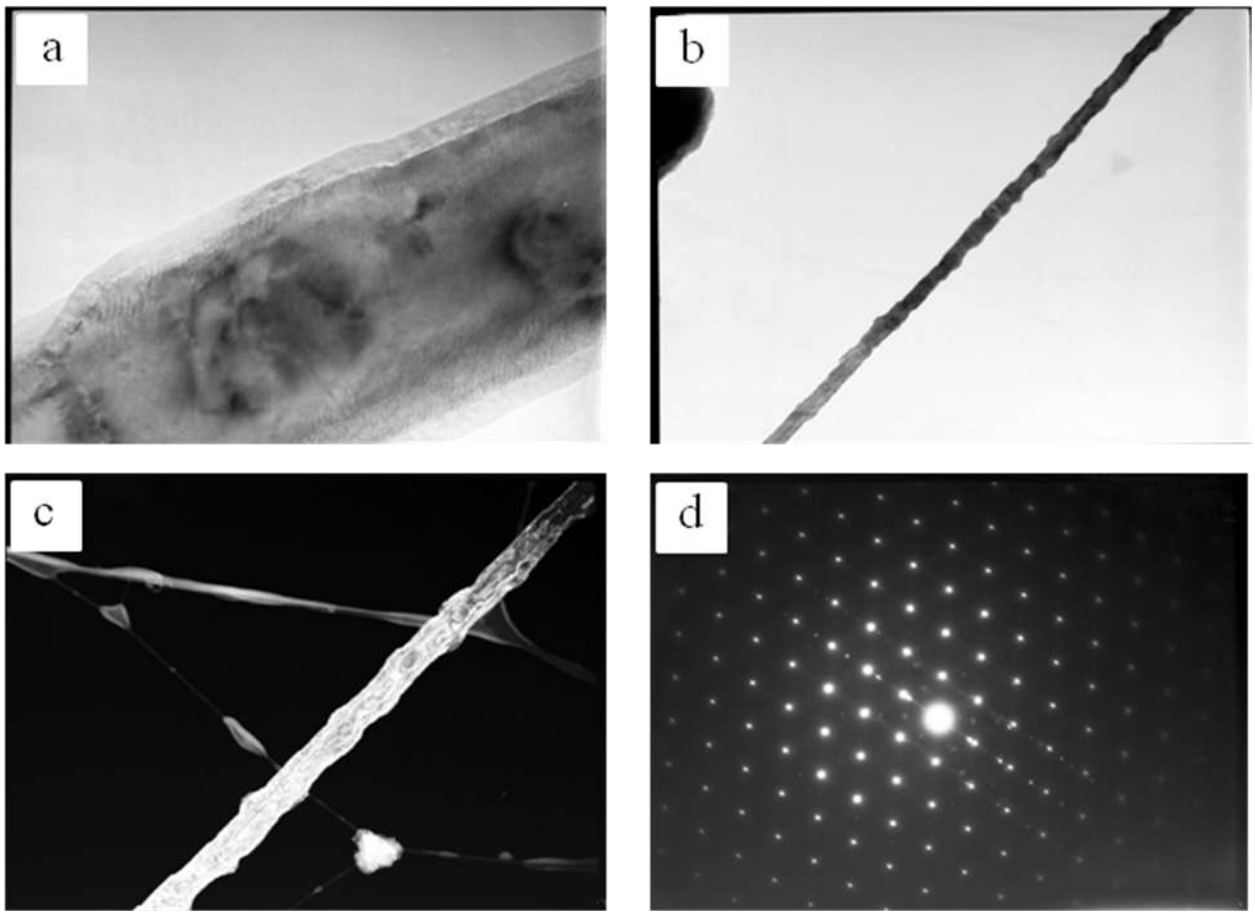

Fig. 33
TEM images of Fe NW's grown on W foil by magnetron sputtering at MPI Stuttgart; (a) bright field image showing a Fe NW with oxide layer visible; (b) lower magnification bright field image of the wire; (c) dark field image of the wire; and (d) electron diffraction pattern of the wire showing local single crystallinity (zone axis for this image unknown).

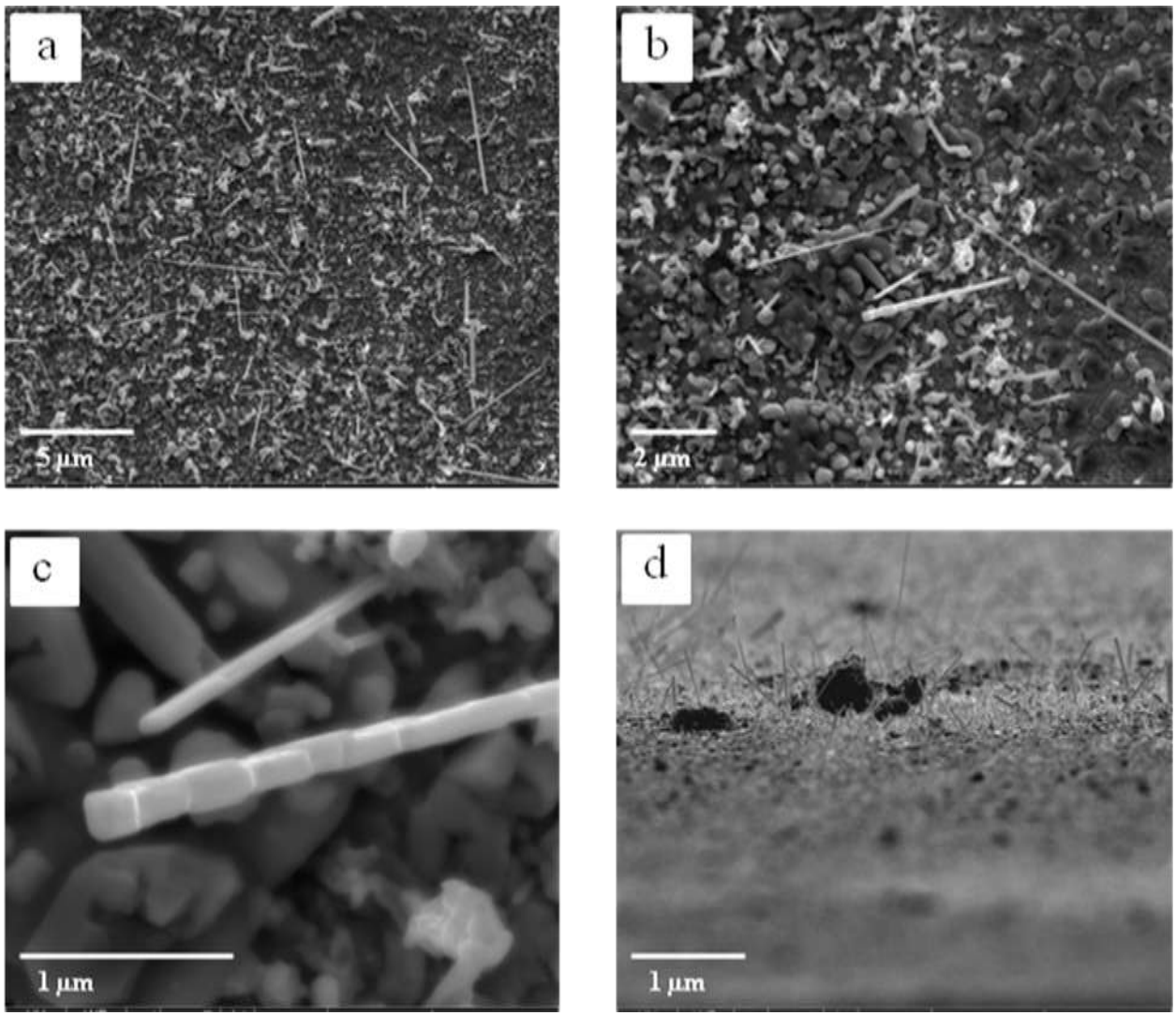

Fig. 34
(a-d) SEM images of Fe NW's grown on W foil by magnetron sputtering at Ames Laboratory.

APPENDIX A

STM TIP-FLASHER

This chapter describes a device for in-situ annealing of tungsten STM tips called a "tip flasher". The tip flasher is useful for initial outgassing of STM tips as well as cleaning tips contaminated from experiments. When imaging metal-on-graphite systems, the tip flasher is critical to efficient experimentation. The tip flasher is a modification of the Omicron Tip Transfer Plate, part # R194578-5, and was inspired by a similar device constructed by a former Thiel group member, Baris Unal [1; 2]. The first working version of the model described herein was constructed by Mark Wallingford, with small modifications later made by David Appy.

The tip flasher consists of a base plate, a top plate, and a middle contact plate, held together by four screws (Fig. 1). The middle contact plate is electrically isolated from the top/bottom plates by a set of three inner ceramic cylinders which surround three of the screws as a sheath. The inner ceramic cylinders have an inner diameter of 1.55 mm, an outer diameter of 2.00 mm, and a length of < 6.00 mm. The exact length of the inner ceramic cylinders is not critical, as long as they are short enough that they do not determine the height of the device (which should be determined by the outer cylinders, described hereafter). The middle plate is held in place by two sets of three outer ceramic cylinders which act as spacers between the middle plate and the top/bottom plates. The outer ceramic cylinders have an inner diameter of 2.50 mm and an outer diameter of 3.15 mm. The set of three outer ceramic cylinders between base plate and middle plate have a length of 1.66 mm. The set of three outer ceramic cylinders between the top plate and middle plate have a length of 2.95 mm. The length of the outer ceramic cylinders is critical to the function of the device. All ceramic pieces must be machined

by hand to the proper length. The group's Dremmel tool is useful for machining these pieces to the proper length. This process is very difficult because of the brittleness of the ceramic pieces. Patience and a steady hand are required. Careful measurement of the ceramic pieces with a micrometer is necessary to ensure that the assembly will fit and make good contact in the manipulator and STM stage. Tolerances on the ceramic cylinder lengths are approximately ± 0.03 mm.

The top and middle plates have a key-hole shaped recess for insertion of the STM tip. The top plate has a magnet at the narrow end of the key-hole for retaining the STM tip, and the middle contact plate has a sharp metal contact strip for contacting the side of the STM tip. The middle plate is machined by hand from a spare top plate. Edges of the middle plate are sharpened to ease insertion into the contact brushes on the manipulator or STM stage. The screw holes on the middle plate must be widened so that the inner ceramic cylinders can fit through, but not the outer cylinders. The metal contact strip is preferably made from a thick Ta foil, sharpened with the Dremmel tool, and spot-welded to the middle plate.

The middle plate portion is what was modified from Baris Unal's original design. In Baris' design, the middle plate was a single strip of thick Ta foil (no separate contact strip). The foil was slanted with respect to the top and bottom plates, so as to accommodate STM tips of various lengths. In the absence of Baris' expertise, we had difficulty with tips slipping under the middle plate during insertion (which destroys the tip). In addition, we were having difficulty making reliable contact in the manipulator head. We replaced Baris' slanted foil with a dedicated middle plate with sharpened edges (to make more reliable contact in the manipulator), and a replaceable contact strip which can be sharpened and replaced relatively quickly and easily. The new design can still accommodate tips of various lengths, as long as the tip is long

enough to reach the contact strip (where the minimum length is adjustable by slight bending of the contact strip).

When mounted in the tip flasher, the STM tip creates an electrical contact between the middle contact plate and the top plate/ground. Fig. 2 shows a side view of the complete assembly with an STM tip resting inside. In practice, the STM tip holder will not always rest flush with the top plate as it is shown in Fig. 2, but may be tilted due to the pull of the magnet. This does not affect the performance of the device, as long as the tip itself is contacting the sharp metal strip. The STM tip is flashed by running current through the tip. This is done in the manipulator, in the same fashion that one would run current through the PBN heater in a double-decker sample holder. The amount of current needed to flash the tip is primarily determined by the sharpness of the contact strip. When the contact strip is sharp, the tip will glow dull red at 3 A, orange at 5 A, and yellow-white at 7 A. If current is passing but the tip is not flashing, or if the current needed to make the tip glow greatly exceeds the given range above, this is an indication that the contact strip probably needs to be sharpened. The contact strip will also naturally degrade over time with use, so regular sharpening/replacement is necessary. The resistance across the circuit is approximately 1 Ω when working properly.

The manipulator feedthrough is rated for 7 A. The atmospheric side of the feedthrough, which connects with the power supply cable, has been modified several times over the years and does not have a defined current limit but can develop hot spots and requires occasional repair. The feed-through assembly becomes warm when running currents > 3 A over several minutes, and gets hot to the touch at > 5 A over tens of seconds. The feed-through can be monitored periodically by touch in between flashings (not during flashing). If the chamber pressure does

not recover immediately, or if the feed-through becomes hot to the touch, wait before the next flashing cycle.

For new STM tips, outgas at low current (~3 A) for several cycles of approximately 1 minute or until chamber pressure enters the mid -9 mbar range. It is generally good practice to start with low current and gradually increase it, even for well-outgassed tips, to prevent over-flashing (melting the tip and/or contact strip). A protocol for flashing a new STM tip is as follows.

1) Check resistance across the circuit at 0.1 A by dividing the displayed voltage by the displayed current. It should be approximately 1 Ω. If current does not pass, try adjusting the tip within the tip flasher using the wobble stick (with power off!).
2) Increase current starting at 1.0 A in 0.5 A increments until an initial gassy burst occurs, stopping when pressure enters the mid -9 mbar range (typically ~ 3 A).
3) Outgas at that power repeatedly, stopping whenever chamber pressure reaches the mid -9 mbar range. These cycles typically last on the order of tens of seconds.
4) When pressure no longer increases after ~ 30 seconds of running current, increase current by 0.5 A.
5) Repeat until the tip flashes orange with little pressure increase. The tip is now outgassed and should produce good tunneling immediately if the apex is well-shaped.

For an STM tip which has already been outgassed, the beginning steps of this protocol can be shortened.

The tip flasher can also be used to transfer tips into and out of the chamber. This is convenient because it saves a carousel space that would otherwise be used by a separate tip transfer plate, and also saves the time because the tip can be annealed immediately after being transferred into the chamber.

References

[1] B. Ünal, A.Belianinov, P.A. Thiel, in: J.T. Yates Jr. (Ed.), Experimental Innovations in Surface Science: A Guide to Practical Laboratory Methods and Instruments, Springer Verlag, in progress.

[2] B. Unal, Scanning tunneling microscopy studies of fivefold surfaces of icosahedral Al-Pd-Mn quasicrystals and of thin silver films on those surfaces, Iowa State University, PhD Thesis, 2008.

Figures

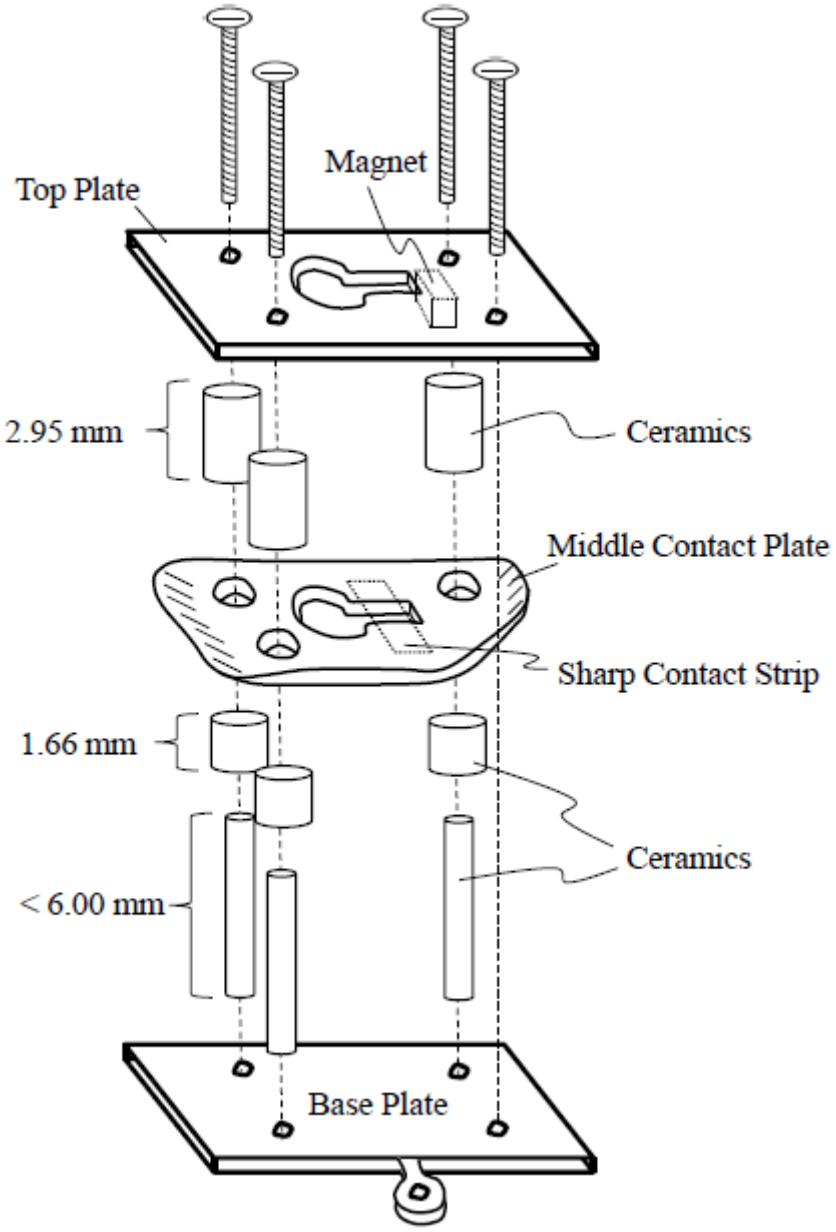

Fig. 1
Schematic diagram of the STM tip flasher.

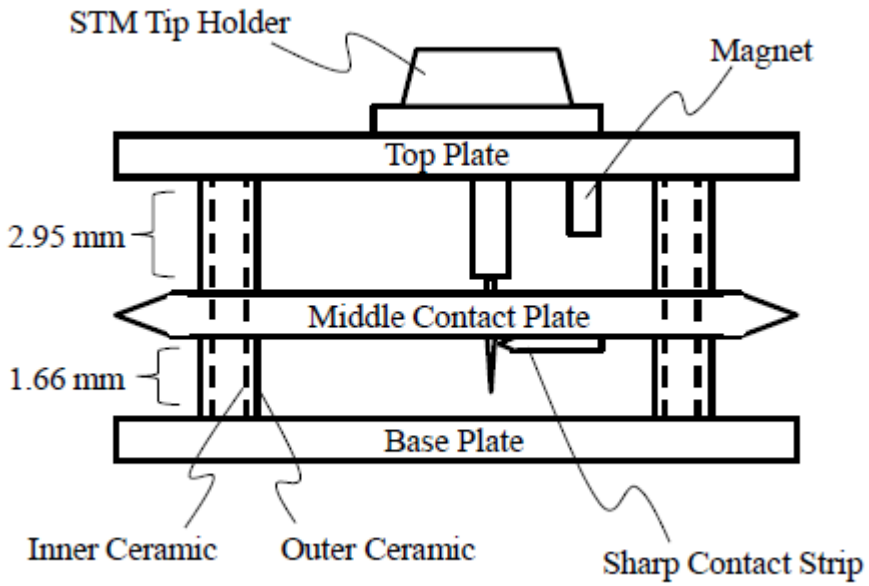

Fig. 2
Side view of the complete STM tip flasher assembly housing an STM tip.

APPENDIX B

PROCEDURE FOR FAST STM TIP-MAKING

The Thiel group Standard Operating Procedures contains a guide for making chemically etched tungsten STM tips called "Making Sharp STM Tips for Wonderful STM Experiments" by Thomas Duguet, 2/9/10. This guide is kept with the tip-etching equipment in 219 Spedding. The procedure therein is good for making a small number of high quality STM tips suitable for imaging most surfaces. This process, however, is slow. Even a good tip-maker may only succeed in making 1-3 good tips per day.

In recent years, the Thiel group has shifted its focus to studying the interaction between metals on carbon surfaces (Cu, Ag, Au, and Dy on HOPG and a-C). These systems are difficult to image due to strong tip-sample interaction. The tip will collect metal nanoclusters from the surface during scanning, which requires periodic cleaning of the tip in-situ with a tip-flasher, and sometimes tip replacement. Cleaning the tip by scanning the sample itself is generally ineffective on HOPG, since the surface lacks sharp contours to knock debris from the tip. Also, there is a very high rate of tip crashing on the carbon surfaces, both during scanning and during the initial approach. We are unsure about the cause of tip crashes during initial approach, but it seems to be an issue with HOPG more than other surfaces. Macroscopically blunt tips (such as those obtained by cutting rather than etching) have a much higher survival rate from tip-crashes. Tips with a very fine point (etched tips) usually bend upon crashing, and are rarely usable thereafter. Additionally, although almost any stable tip will be able to get atomic resolution on a flat surface, very few tips have an apex sharp enough to adequately image 3D objects like metal clusters. Obtaining a tip with a sharp apex (by any method) appears to be mostly a matter of

luck, and there is no convenient way to know the shape of the apex (on the atomic scale) prior to imaging.

In light of the imaging challenges of metal-on-carbon systems, the goal of STM tip making in the Thiel group has shifted from making a small number of high-quality etched tips to making a large number of robust tips that could survive a tip crash while consuming a minimal amount of resources (primarily the tip holders, which are quite expensive). The procedure is as follows:

1) Obtain a length of W wire several cm long. The preferred diameter of wire is 0.0152 in, although smaller diameter wire may also be used.
2) Slide one end of the wire into an STM tip holder (Omicron part # S2701). If 0.0152 in wire is used, it will be a snug fit, so use hemostats (small surgical pliers) or small needle-nose pliers to wiggle the wire in. If a smaller-diameter wire is used, insert the wire part-way in, bend the wire, and then push it all the way in. The bend in the wire will hold it in place in the tip-holder. Do not crimp the tip-holder to secure the wire in place. The tip holders can be re-used many times, which will be necessary for high-throughput applications. Un-crimped tips are stable enough to produce usable images, at least for the types of images used in this thesis work.
3) Attach a pair of hemostats to the far (unused) end of the wire. This is to ensure that the far end of the wire does not shoot off into the distance during the next step.
4) Cut the wire at an angle of approximately 45-60° with respect to the wire axis as shown in Fig. 1. The angle of the cut is non-critical to tip function. The length of exposed wire should be tailored to fit into the current state of the tip flasher (approximately 1-2 mm,

and will vary by user). After cutting, give the side of the wire a very light touch with tweezers to make sure that it is not loose within the holder.

5) An alternate method to cutting the wire is to apply a light spot-weld to the wire and then pull the wire apart. This technique was suggested by Myron Hupalo, and I used it once with moderate success. The theory behind this method is that tungsten has a tendency to splinter when pulled apart and will produce a very sharp apex for imaging 3D objects.
6) Optionally, the apex can be viewed under an optical microscope. However, the optical microscope only provides a relatively macroscopic view of the tip. Over the course of trying ~50 STM tips I could discern no correlation between the visual appearance of the tip and its imaging performance.

Most STM tips produced in this manner will be capable of atomic resolution on the HOPG surface. About 1 in 5 will produce good images of 3D Cu clusters. Again, finding a tip with a particular sharp apex which can effectively image 3D metal clusters is partially a matter of luck, and these metal-on-carbon systems have a high rate of tip mortality, so high-throughput and survivability are the primary concerns.

Figures

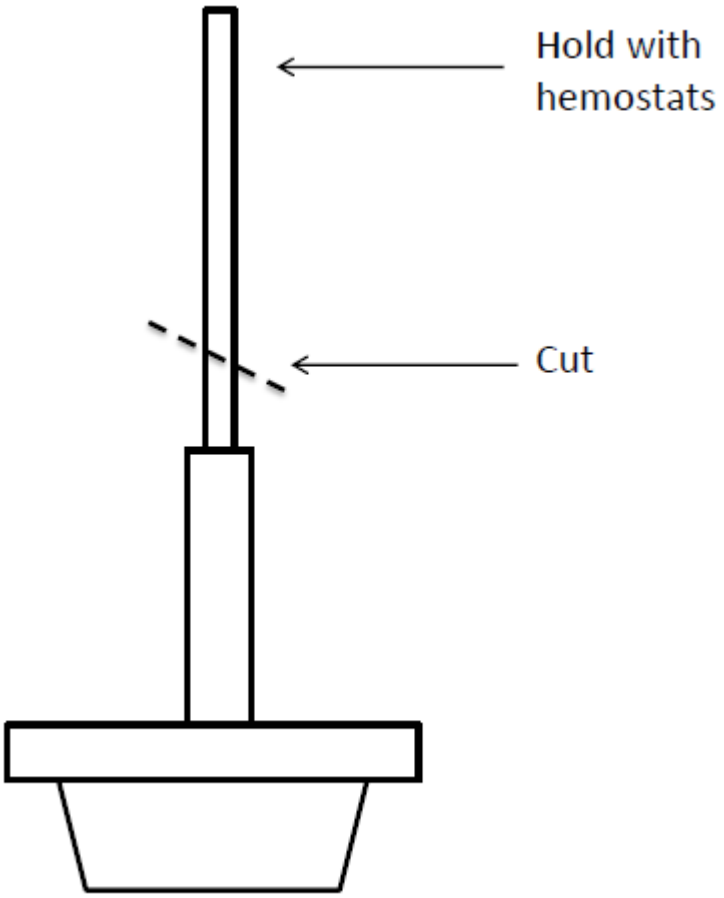

Fig. 1
Diagram illustrating the procedure for fast STM tip making.

APPENDIX C

EVAPORATOR RE-DESIGN

This appendix details the re-design of an evaporator in June of 2011 by Mark Wallingford and David Appy. The evaporator was formerly mounted on the Video Leed Chamber in 222 Spedding, and was moved to the TPD chamber in Room 217, in August of 2014.

The evaporator is mounted on an 8" flange. It has two crucibles surrounded by a cooling shroud which circulates either water or liquid nitrogen (water in recent years). The re-design involved cutting a section from the cooling shroud to accommodate the current leads so that the crucibles and filaments could be lowered farther into the cooling shroud. Additionally, the shutter was repositioned to be flush with the mouth of the cooling shroud. Overall, the new setup was designed to better protect the chamber and sample from stray heat and metal vapor, and also to keep the shutter from contacting the filaments or crucibles if it became tilted (a common occurrence over time). Figs. 1(a) and (b) show schematics of the evaporator head (a) before and (b) after the re-design.

The evaporator re-design was mechanically challenging. We initially drilled two small holes in the shroud, which was very challenging since the shroud is double-layered steel with an internal cavity. Charlie Burg in the Ames Lab machine shop welded around the holes, but the seal was not UHV tight. After a second failed attempt, we had Charlie re-cut larger holes in the shroud, and then expand the holes to be a U-shaped recess in the shroud as seen in Fig. 1(b). After welding around the U-shaped recess, the shroud held UHV. Given the challenges of cutting and welding the cooling shroud, it is *not* advisable to attempt something like this in the future, since the benefits of the new design were marginal at best.

One interesting benefit of this evaporator design is that the extra room allowed us to orient the filaments in a double spiral around the center of the crucibles as in Fig. 1(b) (as opposed to a single loop near the front of the crucibles as in Fig. 1(a)). Bending and spot-welding the filaments so that they made solid contact with the leads and ground post while avoiding direct contact with the crucibles was very difficult. Wrapping the filament wire around a bolt's threading is a good way to form a smooth spiral in the wire. The filaments also bend and deform upon first heating in UHV, often causing shorts. It takes experience to be able to predict the way the filaments will bend upon heating in UHV. Again, this adds another level of difficulty to the design. Benefits of this setup are that the filaments can be retained within the cooling shroud to reduce heat contamination in the chamber, and also that the increased length of filament due to the spiral shape allows for greater electron emission at lower current, which extends filament lifetime. Again, it is questionable as to whether these benefits outweigh the time and effort spent cutting/welding the shroud and positioning the filaments in this manner.

Emission current for this evaporator is measured by placing a resistor (200 Ω is sufficient) between the negative terminal and ground. A voltmeter measures the voltage drop across the resistor. Using V = IR, the calculated current represents the emission current between the filament and crucible. A simplified schematic of the electrical setup for the evaporator is shown in Fig. 2.

Figures

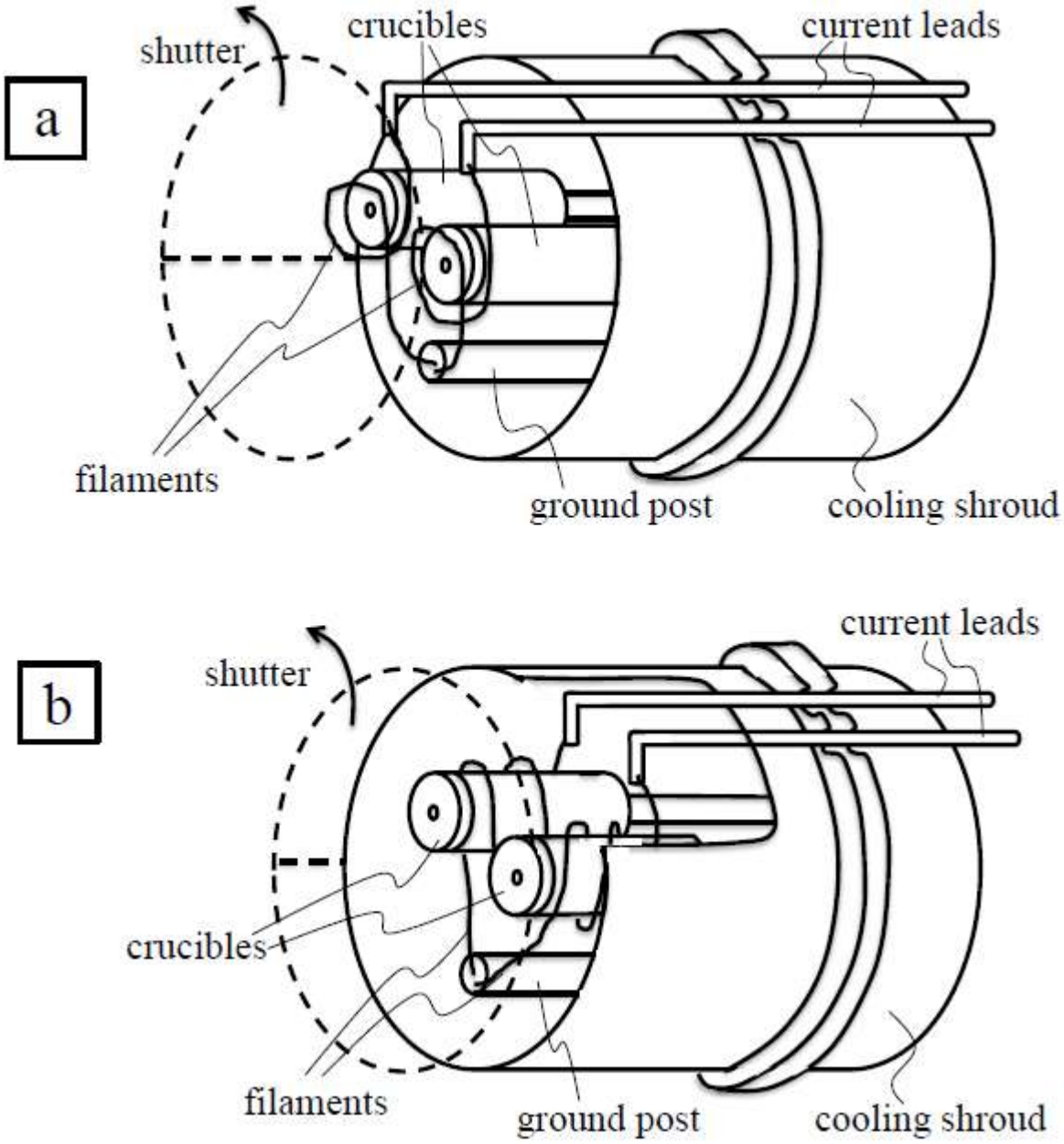

Fig. 1
Schematic diagrams showing the evaporator head (a) before; and (b) after the re-design.

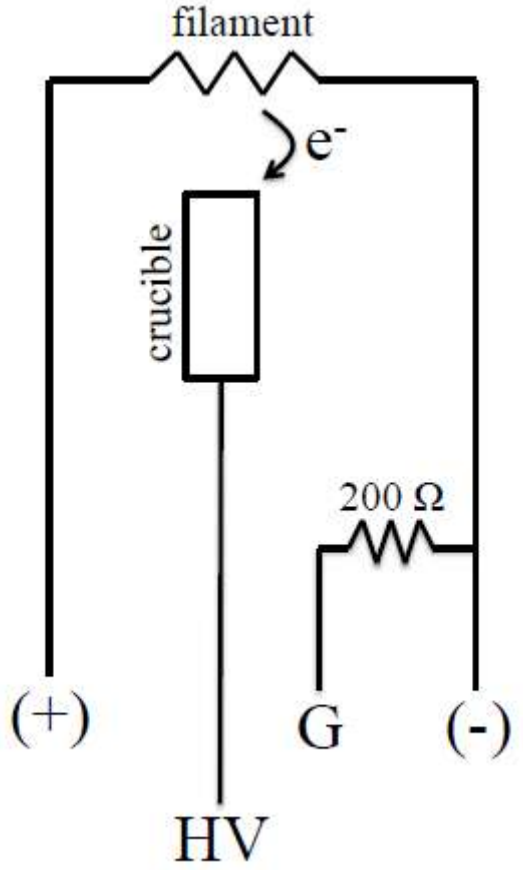

Fig. 2
Simplified schematic of the electrical setup for the evaporator.

APPENDIX D

EXPERIMENT LOG

The following table catalogs of experiments done for this thesis work. The raw data files are labeled by date in the format YYYYMMDD, and are stored in the group computers in folders named "Nanowire STM" and "Nanowire XPS". A detailed summary of each experiment can be found in an Excel worksheet labeled "20130613_Experiment Summary and Worksheet". The accompanying data analysis for these experiments can be found in an Excel spreadsheet labeled "20130626_Worksheet_Cu on HOPG_various_and histograms_DA". A data table with additional information such as evaporator power and island heights can be found in the Excel file "20130626_Data Analysis_Cu on HOPG_V4_DA".

Note - Amorphous carbon samples have different labels in the data files than in this thesis works. Sample 1 → MPI-2; Sample 2 → MPI-3, Sample 3 → MPI-1.

Table 1 – Experiment Log

Date/ Book #, Page #	Instr.	System/ Expt. Name	Sample Treatment, Expt. Details	Image files	Coverage (ML)	Notes
20120301 Bk 2, pg 10	STM	a-C/Si (MPI-2)	Outgas @ 650 K	M1-M39		Good low-mag. images
20120302 Bk 2, pg 11	STM	a-C/Si + Ag (MPI-2)	Clean surface	M1-M23		
			Attempted Ag deposition		Unknown (> 1 ML)	Remote shutter control inoperative (continuously opened, discovered 4/4/12). Tip crash, no images
20120306 Bk 2, pg 14	STM		2nd imaging attempt	M1		Tip crash
20120309 Bk 2, pg 18	STM		Anneal @ 650 K 4 hrs	M1	Unknown (> 1 ML)	Poor tunneling
20120310 Bk 2, pg 19	STM		Next day	M1-M2		Poor tunneling

Table 1 cont. – Experiment Log

Date/ Book #, Page #	Instr.	System/ Expt. Name	Sample Treatment, Expt. Details	Image files	Coverage (ML)	Notes
20120313 Bk 2, pg 20	STM	a-C/Si (MPI-2)	Outgas @ 650 K, STM test	M1-M4		Poor tunneling
20120314 Bk 2, pg 22	STM	a-C/Si + Ag (MPI-2)	Previous sample, (Ag + 650 K)	M5-M45	Unknown (> 1 ML)	Tip issues
		a-C/Si + Ag (MPI-2)	Tip cleaning/test	M1-M23	Unknown (> 1 ML)	Poor tunneling Tip crash
20120315 Bk 2, pg 24	STM		Heat to 500 K, briefly New tip	M1-M7		
20120316 Bk 2, pg 24	STM		New tip	M1-M13		Poor tunneling
20120319 Bk 2, pg 25	STM		New tip	M1- M42		Possible Ag clusters in later images
20120320 Bk 2, pg 26	STM	a-C/Si (MPI-2)	Clean surface			Tip crash, no images
	STM	a-C/Si (MPI-3)	Outgas @ 1100 K Clean surface	M1-M8		Poor tunneling
20120321 Bk 2, pg 27	STM		Heat @ 650 K, 4 hrs New tip	M1-M26		ok
20120322 Bk 2, pg 28	STM			M1-M112		Great atomic res. images
		a-C/Si + Ag (MPI-3)	Ag deposition	M113	Unknown (> 1 ML)	Remote shutter control inoperative (continuously opened, discovered 4/4/12). Tip crash
20120323 Bk 2, pg 31	STM		New Tip	M1-M19		Poor tunneling
			Ag deposition	M20-M40	Unknown (>10 ML)	Ok, began using large negative bias
20120327 Bk 2, pg 34	STM	a-C/Si (MPI-3)	STM test	M1-M21		ok
20120410 Bk 2, pg 43	STM		Heat @ 650 K, briefly STM test (new tip flasher)	M1-M47		ok
20120411 Bk 2, pg 45	STM	a-C/Si (MPI-2)	3 samples mounted on same sample plate. Outgas @ 650 K	M1-M5		
		a-C/Si (MPI-3)		M6-M16		
		a-C/Si (MPI-1)		M17-M21		

Table 1 cont. – Experiment Log

Date/ Book #, Page #	Instr.	System/ Expt. Name	Sample Treatment, Expt. Details	Image files	Coverage (ML)	Notes
20120412 Bk2, pg 47	STM	a-C/Si (MPI-2)	3 samples mounted on same sample plate. Outgas @ 650 K day before.	M1-M15		Interesting Tip Effects. Atomic res. images
		a-C/Si (MPI-3)		M16-M28		
		a-C/Si (MPI-1)		M29-M52		
20120413 Bk 2, pg 49	XPS	a-C/Si (MPI-2)	Outgas @ 1100 K several days before	01-03		Ta and O peaks visible
20120415 Bk 2, pg 50	STM	a-C/Si (MPI-1)	Heat to 600 K briefly	M1-M25		
		a-C/Si (MPI-3)		M26-M32		
		a-C/Si (MPI-2)		M33-M40		M38 - feature
20120503 Bk 2, pg 53	XPS	a-C/Si (MPI-2)	Heat @ 850 K, 2 hrs Testing positions	01-07		Ta peaks still in view
20120504 Bk 2, pg 56	XPS	HOPG ZYH	Outgas @ 850 K, 2 hrs	01-02 Ta peak 01		Small Ta peak visible
		a-C/Si (MPI-2)	Heat @ 850 K, 1 hr	01 Ta peak 01		Ta peak visible
20120620 Bk 2, pg 67	XPS (MPI)	diamond	Heat @ 800 K, 30 min	1		sp^3 reference
		HOPG		2		sp^2 reference
		a-C/Si (MPI)		3		Peak-fitted
		a-C/Si (Ames)		4		Peak-fitted
20120819 Bk 2, pg 79	STM	HOPG ZYH	Outgas @ 600 K, 2 hrs STM test	M1-M18		
20120824 Bk 2, pg 81	XPS	HOPG ZYH	Heat @ 800 K, 4 hrs XPS test			Ta peak visible
20120825 Bk 2, pg 82	STM	HOPG ZYH	Heated @ 850 K, 4 days before STM test	M1-M48		Poor quality, steps unequally decorated
20120827 Bk 2, pg 83	STM	HOPG ZYH + Cu	Heat @ 850 K, 3 hrs Clean Surface	M1-M16		M14-M15 clean step edges
			Cu dep. 20 W, 30 sec	M17-M38	Unknown	No Cu visible M24-M27 superlattice?
20120828 Bk 2, pg 85	XPS	HOPG ZYH + Cu?	Heat @ 850 K, several hrs		Unknown	Ta peak visible Small Cu peak visible
20120829 Bk 2, pg 85	STM	HOPG ZYH + Cu?	STM test	M1-M27	Unknown	Poor tunneling
20120902 Bk 2, pg 88	STM	HOPG ZYH + Cu Calibration # 1	"clean" surface	M1-M7		
			Cu deposition 22 W, 1 min	M8-M32	0.022	Flooding method
			3 min (total)	M33-M57	0.10	
			6 min (total)	M58-M73	0.16	

Table 1 cont. – Experiment Log

Date/ Book #, Page #	Instr.	System/ Expt. Name	Sample Treatment, Expt. Details	Image files	Coverage (ML)	Notes
20120902 Bk 2, pg 88	XPS	HOPG ZYH + Cu	Same as above		0.16	Cu 2p peaks visible
20120906 Bk 2, pg 92	STM	a-C/Si + Cu (MPI-2)	Outgas @ 1000 K, 6 hrs Clean surface	M1-M24		Cu not discernible
			Cu deposition 22W, 1 min	M25-M44	Unknown	
			10 min (total)	M45-M60	Unknown	
20120906 Bk 2, pg 92	XPS	a-C/Si + Cu (MPI-2)	Same		Unknown	Ta peaks visible Cu not visible
20120907 Bk 2, pg 93	XPS	a-C/Si + Cu (MPI-2)	Same	_Cu	Unknown	Cu 2p peaks visible
			Heat @ 1000 K, hrs	_clean		Cu not visible
20120914 Bk 2, pg 94	STM	HOPG ZYH + Cu?	None since 20120902 STM test	M1-M21	Unknown	Poor tunneling M5-M6 interesting features
20120916 Bk 2, pg 96	STM	HOPG ZYH + Cu?	STM test	M1-M15	Unknown	Poor tunneling
20120919 Bk 2, pg 98	STM	HOPG ZYH + Cu?	Heat @ 1000 K, hrs STM test	M1-M44	Unknown	M27-M44 beautiful step edge decoration First instance of "cauliflower"?
20120921 Bk 2, pg 100	STM	HOPG ZYH + Cu	Cleave, outgas @ 950 K Clean Surface	M1-M14		Some step edge decoration. M3 nice terrace undulation
			Cu deposition 22 W, 30 sec	M15-M21	unknown	Poor tunneling
			5 min (total)	M22-M33		
			15 min (total)	M34-M39		
20120923 Bk 2, pg 103	STM	HOPG ZHY + Cu Calibration #2	Cleave, outgas @ 1000 K, 2 hrs Clean Surface	M1-M6		
			Cu deposition 22 W, 15 min	M7-M68	0.022	First good data set M58-M64, no islands?
			45 min (total)	M69-M98	0.11	
			90 min (total)	M99-M139	0.17	
20120925 Bk 2, pg 106	STM	HOPG ZYH + Cu Incremental Heating, 1st attempt	None since above 300 K	M1-M36	Unknown, prev. 0.17	
			375 K, 30 min	M37-M88		
			450 K, 30 min	M89-M106		Cu islands still present
20120926 Bk 2, pg 108			530 K, 30 min	M1-M8		Poor tunneling

Table 1 cont. – Experiment Log

Date/ Book #, Page #	Instr.	System/ Expt. Name	Sample Treatment, Expt. Details	Image files	Coverage (ML)	Notes
20130210 Bk 2, pg 122	XPS	HOPG ZYH a-C/Si (MPI-2)	Unheated XPS test	a-C_pre-heat HOPG_pre-heat		Mystery peak at 192 eV, O peak present
20130213 Bk 2, pg 124	XPS	HOPG ZYH a-C/Si (MPI-2)	Heat @ 625 K, 6 hrs	_post-heat _post-heat		Noisy, O peak present
		Cu NW on a-C	Unheated	_pre-heat		Cu present
20130215 Bk 2, pg 125	XPS	HOPG ZYH	Prev. heated @ 625 K, 6 hrs	_post-heat_GREAT		Great spectrum, no O peak. X-position critical for double-decker sample holder
20130222 Bk 2, pg 127	STM	HOPG ZYH	Cleaved, imaged in air (trouble-shooting STM)	M1-M47		Atomic res, clean step edges. M1-M2 interesting feature
20130224 Bk 2, pg 128	STM	HOPG ZYH	STM test, pre-bake	M1-M13		M3-M5 intercalated defect. M10-M11 complex terrace region, interesting step edges
20130308 Bk 2, pg 134	STM	HOPG ZYH Double-Decker	Previously heated @ 950 K	M1-M14		
		HOPG ZYH Single plate	?	M18-M19		
20130309 Bk 2, pg 135	STM	HOPG ZYH + Cu Single Plate	Clean Surface	M1-M44		M6-M7 Great blanket terrace morphology
			Cu deposition 19 W, 1 min	M45-M84	Unknown (very low)	M45-M62 imaging small clusters over ~30 min
20130312 Bk 2, pg 139	STM	HOPG ZYH Double Decker	Heat @ 950 K Clean Surface	M1-M5 M7-M10		
		HOPG ZYH Single Plate	Prev. heated @ 950 K (20130308)	M6		
20130313 Bk 2, pg 140	STM		None since above	M1-M10		Step edge decoration
20130313 Bk 2, pg 140	XPS	HOPG ZYH Double-Decker	Clean Surface XPS test			
20130314 Bk 2, pg 140	STM	HOPG ZYH	Prev. heated @ 950 K Clean Surface	M1-M25		M7-M8 crap on terraces M13-M19 intercalated defect

Table 1 cont. – Experiment Log

Date/ Book #, Page #	Instr.	System/ Expt. Name	Sample Treatment, Expt. Details	Image files	Coverage (ML)	Notes
20130314 Bk 2, pg 140	STM	HOPG ZYH	Same as above	M1-M48		M30-M48 Great terrace defect with scattering
20130315 Bk 2, pg 143	STM	HOPG ZYH Big Survey	Cleave, outgas @ 850 K	M1-M51		See file 20130315_HOPG ZYH_big survey
20130218 Bk 2, pg 147	STM	HOPG ZYH + Cu	Prev. heated @ 850 K (thick sample, temp. probably overestimated) "clean" surface	M1-M35		Stripes and channels
			Cu deposition 19 W, 1 min	M36-M37	Unknown	M36 strange high ridge
			23.5 W, 1 min	M38-M43		Poor tunneling
			23.5 W, 10 min (total)	M44-M47		
20130319 Bk 2, pg 149	STM	HOPG ZYH + Cu	From above, heat @ 950 K overnight (thick sample, temp. probably overestimated)	M1-M34	Unknown	Features on surface. M26 terrace undulations
			Cu deposition 23.5 W	M35-M36	Unknown	Poor tunneling
20130320 Bk 2, pg 152	STM	HOPG ZYH + Cu	Cleave, unheated	M1-M4		
			Outgas @ 950 K	M5-M12		
			Cu deposition 23.5 W, 10 min	M13-M31	0.60	Poor tunneling M23-M26 triple step edge
			20 min (total)	M32-M36	1.4	Poor tunneling
			40 min (total)	M37-M40	2.6	Poor tunneling
			Heat @ 950 K, 1 hr	M41-M48	0.028	M48 small flat island (defect?)
20130321 Bk 2, pg 153	STM	HOPG ZYH + Cu post-heat	Heat overnight @ 920 K	M1-M4	unknown	M1-M8 interesting surface layering
			Heat @ 950 K, 1 hr	M5-M16		M9-10 broken step edge? M16 step decoration
20130326 Bk 2, pg 162	STM		None since above	M1		poor

Table 1 cont. – Experiment Log

Date/ Book #, Page #	Instr.	System/ Expt. Name	Sample Treatment, Expt. Details	Image files	Coverage (ML)	Notes
20130328 Bk 2, pg 163	STM	HOPG ZYH + Cu, low temp	Cleave, outgas @ 540 K Clean surface Imaged @ 125 K (all)	M1-M32		
			Cu deposition 23.5 W, 10 min Imaged @ 125 K	M33-M36	0.65	Poor tunneling / tip imaging
			20 min	M37-M40	0.77	Poor tunneling / tip imaging
			40 min	M41-M53	1.7	Poor tunneling / tip imaging M42-M53 good large scale images of step edges
20130401 Bk 2, pg 165	STM	HOPG ZYH + Cu?	Heat @ 620 K, 1 hr, prev. history unknown STM test	M1-M19	unknown	Poor tunneling
20130402 Bk 2, pg 167	STM	Si(111) + Cu Attempted Cu calibration	Flash Si(111) 4 cycles, program "Si-111-7x7-preparation". Cool to ~125 K Clean surface	M1-M13		Nice terraces Si(111) lattice visible, noisy
			Cu deposition 19 W, 1 min	M14-M19	Nothing?	Very noisy
			22 W, 1 min	M20-M27	Unknown	Multiple areas scanned, no apparent change on surface
			23.5 W, 1 min	M28-M32		Still no apparent change on surface
			23.5 W, 10 min (total)	M33-M43		Possibly some change
			25 W, 1 min	M44-M71		Noise issues, difficult to tell
20130403 Bk 2, pg 170	XPS	Si(111) + Cu	None since above		Unknown	Cu peaks visible
20130404 Bk 2, pg 171	STM	HOPG ZYH + Cu	Cleaved and heated 1 week ago "clean" surface STM test	M1-M6		M1 interesting stripes on surface
			Cu deposition 23.5 W, 10 min	M7-M26	0.21	M7-M12 very high striped feature. M15 island size changes mid-scan

Table 1 cont. – Experiment Log

Date/ Book #, Page #	Instr.	System/ Expt. Name	Sample Treatment, Expt. Details	Image files	Coverage (ML)	Notes
20130411 - 20130420 Bk 2, pg 175-182		Temp. calibrations, STM stage				Pump-down only, removing window on bell-jar in between trials
20130424 Bk 2, pg 183	STM	HOPG ZYA	Cleave, unheated STM test	M1-M6		
20130505 Bk 2, pg 190	STM	HOPG ZYA + Cu	Cleave, unheated Clean surface	M1-M41		M6 some step edge decoration. Good step edge images
			23.5 W, 10 min	M42-M54	0.061	Good Cu statistics
			20 min (total)	M55-M61	0.17	
			40 min (total)	M62-M69	0.31	
20130506 Bk 2, pg 192	STM	HOPG ZYH + Cu	Cleave, unheated Clean surface	M1-M20		
			23.5 W, 10 min	M21-M24	0.17	Good Cu statistics
			20 min (total)	M25-M27	0.30	
			40 min (total)	M28-M35	0.52	M28-M30 tall step edge w/no islands
20130510 Bk 2, pg 196	STM	HOPG ZYA	Cleave, outgas @ 450 K STM test	M1-M19		ok
20130511 Bk 2, pg 199	STM	HOPG ZYA Atomic Res. Survey 1	None since previous day	M1-M154		M1-M11 fingerprint pattern and straight ridges. M22-M36 ridge close-up. M40-M46 step edges close up. M47-48 fingerprint. M50-154 atomic res survey.
20130512 Bk 2, pg 201	STM	HOPG ZYA	None since 5/10 STM test	M1-M17		Interesting morphology

Table 1 cont. – Experiment Log

Date/ Book #, Page #	Instr.	System/ Expt. Name	Sample Treatment, Expt. Details	Image files	Coverage (ML)	Notes
20130513 Bk 2, pg 202	STM	HOPG ZYA + Cu Incremental Heating Expt. #1 and temp calibration	Cleave, heat incrementally up to 950 K, 1.5 hrs (temp calibration) Clean surface	M1-M15		Great cauliflower
			Cu deposition 23.5 W, 10 min	M16-M20	1.8	Poor tunneling M18-M20, Cu on cauliflower
			20 min (total)	M21-M23	2.6	Poor tunneling
			40 min (total)	M24-M27	1.1	M24-M25 change in tip condition
			After 400 K, 15 min	M28-M33	0.82	Poor tunneling
			500 K	M34-M38	1.1	Poor tunneling
			600 K	M39-M48	0.65	M45 lava lamp
			700 K	M49-M52	0.79	
			800 K	M53-M59	0.78	Small feature visible after equalize
			900 K	M60-M79	0.045	M73, 25 nm high island
20130515 Bk 2, pg 207	XPS	HOPG ZYA + Cu post-heat	None since above			Very small Cu peak visible
20130516 Bk 2, pg 209	XPS					
20130516 Bk 2, pg 209	STM	HOPG ZYA	Cleave, unheated STM test	M1-M29		Interesting surface features and step edges. M20-29 carbon ribbon 1 atom high

Table 1 cont. – Experiment Log

Date/ Book #, Page #	Instr.	System/ Expt. Name	Sample Treatment, Expt. Details	Image files	Coverage (ML)	Notes
20130517 Bk 2, pg 211	STM	HOPG ZYA + Cu Incremental Heating Expt. #2	Cleave, outgas @ 500 K briefly Clean surface	M1-M4		
			Outgas @ 950 K, 1.5 hrs Clean surface	M5-M9		
			Cu deposition 23.5 W, 10 min	M10-M18	0.08	M14 hexagons, best image
			20 min (total)	M19-M26	0.21	
			40 min (total)	M27-M32	0.51	
			After 500 K, 15 min	M33-M38	0.48	M36 dragged island
			600 K	M39-M45	0.63	M40-M44 trench w/island
			700 K	M46-M64	0.46	M56-M63 small island w/scattering
			800 K	M65-M69	0.24	M65, M68, M69, 1 nm smooth ridge
			900 K	M70-M77	0	M72 big island. M74-M77 small islands w/scattering
			950 K, 1 hr	M78-M86	0	M81-M86 small islands w/scattering
20130519 Bk 2, pg 216	STM	HOPG ZYA + Cu, post-heat	None since above STM test	M1-M15		Poor tunneling. M10-M11 interesting multi-terrace features. M1, M12 small features visible w/equalize
20130520 Bk 2, pg 217	STM			M1-M15		Small islands visible
20130521 Bk 2, pg 219	STM			M1-M27		
			Heat to 500 K, briefly New Tip	M28-M54		Return of the Elder Tip. M52 good atomic res of small feature. M57-M58 are these features real?

Table 1 cont. – Experiment Log

Date/ Book #, Page #	Instr.	System/ Expt. Name	Sample Treatment, Expt. Details	Image files	Coverage (ML)	Notes
20130522 Bk 2, pg 223	STM	HOPG ZYA Atomic Res. Survey 2	Cleave, outgas @ 500 K Clean Surface	M1-M149		M91 best lattice image. M113 ripple over lattice. M144 interesting graphite terrace. M145-M147 intercalated defect. M148-M149 stripes are real.
	STM	HOPG ZYA + Cu	Cu deposition 23.5 W, 30 sec	M150-M184	0.0034	M167-M168 residue from sheared islands. M170 good image of tiny island.
20130523 Bk 2, pg 226	STM	HOPG ZYA	Cleaved, unheated surface	M1-M12		Small amount of step edge decoration
20130523 Bk 2, pg 226	XPS	HOPG ZYA	Same as above			
20130524 Bk 2, pg 228	STM	HOPG ZYA Incremental heating of clean surface	Heated to 500 K, 1 hr	M1-M13		More step edge decoration at higher temps, but not to the extent of "cauliflower". Inconclusive
			600 K	M14-M15		
			700 K	M28-M38		
			800 K	M39-M50		
			900 K	M51-M65		
			950 K	M66-M87		
20130524 Bk 2, pg 228	XPS	HOPG ZYA Full impurity scan	unheated	_full impurity scan		Nothing special
20130527 Bk 2, pg 228	XPS	HOPG ZYA Full impurity scan	After heating (above)	_full impurity scan		Nothing special

Table 1 cont. – Experiment Log

Date/ Book #, Page #	Instr.	System/ Expt. Name	Sample Treatment, Expt. Details	Image files	Coverage (ML)	Notes
20130529 Bk 2, pg 229	XPS	Cu NW on a-C/Si	Unheated			Messy spectra, Cu peaks visible
20130530 Bk 2, pg 230	STM	Cu NW on a-C/Si	Unheated	M1-M8		Could not image. Tip crash
20130601 Bk 2, pg 232	STM	HOPG ZYA + Cu post-heat	Prev. heated 20130522 w/small Cu STM test / tip check	M1-M40		M14-M18, M19 striations. M19-M31 intercalated defect vs. surface defect. M34 nice big image
20130602 Bk 2, pg 233	XPS	Cu NW on a-C/Si	Heat to 400 K, 1 hr (indirect heating)	_after 400K		Cu peaks visible No significant change
			500 K	_after 500K		
20130603 Bk 2, pg 235			600 K	_after 600K		
			700 K	_after 700K		
20130604 Bk 2, pg 236			800 K	_after 800K		
20130604 Bk 2, pg 236	STM	Cu NW on a-C/Si	From above	M1		Tip crash
20130605 Bk 2, pg 238	XPS	Cu NW on a-C/Si	Heat to 900 K, 1 hr	_after 900K		No significant change
20130605 Bk 2, pg 238	STM	Cu NW on a-C/Si	From above	M1-M8		Interesting images Inconclusive
20130606 Bk 2, pg 240	XPS	Cu NW on a-C/Si	930 K, over night	_after 60W		No significant change
20130606 Bk 2, pg 240	STM	Cu NW on a-C/Si	From above			Could not image
20130607 Bk 2, pg 240	XPS	a-C/Si	Heat @ 650 K	_clean		Clean reference
20130607 Bk 2, pg 240	STM	a-C/Si	From above	M1-M12		ok
20130608 Bk 2, pg 241	XPS	HOPG ZYA + Cu	Cleave, outgas @ 500 K Clean surface	_clean		Clean reference
			Cu deposition 23.5 W, 40 min	_w_Cu	Unknown	Cu peaks visible
20130609 Bk 2, pg 242	STM	a-C/Si + Cu	Heat @ 500 K, briefly Clean surface	M1-M4		
			Cu deposition 23.5 W, 10 min	M5-M7	Unknown	Cu not distinguishable in STM images
			20 min (total)	M8-M9		
			40 min (total)	M10-M15		
20130609 Bk 2, pg 242	XPS	a-C/Si + Cu	From above	a-C_w_Cu	Unknown	Cu peaks visible

Table 1 cont. – Experiment Log

Date/ Book #, Page #	Instr.	System/ Expt. Name	Sample Treatment, Expt. Details	Image files	Coverage (ML)	Notes
20130611 Bk 2, pg 243	XPS	Cu foil	Heat briefly @ 500 K	_before 1st sputter		Looks good, tiny O peak
			Anneal @ 830 K, 20 min	_after anneal		O peak gone
			Ar sputter 1.5 kV, 30 min Anneal @ 870 K, 45 min	_after 2nd anneal		Stronger signal, no O peak
20130611 Bk 2, pg 243	STM	Cu foil	After anneal @ 830 K (from above)	M1-M10		
			After sputter + anneal @ 870 K (from above)	M11-M30		Terraces visible
20130724 Bk 2, pg 246	STM	Cu NW on a-C/Si	Direct heating (current through sample) @ 1270 K, 30 min 1410 K, briefly	M1-M6		Rough surface
20130725 Bk 2, pg 248	STM	Cu NW on a-C/Si (MPI-3)	Direct heating @ 1430 K, 1 hr	Middle part		Sample appears melted on one side. A-C has drifted laterally? Middle part mountainous.
				Right side M1-M16		Right (melted) side. Plains w/crap on them.
				Left side M17-M20		Left (opaque) side. Rough
20130817 Bk 2, pg 252	STM	Ag NW on a-C/Si (MPI)	Resistively heated @ 1020 K, 2 hrs	M1-M34		Holes clearly visible (many)
20130822 Bk 2, pg 254	STM	Ag NW on a-C/Si (Ames)	Resistively heated @ 1020 K, 2 hrs	M1-M34		Large area searched. Mostly bare, two big holes found (donut shape, compare w/SEM images of Ag NW samples)
20130929 Bk 2, pg 255	STM	HOPG ZYA + Cu	Cleave, outgas @ 500 K Clean surface	M1-M12		Defects on clean surface visible
			Cu deposition 23.5 W, 10 min	M13-M28	Unknown	Poor tunneling, not used
			20 min (total)	M29-M34		
			40 min (total)	M35-M39		

Table 1 cont. – Experiment Log

Date/ Book #, Page #	Instr.	System/ Expt. Name	Sample Treatment, Expt. Details	Image files	Coverage (ML)	Notes
20130930 Bk 2, pg 256	STM	HOPG ZYA + Cu	Cleave, outgas @ 500 K Clean surface	M1		
			Cu deposition 28 W, 5 min	M2-M13	Unknown	Experiment aborted, sample plate malfunction
20131002 Bk 2, pg 260		Installed e-beam heater on manipulator				Very temperamental
20131014 – 20131019 Bk 2, pg 264-277		Temp calibrations w/ e-beam heater		20131023_temp calibrations_e-beam heater		
20131105 Bk 2, pg 278	STM	HOPG ZYH	Cleave, unheated STM test	M1-M21		
20131106 Bk 2, pg 279	STM	HOPG ZYH + Cu and heating	From above, outgas @ 800 K Clean surface	M1-M2		
			Cu deposition 30 W, 1 min	M3-M8	Unknown	Tip effects, poor tunneling
			2 min (total)	M9-M16		
			4 min (total)	M17-M26		
			8 min (total)	M27-M31		
			16 min (total)	M32-M37		
			Heat @ 1300 K, 15 min	M38-M55		
20131107 Bk 2, pg 282	STM	HOPG ZYH + Cu and heating	Cleave, outgas @ 800 K Clean surface	M1-M5		
			Cu deposition 35 W, 1 min	M6-M12	0.95	High island density
			5 min (total)	M13-M17	3.9	M16-M17 µm x µm image with high island density
			Heat @ 1300 K	M18-M25		Poor tunneling

Table 1 cont. – Experiment Log

Date/ Book #, Page #	Instr.	System/ Expt. Name	Sample Treatment, Expt. Details	Image files	Coverage (ML)	Notes
20131113 Bk 2, pg 285	STM	HOPG ZYA + Cu	Cleave, outgas @ 800 K Clean surface	M1-M6		
			Cu deposition 32 W, 10 sec	M7-M26	0.096	Good statistics ***Begin routine double-imaging**
			20 sec (total)	M27-M46	0.21	
			40 sec (total)	M47-M66		Poor tunneling, islands not imaging
			80 sec (total)	M69-M89		
			160 sec (total)	M90-M97		
20131115 Bk 2, pg 287	STM	HOPG ZYA + Cu and heating		M1-M26	0.78	Islands reappeared mid-scan
			From above, heat @ 1200 K, 1.5 hrs	M27-M53		Good images of residues
20131117 Bk 2, pg 288	STM	HOPG ZYA + Cu	Cleave, outgas @ 800 K Clean surface	M1-M2		
			Cu deposition 34 W, 40 sec	Area 1 M3-M10 Area 2 M11-M14	Unknown	Tip effects changing mid-image
20131118 Bk 2, pg 289						Adjusted Cu crucible upward w/respect to filament
20131125 Bk 2, pg 294	STM	HOPG ZYA + Cu	Cleave, outgas @ 800 K Clean surface	M1-M8		
			Cu deposition 30 W, 10 sec	M9-M10	0	Evaporator behavior has changed
			35 W, 10 sec	M11-M30	0.076	ok
			35 W, 20 sec (total)	M31-M34		Interrupted by power outage
20131126 Bk 2, pg 295	STM	HOPG ZYA + Cu and heating	Cleave, outgas @ 800 K Clean surface	M1-M16		
			Cu deposition 34 W, 5 sec	M17-37 M40-43	0.0097	good
			Quick a-C test	M38-M39		
			Heat @ 1200 K	M44-M53		
20131213 Bk 3. Pg 1	STM	HOPG ZYA	Cleav, unheated STM test	M1-M11		Weird textured feature
20140109 Bk 3, pg 3	STM	HOPG ZYA	STM test after vacuum break	M1-M24		STM Functional
20140114 Bk 3, pg	STM	HOPG ZYA	Heat @ ?? STM test	M1-M15		ok

Table 1 cont. – Experiment Log

Date/ Book #, Page #	Instr.	System/ Expt. Name	Sample Treatment, Expt. Details	Image files	Coverage (ML)	Notes
20140115 Bk 3, pg 4	STM	HOPG ZYA	STM test	M1-M4		M1 interesting morphology
20140117 Bk 3, pg 5	STM	HOPG ZYA	After pump-down STM test	M1		Functional
20140129 Bk 3, pg 6	STM	HOPG ZYA + Cu Incremental Heating Expt. #3	Cleave, outgas @ 1300 K Clean surface	M1-M2		
			Cu deposition 35 W, 1 min (300 K)	M3-M18	1.01	
			After 500 K, 15 min	M19-M28	0.86	
			600 K	M29-M40	0.92	
			700 K	M41-M56	1.04	
			800 K	M57-M71	0.85	
			900 K	M72-M82	0.23	Significant coarsening
			1300 K, 20 min	M83-M88		
20140215 Bk 3, pg 9	STM	HOPG ZYA + Cu Ion Damage Expt. #1	Cleave, outgas @ 800 K Clean surface	M1-M4		Fewer islands than expected, but OK
			Cu deposition 38 W, 10 sec HV ON, Fil. ON	M5-M19	0.17	Control #1
20140216 Bk 3, pg 11			Cleave, outgas @ 800 K Clean surface	M1-M2		Experimental runs – good, no terrace nucleation. M12 tall ridge on step edges
			Cu deposition 38 W, 10 sec HV OFF, Fil. OFF	M3-M10		
			Cleave, outgas @ 800 K Clean surface	M11		
			Cu deposition 38 W, 10 sec HV ON, Fil. OFF	M12-M15		
			Cleave, outgas @ 800 K Clean surface	M16		
			Cu deposition 38 W, 10 sec HV OFF, Fil. ON	M17-M18		
20140217 Bk 3, pg 13			Cleave, outgas @ 800 K Clean surface	M1-M2		
			Cu deposition 38 W, 10 sec HV ON, Fil. ON	M3-M15	0.26	Control #2

Table 1 cont. – Experiment Log

Date/ Book #, Page #	Instr.	System/ Expt. Name	Sample Treatment, Expt. Details	Image files	Coverage (ML)	Notes
20140218 Bk 3, pg 14	STM	HOPG ZYA + Cu Ion Damage Expt. #1	Cleave, outgas @ 800 K Clean surface	M1-M4		
			Cu deposition 38 W, 10 sec HV ON, Fil. ON	M5-M13	0.12	Control #3
20140218 Bk 3, pg 14	STM	HOPG ZYA + Cu Ion Damage Expt. #2	Cleave, outgas @ 800 K Clean surface	M14-M15		
			Cu deposition 48 W, 10 sec HV ON, Fil. ON	M16-M26	2.8	Control #1
			Cleave, outgas @ 800 K Clean surface	M27-M28		Experimental runs – good. M1-M6 triple step edge, both before and after Cu
			Cu deposition 48 W, 10 sec HV ON, Fil. OFF	M29-M38		
20140219 Bk 3, pg 15			Cleave, outgas @ 800 K Clean surface	M1		
			Cu deposition 48 W, 10 sec HV OFF, Fil. ON	M2-M7		
			Cleave, outgas @ 800 K Clean surface	M8-M9		
			Cu deposition 48 W, 10 sec HV OFF, Fil. OFF	M10-M13		
20140220 Bk 3, pg 17			Cleave, outgas @ 800 K Clean surface	M1-M5		
			Cu deposition 48 W, 10 sec HV ON, Fil. ON	M6-M16	3.3	Control #2
20140221 Bk 3, pg 18	STM	HOPG ZYA + Cu	Cleave, outgas @ 800 K Clean surface	M1		
			Cu deposition 35 W, 10 sec	M2-M7	Low	M6 very small islands on step edge
			Mount new sample Cleave, outgas @ 800 K Clean surface	M8-M13		

Table 1 cont. – Experiment Log

Date/ Book #, Page #	Instr.	System/ Expt. Name	Sample Treatment, Expt. Details	Image files	Coverage (ML)	Notes
20140223 Bk 3, pg 19	STM	HOPG ZYA + Cu	Cleave, outgas @ 800 K Clean surface	M1-M2		
			Cu deposition 23.5 W, 10 min	M3-M7	Low	Only slight decoration on step edge
201302224 Bk 3, pg 20	STM	HOPG ZYA + Cu and heating	Cleave, outgas @ 800 K Clean surface	M1-M6		
			Cu deposition 32 W, 10 sec	M7-M10		Ineffective Evaporator behavior has changed again
			35 @, 1 min	M11-M16		
			Re-cleave, outgas @ 800 K Clean surface	M15-M16		
			Cu deposition 48 W, 10 sec	M17-M32	0.93	
			Heat @ 1300 K, 1 hr	M33-M36		M35 good pancakes
20140225 Bk 3, pg 22	STM	HOPG ZYA post-heated surface + Cu	None since above	M1-M55		Great images of various kinds of defects. Pancakes
			Cu deposition 35 W, 1 min	M56-M70	0.023	Possible QSE?
20140226 Bk 3, pg 23	STM	HOPG ZYA + Cu Incremental Heating Expt. #4	Cleave, outgas @ 800 K Clean surface	M1-M3		
			Cu deposition 40 W, 1 min	M4		Not enough Cu
			10 min (total)	M5-M15	0.60	
			After 500 K, 15 min	M16-M25	0.38	
			600 K	M26-M35	0.45	
			700 K	M36-M52	0.16	

Table 1 cont. – Experiment Log

Date/ Book #, Page #	Instr.	System/ Expt. Name	Sample Treatment, Expt. Details	Image files	Coverage (ML)	Notes
20140227 Bk 3, pg 25	STM	HOPG ZYA + Cu Incremental Heating Expt. #4 Cont.	800 K	M1-M15	0.064	
			900 K	M16-M24		M18 faceted Cu island
			1300 K, 1 hr	M25-M53		M31-M52 Very nice moiré
		Post-heated surface + Cu 20 atom Experiment	Cu deposition 35 W, 4 sec	M54-M66	Very low	Tiny islands difficult to image
20140401 Bk 3, pg 29		Flux monitor + shutter videos/ experiments		See "ion flux videos" folder		
20140402 Bk 3, pg 30	XPS	Cu foil	Heat to 600 K, briefly			Ag contamination
20140403 Bk 3, pg 31	STM	Cu foil	Sputter 1 kV, 3 min Anneal @ 900 K, cool @ 3 K/min	M1-M17		Blotchy, some terraces
20140403 Bk 3, pg 31	XPS	Cu foil	From above			Ag gone, tiny O peak
20140405 Bk 3, pg 31	STM	Cu foil	2 sputter/anneal cycles (as above)	M1-M3		ok
20140407 Bk 3, pg 36	STM	Cu foil Cu on Cu calibration	Sputter 1.5 kV, 15 min, anneal @ 900 K, cool @ 3 K/min Clean surface	M1-M8		
			Cu deposition 35 W, 5 min	M9-M20	> 1	Too much Cu (islands on islands) M16-M18 double tip
20140408 Bk 3, pg 38	STM	Cu foil Cu on Cu calibration	Sputter 1.0 kV, 9 min, anneal as above Clean surface	M1		Good ~ 0.04 ML/min
			Cu deposition 32 W, 1 min	M2-M4	0.05	
			2 min (total)	M5-M7	0.08	
			3 min (total)	M8-M9	0.12	
			5 min (total)	M10-M12	0.18	
			10 min (total)	M13-M16	0.38	

Table 1 cont. – Experiment Log

Date/ Book #, Page #	Instr.	System/ Expt. Name	Sample Treatment, Expt. Details	Image files	Coverage (ML)	Notes
20140408 Bk 3, pg 38	STM	HOPG ZYA + Cu Calibration	Cleaved previously, heat @ 800 K, brief Clean surface	M17-M20		Good clean surface images
			Cu deposition 32 W, 1 min	M21-M29	0.13 / 0.034	Hemisphere / sphere model
			2 min (total)	M30-M35	0.40 / 0.010	
			3 min (total)	M36-M42	0.62 / 0.15	
			5 min (total)	M43-M51		Poor tunneling
20140410 Bk 3, pg 42	STM	Cu foil Cu on Cu calibration, HV ON vs. OFF	Sputter 1.0 kV, 9 min Anneal @ 900 K, cool @ 3 K/min Clean surface	M1-M3		Great images ~1.8 ML/min Coverage is 74 % w/HV OFF
			Cu deposition 38 W, 10 sec HV ON	M4-M9	0.30	
			20 sec (total)	M10-M14	0.60	
			Anneal @ 900 K, cool @ 3 K/min Clean surface	M15-M17		
			Cu deposition 38 W, 10 sec HV OFF	M18-M22	0.26	
			20 sec (total)	M23-M26	0.40	
20140411 Bk 3, pg 45	STM	HOPG ZYA + Cu Ion Damage Expt. #3	Cleaved prev., heat to 800 K briefly Clean surface	M1-M2		Good intermediate coverage 1.3 ML/min
			Cu deposition 43 W, 10 sec HV ON, Fil. ON	M3-M12	0.22	
			Cleave, outgas @ 800 K Clean surface	M13-M16		
			Cu deposition 43 W, 10 sec HV OFF, Fil. OFF	M17-M20		
			Cleave, outgas @ 800 K Clean surface	M21		
			Cu deposition 43 W, 10 sec HV ON, Fil. ON	M22-M25		

Table 1 cont. – Experiment Log

Date/ Book #, Page #	Instr.	System/ Expt. Name	Sample Treatment, Expt. Details	Image files	Coverage (ML)	Notes
20140413 Bk 3, pg 47	STM	Cu foil Cu on Cu calibration HV + Fil. ON vs. OFF	Sputter 1.0 kV, 9 min Anneal @ 900 K, cool @ 3 K/min Clean surface	M1		Good images Coverage is 74 % ± 5 % w/ HV + Fil. OFF
			Cu deposition 38 W, 10 sec HV ON, Fil. ON	M2-M5		
			20 sec (total)	M6-M9		
			Recleave, outgas @ 800 K	M10		
			Cu deposition 38 W, 10 sec HV OFF, Fil. OFF	M11-M15		
			20 sec (total)	M16-M23		
20140416 Bk 3, pg 49	STM	HOPG ZYA + Cu and heating, Cu deposition on post-heated surface	From above, Cu deposition, 43 W, 1 min Heat @ 1200 K, 15 min (post-heated surface)	M1-M7		
			Deposit additional Cu 43 W, 2 min (total) Heat @ 1300 K, 15 min (post-heated surface)	M8-M11		
			Cu deposition 32 W, 1 min	M12-M13		Poor tunneling
20140417 Bk 3, pg 51	STM	HOPG ZYA + Cu on post-heated surface Incremental Heating Expt. #5 and QSE hunt	Cleave, outgas @ 800 K Cu deposition 43 @, 2 min Heat @ 1200 K, 30 min (“clean” post-heated surface)	M1-M5		Good statistics, no apparent QSE
			Cu deposition 25 W, 1 min	M6-M20	0.074	
			After 400 K	M21-M32	0.079	
			500 K	M33-M46	0.058	
			600 K	M47-M60	0.059	
			700 K	M61-M78	0.069	
			800 K	M79-M84	0.056	
			900 K	M85-M86	0.0008	
			1200 K, 10 min			Wobble stick began leaking

Table 1 cont. – Experiment Log

Date/ Book #, Page #	Instr.	System/ Expt. Name	Sample Treatment, Expt. Details	Image files	Coverage (ML)	Notes
20140501 Bk 3, pg 59	STM	HOPG ZYA + Cu on post-heated surface, QSE hunt	From previous, Heat @ 1200 K, 30 min "Clean" post-heated surface	M1-M9		Not great, islands a little too big. No QSE
			Cu deposition 27.5 W, 1 min	M10-M14	0.039	
20130505 Bk 3, pg 63	STM	HOPG ZYA + Cu on post-heated surface, QSE hunt	Cleaved 2 days prior Deposit Cu, 48 W, 1 min, heat @ 1200 K, 30 min "clean" post-heated surface	M1-M5 (M6 is test on a-C)		Poor tunneling
			Cu deposition 22 W, 10 sec	M7-M11		
			1 min (total)	M12-M16		
20130506 Bk 3, pg 63	STM	HOPG ZYA + Cu on post-heated surface, QSE hunt	From above, heat @ 1200 K, 15 min "clean" post-heated surface	M1-M7		
			Cu deposition 22 W, 2 min	M8-M11	0.021	Only a couple of good images
20130508 Bk 3, pg 68	STM	HOPG ZYA + Cu on post-heated surface, QSE hunt	Cleaved 1 day prior, deposit Cu, 50 W, 10 sec Heat @ 1300 K, 30 min "clean" post-heated surface	M1-M4		
			Cu deposition 22 W, 2 min	M5-M12	0.020	Not great
20140509 Bk 3, pg 69	STM	HOPG ZYA + Cu on post-heated surface, QSE hunt	From above, heat @ 1300 K, 10 min "clean" post-heated surface			Poor tunneling in general. M6 beautiful mystery image
			Cu deposition 22 W, 1 min	M1-M4		
			Heat @ 1300 K, 10 min			
			Cu deposition 22 W, 30 sec	M5-M12		

Table 1 cont. – Experiment Log

Date/ Book #, Page #	Instr.	System/ Expt. Name	Sample Treatment, Expt. Details	Image files	Coverage (ML)	Notes
20140513 Bk 3, pg 71	STM	a-C/Si (Ames) + Cu and heating	Outgas @ 800 K Clean surface	M1-M13		Great
			Cu deposition 43 W, 10 sec	M14-M17	0.22	
			1 min (total)	M18	1.3	One good one. Marked change in surface morphology
			Heat @ 800 K, 20 min	M19-M30	0.08	Coverage based on STM images. Sparse tall islands, substrate undulating
20140513 Bk 3, pg 71	XPS	a-C/Si (Ames) + Cu and heating	Corresponding to the files above	_ok (clean surface)		No Cu visible
				_43W 10sec	0.22	Cu visible
				_43W 1 min	1.3	Marked increase in Cu
				_43W 1 min_after 800K	0.08	Very little Cu visible

ACKNOWLEDGEMENTS

I would like to express my sincere gratitude to Professor Patricia A. Thiel for her support and guidance throughout my graduate studies. She is a consummate professional, and taught me what it means to be a responsible, conscientious, and resourceful scientist. Knowing that I aspired to be an educator, when the opportunity to pursue a lectureship position at Iowa State University appeared, she encouraged me to apply, and allowed me to accelerate my degree in order to accept the position. I will be forever grateful for that opportunity. Pat has been a wonderful supervisor, mentor, and friend. Thank you, Pat.

I would also like to thank the members of my Program of Study Committee: Jim Evans, Sam Houk, Emily Smith, and Joe Burnett for their support and guidance.

I also want to acknowledge former and current Thiel group members for their help, assistance, and camaraderie. When I first joined the group, Alex Belianinov, Chad Yuen, and Dahai Shao welcomed me into their office space and trained me in the ways of UHV. Dahai also assisted with some of the data analysis in this work. Shortly after I joined the group, we hired a scientist, Mark Wallingford. Mark and I trained together for nearly a year, where we developed a unique combination of mutual respect and moderate annoyance with one another. Further thanks go out to Emma Kwolek, my successor in the ongoing metal-on-graphite research, who made substantial contributions to this thesis work, and who was also a good office-mate. I would also like to thank Baris Unal for his advice and expertise, and Selena Russell and Holly Walen for general helpfulness and support.

Furthermore, special thanks to our collaborator Dr. Gunther Richter of the Max Planck Institute for Intelligent Systems in Stuttgart, Germany, for hosting me for three weeks and

sharing his instrumentation and his knowledge of metal nanowires. A significant portion of the work in this thesis was performed in Stuttgart under Gunther's tutelage. Thanks, also, to the members of Gunther's group who made my stay in Germany so enjoyable, especially Christian Kappel and Ilse Lakemeyer.

I would also like to acknowledge members of the Ames Laboratory for their assistance. Special thanks to Jim Anderegg for his generous donation of HOPG samples, and also for his time in helping us troubleshoot various instruments over the years. Thanks to Ryan Ott and Matt Besser for conducting the magnetron sputtering experiments here in Ames. Thanks to Jim Evans, C. Z. Wang, Huaping Lei, and Yong Han for their theoretical work which was critical to this thesis and related publications. Further thanks go out to fellow experimentalists Michael Tringides, Myron Hupalo, and Matt Hershberger who provided critical insight and assistance with STM imaging of these very challenging metal-on-carbon systems.

Not to be forgotten, sincere thanks to my friends for helping me retain my sanity during the long Iowa winters and long experimental runs. Specifically, Mark Juetten, Jonna Berry, Paul Cole, and Zak Weinstein have been great companions to me, and I hope they always will be. I should also acknowledge my very special friends James and Amber Morrighan, who have included me as a part of their wonderful growing family, and who are the reason I applied to Iowa State University. They also gave me a cat.

In addition, my parents Ralph and Teresa, who share the dedication of this work, and my brother Michael, have supported me unconditionally throughout this entire process, and for that I am grateful.

Last, but certainly not least, my heartiest salute goes out to the gentlemen at the weekly poker game (who shall remain anonymous). Nearly every Saturday night, I had the opportunity

to relieve the stresses of research by exchanging money and banter with this exceptional group of idiots. There is no better home-game, anywhere. May it never die!